



Thesis submitted for the degree of  
Master of Philosophy at the  
University of Leicester

Mapping of spatiotemporal changes across the East African Rift  
System to identify geothermal anomalies using MODIS land  
surface temperatures

Sadie Holmes

University of Leicester

Department of Physics and Astronomy

Submitted: 2017

# **Declaration**

I hereby declare that no part of this thesis has been previously submitted to this or any other university as part of the requirement for a higher degree. The work within this document has been conducted by the undersigned except for contributions where acknowledged in the text.

Sadie Holmes, September 2016

**MAPPING OF SPATIOTEMPORAL CHANGES ACROSS THE EAST  
AFRICAN RIFT SYSTEM TO IDENTIFY GEOTHERMAL ANOMALIES  
USING MODIS LAND SURFACE TEMPERATURES**

**Sadie Holmes**

**Abstract**

A range of satellite datasets, including MODIS land surface temperature (LST), are used to identify geothermal anomalies associated with rift basins across the East African Rift System. Monthly and yearly absolute LST means are generated from January 2003 to December 2013 and show regions of warmer LSTs in relevant basins. However, without auxiliary data it is not possible to show that these are related to geothermal anomalies. Two approaches are applied to delineate the LST more clearly - principal component analysis (PCA) and normalisation of the LST with respect to elevation. The first technique uses PCA to delineate the known physical parameters influencing LST and reveals elevation to be dominant. Consequently, steps have been taken to minimise the effects on LST. This has been achieved via normalisation, whereby absolute LST is recalculated, using linear regression analysis, to equivalent normalised LST at an elevation of 0 m. Several previously masked areas, including the Ethiopian Dome, have since been revealed as warmer and with an increased likelihood of relationship to geothermal heat flux since they correspond to emissivity and tectonic patterns. Note the impressive manner in which volcanoes including Mount Elgon, cold in absolute LST because of elevation, are also identified as warmer post normalisation. Caution must still be exercised with respect to the warm anomalies in normalised LST, as these can still not be conclusively confirmed as geothermal anomalies. A restricted PCA of the normalised LST shows that these are still sensitive to emissivity as expected but particularly in a well-defined region around Lake Turkana. In conclusion, the likelihood of identifying a geothermal anomaly is best associated with the normalised LST and where high frequency spatial structure is observed. Identified regions should be checked against the restricted PCA. Future work should incorporate the use of other indicators of geothermal activity or heat flux to better identify the LST variance that corresponds to geothermal anomalies.

# **Acknowledgements**

I would like to thank my supervisors Darren Ghent, John Remedios and Martin Insley for their guidance and support. I would also like to acknowledge Tullow Oil plc for funding this project.

# Contents Page

List of Tables .....	v
List of Figures .....	viii
Acronyms and Abbreviations .....	xviii
Geological timeline.....	xx
1. Introduction .....	1
1.1 Tectonic Setting .....	4
1.1.1 Eastern Branch.....	10
1.1.2 Western Branch.....	13
1.1.3 Lithology.....	13
1.1.4 Petroleum Potential.....	14
1.1.5 Basin Modelling.....	19
1.1.6 Geothermal Gradients and Systems .....	21
1.2 Physiography.....	25
1.3 Climate .....	30
1.4 Summary .....	34
2. Remote Sensing and Physical Parameters .....	35
2.1 Radiative Transfer .....	35
2.2 Land Surface Temperature .....	38
2.3 Contributing Factors.....	40
2.3.1 Thermal Inertia .....	41
2.3.2 Thermal Conductivity .....	42
2.3.3 Specific Heat Capacity.....	46
2.3.4 Thermal Diffusivity .....	47
2.3.5 Emissivity .....	47

2.3.6	Vegetation and Land Cover .....	48
2.3.7	Hydrological Parameters.....	49
2.3.8	Topography and Geolocation.....	50
2.3.9	Satellite Viewing Geometry.....	51
2.4	Targeting Hydrocarbon Basins .....	51
2.5	LST Studies.....	52
2.6	Summary .....	58
3.	Methods .....	60
3.1	Instruments and Data Selection.....	60
3.1.1	MODIS.....	60
3.1.2	Shuttle Radar Topography Mission .....	65
3.1.3	ATSR LST Biome V2: GlobCover Derivative.....	65
3.1.4	USGS ESRI Shape Files .....	67
3.1.5	Tropical Rainfall Measurement Mission .....	68
3.1.6	Climate Change Initiative Soil Moisture .....	70
3.2	Analysis.....	71
3.2.1	Absolute LSTs .....	71
3.2.2	Host Rock-Basin Comparisons .....	75
3.2.3	Principal Component Analysis .....	76
3.2.4	Normalised LSTs with respect to elevation .....	81
3.2.5	Climatology and Anomalies .....	85
3.2.6	Lithological Comparison .....	85
3.2.7	Summary .....	86
4.	Results and Discussion: Part 1 .....	88
4.1	Absolute LSTs.....	89
4.1.1	Monthly Mean LSTs .....	89

4.1.2	Absolute Yearly Means .....	104
4.1.3	Discussion .....	115
4.1.4	LST Means: Limitations and Uncertainties .....	117
4.2	Host Rock-Basin Comparison .....	119
4.2.1	Specific Basins .....	124
4.2.2	Discussion .....	128
4.3	Full Principal Component Analysis .....	132
4.3.1	Spatial Variation .....	132
4.3.2	Temporal Variation .....	140
4.3.3	Understanding the Temporal Variation .....	143
4.3.4	Discussion .....	145
4.4	Summary of Results .....	147
5.	Results and Discussion: Part 2 .....	148
5.1	Normalised LSTs with respect to elevation .....	148
5.1.1	Land Cover-Elevation-LST Analysis .....	148
5.1.2	Normalisation for 2006 Yearly Means .....	158
5.1.3	Absolute-Normalised Transects .....	160
5.1.4	Host Rock-Basin Comparison .....	167
5.1.5	Discussion .....	171
5.2	Absolute and Normalised Climatology .....	173
5.2.1	Discussion .....	177
5.3	Lithological Comparison .....	178
5.3.1	Discussion .....	180
5.4	Restricted Principal Component Analysis .....	181
5.4.1	Spatial Variation .....	181
5.4.2	Discussion .....	182

5.5	Summary of Results .....	186
6.	Conclusions and Future Work .....	187
6.1	Summary of Findings .....	187
6.2	Implications of this study .....	189
6.3	Future Recommendations.....	190
6.3.1	Improvement of absolute LST dataset .....	190
6.3.2	Uncertainty Analysis.....	191
6.3.3	Verification of Geothermal Anomalies.....	192
6.3.4	Progression of PCA .....	192
6.3.5	Progression of Normalisation of LST.....	193
6.3.6	Alternative LST Sensors .....	195
6.4	Summary of Conclusions .....	197
	Appendix.....	199
	References.....	231

# List of Tables

Table 1: Basin details as shown in Figure 5 and as provided by Tullow Oil plc. A full list of basins can be found in Appendix 1.....	8
Table 2: Lithology classifications corresponding to Figure 10. Specific details of lithology are taken from Dunkley et al. (1993).....	15
Table 3: Geothermal activity summary for Quaternary volcanoes within the Eastern branch rift axis as modified from Dunkley et al. (1993).....	23
Table 4: Summary table of significant lakes within the EARS.....	29
Table 5: Thermal conductivities of common rock types. All values vary depending on porosity, schistosity*, etc. Data ranges are from Schön (2015).....	42
Table 6: Thermal conductivities of rock types affected by various schistositities. Data ranges are from Schön (2015) as in Cermak and Rybach (1982).....	46
Table 7: Thermal conductivities of superficial deposits, which vary dependent upon the saturation of the sediments (BGS, 2011).....	46
Table 8: LST studies are summarised, detailing datasets used, area of interest and the aim of the study. All are discussed in further detail within the text.....	53-54
Table 9: Satellite and instrument specifications for the MODIS dataset (NASA, 2016).....	61
Table 8: Longitudes and latitudes that define tiles used within this analysis. Tiles are named according to the most dominant country or geographical feature present.....	64
Table 9: ALB2 land cover classification, detailing the biome that each ALB2 number describes (NASA LP DAAC. USGS EROS, 2001; Ghent, 2012).....	67
Table 10: Land cover groups used within the Land cover- Elevation-LST analysis are now shown. Land cover groups have been selected from the University of Leicester ALB2 dataset, as explained previously in chapter 3.1.3.....	84

Table 11: Yearly MODIS LSTs for the Aqua dataset, across the Turkana region that is $10^{\circ} \times 10^{\circ}$ grid of $0.01^{\circ}$ resolution.....	113
Table 12: Mean, maximum and minimum night time yearly MODIS LSTs for the absolute Aqua dataset for host rock to basins, across the Turkana region tile that is a $10^{\circ} \times 10^{\circ}$ grid of $0.01^{\circ}$ resolution.....	122
Table 13: Pearson correlation coefficients and gradients for the Turkana tile basins. MODIS LSTs are from the Aqua dataset for night time 2006.....	125
Table 14: PCA results for the Turkana region of MODIS LST Aqua data for June 2006 day time.....	133
Table 15: PCA results for the Turkana region of MODIS LST Aqua data for June 2006 night time.....	133
Table 16: PCA results for the Turkana region of MODIS LST Aqua data for December 2006 day time.....	136
Table 17: PCA results for the Turkana region of MODIS LST Aqua data for December 2006 night time.....	136
Table 18: Gradients and Pearson correlation correlations for anomalous areas as identified from PCA.....	140
Table 19: Gradients and correlations coefficients between MODIS LST and elevation, as calculated by IDL functions referred to in the text for June 2006.....	149
Table 20: Gradients and Pearson correlation coefficients (R) between elevation and the 2006 yearly MODIS LST means across the $10^{\circ} \times 10^{\circ}$ grid of Turkana region at $0.01^{\circ}$ resolution.....	154
Table 21: Gradients and Pearson correlation coefficients (R) for 2003 through to 2013 between elevation and the yearly MODIS LST means across the $10^{\circ} \times 10^{\circ}$ grid of Turkana region at $0.01^{\circ}$ resolution.....	155

Table 22: Maximum and minimums for the absolute, yearly MODIS LST means and the normalised, yearly MODIS LST means with respect to the SRTM elevation across the $10^{\circ} \times 10^{\circ}$ grid of Turkana region at $0.01^{\circ}$ resolution.....	160
Table 23: Mean, maximum and minimum night time yearly MODIS LSTs, for the Aqua normalised dataset, across the $10^{\circ} \times 10^{\circ}$ grid of the Turkana region at $0.01^{\circ}$ resolution, for host rock and basins.....	170
Table 24: Normalised PCA results for the Turkana region of MODIS LST Aqua data for December 2006 day time.....	183
Table 25: Normalised PCA results for the Turkana region of MODIS LST Aqua data for December 2006 night time.....	183

# List of Figures

Figure 1: Google Earth (2016) image highlighting the EARS area of interest.....	2
Figure 2: EARS relief map as taken from Kearey et al. (2013).....	4
Figure 3: Evolutionary stages of an intracontinental rift as adapted from Ebinger (2005).....	5
Figure 4: Sketch of the currently favoured geodynamic processes occurring beneath the EARS as taken from Civiero et al. (2015).....	6
Figure 5: Google earth (2016) image of the EARS with rift basin outlines (orange), as provided by Tullow Oil plc.....	7
Figure 6: Elevation of the Afar region.....	9
Figure 7: Cross section of the EARS showing the separate branches and the thick Archean craton as taken from Wichura et al. (2010).....	10
Figure 8: Eastern branch elevation.....	11
Figure 9: Elevation of the western branch.....	12
Figure 10: Geological map as taken from Tullow Oil plc ESRI ArcGIS shape files. Lithology has been determined from the United States Geological Survey (USGS).....	14
Figure 11: Locality of the Albertine, Lokichar and Tanganyika basins, as identified from Tullow Oil plc (2016) ESRI ArcGIS shape files.....	16
Figure 12: Location of sites with confirmed hydrocarbons as reported by Tullow Oil plc (2014).....	17
Figure 13: The oil and gas window as taken from McCarthy et al. (2011). Catagenesis is the process in which the chemical bonds in kerogens are cracked and form hydrocarbons.....	18

Figure 14: Example of a typical oil field taken from McCarthy et al. (2011), showing the geological features necessary for successful accumulation, migration and trapping.....	19
Figure 15: Schematic diagram showing typical surface expressions as a result of underlying hydrocarbons from Yang et al. (2000) (after Duchscherer, 1982).....	20
Figure 16: Geothermal gradients (red) within the Earth as adapted from Leigh University (2010) and Kearney et al. (2013).....	22
Figure 17: Eastern branch of the EARS, showing geothermal features taken from Lagat (2010).....	24
Figure 18: Cross sections displaying elevation along axes and cross axes, as taken from Corti (2016). Topography within this dataset has been taken from the Shuttle Radar Topography Mission (SRTM) (resolution: 90 m).....	26
Figure 19: Topography is taken from the Shuttle Radar Tomography Mission (SRTM) (resolution: 100 m).....	27
Figure 20: Hypsographic DEM of the EARS as taken from Chorowicz (2005), showing the locality of faults within the rift system.....	28
Figure 21: Mean annual rainfall with elevation for the Turkana-Baringo area as taken from Allen and Darling (1992).....	30
Figure 22: Schematic map showing the overall ITCZ migration, as taken from Danley et al. (2012).....	31
Figure 23: Schematic diagram taken from Verschuren et al. (2009) showing the influence of the ITCZ across the EARS.....	32
Figure 24: Typical rainfall and temperatures for central EARS region as taken from Verschuren et al. (2009).....	33
Figure 25: Inter-hemispheric solar insolation between 20° N and 20° S latitude as taken from Verschuren et al. (2009).....	33

Figure 26: Graph showing blackbody thermal emission intensity as a function of wavelength for absolute temperatures as taken from Carroll and Ostlie, 2006.....	36
Figure 27: Schematic diagram of the Earth’s energy budget as taken from Trenberth et al. (2009).....	39
Figure 28: Global maximum LSTs from 2003 to 2009 measured by NASA’s earth observation instrument MODIS, as taken from NASA Earth Observatory (2016).....	40
Figure 29: Diurnal cycles where $\Delta T$ refers to thermal inertia taken from Rees (2013).....	41
Figure 30: Thermal conductivities varying as a function of porosity and composition as taken from Schön (2015) after Griffiths et al. (1992).....	43
Figure 31: Compositional diagrams showing mineral thermal conductivities as adapted from Clauser and Huenges (1995).....	44
Figure 32: Typical broadband surface albedo, as modified from Rees (2003).....	45
Figure 33: Specific heat capacity for magmatic and sedimentary rocks as taken from Schön (2015). Data originates from Vosteen and Schellschmidt (2003).....	47
Figure 34: Typical emissivities of materials of normal incidence in the range 3 $\mu\text{m}$ to 15 $\mu\text{m}$ taken from Rees (2013). Data is averaged from a large sample of MODIS datasets.....	48
Figure 35: Elevation versus LST (for September 2004) across the Afar Depression as taken from Miliareisis (2009).....	50
Figure 36: PCA results as taken from Miliareisis (2009).....	57
Figure 37: Flow diagram of the initial pre-processing steps applied to the MODIS dataset prior to the implementation of analyses within this thesis.....	62

Figure 38: ALB2 land cover as generated at the University of Leicester; for the EARS mapped on a 0.01° x 0.01° resolution grid ((NASA LP DAAC USGS EROS, 2001; Ghent, 2012).....	66
Figure 39: Lithology for the Turkana region, regrided from Tullow Oil plc ESRI ArcGIS shape files to a 10° x 10° grid of 0.01° resolution.....	69
Figure 40: Basin outlines derived from the shape files in Figure 5 as provided by Tullow Oil plc.....	69
Figure 41: Flow diagram showing main sequence of analysis.....	72
Figure 42: Night time MODIS LST from Aqua for 1 <sup>st</sup> January 2006 over the Turkana region on a 10° x 10° grid of 0.01° resolution.....	73
Figure 43: Flow diagram outlining the steps taken within this study's PCA.....	79
Figure 44: Variables include (a) elevation, (b) fv, (c) tcwv, (d) emissivity channel 1, and (e) emissivity channel 2.....	80
Figure 45: Examples figures of the elevation-LST analysis.....	82
Figure 46: ALB2 land cover classification for the Turkana region on a 10° x 10° grid of 0.01° resolution.....	83
Figure 47: Google Earth image (2016) with country boundaries highlighted across the EARS.....	88
Figure 48: Absolute monthly mean MODIS LSTs, taken from the Aqua dataset, across the Afar region, on 30° x 20° grids of 0.01° resolution.....	90
Figure 49: Absolute monthly mean MODIS LSTs, taken from the Aqua dataset, across the EARS region, on 20° x 40° grids of 0.01° resolution.....	92
Figure 50: MODIS LST frequencies, as taken derived from the Aqua dataset, for the Afar (30° x 20° areal extent) and main EARS (20° x 40° areal extent) region.....	94

Figure 51: Monthly absolute MODIS LSTs derived from the Aqua dataset, across the Afar (30° x 20° areal extent) and main EARS (20° x 40° areal extent) regions; for day and night, January 2003 to December 2013.....	95
Figure 52: Maximum and minimum ranges of monthly MODIS LSTs, taken from the Aqua dataset, across the Afar and EARS regions of 0.01° resolution.....	97
Figure 53: Absolute night time monthly MODIS LSTs, from the Aqua dataset, across the Turkana area for June 2006 on a 10° x 10° grid of 0.01° resolution and corresponding Google Earth image (2016).....	98
Figure 54: Absolute monthly MODIS LST frequencies, derived from the Aqua dataset, for the Turkana region that is a 10° x 10° grid of 0.01° resolution.....	99
Figure 55: Temporal variation of whole tile monthly mean MODIS LSTs, derived from the Aqua dataset, across the Turkana region that is a 10° x 10° grid of 0.01° resolution.....	100
Figure 56: Maximum and minimum absolute MODIS LSTs, taken from the Aqua dataset, from January 2003 to December 2013 for the Turkana region that is a 10° x 10° grid of 0.01° resolution.....	101
Figure 57: Monthly mean emissivities in both channel 1 and channel 2 from January 2005 through to December 2008 across the Turkana region that is a 10° x 10° grid of 0.01° resolution.....	102
Figure 58: Monthly mean emissivities from MODIS channels 1 and 2, as described in Chapter 3.1.1, for June 2006 across the Turkana region on 10° x 10° grids of 0.01° resolution.....	103
Figure 59: Monthly mean fv from January 2005 through to December 2008 across the Turkana region that is a 10° x 10° grid of 0.01° resolution.....	105
Figure 60: Monthly mean tcwv from January 2005 through to December 2008 across the Turkana region that is a 10° x 10° grid of 0.01° resolution.....	105

Figure 61: 2006 yearly mean MODIS LSTs, for the Aqua dataset, across the Afar region that is a 30° x 20° grid of 0.01° resolution.....	106
Figure 62: Maximum and minimum 2006 MODIS LSTs, for the Aqua dataset, across the Afar region that is a 30° x 20° grid of 0.01° resolution.....	107
Figure 63: 2006 yearly mean MODIS LSTs, for the Aqua dataset, across the main EARS region that is a 20° x 40° grid of 0.01° resolution.....	108
Figure 64: Maximum and minimum 2006 MODIS LSTs, for the Aqua dataset, for the Aqua dataset, across the main EARS region that is a 20° x 40° grid of 0.01° resolution.....	109
Figure 65: MODIS LST frequencies, from the Aqua dataset, for the 2006 yearly means across the Afar and main EARS regions.....	110
Figure 66: Night time MODIS LSTs, for the Aqua dataset, from 2005 to 2008 across the Turkana region that is a 10° x 10° grid of 0.01° resolution.....	111
Figure 67: MODIS LST frequencies for the 2006 yearly means of the Aqua dataset, across Turkana tile that is a 10° x 10° grid of 0.01° resolution.....	112
Figure 68: Minimum and maximum mean MODIS LSTs per pixel, for the night time 2006 Aqua dataset, across the Turkana region on a 10° x 10° grid of 0.01° resolution.....	114
Figure 69: Diurnal differences for mean MODIS LSTs of the Aqua dataset, across the Turkana region that is 10° x 10° grid of 0.01° resolution.....	115
Figure 70: Night time MODIS LST uncertainty for the 5th February 2006, as obtained from the Aqua MODIS Level 3 auxiliary product on a 10° x 10° grid of 0.01° resolution across the Turkana region.....	118
Figure 71: Night time MODIS LSTs of 2006 for the Turkana region on 10° x 10° grid of 0.01° resolution.....	120

Figure 72: MODIS LST frequencies of the host rock and basins for the Aqua 2006 night time dataset, across the Turkana region on a 10° x 10° grid of 0.01° resolution.....	121
Figure 73: The Lake Victoria, 10° x 10° grid tile of 0.01° resolution, for 2006 night time MODIS LSTs for the Aqua dataset.....	123
Figure 74: Absolute host rock MODIS LSTs with respect to original elevation for the 2006 Aqua night time yearly mean.....	124
Figure 75: West Lokichar, Lokichar and Turkana basins are highlighted, as taken from the basin outlines supplied by Tullow Oil plc, as described in Chapter 3.1.4.....	126
Figure 76: West Lokichar, Lokichar and Turkana basins: Elevation versus absolute MODIS, 2006 night time LSTs from the Aqua dataset.....	126
Figure 77: Locality of Suguta and South Kerio basins within the Turkana region tile, supplied by Tullow Oil plc as detailed in Chapter 3.1.4.....	127
Figure 78: Absolute Aqua 2006 night time MODIS LSTs for the Suguta and South Kerio basins.....	127
Figure 79: Locality of the Afar Basin highlighted within the Turkana region tile. Basin outlines have been supplied from Tullow Oil plc, as described in Chapter 3.1.4.....	129
Figure 80: Absolute 2006 night time MODIS LSTs, taken from the Aqua dataset, for the Afar Basin.....	129
Figure 81: Average 2006 night time, MODIS LSTs versus elevation for the host rock and basins of interest as discussed within the text.....	131
Figure 82: Principal components for the PCA with respect to the MODIS LST day time June 2006 Aqua data, across the Turkana region. (a) PC1, (b) PC2, (c) PC3, (d) PC4 and (e) PC5.....	134

Figure 83: Principal components for the PCA with respect to the MODIS LST night time June 2006 Aqua data, across the Turkana region. (a) PC1, (b) PC2, (c) PC3, (d) PC4 and (e) PC5.....	135
Figure 84: Principal components for the PCA with respect to the MODIS LST day time December 2006 Aqua data, across the Turkana region. (a) PC1, (b) PC2, (c) PC3, (d) PC4 and (e) PC5.....	137
Figure 85: Principal components for the PCA with respect to the MODIS LST night time December 2006 Aqua data, across the Turkana region. (a) PC1, (b) PC2, (c) PC3, (d) PC4 and (e) PC5.....	138
Figure 86: Example of anomalies in PC1 night time June 2006 as highlighted by low component loadings representing the emissivity channels 1 and 2 is shown to the right. The component loadings here are generated with respect to the MODIS LST 2006 June night time data as taken from the Aqua dataset, across the 10° x 10° grid of the Turkana region at 0.01° resolution The four main anomalous areas, where by the PC is less than -3 are isolated and displayed to the left.....	139
Figure 87: Elevation versus MODIS LSTs for night 2006, as taken from the Aqua dataset, for anomalies highlighted by PCA.....	141
Figure 88: Absolute MODIS LST PC1 component loadings across the Turkana region for the period 2005 to 2008 from the Aqua dataset.....	142
Figure 89: Absolute MODIS LST PC1 component loadings and corresponding TRMM precipitation data and CCI soil moisture data (grey bars).....	144
Figure 90: Elevation versus monthly MODIS LST gradients as generated from the idl functions: LINFIT, LINFIT with errors and LADFIT across the 10° x 10° grid of Turkana region at 0.01° resolution.....	150
Figure 91: Density plot and scatter plot comparison for elevation versus the 2006 night time yearly MODIS LST means across the 10° x 10° grid of Turkana region at 0.01° resolution.....	151

Figure 92: Elevation versus the 2006 yearly MODIS LST means for the Lake Turkana and Lake Edward tiles. Both tiles are on $10^{\circ} \times 10^{\circ}$ grids of $0.01^{\circ}$ resolution.....	152
Figure 93: Elevation versus 2006 night time MODIS LSTs across the $10^{\circ} \times 10^{\circ}$ grid of Turkana region at $0.01^{\circ}$ resolution for selected land cover types.....	156
Figure 94: Elevation versus land cover across the $10^{\circ} \times 10^{\circ}$ grid of Turkana region at $0.01^{\circ}$ resolution.....	157
Figure 95: Night time 2006 MODIS LST means versus land cover type the $10^{\circ} \times 10^{\circ}$ grid of Turkana region at $0.01^{\circ}$ resolution. Land cover data has been taken from the University of Leicester ALB2 dataset, as described in Chapter 3.....	157
Figure 96: Absolute and normalised MODIS LST means for night time 2006 across the $10^{\circ} \times 10^{\circ}$ grid of Turkana region at $0.01^{\circ}$ resolution. Mean LSTs have been calculated using NASA's Aqua dataset.....	159
Figure 97: Google Earth (2016) terrain map showing locality of absolute-normalised LST transects, as discussed within Chapter 5.1.3. All transects span the Turkana region tile that is a $10^{\circ} \times 10^{\circ}$ grid of $0.01^{\circ}$ resolution.....	161
Figure 98: Cross section along $1.145^{\circ}$ N latitude.....	162
Figure 99: Cross section along $7.5^{\circ}$ N latitude.....	163
Figure 100: Cross section along longitude $36.5^{\circ}$ E.....	164
Figure 101: Cross section along longitude $39.5^{\circ}$ E.....	166
Figure 102: The Turkana and Lake Victoria tiles with basin outlines as supplied by Tullow Oil plc (thicker black lines). LSTs are for the night time, 2006 yearly, MODIS LST means.....	168
Figure 103: 2006 MODIS LST frequencies of the host rock and basins, from the Aqua dataset, across the $10^{\circ} \times 10^{\circ}$ grid of the Turkana region at $0.01^{\circ}$ resolution.....	169

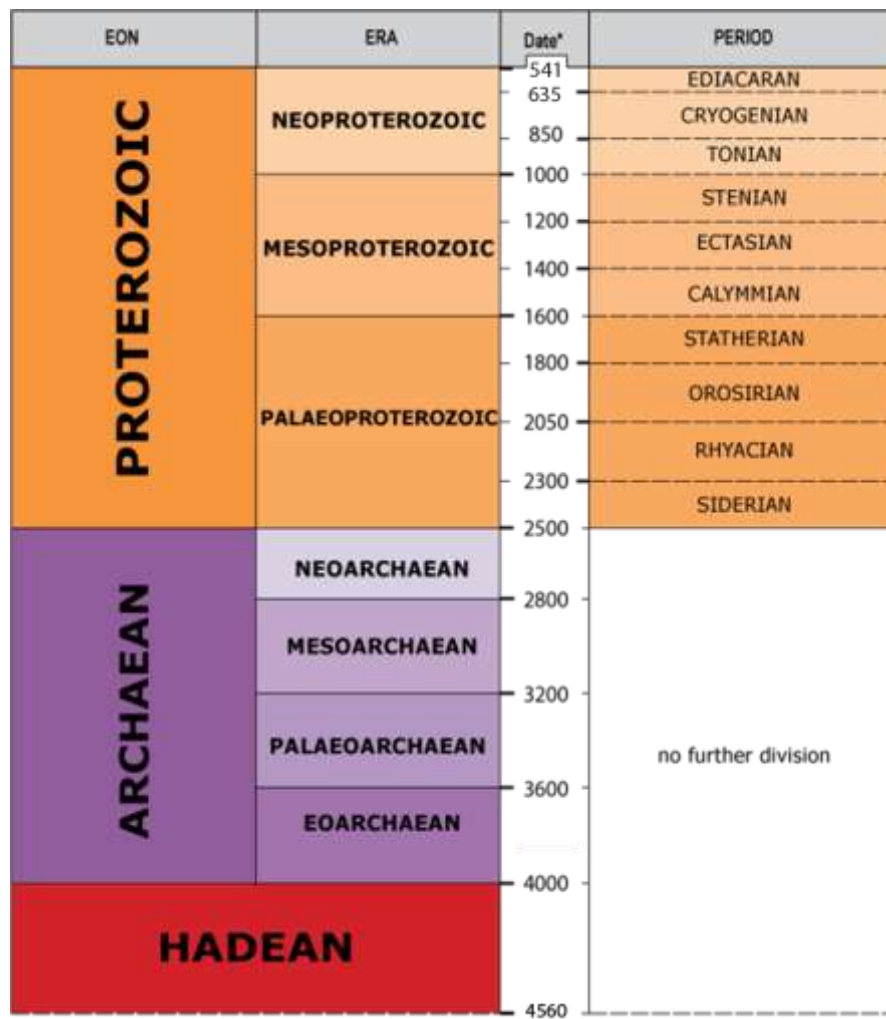
Figure 104: Absolute and normalised MODIS LST yearly means, as calculated from the Aqua dataset, from 2003 through to 2013 for the basin and host rock across the 10° x 10° grid of the Turkana region at 0.01° resolution.....	170
Figure 105: Absolute, night time climatology, derived from the Aqua MODIS LST dataset for 2003 through to 2013, across the 10° x 10° grid of the Turkana region at 0.01° resolution.....	175
Figure 106: Normalised, night time climatology, derived from the Aqua MODIS LST dataset for 2003 through to 2013, across the 10° x 10° grid of the Turkana region at 0.01° resolution.....	176
Figure 107: Lithology versus Aqua MODIS, mean LSTs for 2006, across the 10° x 10° grid of the Turkana region at 0.01° resolution. Lithology data has been supplied by Tullow Oil plc, as described in Chapter 3. No unit refers to a lack of mapped data.....	179
Figure 108: Comparison of lithology and Aqua MODIS, mean channel 1 and channel 2 emissivities for 2006, across the 10° x 10° grid of the Turkana region at 0.01° resolution. Lithology data has been supplied by Tullow Oil plc, as described in Chapter 3.....	179
Figure 109: Principal components for the normalised PCA with respect to the MODIS LST day time December 2006 Aqua data, across the 10° x 10° grid of the Turkana region of 0.01° resolution. (a) PC1, (b) PC2, (c) PC3, and (d) PC4.....	184
Figure 110: Principal components for the normalised PCA with respect to the MODIS LST night time December 2006 Aqua data, across the 10° x 10° grid of the Turkana region of 0.01° resolution. (a) PC1, (b) PC2, (c) PC3, and (d) PC4.....	185

# Acronyms and Abbreviations

ALB2	: ATSR LST Biome V2
ATSR	: Along Track Scanning Radiometers
BGS	: British Geological Survey
CCI	: Climate Change Initiative
EARS	: East African Rift System
ECMWF	: European Centre for Medium-Range Weather Forecasts
ECMWF ERA	: European Centre for Medium-Range Weather Forecasts Reanalysis Project
ECV	: Essential Climate Variables
ENVISAT	: Environmental Satellite
EOS	: Earth Observing System
EROS	: Earth Resources Observation Systems
ESA	: European Space Agency
ESRI	: Environmental Systems Research Institute
EUMETSAT	: European Organisation for the Exploitation of Meteorological Satellites
DEM	: Digital Elevation Model
GES DISC	: Goddard Earth Sciences Data and Information Services Center
GIS	: Geographic Information System
FV	: Fraction Vegetation
ITCZ	: Intertropical Convergence Zone
JAXA	: Japan Aerospace Exploration Agency

LP DAAC	: Land Processes Distributed Active Archive Center
LST	: Land Surface Temperature
MAS	: MODIS Airborne Simulator
MERIS	: MEdium Resolution Imaging Spectrometer
MOD	: Terra product
MODIS	: Moderate Resolution Imaging Spectroradiometer
MYD	: Aqua product
NASA	: National Aeronautics and Space Administration
NE[Δ]T	: Noise-Equivalent Temperature Difference
PC	: Principal Component
PCA	: Principal Component Analysis
RMS	: Root Mean Square
SEVIRI	: Spinning Enhanced Visible and Infrared Imager
SNR	: Signal to Noise ratio
SRTM	: Shuttle Radar Topography Mission
TCWV	: Total Column Water Vapour
TFVI	: Thermal Field Variance Index
TRMM	: Tropical Rainfall Measuring Mission
USGS	: United States Geological Survey

# Geological timeline



*Pre Cambrian geological time chart taken from the British Geological Survey (BGS) (2016).*

*Date\* based on The Geologic Timescale 2012 by Gradstein et al. (2012).*

*\*Units of date are Ma (Million years ago).*

EON	ERA		Date*	PERIOD	
<b>PHANEROZOIC</b>	<b>CENOZOIC</b>		2.6	QUATERNARY	
			23	NEOGENE	
			66	PALAEOGENE	
	<b>MESOZOIC</b>		145	CRETACEOUS	
			201	JURASSIC	
			252	TRIASSIC	
	<b>PALAEOZOIC</b>		299	PERMIAN	
	<b>LATE</b>		359	CARBONIFEROUS	
	<b>EARLY</b>		419	DEVONIAN	
			444	SILURIAN	
			485	ORDOVICIAN	
			541	CAMBRIAN	
	PROTEROZOIC (part)	NEOPROTEROZOIC (part)			

*Phanerozoic geological time chart taken from the BGS (2016).  
Date\* based on The Geologic Timescale 2012 by Gradstein et al. (2012).  
\*Units of date are Ma (Million years ago).*

# 1. Introduction

The East African Rift System (EARS) is one arm of an active continental rift that has been evolving since the Tertiary ( $65.5 \pm 0.3$  Ma) (Figure 1). It spans an extensive area crossing the equator, several climatic boundaries and a plethora of notable geological features. Interest in the region has peaked within recent years due to the increased demand for energy in an unstable market, with fluctuating hydrocarbon costs and increased decommissioning in regions such as the once hydrocarbon rich North Sea. It is therefore becoming ever more important to locate new hydrocarbon rich sites.

An abundance of geological and geophysical surveys have previously been deployed in attempts to clarify the region's complex nature and its hydrocarbon prospects but as a result of costs, inaccessibility and the extensive area, there is a constant search to find a more convenient way of mapping this region. Earlier studies have made attempts to illuminate the rifted basins that are often the sites of hydrocarbon accumulation via gravimetrics (Fairhead, 1976; Birt et al., 1997) and more typically seismic studies (Dunkelman et al., 1989; Birt et al., 1997; Africa Oil Corp, 2010; Tullow Oil plc, 2013; Civiero et al., 2015). Recent interest has turned to whether elevated geothermal gradients as result of hydrocarbon, rifted basins present in the EARS can be detected via satellite-derived land surface temperature (LST) data and whether this is a more viable means of mapping potential prospects and improving basin models.

LST refers to the measure of heating of the land surface or radiative skin temperature and is a key indicator of the surface energy budget (Wan and Li, 1997; Li et al., 2014; NOAA, 2015; Zeng et al., 2015). It differs from the radiometric temperature which is defined as the radiance emitted from the land surface and is dependent upon the distribution of the LST and the emissivity\* (Becker and Li, 1995; Liang et al., 2012). In contrast, LST is driven by a number of physical variables including elevation, land

---

\* Emissivity refers to the ratio of energy radiated from a material's surface to that of the energy radiated from a blackbody (National Physics Laboratory, 2014), as detailed later in Chapter 2.3.5.

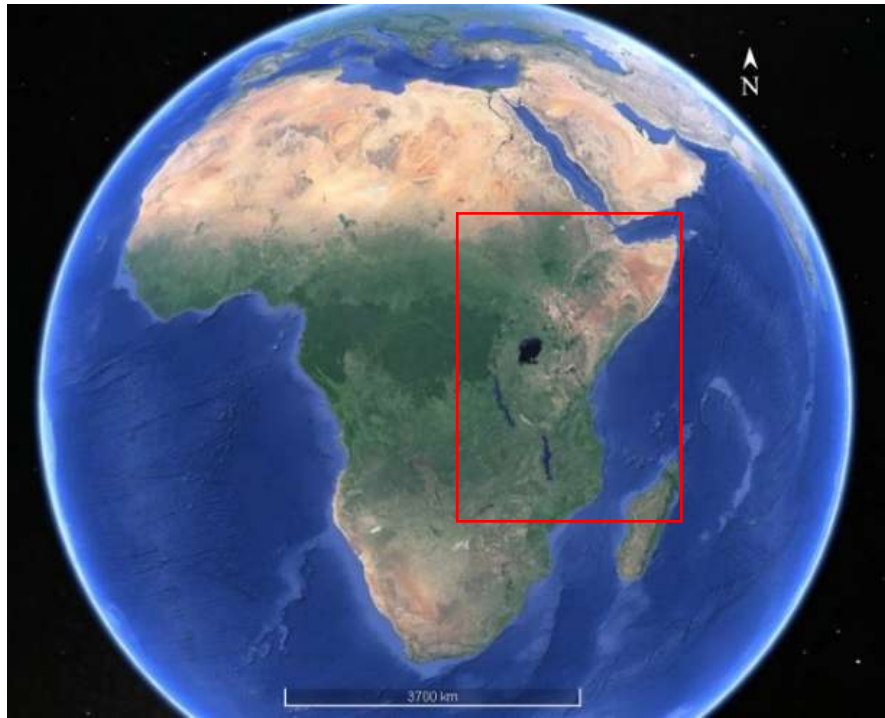


*Figure 1: Google Earth (2016) image highlighting the EARS, area of interest.*

cover, solar heating and ground heating from sources within the Earth. The contributing variables must be considered to understand the origin of the LST signal and thus determine whether it is associated with geothermal activity. This is discussed further in Chapter 2.

In terms of scientific research this study is significant as it aims to analyse the latest satellite data for LST in terms of land terrain characteristics. Understanding the relationships and correlations between LST and variables including elevation, emissivity and fractional vegetation will enable a better understanding of land-surface dynamics over the East African region and therefore have a value to environmental science also. Furthermore it is hoped that such techniques will be able to highlight the magnitude of potential geothermal anomalies associated with hydrocarbon rift basins and thus the effect of deep geological processes on the surface, as there is currently a significant lack of such literature available.

This study henceforth presents an approach of delineating geothermal anomalies using satellite-derived LSTs. The LST data employed is a product derived from radiance signals observed by NASA's MODIS (or the MOderate Resolution Imaging

Spectroradiometer) Earth observation instrument as deployed on board both the Aqua and Terra satellites (NASA, 2016). This dataset spans the area of the rift valley highlighted in Figure 1 and the time period from beginning 2003 to end 2013. In addition to the LST datasets, auxiliary MODIS data has also been employed and includes two channels of emissivity from the MODIS dataset, fractional vegetation from the Geoland-2 FCOVER dataset (Baret et al, 2013) and total column water vapour from the European Centre for Medium-Range Weather Forecasts (ECMWF) ERA-Interim reanalysis (Dee et al, 2011). Elevation data from the Shuttle Radar Topography Mission is also extensively referenced and analysed throughout this study (Farr et al., 2007). Finally, United States Geological Survey lithology (Tullow Oil plc, 2016), Tropical Rainfall Measurement Mission (Huffman and Bolvin, 2014) and Climate Change Initiative Soil Moisture (Liu et al., 2012) data are also incorporated to fulfil the goals of this study.

A number of statistical techniques are applied to the datasets, including the generation of a regional mean LST map on both monthly and yearly timescales. Principal component analysis is also applied in an attempt to clarify the influence of the previously mentioned physical variables on the LST. Following this, the LST dataset is then normalised with respect to most dominant factors to further delineate the signal and identify regions of potential geothermal activity.

In summary of the above, the main objectives of this thesis are therefore as follows:

1. To remotely identify the locality of hydrocarbon basins within the East African Rift system.
2. To delineate the LST signal and determine the most dominant factors with respect to this; in order to delineate potential regions of geothermal activity.

The remainder of this chapter now discusses the region's geology in order to highlight notable features and to further detail the importance of this region in terms of its hydrocarbon potential. Additional information on basin modelling is also given to provide the reader with an understanding of how such an LST dataset could be useful within the energy industry.

## 1.1 Tectonic Setting

The EARS is one of three arms of an active, continental rift zone which is situated at the boundaries between the diverging Arabian, Somalian (Indian) and Nubian (African) plates (Omenda, 2008; Saemundsson, 2008) (Figure 2). These plates are diverging at various rates from  $2.6 \text{ cm yr}^{-1}$  in the Red Sea Rift to approximately  $0.7 \text{ cm yr}^{-1}$  in the main EARS rift and  $0.5 \text{ cm yr}^{-1}$  within the sub branches of the main rift (Saemundsson, 2008). Note that the third arm of this triple junction\* is the Gulf of Aden.

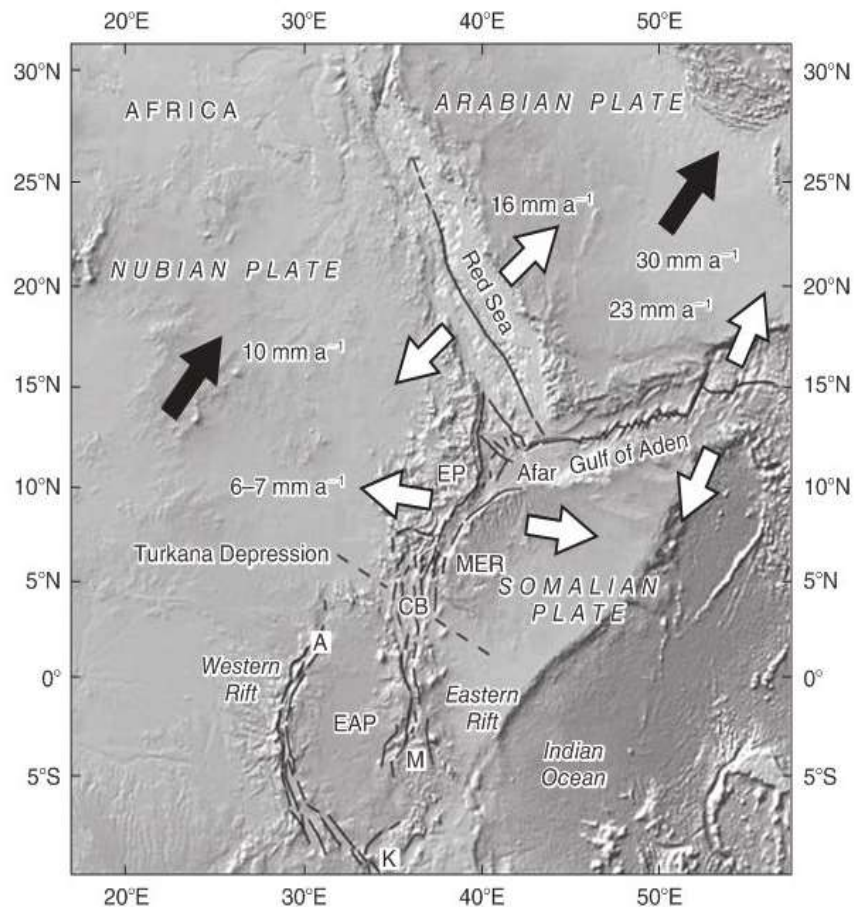


Figure 2: EARS relief map as taken from Kearey et al. (2013). White arrows indicate relative plate velocities, whilst black arrows denote absolute plate motion. Letters refer to several basins present: A, Albert Basin; CB, Chew Bahir Basin; K, Karonga Basin and M, Manyara Basin. Additional features include: EAP, East African Plateau; EP, Ethiopian Plateau and MER, Main East African rift.

\* Triple junction refers to the point at which three tectonic plates meet. This can take several forms depending on whether the plates are diverging, converging or simply passive. In the case of the EARS all plates are diverging.

Extensional regimes form as a result of divergent settings; where continental crust is thinned over millions of years. In the EARS, the extensional regime has resulted in the formation of an approximately north-south aligned rift that consists of numerous fault-bounded segments (Dunkley et al., 1993). Rift formation occurred in a number of steps,

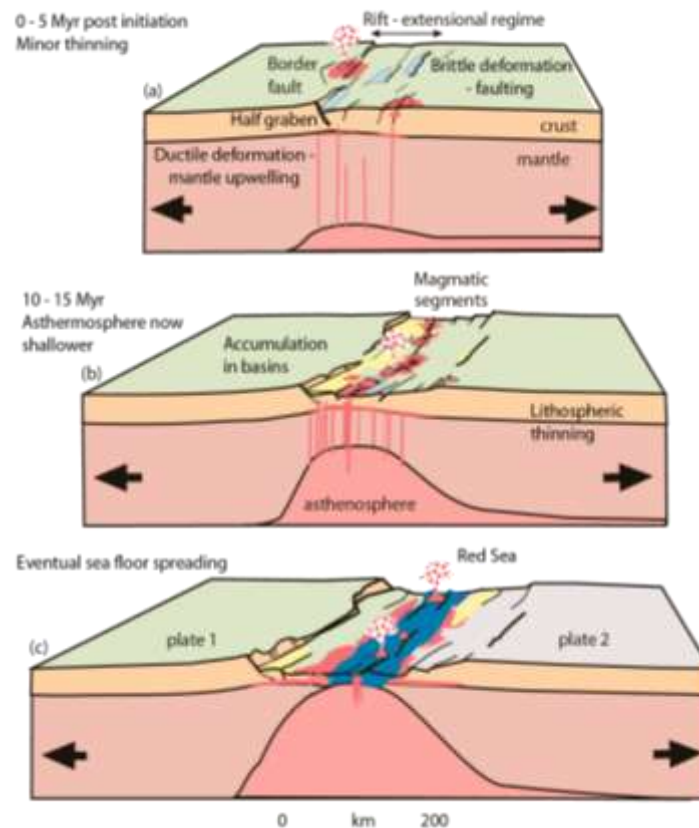
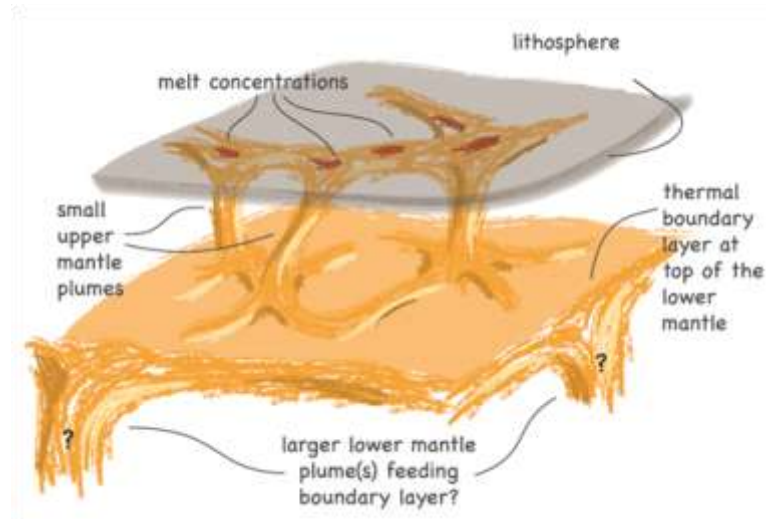


Figure 3: Evolutionary stages of an intracontinental rift as adapted from Ebinger (2005). (a) The continental interior is initially compressed. Rifting initiates due to mantle plumes and takes advantages of pre-existing weaknesses in the lithosphere\*. (b) Volcanism occurs as upwelling material reaches the surface. Accumulation of sediments occurs in the basins. (c) Sea floor spreading initiates and new oceanic crust forms, as in the Afar Depression.

---

\* The lithosphere is the uppermost layer of the Earth comprising all crust, both continental and oceanic, as well as the brittle part of the uppermost mantle. It is generally deformed by brittle fracture. The asthenosphere refers the weak zone within the upper mantle, underlying the lithosphere, where mantle rocks deform by plastic flow. (Allaby, 2008).



*Figure 4: Sketch of the currently favoured geodynamic processes occurring beneath the EARS as taken from Civiero et al. (2015). Mantle upwelling is thought to be responsible for the elevated geothermal gradients present.*

beginning 35 Ma to 30 Ma. Figure 3 is a schematic depiction summarising the main geological processes involved in the rifting of a continental interior and the resulting topographical features. Chapter 1.2 provides further detail on topography.

The initial trigger of the extensional regime is thought to originate from mantle upwelling via plumes (Ebinger, 1989; Ring, 2014) (Figure 4). The impact of this upwelling material is increased upward heat flow within the Earth, which is expressed at the surface via geological processes such as doming and volcanism (Figure 3). Further details are provided in Chapter 1.1.6.

Simultaneously to mantle upwelling and its associated ductile deformation, brittle deformation also occurs at the surface as a result of extension. Faulting and consequential subsidence often occurs causing the crust to form elongated, narrow, half grabens\* (Figure 3). These are the features that ultimately form rift basins (Chorowicz, 2005; Omenda, 2008). Figure 5 displays the localities of rifted basins within the EARS. Significant basin details are found in Table 1.

---

\* Half grabens refer to topographic depressions that are bounded by faults on one side (see Figure 3).

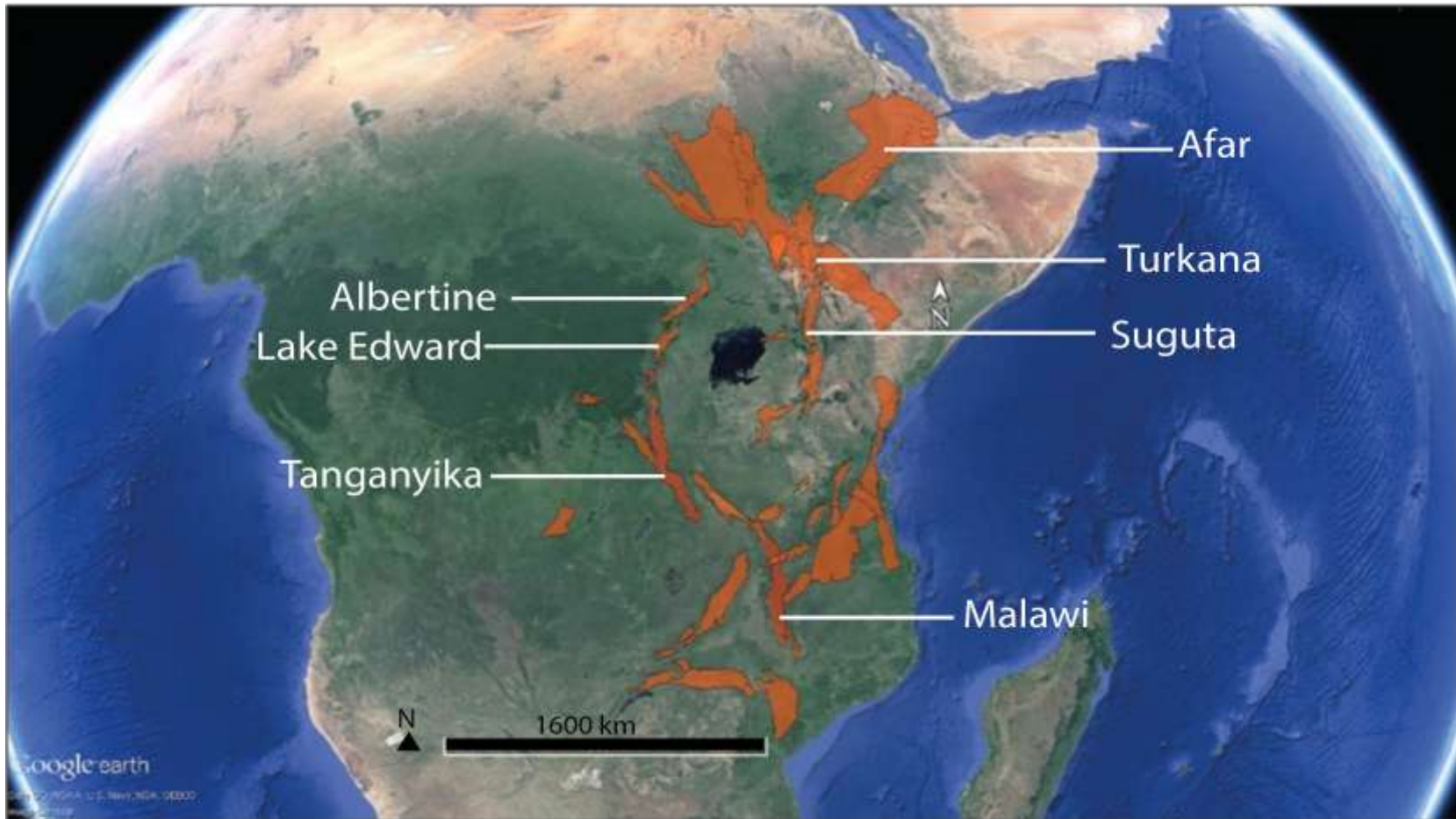


*Figure 5: Google Earth (2016) image of the EARS with rift basin outlines (orange), as provided by Tullow Oil plc. Several basins that are frequently referenced throughout this thesis have been additionally highlighted on the map. Coordinates and geological ages of specific basins can be found in Table 1.*

*Table 1: Basin details as shown in Figure 5 and as provided by Tullow Oil plc. A full list of basins can be found in Appendix 1. The age of geological periods is found in the timeline prior to this chapter.*

Basin	Basin age	Central coordinates of basin	
		Latitude ( $^{\circ}$ N)	Longitude ( $^{\circ}$ E)
Adama	Cenozoic to recent	8.86	39.84
Afar	Cenozoic to recent	10.06	39.84
Albertine	Cenozoic to recent	1.75	30.86
Gatome	Cenozoic to recent	4.38	35.30
Lake Edward	Cenozoic to recent	-0.38	29.73
Lokichar	Cenozoic to recent	2.71	35.77
Lokichar west	Cenozoic to recent	2.19	35.39
Lotikipi	Cenozoic to recent	4.12	34.76
Lotikipi east	Cenozoic to recent	3.20	35.24
Malawi	Cenozoic to recent	-11.92	34.47
Nyanza Trough	Cenozoic to recent	-0.25	34.57
Rukwa	Cenozoic to recent	-7.78	32.03
South Kerio	Cenozoic to recent	0.81	35.69
Suguta	Cenozoic to recent	0.91	36.17
Tanganyika	Cenozoic to recent	-6.06	29.85
Turkana	Cenozoic to recent	4.55	36.08
Anza Graben	Mesozoic	2.27	38.22
Melut East	Mesozoic	9.55	33.58
Melut West	Mesozoic	7.26	32.72
Mongalla	Mesozoic	5.50	32.18
Melut	Late Jurassic Cretaceous	8.93	33.27
Pibor Post	Late Jurassic Cretaceous	6.90	33.56
Remnant Bugiri	Karoo	0.56	33.73
Remnant Dagusi	Karoo	0.15	33.57
Remnant Entebbe	Karoo	0.06	32.45

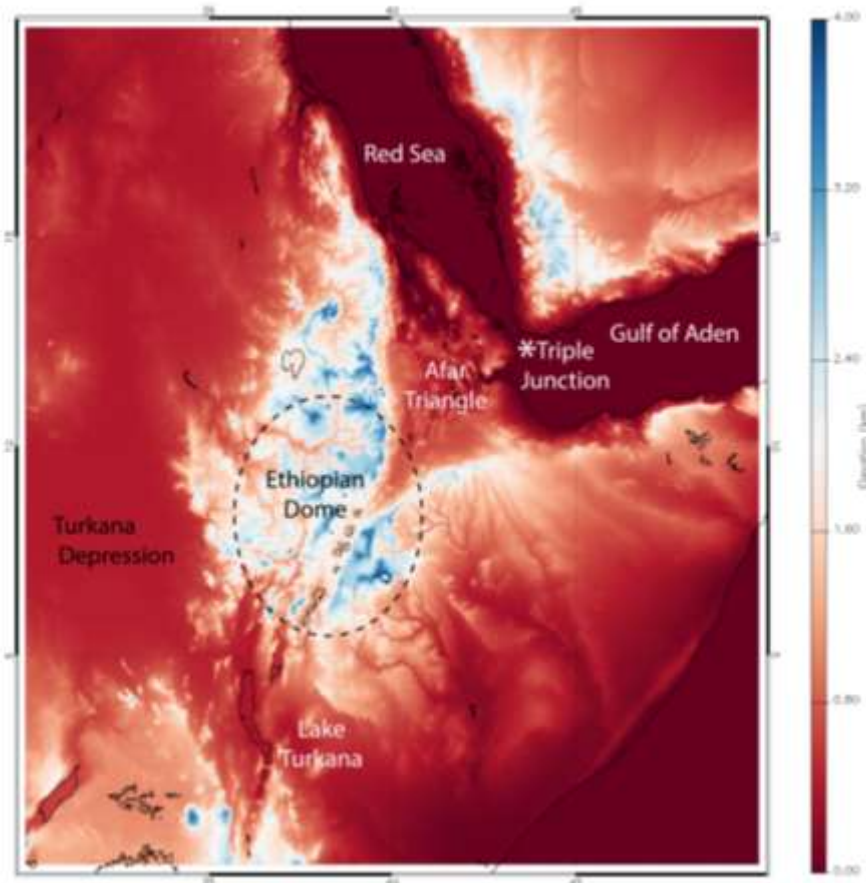


*Figure 6: Elevation of the Afar region. Topography is taken from the Shuttle Radar Tomography Mission (SRTM) (spatial resolution: 100 m) (NASA Land Processes Distributed Active Archive Center (LP DAAC). USGS/Earth Resources Observation and Science (EROS) Center, Sioux Falls, South Dakota, 2001).*

In terms of its locality, rifting originated in the Afar Depression (Chorowicz, 2005; Omenda, 2008; Danley et al., 2012) (Fig). Being the oldest rift segment, the Afar region has now thinned to such an extent that active sea floor spreading occurs, as within the Red Sea. The remainder of the EARS is still within an embryonic stage of rifting, with crust considered continental although partially thinned.

From the Afar region, rifting migrated through the uplifted Ethiopian Dome before re-emerging in the south near Lake Turkana (Figure 6). At this point the broad low of the Turkana Trough should be noted. This feature is thought to have arisen via consequential down warping, following the uplift during the Miocene (Savage and Williamson, 1978).

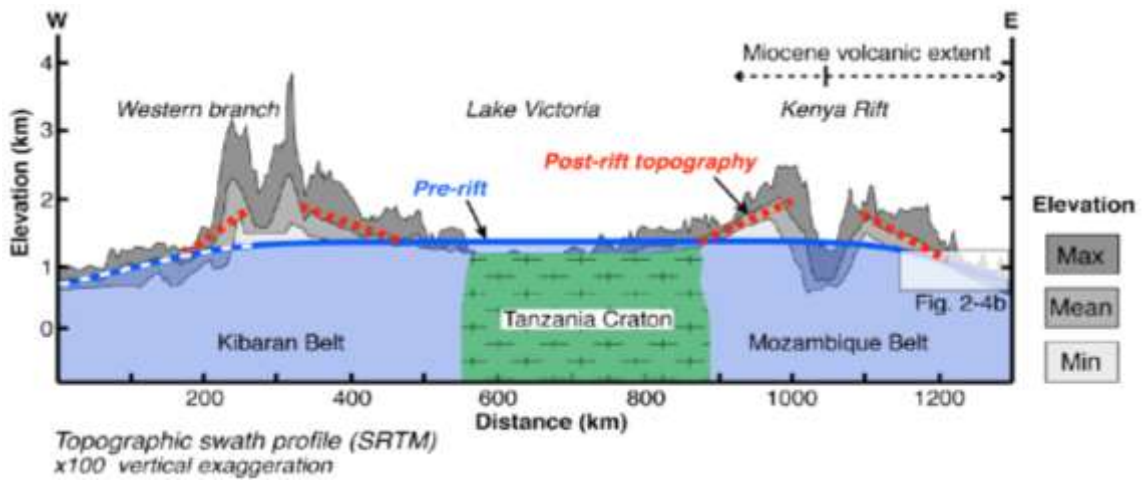


Figure 7: Cross section of the EARS showing the separate branches and the thick Archean craton as taken from Wichura et al. (2010).

Following initial southern propagation, extensional stress was later transported westwards at the intersection of the Tanzanian craton\* (Figure 7), as a result of the thick cratonic body inhibiting further southern propagation (Omenda, 2008). The transformation led to the bifurcation of the rift at 5° N with the formation of a separate western branch between 25 Ma and 10 Ma (Ebinger, 1989; Omenda, 2008).

The branches of the EARS are thought to have formed separately, undergoing different phases of development. However, both are composed of north-south aligned half grabens. Simultaneously the topographic low of Lake Victoria was created. This lake spans both sides of the equator and lies in neither the eastern nor western branch. It is thought to have formed as a consequence of drainage alteration and is not associated with rifting (Danley et al., 2012).

### 1.1.1 Eastern Branch

The eastern branch of the EARS extends 900 km in length, from the failed Mesozoic rift of Lake Turkana to the Tanzanian Plateau in the south (Dunkley et al., 1993; Ring,

---

\* Craton refers to continental crust that is no longer affected by orogenic activity and has demonstrated such stability for approximately 1000 Ma. An example outside of the EARS is that of the Canadian Shield (Allaby, 2008).

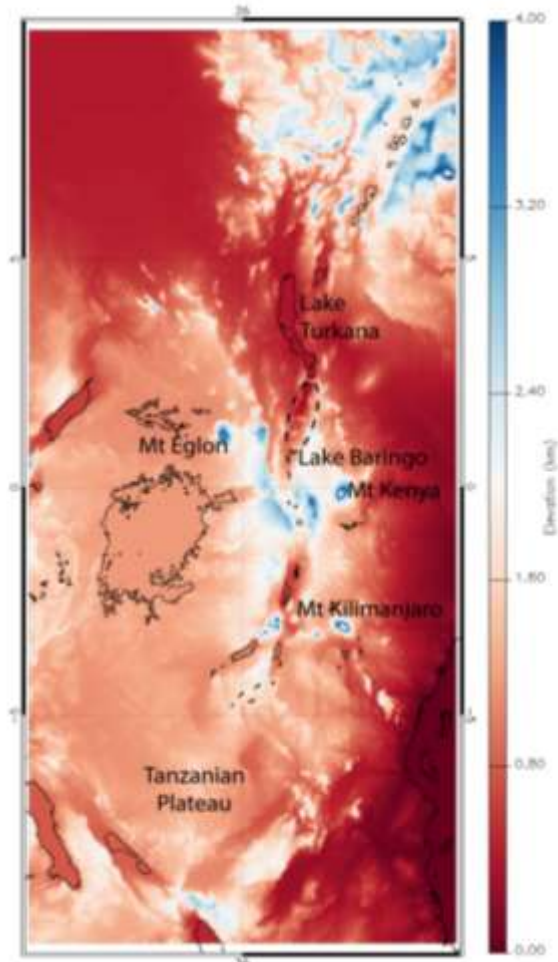
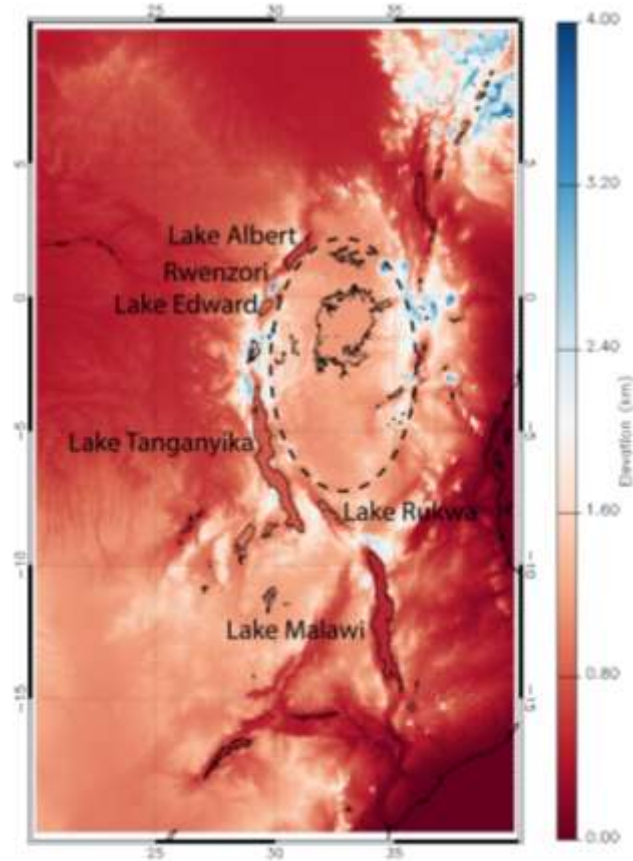


Figure 8: Eastern branch elevation. The dashed line refers to the locality of the Quaternary volcanic centres along the rift axis. Topography is taken from the SRTM (spatial resolution: 100 m) (NASA Land Processes Distributed Active Archive Center (LP DAAC). USGS/Earth Resources Observation and Science (EROS) Center, Sioux Falls, South Dakota, 2001).

2014) (Figure 8). This section of the EARS is often referred to as the main EARS and is composed of a series of half graben structures, bounded by N-NNE trending faults (Dunkley et al., 1993; Vétel et al., 2005). To the south of the main rift lies the most juvenile segment: the Tanzanian sector (Chorowicz, 2005). Rift basins here contain thin sediment layers – a stark contrast to the thicker sediment successions further north (Ring, 2014). Beyond the Tanzanian sector, the rift barely exists and thus this segment is often considered as the termination point of the eastern branch.

In terms of geology, the eastern branch is disseminated by a series of Quaternary volcanic centres that are generally located along its rift axis between lakes Turkana and



*Figure 9: Elevation of the western branch. The dashed black refers to the approximate location of the Archaean craton. Topography is taken from the SRTM (spatial resolution: 100 m) (NASA Land Processes Distributed Active Archive Center (LP DAAC). USGS/Earth Resources Observation and Science (EROS) Center, Sioux Falls, South Dakota, 2001).*

Baringo (Dunkley et al., 1993; Omenda, 2008); that from north to south include: Barrier Volcanic Province, Namarunu, Emurangogolak, Silali, Paka, Chepchuk and Korosi (Dunkley et al., 1993). A number of off-rift volcanoes also occur and include Mount Elgon and Mount Kilimanjaro (Figure 8). These volcanic centres are recorded throughout literature as being closely related to high temperature geothermal systems (Saemundsson, 2008), as are later discussed in Chapter 1.1.3.

Faulting is another rift associated feature that is abundant across the branch, with generally normal faults\* acting as conduits for hydrothermal fluids (Chorowicz, 2005).

---

\* Normal faults are faults that typically occur in extensional settings, where the footwall is up thrown relative to the hanging wall. Footwall refers to the unit of rock sitting below the fault, as opposed to the overriding hanging wall.

These fluids are key indicators to increased heat flow. In terms of seismicity, few momentous events are recorded; however, micro swarms of seismicity are common.

### **1.1.2 Western Branch**

The western branch is found bending westwards around the Archaean craton, from Uganda in the north to Malawi in the south (Figure 7). Similarly to the east, the lakes follow the trend of rifting (Figure 9). However, the western rift has several notably different characteristics to the east, including restricted volcanism and more pronounced seismic activity. The volcanic activity within this region preceded or was concurrent with initial faulting and subsidence but has since decreased (Ebinger, 1989). It is now located in four isolated centres which from north to south are: the Toro-Ankole, Virunga, South Kivu and Rungwe volcanic fields (Omenda, 2008; Ring, 2014).

In addition to this, parts of the branch are associated with some of the greatest uplift observed across the EARS (Chorowicz, 2005), including the Rwenzori Mountains (Ebinger, 1989; Ring, 2014) (Figure 9). Previous literature states that some of the greatest recorded absolute subsidence on Earth also occurs within the western branch (Ring, 2014). Several notably deep basins are therefore present including Tanganyika and Albertine. These basins again, consist of half grabens that are often filled with sediments of often hydrocarbon source rock quality (Saemundsson, 2008; Danley et al., 2012).

### **1.1.3 Lithology**

The lithology of the EARS is summarised in Figure 10, with 8 major stratigraphic units mapped. The units are further detailed in Table 2 in which they are grouped into 5 main classes. From Figure 10, it is clear that Pre-Cambrian undifferentiated basement rocks dominate the western half of the region. Conversely, the eastern half is predominately more igneous, with increasingly broader sediment deposits of varying geologic ages. Previous studies have attempted to understand the impact of the lithology with respect

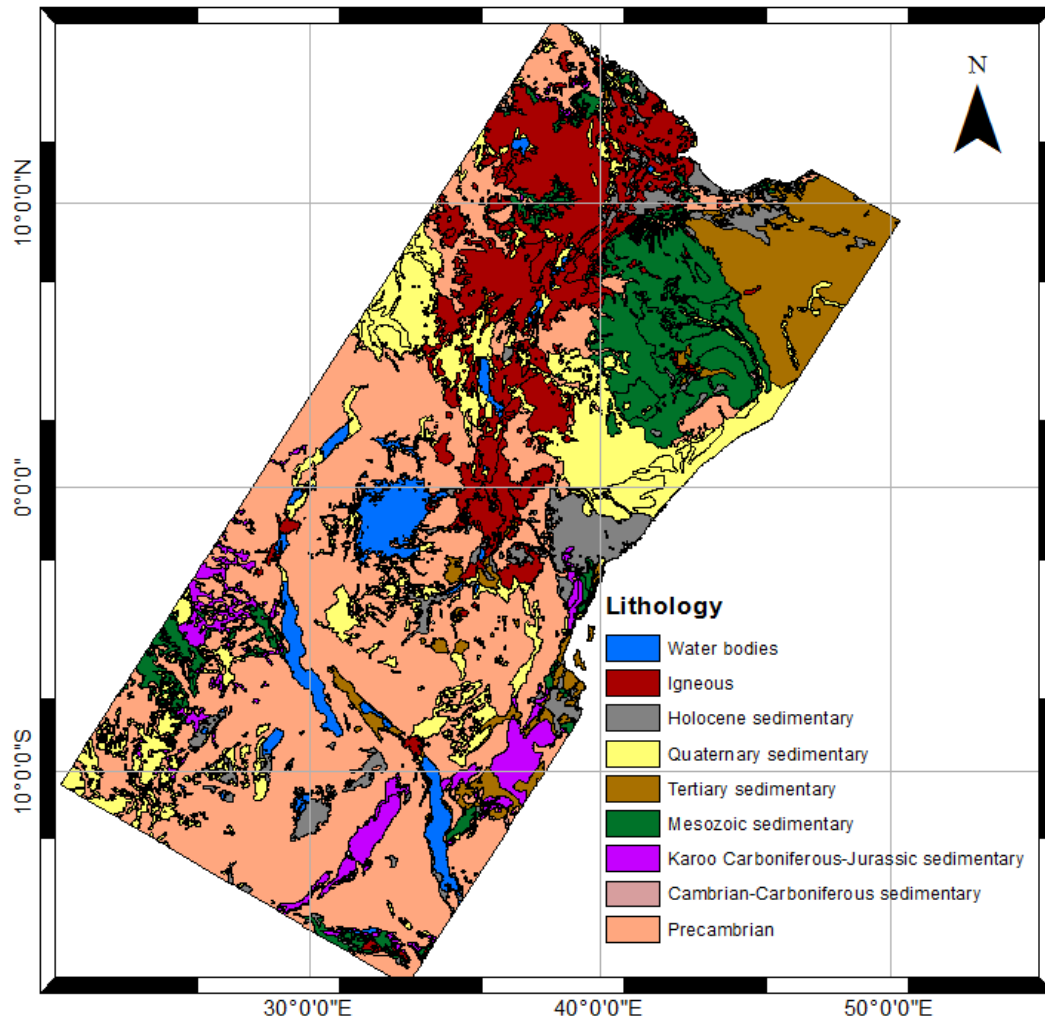


Figure 10: Geological map as taken from Tullow Oil plc ESRI ArcGIS shape files (2016). Lithology has been determined from the United States Geological Survey (USGS).

to the LST with a range of characteristics including grain size, porosity and colour all effecting the LST (Janza et al.,1975; Coolbaugh et al., 2000; Calvin et al., 2005). See Chapter 2 for more details.

#### 1.1.4 Petroleum Potential

The petroleum potential of Africa is for the most part not characterised in detail. The presence of features including oil seeps and organic rich shales at lakes Albert and Tanganyika were the first indicators of plentiful hydrocarbons (Schull, 1988; Tiercelin

Table 2: Lithology classifications corresponding to Figure 10. Specific details of lithology are taken from Dunkley et al. (1993).

Geological Period	Subgroups (age Ma, unless otherwise stated)		Lithology
Igneous			Dark igneous rocks
Holocene	(11,700 ± 99 yrs - )	-	Sedimentary – unconsolidated material.
Quaternary	Pleistocene (2.588 - 11,700 ±99 yrs)	-	Sedimentary – unconsolidated to consolidated material, including bedded diatomites, conglomerates, sands and volcaniclastic deposits.
	Quaternary (undivided) (2.588 - )	-	
	Quaternary – Tertiary (65.5 ± 0.3 - )	-	
Mesozoic	- Quaternary (2.588 - )	-	Mainly dark colour igneous rocks. Various basalts from hawaiites to mugearites. Phonolites of intermediate composition. Pyroclastic flows, trachytes, pumice, tuff and microsyenite.
Quaternary	Tertiary (65.5 ± 0.3 - 2.588)	-	
	Mesozoic (251.0 ± 0.4 - 65.5 ± 0.3)	-	
Cambrian	- Tertiary (65.5 ± 0.3 - 2.588 )		Sedimentary – mainly consolidated sedimentary units.
Tertiary	Mesozoic (251.0 ± 0.4 - 65.5 ± 0.3)	Cretaceous	
		Lower Cretaceous	
		Cretaceous- Jurassic	
		Jurassic	
		Lower Jurassic	
		Jurassic - Triassic	
Karoo Carboniferous – Jurassic (359.2 ± 2.5 - 145.5 ± 4.0)	Jurassic-Carboniferous		
	Triassic-Permian		
	Permian-Carboniferous		
Cambrian – Carboniferous (542.0 ± 1.0 - 359.2 ± 2.5)	Ordovician		
	Cambrian		
	Palaeozoic – Pre Cambrian		
Pre Cambrian	( > 542.0 ± 1.0 )	-	Undifferentiated basement rocks including gniesses, schists and metasediments.

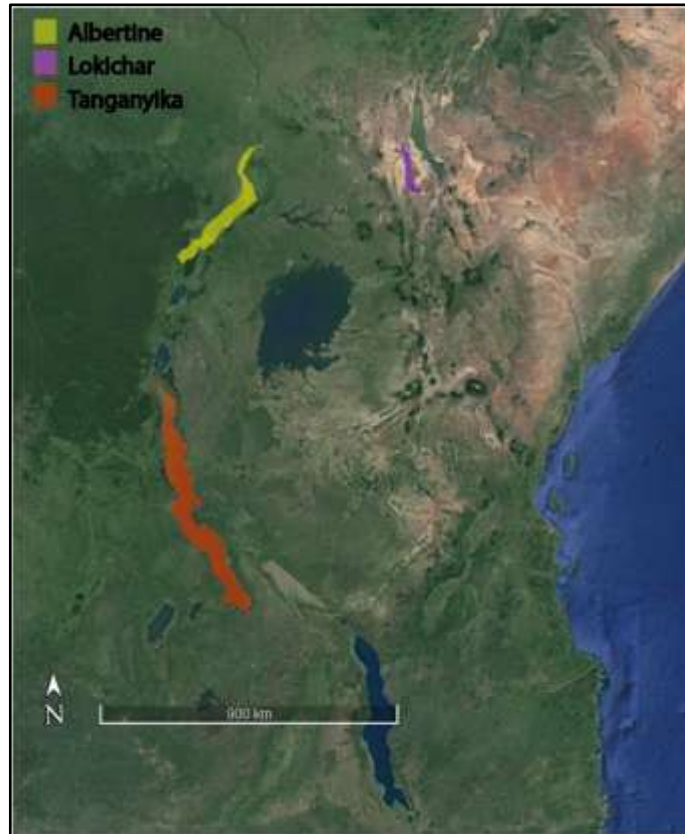


*Figure 11: Locality of the Albertine, Lokichar and Tanganyika basins, as identified from Tullow Oil plc (2016) ESRI ArcGIS shape files.*

et al., 1993; Talbot et al., 2004) (Figure 11). The identification of such features suggests the components required for oil formation and accumulation are present within the EARS. Since the discovery of these features, an abundance of production wells have been established by companies including Tullow Oil plc (Figure 12).

For oil formation, source rocks containing a high percentage of organic carbon and hydrogen are necessary. Several sediments of source rock quality are found in rift basins across the EARS including Albertine, Tanganyika and most notably the Lokichar (Talbot et al., 2004; Tiercelin et al., 2004) (Figure 11). Specific pressures and temperatures are then required for diagenesis\* of sediments; of which both occur with increasing burial of sediments as in basins (Tiercelin et al., 2004). The mechanism by

---

\* Diagenesis refers to the natural processes that occur from sediment deposition to the lithification into sedimentary rock (McCarthy et al., 2011).

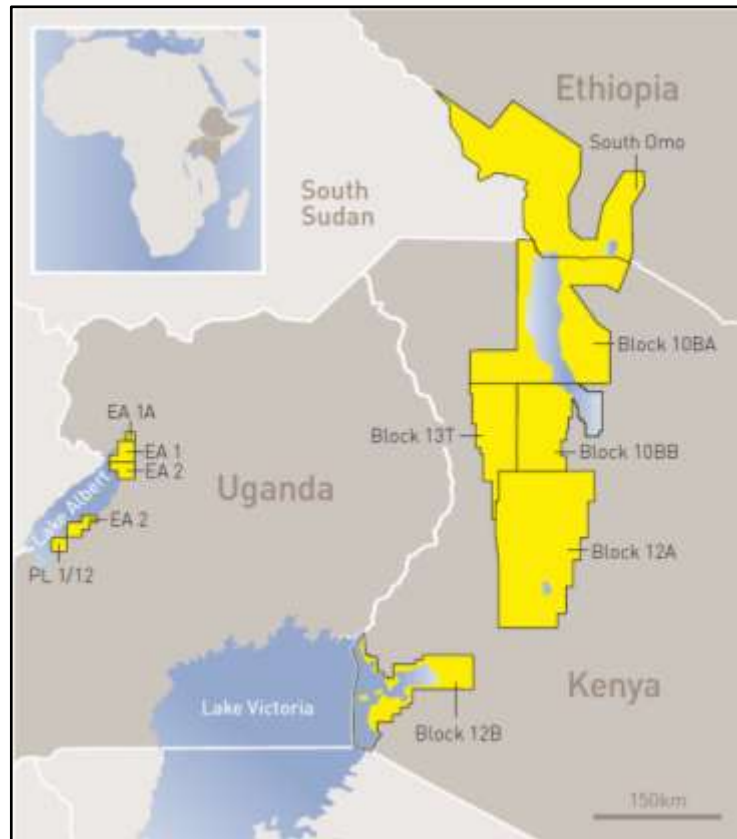


*Figure 12: Location of sites with confirmed hydrocarbons as reported by Tullow Oil plc (2014). Blocks refer to an area of land awarded to a certain company providing them with the rights to explore and drill. Lokichar Basin discoveries are located within blocks 10BB and 13T (approximately 5,800 km<sup>2</sup> and 6,250 km<sup>2</sup>, respectively).*

which source rocks become kerogens\* and then in turn hydrocarbons varies dependent upon burial history, tectonic setting and the rocks present (McCarthy et al., 2011). The region in which this occurs is known as the oil or gas window (Figure 13).

Proceeding diagenesis, a reservoir to store the oil is required as are conduits to enable accumulation (e.g. fractures, faults and connected pore space) (Figure 14). Several potential reservoir rocks are found in the EARS, including thick sequences of porous sandstones (Tiercelin et al., 2004). An abundance of conduits are also available, including rift associated faults (Talbot et al., 2004). For accumulation, a trap or seal is

---

\* Kerogens are insoluble organic matter that form from heating source rock. Further heating and burial of the kerogens themselves results in the generation of oil and gas. (McCarthy et al., 2011).

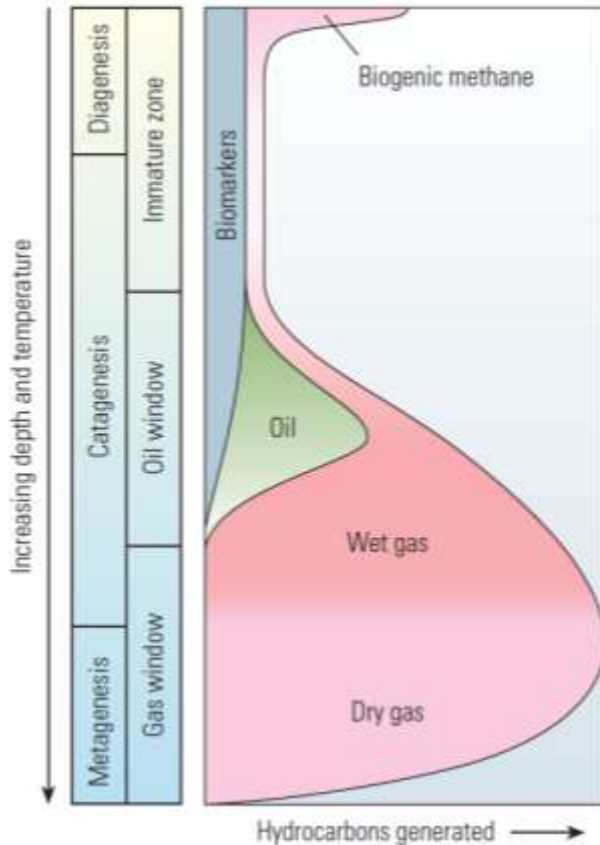


Figure 13: The oil and gas window as taken from McCarthy et al. (2011). Catagenesis is the process in which the chemical bonds in kerogens are cracked and form hydrocarbons.

Metagenesis refers to the final stage of maturation, where all organic matter is transformed to hydrocarbons.

Wet gas refers to gas that contains less methane and more complex hydrocarbons. Dry gas refers to gas that occurs in the absence of liquid hydrocarbons (Schlumberger, 2016).

required to inhibit migration and include but are not limited to impermeable faulted sequences, anticlines\* and domes.

The aforementioned elevated, rift basin geotherms are the focus of this study. Tissot and Welte (1984) report that temperatures and pressures for optimum oil generation typically occur between 2 km and 3 km depth. So although identification of hydrocarbon basins themselves is not necessarily viable from remote sensing, the detection of related temperature anomalies may be a possible. There are few studies detailing the size of such anomalies, instead only referring to the relative temperatures. Chapter 2 details previous work in this area. Furthermore, a number of related surface alterations are also able to be remotely sensed and can act as supporting evidence for the LSTs measured (Yang et al., 2000) (Figure 15).

---

\* Anticlines are structural geological features. They are folds of stratified rock whose limbs dip downwards from a central ridge as seen towards the left of Figure 14.

### 1.1.5 Basin Modelling

Geologists within the petroleum industry are often tasked with basin modelling. Basin modelling uses simplified mathematics to describe complex geological systems through time (Kuper, 2016). They are used as the basis for extrapolation and prediction across regions of potential prospects and aim at reducing uncertainties in evaluation. The models combine numerous input parameters including stratigraphy, lithology and temperature data, where available, to reconstruct basin history (Kuper, 2016). Inputs are derived from a variety of resources including structural maps, seismic interpretations, source rock geochemistry and uplift history. The resultant models describe full burial history detailing structural development, sedimentation rate, uplift and erosion. However, the primary goals in modelling are to calculate source rock maturity, oil generation, expulsion and migration. The understanding of these hydrocarbon processes all concern temperature.

Models consider both the present day temperature and temperature history. The model input for temperature variation within the Earth, i.e. the geothermal gradients as are discussed in Chapter 1.1.6, can originate from a variety of sources but most typically

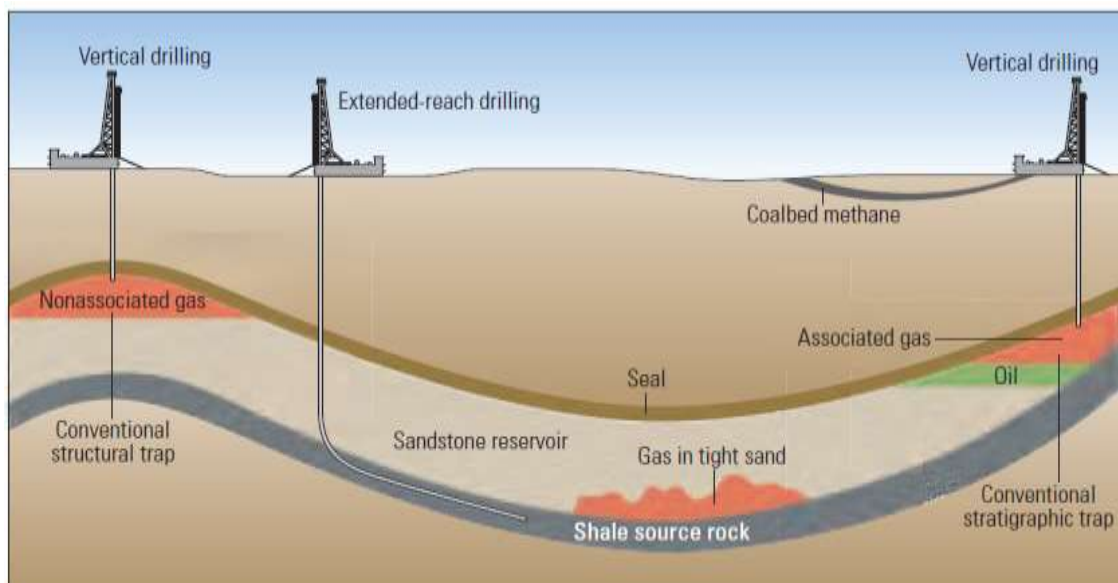


*Figure 14: Example of a typical oil field taken from McCarthy et al. (2011), showing the geological features necessary for successful accumulation, migration and trapping of hydrocarbon prospects, including both gas and oil.*

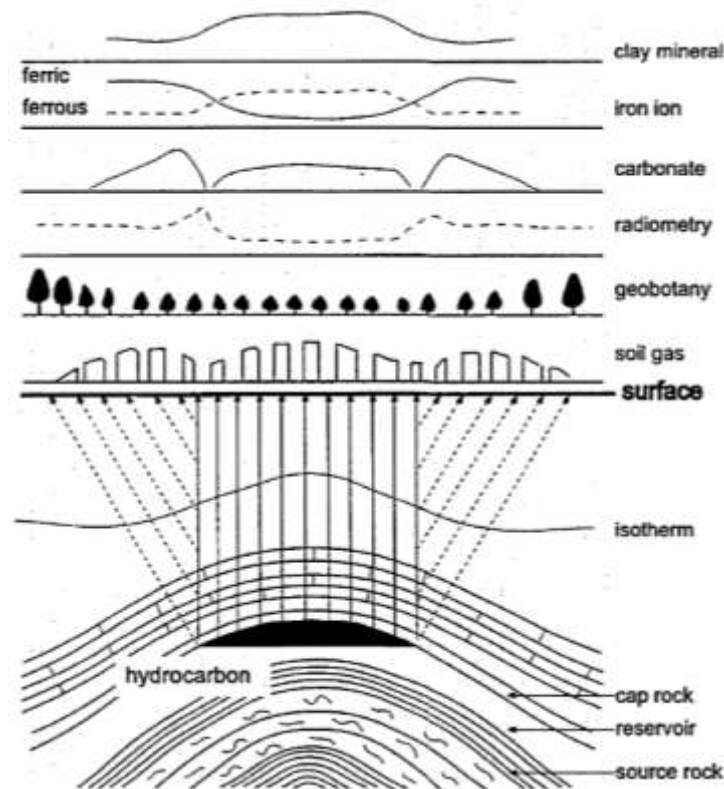


Figure 15: Schematic diagram showing typical surface expressions as a result of underlying hydrocarbons from Yang et al. (2000) (after Duchscherer, 1982). Specific values for each characteristic are not detailed. Note the peak of the isotherm (line of equal temperature) above the hydrocarbon accumulation.

from drilling sites where numerous datasets are attained including drill stem test (DST)\* and mud in/out temperatures\*\* (Kuper, 2016). Where there is an absence of data, geological interpretation can be used to predict geothermal gradients within the basins.

Further to the geothermal gradients, LST data is also an important parameter in basin modelling. This is as the LST is the surface boundary of the geothermal gradient and hence changes in LST directly impact prospect evaluation. Moreover, if thermal

---

\* DST temperature data is obtained during a procedure used to determine productivity, pressure, permeability and extent of a hydrocarbon reservoir (Schlumberger, 2016).

\*\* Mud in/out temperatures are obtained from the circulation of mud during drilling to determine bottom hole temperatures (Holmes and Swift, 1970).

conductivity and heat flow remain constant temperature-depth profiles are fixed with the exception of the LST (Kuper, 2016). Given the narrow temperature interval of hydrocarbon generation in the EARS, this therefore means that small changes in LST can significantly affect the estimated potential of a basin (Kuper, 2016). LST therefore has a direct influence on modelling results, and thereby, conclusions on hydrocarbon viability, which will ultimately effect exploration decisions.

Accurate LST data is therefore a necessity for basin models. Currently it is easier to estimate offshore surface temperatures than LST. Offshore temperatures are often derived from water temperature data directly taken from drilling or probes (Kuper, 2016). LST on the other hand is less well understood as a result of diurnal shifts and seasonal fluctuations. Moreover, direct measurements of air temperatures are often not relevant to the surface. These temperatures are frequently used as the LST input and therefore degrade the accuracy of conclusions drawn (Kuper, 2016). New data is therefore required to improve basin model accuracy.

#### **1.1.6 Geothermal Gradients and Systems**

Heat flow within the Earth is combination of conduction in the Earth's core and crust and convection in the Earth's outer core and mantle. It originates from primordial heating during the Earth's formation and differentiation and as a result of radiogenic decay within the crust and mantle (Kearney et al., 2013). The total heat flow in a given locality is therefore constrained by, and dependent upon, the crustal thickness and proximity of the underlying mantle to the surface (Miliaresis, 2009) (Figure 3 and Figure 5).

Temperature variations across the Earth are thought of in terms of thermal gradients, which are functions of the thermal conductivity of rock (Kuper, 2016). The thermal gradient therefore constantly changes dependent upon numerous lithological characteristics, as discussed in Chapter 2. Geothermal gradients, which are of interest within this study, consider how the thermal gradient varies from the surface to a point at depth into the Earth. They are recorded throughout literature as varying between  $293 \text{ K km}^{-1}$  ( $20 \text{ }^\circ\text{C km}^{-1}$ ) and  $313 \text{ K km}^{-1}$  ( $40 \text{ }^\circ\text{C km}^{-1}$ ) (Liu and Lei, 2013; Oxford Index,

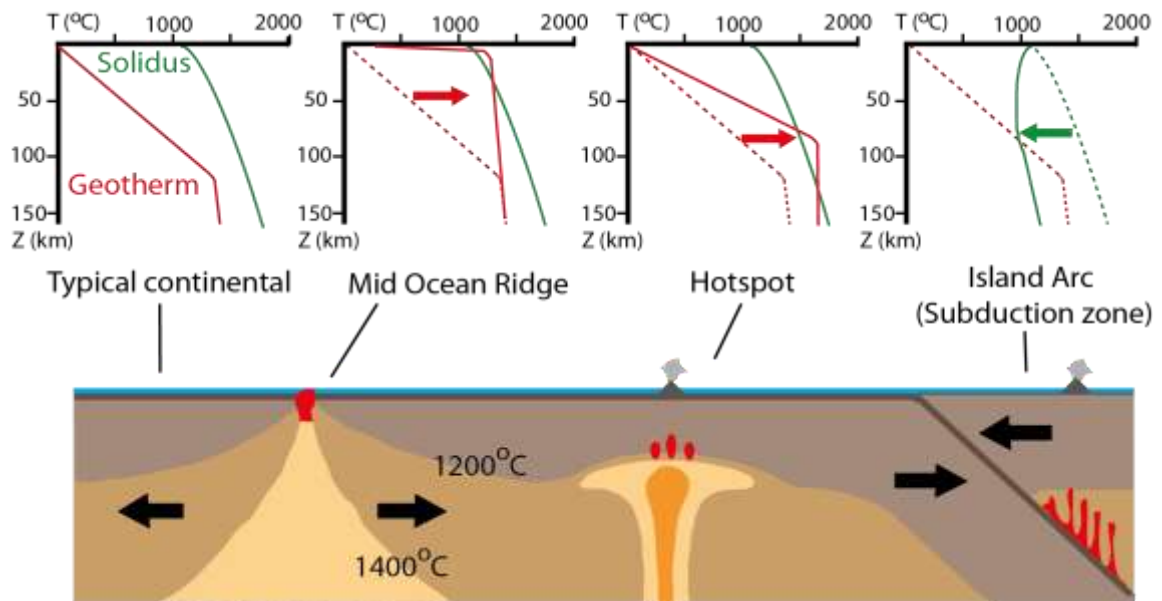


Figure 16: Geothermal gradients (red) within the Earth as adapted from Leigh University (2010) and Kearney et al. (2013). The green line refers to the solidus and the dashed red line refers to the original position of the typical continental geotherm. The geotherm of the EARS lies between that of a continent and mid ocean ridge.

2016). Figure 16 shows a variety of geological settings and their corresponding geothermal gradients with respect to the solidus\* of rock. The gradient for a rift basin is generally between that of a continental setting and an active mid ocean ridge. Unlike rift settings, the geothermal gradient of a cratonic region, such as in the EARS, is minimised as a result of the crustal body inhibiting upwards heat flow. In addition to this, temperatures are also found to vary laterally, as is most prevalent within rifted areas which tend to show large thermal heterogeneity and are difficult to predict due to the dynamic and evolving tectonic setting.

Elevated geothermal gradients often create surface expressions which have been the focus of several studies (Yang et al., 2010) (Figure 15). This includes work on volcanoes and calderas, such as the eastern branch rift axis volcanics, which are typically coincident with high temperature geothermal systems (Dunkley et al., 1993) (Table 3). High temperature systems are found to be abundant and active across the rift system but notably more so in the eastern branch (Figure 17).

\* The solidus refers to the temperature beyond which rocks melt.

Volcanoes and calderas are not the only indication of elevated geotherms, with one of the most notable areas of increased heat flow within the Suguta Valley (Dunkley et al., 1993; Omenda, 1998) (Figure 17). The valley is located south of Lake Turkana and is reported as synonymous with the inner trough of the rift (Dunkley et al., 1993). Hot springs in this region are recorded up to 355 K (82 °C) (Allen and Darling, 1992). Boreholes in this area have additionally indicated that hydrothermal fluids are widespread hinting at the extensive area whereby geotherms are elevated (Dunkley et al., 1993).

The Olkaria geothermal field is an additional high temperature system located within the EARS, 120 km northwest of Nairobi, Kenya (Figure 17). It is a volcanic complex that is composed of series of lava domes that are fault bounded (Mwangi, 2005). The region has undergone significant hydrothermal alteration, including the precipitation of secondary minerals such as clays and oxides (Omenda, 1998). Temperatures in excess of 573 K (300 °C) have been recorded from geothermal wells drilled to depths of 2.6 km across the area (Omenda, 1998). The Olkaria field is consequently the site of a geothermal power station, which is currently considering expansion to include additional areas surrounding the Quaternary volcanoes listed in Table 3 (Figure 17).

Geothermal systems also occur within the western branch, though activity is subdued and previous studies therefore focus on the eastern branch (Omenda, 2008). Geothermal activity is typically associated with the branch's four main volcanic fields, as well as a

*Table 3: Geothermal activity summary for Quaternary volcanoes within the Eastern branch rift axis as modified from Dunkley et al. (1993).*

Locality	Area of activity (km <sup>2</sup> )	Maximum LST (K)	Style and strength of activity
Emuruangogolak	8	369	Hot steaming ground Moderately strong fumaroles
Silali	20	370	Hot steaming ground Moderately strong fumaroles
Paka	32	371	Hot steaming ground Moderately strong fumaroles
Chepchuk	2.5	369	Hot altered ground Weak fumaroles
Korosi	33	369	Hot altered ground Weak fumaroles

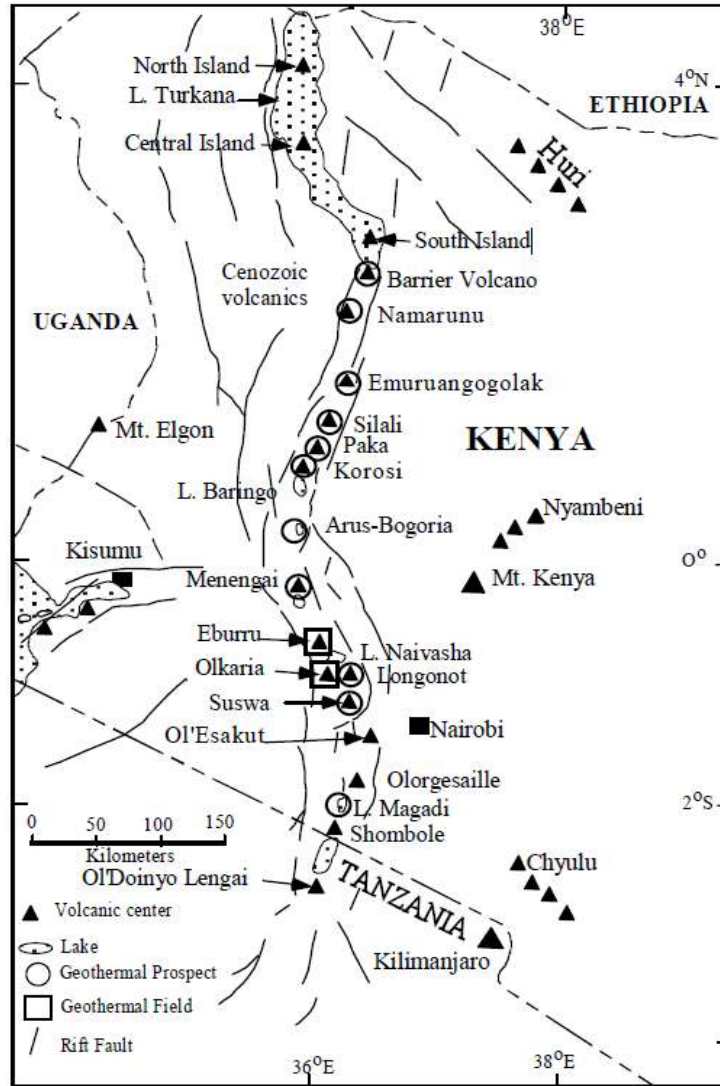


Figure 17: Eastern branch of the EARS, showing geothermal features taken from Lagat (2010). Notable features discussed within this study include the Olkaria geothermal field, which is an area of some of the greatest geothermal activity across the EARS.

number of lower temperature systems such as within the Tanganyika-Rukwa-Malawi fault zone (Chorowicz, 2005); which is disseminated by a series of hot springs that record temperatures in excess of 359 K (86 °C) (Omenda, 2008).

At this point it should be noted that migration of geotherm fluids to surface is often aided by the presence of faults, fractures and pre-existing weaknesses that act as conduits (Lagat, 2010; Tianyu et al., 2012). Heat loss from the system is also thought to occur naturally via conduction through soils (Shako and Mutua, 2011), with porosity a notable factor affecting LST, as will be discussed later in Chapter 2.

In addition, more localised surface expressions also exist. These expressions include: the alteration of surface rock with precipitation of sinter\* (Dunkley et al., 1993; Coolbaugh et al., 2000; Calvin et al., 2005), reddened and bleached ground (Dunkley et al., 1993) and advanced argillic alteration\*\* (Dunkley et al., 1993; Calvin et al., 2005). In addition to this, marked changes in vegetation are often present as a result of the soil temperatures allowing for the growth of different plant species and often as a result of hydrothermal alteration leaching minerals and thus affecting nutrients available for plant growth (Burns and Leathwick, 1995). Secondary mineral deposits as a result of percolating hydrothermal fluids are also often observed, as previously mentioned (Omenda, 1998; Dunkley et al., 1993; Coolbaugh et al., 2000; Calvin et al., 2005).

The aforementioned surface expressions are all useful alternatives to identify geothermal gradients as opposed to the LST data employed within this study. Such features will therefore be able to either compliment results or disagree with the conclusions made within this study.

## **1.2 Physiography**

Figure 18 to Figure 20 show the topography of the EARS that ranges between 0 m and greater than 4000 m. Figure 18 displays a sample of cross sections, both along and across the axes of the rift valley. The distribution and intensity of the topographic features is attributed to the underlying geology, as discussed in Section 1.1 (Sabins, 1996; Civiero et al., 2015). The topography of the region is important within this study as variations in elevation affect LSTs; with earlier studies reporting an inverse linear relationship, as is discussed later in Chapter 2 (Saraf et al., 2005; Miliareisis, 2009).

Higher elevations of up to approximately 4000 m are recorded at several localities, including the uplifted Ethiopian Dome, the Rwenzori Mountains and numerous volcanoes that vary between active, dormant and extinct. In addition to this,

---

\* Sinter refers to a fine grained, silicic or calcic rich rock.

\*\* Argillic alteration refers to the hydrothermal alteration of rocks from their original minerals to clay minerals.

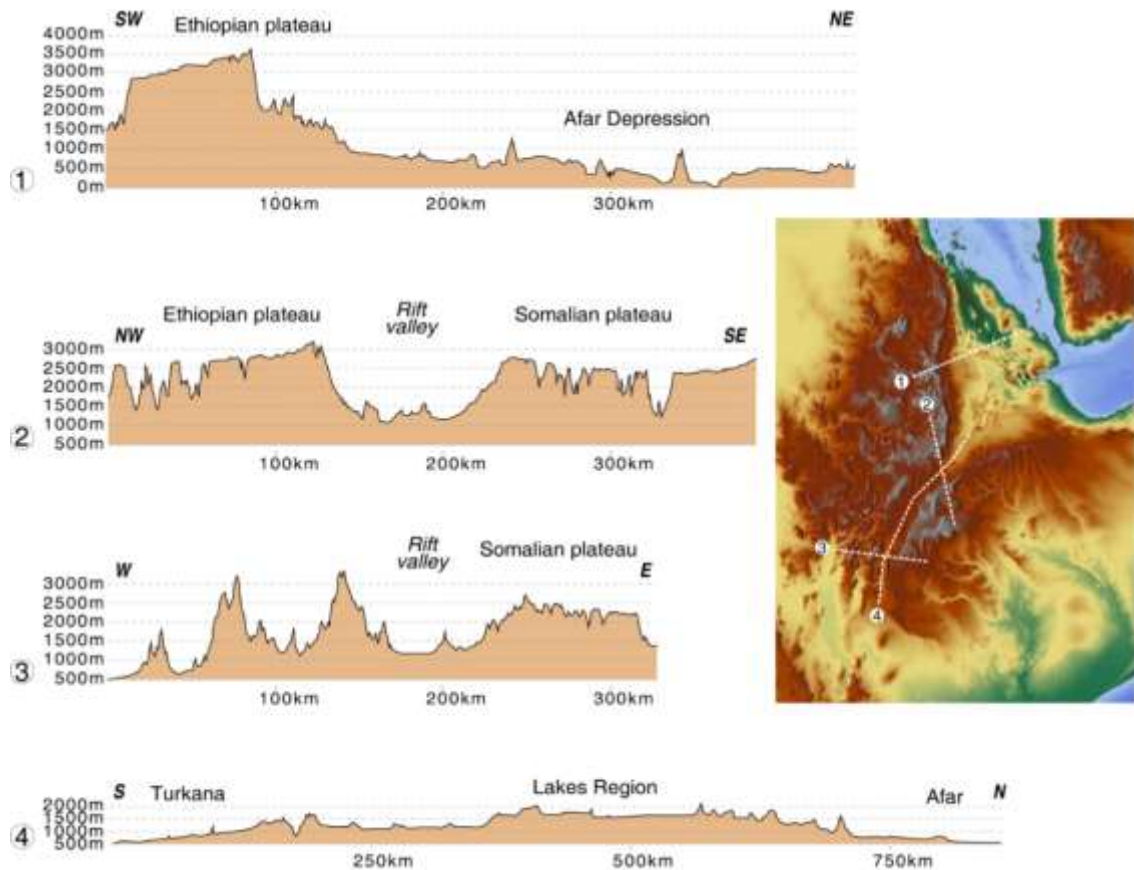
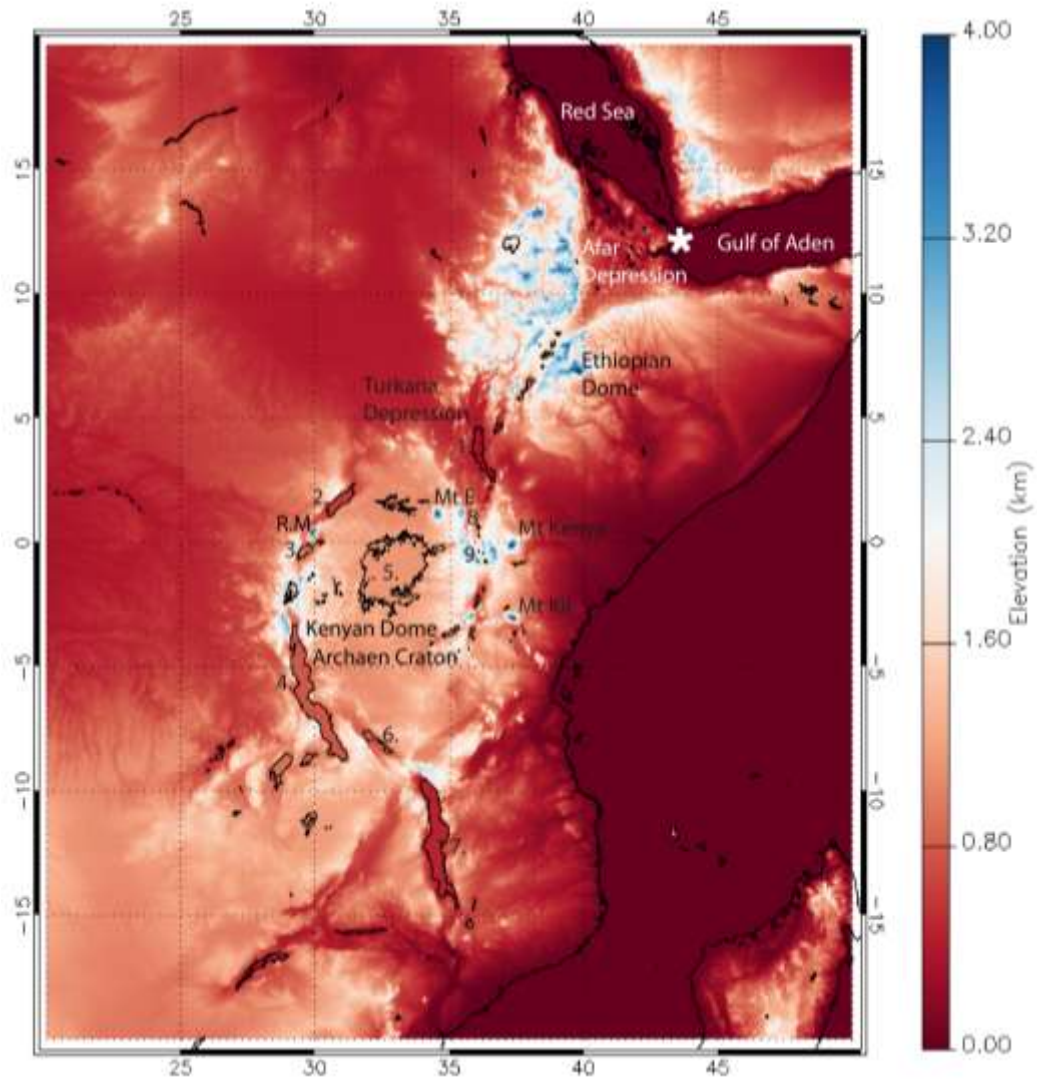


Figure 18: Cross sections displaying elevation along axes and cross axes, as taken from Corti (2016). Topography within this dataset has been taken from the Shuttle Radar Topography Mission (SRTM) (spatial resolution: 90 m).

escarpments marking the rift's boundaries are also of greater elevation, again due to rift associated uplift and faulting (Figure 20).

A number of lower elevations are also present and include the northerly Afar Depression and the northwest-southeast trending Turkana Trough. Additional depressions take the form of rifted basins as outlined in Section 2. These basins are typically infilled with water and thick sedimentary sequences that are deposited as a result of the downward flow into the basin. Examples of lake and sediment filled basins include that of Turkana and Tanganyika. An example of a sediment only basin is the Suguta Basin where the palaeo-lake of Suguta once lay. Table 4 provides an overview to the main rift associated lakes present within the EARS. The non-rift associated Lake Victoria has also been included.



*Figure 19: Topography is taken from the Shuttle Radar Tomography Mission (SRTM) (spatial resolution: 100 m) (NASA Land Processes Distributed Active Archive Center (LP DAAC). USGS/Earth Resources Observation and Science (EROS) Center, Sioux Falls, South Dakota, 2001).*

*Lakes are denoted by numbers: 1. Lake Turkana; 2. Lake Albert; 3. Lake Edward; 4. Lake Tanganyika; 5. Lake Victoria; 6. Lake Ruwka; 7. Lake Malawi; 8. Lake Baringo and 9. Lake Bogoria. R.M refers to the Rwenzori Mountains; Mt E to Mount Elgon; Mt Kil to Mount Kilimanjaro and \* to the approximate locality of the triple junction between the Gulf of Aden, Red Sea and EARS.*

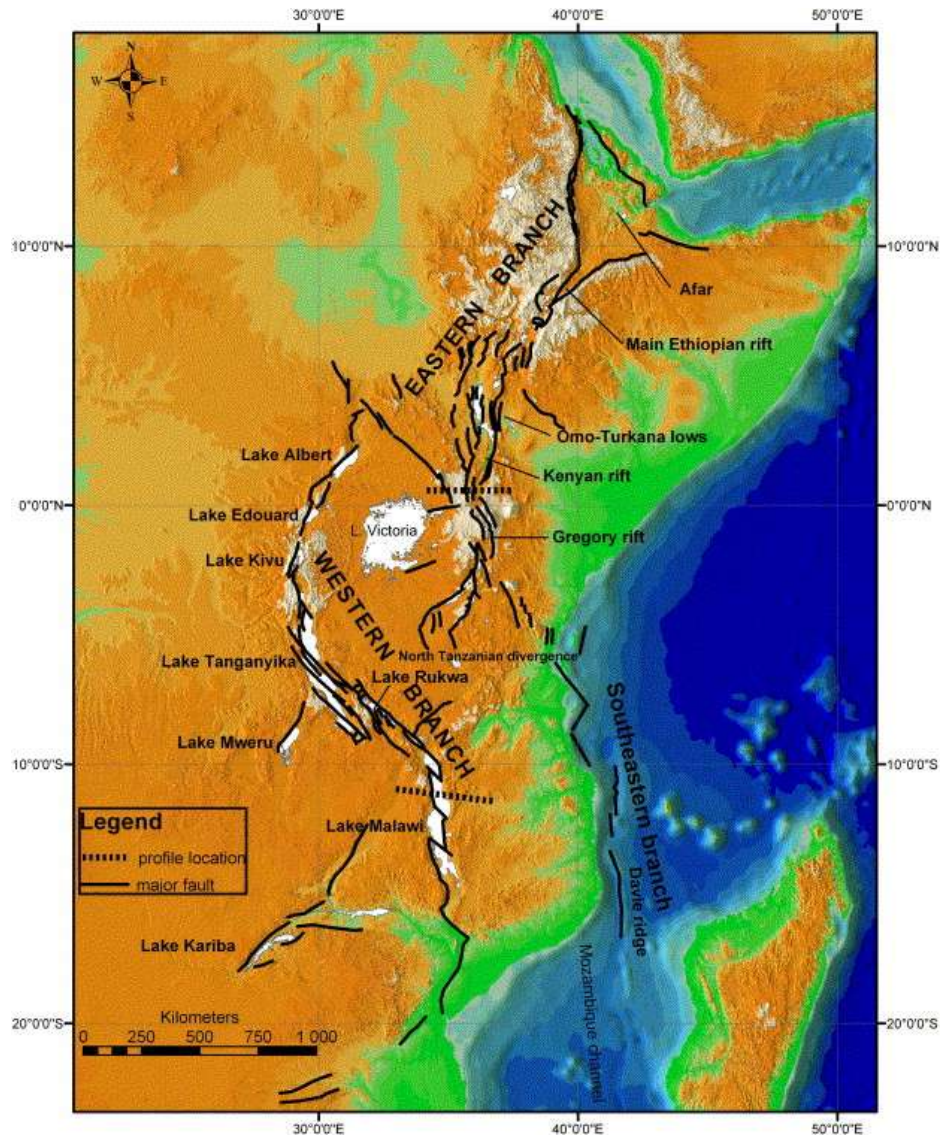


Figure 20: Hypsographic DEM of the EARS as taken from Chorowicz (2005), showing the locality of faults within the rift system. Colours vary for low elevations (grey) to high elevations (light colours). White areas are representative of water bodies. Black lines represent major faults.

Table 4: Summary table of significant lakes within the EARS.

[1] Danley et al. (2012); [2] Chorowicz (2005); [3] Olago and Odada (2000); [4] Cohen et al. (1993); [5] Rosendhal et al. (1992); [6] Dunkelman et al. (1988); [7] Dunkley et al. (1993); [8] Van Damme and Pickford (2003); <sup>[9]</sup> Harvey (1976); <sup>[10]</sup> Kiage and Liu (2009); <sup>[11]</sup> Russell et al. (2003); <sup>[12]</sup> Cockerton et al. (2015); <sup>[13]</sup> Odada et al. (2006); <sup>[14]</sup> Nicholson (1999).

Country	Lake	Branch of EARS	Formation age (Ma)	Average depth (m)	Maximum depth (m)	Surface area (km <sup>2</sup> )	Elevation (m)	Maximum sediment thickness (km)
Uganda, DR Congo	Albert	West	2.5 <sup>[9]</sup>	25 <sup>[9]</sup>	56-58 <sup>[9]</sup>	5,300 <sup>[9]</sup>	618 <sup>[2]</sup>	5 <sup>[10]</sup>
Uganda, DR Congo	Edward	West	2.5 <sup>[9]</sup>	-	117 <sup>[11]</sup>	2,325 [11]	912 [11]	-
Malawi, Mozambique	Malawi	West	>8.6 <sup>[11]</sup>	264 <sup>[11]</sup>	700 <sup>[11]</sup>	29,500 <sup>[11]</sup>	472 <sup>[2]</sup>	> 4 <sup>[11]</sup>
Tanzania	Rukwa	West	-	4 <sup>[14]</sup>	-	3,700 <sup>[14]</sup>	800 <sup>[2]</sup>	< 1.2 <sup>[2]</sup>
Tanzania, DR Congo, Zambia, Burundi	Tanganyika	West	9-12 <sup>[11]</sup>	580 <sup>[11]</sup>	1470 <sup>[11]</sup>	32,600 <sup>[11]</sup>	773 <sup>[2]</sup>	4 – 5 <sup>[2][4][5]</sup>
Kenya, Ethiopia	Turkana	East	20 – 30 <sup>[7]</sup>	35 <sup>[3]</sup>	125 <sup>[3]</sup>	6,500 <sup>[3]</sup>	< 500 <sup>[7]</sup>	2 – 4 <sup>[6]</sup>
Tanzania, Uganda, Kenya	Victoria	Neither	>0.4-1.6 <sup>[11]</sup>	40 <sup>[11]</sup>	79 <sup>[11]</sup>	68,800 <sup>[11]</sup>	1134 <sup>[12]</sup>	60 <sup>[11]</sup>

### 1.3 Climate

Climate varies spatially across the EARS and is important within this project as it alters a number of variables seasonally, including vegetation and water vapour. Cenozoic ( $65.5 \pm 0.3$  Ma to present) uplift is one parameter that affects climate, with mountainous regions creating orographic barriers to moisture bearing winds from the Indian Ocean (Sepulchre et al., 2006; Wichura et al., 2010). Allen and Darling (1992) successfully show the correlation between precipitation and elevation for the region between Lake Turkana and Lake Baringo (Figure 21).

Locally, the climate is also dependent upon precipitation changes associated with the inter tropical convergence zone (ITCZ) (Verschuren et al. 2009). The ITCZ refers to a narrow zone in which north-easterly and south-easterly trade winds originating from different hemispheres converge (Iyengar et al., 2001). This zone seasonally migrates between the Tropics of Cancer and Capricorn in June and December, respectively (Figure 22). The consequence of such a dynamic body is a wet-dry monsoonal climate. This cyclical wet-dry pattern varies slightly for each region (Figure 23) (Verschuren et al. 2009). For example Lake Tanganyika is within the ITCZ's migration path twice a

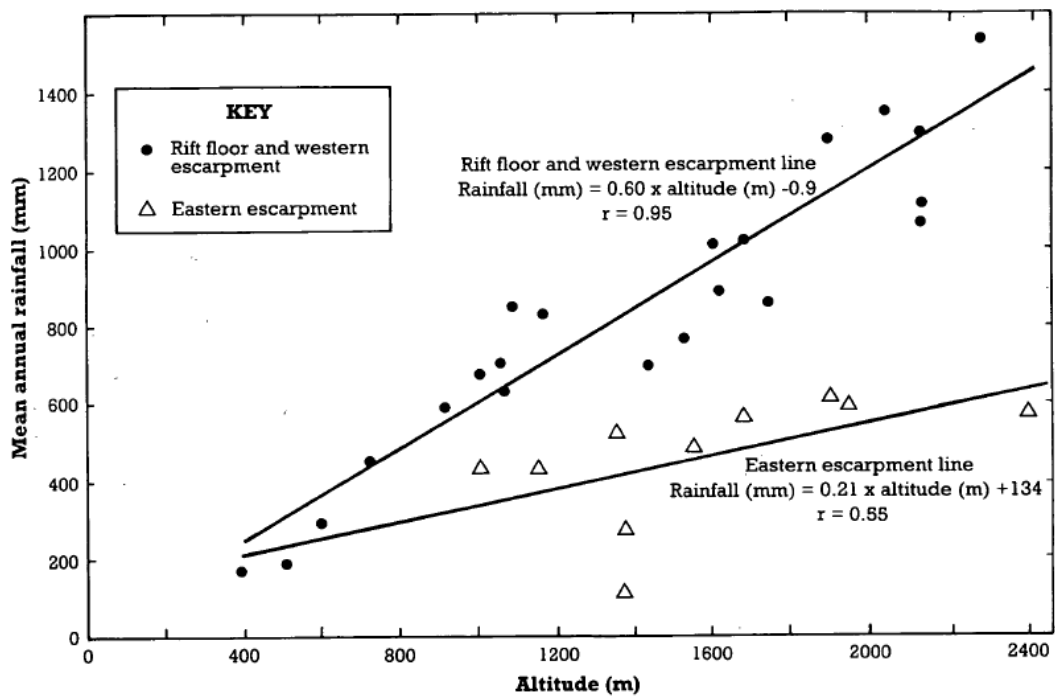


Figure 21: Mean annual rainfall with elevation for the Turkana-Baringo area as taken from Allen and Darling (1992).

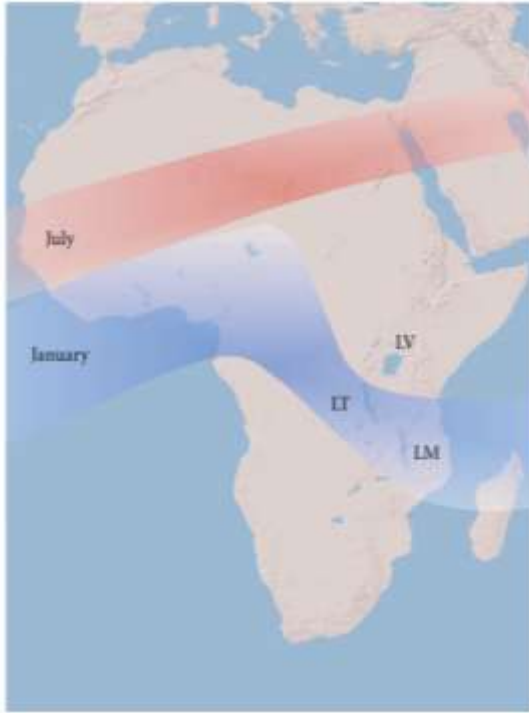


Figure 22: Schematic map showing the overall ITCZ migration, as taken from Danley et al. (2012).

LM: Lake Malawi  
 LT: Lake Tanganyika  
 LV: Lake Victoria.

year between September and May, resulting in a long wet season that quietens in January and February and a shorter drier season when the ITCZ is south of the lake. Lake Victoria also experiences two passages of the ITCZ, resulting in two wet and two dry seasons. Lake Malawi however is only subject to the ITCZ once a year resulting in an annual wet-dry cycle (Danley et al., 2012).

The vast area over which the EARS spans therefore exhibits an abundance of climatically distinct differences. Respectively from north to south, these differences include climatic zones from arid to semi-arid, mean annual rainfalls of 200 mm to 650 mm and day time temperatures along the rift floor from greater than 45 °C to approximately 30 °C (Dunkley et al., 1993). Figure 24 displays the difference in rainfall between areas both within the central EARS and also shows how air temperature can fluctuate within the same region. An additional plot of inter-hemispheric solar insolation is also provided in Figure 25 to further clarify the dynamic nature of the climate across the EARS, whereby solar insolation refers to the amount of radiation reaching a given area and thus indicates the changing seasons and corresponding long and short rains within the region. Thus all of the aforementioned generates fluctuating LSTs within a given region across a yearly cycle.

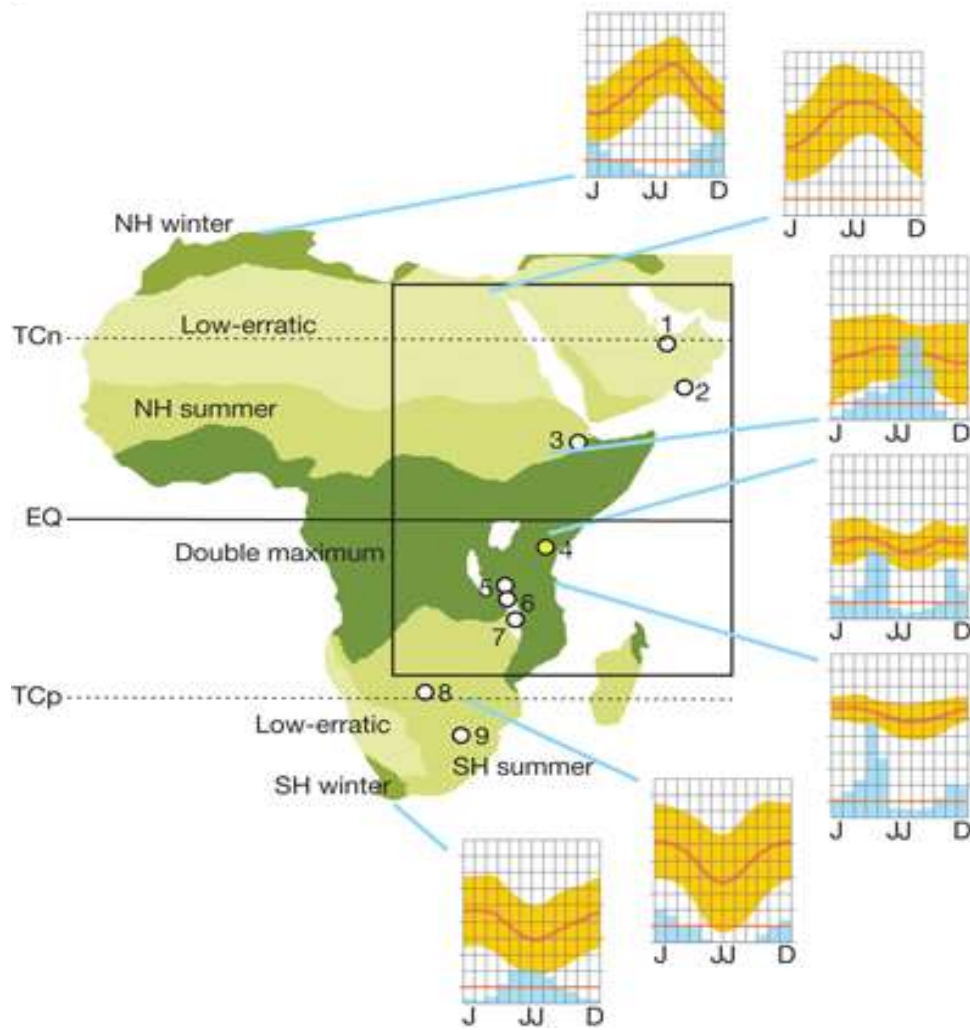


Figure 23: Schematic diagram taken from Verschuren et al. (2009) showing the influence of the ITCZ across the EARS. Numbers 1 to 9 are reference points as follows 1: Rub'al-Khali ( $23^{\circ}$  N), 2: Qunf Cave ( $17^{\circ}$  N), 3: Lake Abhé ( $11^{\circ}$  N), 4 Lake Challa ( $3^{\circ}$  S), 5: Lake Rukwa ( $8^{\circ}$  S), 6: Lake Massoko ( $9^{\circ}$  S), 7: Lake Malawi ( $10^{\circ}$  S), 8: Okavango ( $20^{\circ}$  S) and 9. Lake Tswaing ( $25^{\circ}$  S). The inset graphs are schematics of climate throughout the year. Precipitation (blue bars) is provided on a monthly basis at intervals of 50 mm. Daily mean temperatures (red line) and the corresponding ranges (orange shading) are at intervals of  $5^{\circ}$  C. Data has been collated from the representative climate stations as indicated on the map, which from north to south are as follows; Algiers, Cairo, Addis Ababa, Nairobi, Dar Es Salaam, Gantsi and Cape Town. Acronyms are also as follows; NH, Northern Hemisphere; SH, Southern Hemisphere. EQ, Equator; TCn, Tropic of Cancer; TCp, Tropic of Capricorn. The black box refers to a number of insets that show in more detail, the influence of the ITCZ; which can be found in Appendix 2.

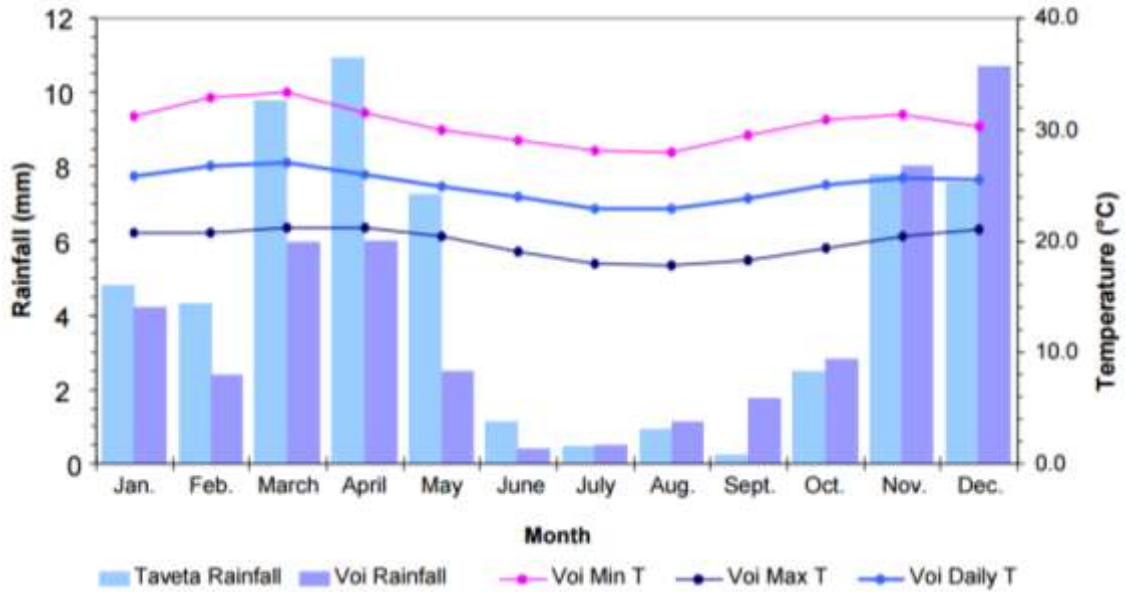


Figure 24: Typical rainfall and temperatures for central EARS region as taken from Verschuren *et al.* (2009). Monthly rainfall data is averaged from 1978-2005 for the Taveta region, 7km southwest of Lake Challa (Yellow dot – point 4 in Figure 23). Monthly rainfall and minimum, maximum, and mean daily surface air temperature are averaged from 1957 to 2007 for Voi, 90 km east of Lake Challa.

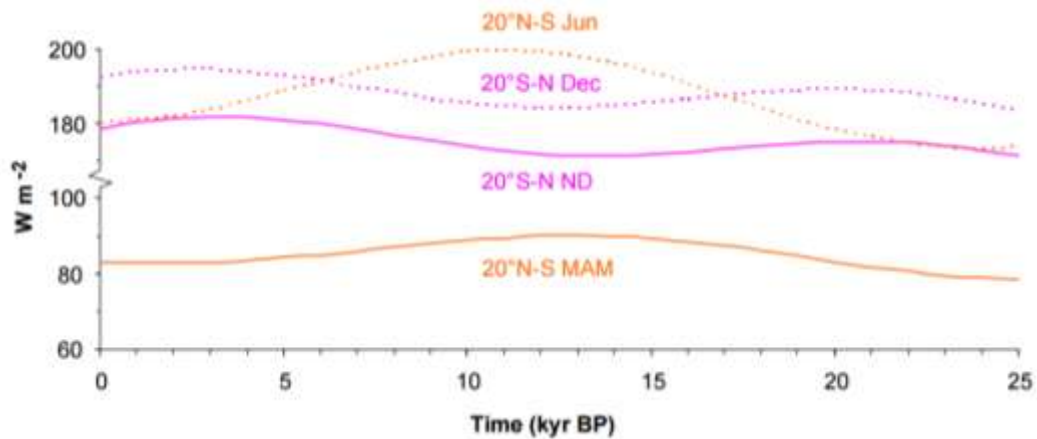


Figure 25: Inter-hemispheric solar insolation between 20° N and 20° S as taken from Verschuren *et al.* (2009). Bold lines refer to equatorial rain seasons, with long rains in March-April-May and short rains in November-December. Stippled lines refer to June and December.

## 1.4 Summary

Elevated geothermal gradients across the EARS tend to coincide with rifted basins. These basins are often the sites of hydrocarbon accumulation. The increased likelihood of hydrocarbon prospects within such basins and the corresponding increase in geothermal gradients mean that basin identification is becoming ever more important.

The challenge within this study is therefore to identify the regions across the EARS where elevated geothermal gradients might exist. This will be determined by highlighting areas where the LST is above average when compared to the surroundings. Identification of such areas will prove useful in enhancing the accuracy of current basin models which vary significantly dependent upon LST input. This is particularly true for the EARS, where relatively small differences in LST create significant impacts in hydrocarbon evaluation.

A second challenge is to understand whether warmer LSTs are related to sites of elevated geothermal gradients or alternatively, additional parameters such as topography. In this study, remotely sensed data is analysed in an attempt to answer such questions. Satellite-derived LST data is studied to isolate the areas of unexplained variance, i.e. regions that cannot be explained by variables such as topography, as are further detailed in Chapter 2.3. It is thought that this unexplained variance will correspond to geothermal anomalies.

In light of the aforementioned challenges, the following chapter now discusses the theory behind remote sensing and the parameters which influence LST. Previous studies with respect to LST and the remote identification of geological features are also noted. Chapter 3 then discusses the datasets employed within this thesis and the analyses applied to them, including both principle component analysis and normalisation of the LST with respect to elevation. Chapter 4 and Chapter 5 then present results of the analyses, discussing notable geographical features and the previously mentioned hydrocarbon, rift basins throughout. This thesis is then summarised in Chapter 6 where the objectives of this study are considered with respect to the findings. Finally, future work to improve and enhance this study is considered.

## 2. Remote Sensing and Physical Parameters

Remotely sensed datasets from Earth orbiting satellites have been selected for use within this study for a variety of reasons including their ability to delineate broad, inaccessible regions, via a singular sensor over a long duration of time, their fine resolution and capability to produce quasi-simultaneous observations of a region. Moreover, remotely sensed datasets are often convenient and widely accessible. It is thought that such datasets would prove a useful resource for exploration companies such as Tullow Oil plc, in providing an extra dimension to initial desk studies. This section now discusses the physics behind such datasets, the factors affecting LST and previous work in this field.

### 2.1 Radiative Transfer

Remotely sensed LST datasets originate from satellites that measure the top of atmosphere (TOA) (or Planck function\* equivalent) brightness temperatures (BT), i.e. the intensity of a given radiance travelling upwards from the TOA towards the satellite as modified by atmospheric processes (Susskind et al., 1983; Dash et al., 2002). Before LST datasets are studied, the basics of radiation propagation must be understood. This is explained by radiative transfer theory (Dash et al., 2002; Modest, 2013).

Atmospheric radiative transfer is the process of energy transfer in the form of electromagnetic radiation (Vidot, 2014), specifically in the thermal infrared for LST as a consequence of Wien's Law (Bernard et al., 2013). Wien's law describes the inverse relationship between the wavelength of the peak emission of a black body and its corresponding temperature (Figure 26), as follows:

$$\lambda_{\max} = b / T \quad (\text{Units: } m) \tag{Eq. (2.1)}$$

Here,  $\lambda_{\max}$  refers to the peak wavelength (m), b to Wien's displacement constant ( $2.90 \times$

---

\*Planck's function relates the intensity of the radiative energy emitted by a black body as a function of wavelength to its temperature (Dash et al., 2002).

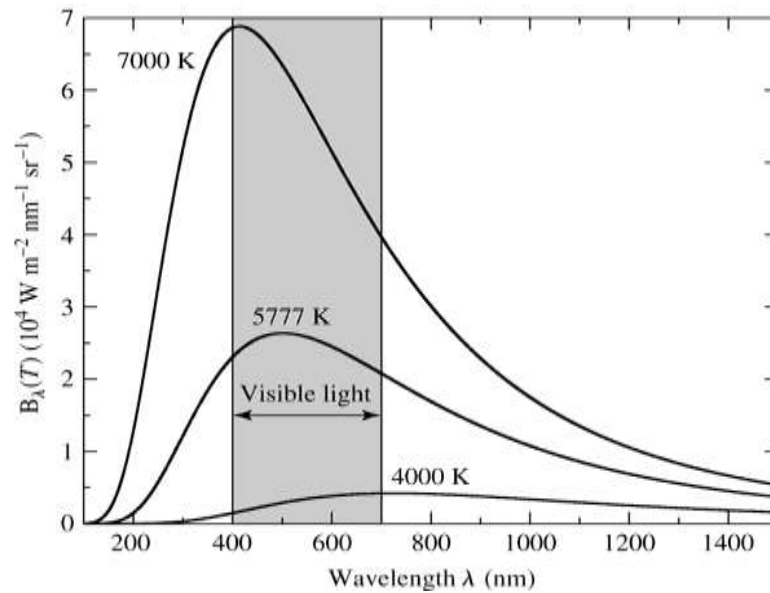


Figure 26: Graph showing blackbody thermal emission intensity as a function of wavelength for absolute temperatures as taken from Carroll and Ostlie, 2006. Average LST for the Earth ranges approximately 300 K to 340 K (NASA, 2016). Therefore using the Wien's law, the peak emission for LST ranges between approximately 10  $\mu\text{m}$  and 8  $\mu\text{m}$ . This wavelength lies within the thermal infrared part of the spectrum.

$10^{-3}$  m K) and T to the temperature of the black body (K) (Bernard et al., 2013). For LST, the thermal infrared region of the electromagnetic spectrum is where the peak radiation wavelength is emitted, i.e. it is the region where LST is most dominant and therefore the region where it is most clearly observed (Figure 26).

Here, atmospheric radiative transfer describes the propagation of a radiation beam through the atmosphere and the interaction with the atmospheric constituents including cloud (Vidot, 2014). These interactions act to either attenuate or enhance the intensity of the radiation beam. The processes include emission which increases radiation, absorption which decreases radiation and scattering which may both increase and decrease radiation (Modest, 2013). The interactions involved in radiative transfer are mathematically explained by the radiative transfer equation.

The radiative transfer equation is based upon the law of conservation of energy. It is applied based upon the assumptions that (1) the atmosphere is at thermodynamic equilibrium up to between 50 km and 70 km; (2) scattering is negligible, i.e. cloud free conditions exist, and (3) the Earth's surface is Lambertian, i.e. isotropically reflecting

and Kirchhoff's law\* applies for all angles (Modest, 2013). The radiative transfer equation can be written as follows (Susskind et al., 1983; Dash et al., 2002):

$$L_i^{sat} = \int_{\lambda_1}^{\lambda_2} f_i(\lambda) \varepsilon(\lambda) B(\lambda, T_s) \tau(\lambda) d\lambda + \int_{\lambda_1}^{\lambda_2} \int_{p=0}^{p_s} f_i(\lambda) B(\lambda, T_p) \frac{d\tau}{dp} d\lambda dp + \int_{\lambda_1}^{\lambda_2} \int_{\theta=0}^{\pi/2} \int_{\phi=0}^{2\pi} (1 - \varepsilon(\lambda)) f_i(\lambda) L^\alpha(\lambda, \theta, \phi) \tau(\lambda) \sin 2\theta d\lambda d\theta d\phi \quad (Units: Wm^{-2} sr^{-1} m)$$

*Eq. (2.2)*

Where,  $L$  refers to the radiance;  $i$  to a certain satellite channel;  $\lambda$  to wavelength;  $\lambda_1$  and  $\lambda_2$  to the limits of the spectral range, i.e. the upper and lower limits of the channel's bandwidth;  $f_i$  to the normalised channel response function;  $\varepsilon(\lambda)$  to the spectral emissivity of the surface;  $B$  to Planck's function;  $T_s$  to the surface temperature;  $p$  and  $p_s$  to the pressure and pressure at the Earth's surface, respectively;  $T_p$  to the mean air temperature at a given pressure;  $\theta$  to the zenith angle;  $\phi$  to the azimuth angle,  $L^\alpha$  to the atmospheric radiance at the surface and finally,  $\tau(\lambda)$  to the spectral transmissivity of the atmosphere (Dash et al., 2002). The aforementioned spectral transmissivity ( $\tau(\lambda)$ ) is a dimensionless quantity that describes the ratio of transmitted spectral flux, i.e. the radiance travelling through a material to the incident radiance on the material (Palmer, 1995). It is therefore written as follows:

$$\text{Transmissivity} = \frac{I}{I_0} = e^{-\tau} \quad (No \text{ units})$$

*Eq. (2.3)*

Here,  $I_0$  refers to the initial intensity,  $I$  to the intensity of radiation once it has travelled through a given medium and  $\tau$  to the optical depth. The transmissivity thus ultimately provides the optical depth term that is necessary to fully solve this equation; where the optical depth describes the ability of a medium to absorb radiation travelling through it (Dash et al., 2002).

---

\* Kirchhoff's law states that if a medium absorbs energy at a certain wavelength, it will also emit energy at the wavelength (Ackerman and Knox, 2006).

Now simplifying the radiative transfer equation (Eq. 2.2), the first right hand side term describes the radiance emitted by the ground and attenuated by the atmosphere; the second term, the radiance emitted by the atmosphere and the third term to the radiance that is emitted by the atmosphere and reflected by the ground, as follows:

$$L_i^{TOA} = B_i(T_i^{TOA}) = L_i^{ground} + L_i^{atm} + L_i^{atm\_ref} \quad Eq. (2.4)$$

Where  $L_i^{TOA}$  refers to the TOA radiance for a satellite channel.  $B_i(T_i^{TOA})$  to the Planck function,  $L_i^{ground}$  and  $L_i^{atm}$  to radiance emitted by the ground and atmosphere, and  $L_i^{atm\_ref}$  to radiance that is emitted by the atmosphere and reflected by the ground. Following the application of the aforementioned radiative transfer equation, numerical models can be derived from which radiation measurements are interpreted (Vidot, 2014). These interpretations can then be utilised and further processed to generate the LST maps seen later within this thesis. Details on the specific algorithm used to retrieve the LSTs within this thesis are later provided within Chapter 3.1.1.

## 2.2 Land Surface Temperature

LST is a measure of the heating of the land surface, i.e. it is the radiative skin temperature (Wan and Li, 1997; Zeng et al., 2015). It plays a key role in interactions and energy fluxes at the surface–atmosphere interface (Van De Kerchove et al., 2013). LST differs from radiometric temperature, which is defined as the radiance emitted from the land surface and is dependent upon the distribution of the LST and the emissivity (Becker and Li, 1995; Liang et al., 2012). Moreover LST is often recorded as different to air temperatures (Gallo et al., 2010). The difference between LST and air temperature is a result of the way heat is transferred and transmitted. Air temperatures are mainly affected by circulation and moisture, whereas LSTs are the result of direct heating by solar radiation, emission to the atmosphere, latent heat\*, sensible heat\*\* and

---

\* Latent heat refers to temperature with phase change.

\*\* Sensible heat refers to temperature change with no phase change.

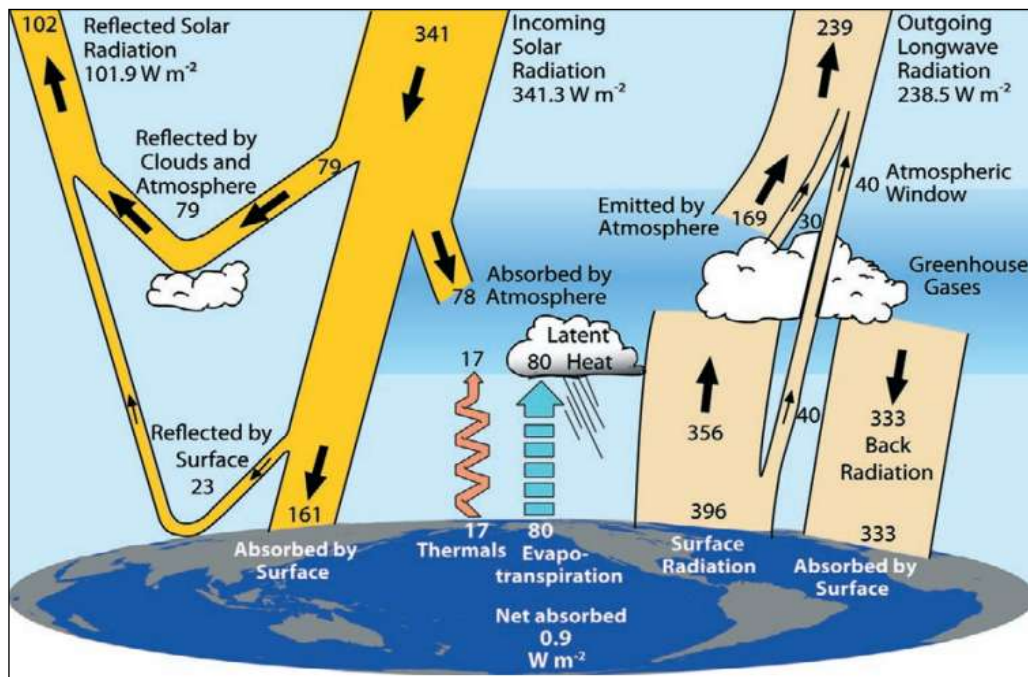
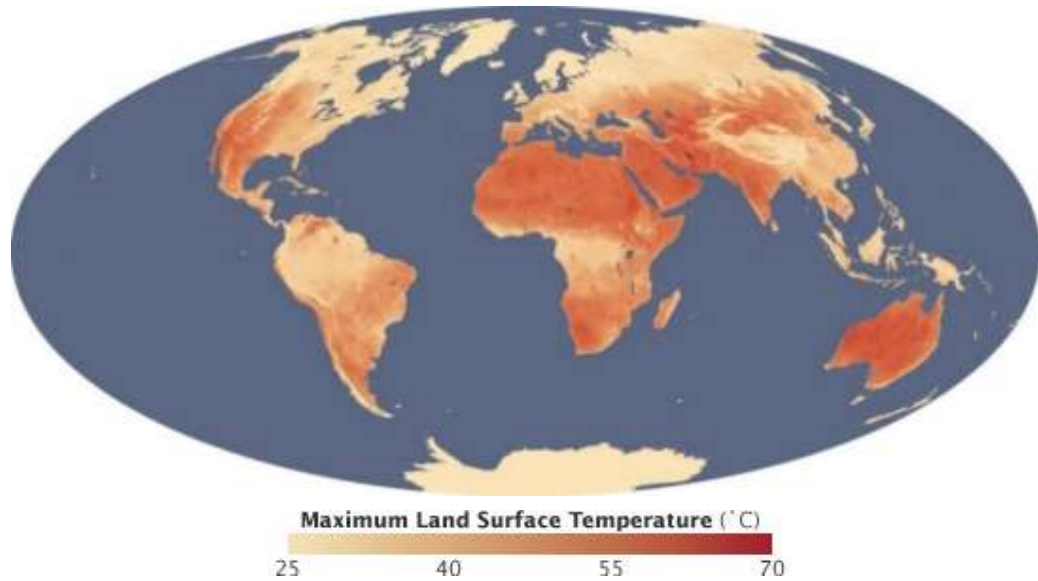


Figure 27: Schematic diagram of the Earth's energy budget as taken from Trenberth et al. (2009). The data provided has been calculated for the period from March 2000 to May 2004 ( $W m^{-2}$ ). The arrows present indicate the flow of energy and are proportional to their importance within the system.

heat transfer from upwelling mantle. A schematic diagram of the Earth's energy budget is now provided in Figure 27 to summarise the distribution of energy, as discussed within this section.

Further to the above, Figure 28 now shows an example of the global maximum LST distribution, whereby the EARS is notably warmer than higher latitude regions. From this it is clear that the highest LSTs on Earth are often recorded in desert environments where the ground is of a high albedo and composed of mostly dry soils. This is further enhanced with clear skies and little wind.

Thermal signals recorded by MODIS are affected by both the real LST signal and errors in the LST. The real signal is a result of variation in elevation, land cover, vegetation, soil moisture, solar heating and ground heat. Instrumental errors in retrieving the LST signal correspond to errors in emissivity, aerosols, cloud coverage and water vapour. The influence of additional physical variables, not related to ground heat and the



*Figure 28: Global maximum LSTs from 2003 to 2009 measured by NASA's earth observation instrument MODIS, as taken from NASA Earth Observatory (2016).*

interference of errors in the LST pose a problem when trying to detect geothermal anomalies. A number of anomalies are thought to occur within the EARS as a result of elevated geothermal gradients. It is therefore important to determine the extent and intensity of anomalies related to the real LST signal as opposed to the related errors and additional physical variables. Moreover, it is necessary to fully clarify what is considered a geothermal anomaly, with a lack of definitive answers in previous literature (Cievetta et al., 1974; Miliareisis, 2009).

### **2.3 Contributing Factors**

The parameters affecting the LST signal are now discussed. A holistic approach is applied to understand the relationship between the physical variables and the LST as a result of their highlighted interconnected nature.

### 2.3.1 Thermal Inertia

One of the most significant factors is thermal inertia. Thermal inertia describes the amplitude of the fluctuations in seasonal and diurnal cycles (Rees, 2013) (Figure 29). It describes the tendency of a medium to resist temperature change and is defined as:

$$I = (k\rho c)^{1/2} \text{ (Units: } J m^{-2} K^{-1} s^{-1/2}\text{)} \quad \text{Eq. (2.5)}$$

Where  $I$  is thermal inertia,  $k$  is thermal conductivity,  $\rho$  is bulk density of the material and  $c$  the specific heat capacity (Presley, 2002). Specific heat capacity and thermal conductivity are discussed later. Thermal inertia is important to consider as to not falsely identify anomalies. For a feature to be anomalous it is expected to remain consistently different to its surrounding both spatially and temporally.

Previous literature has identified links between LST, thermal inertia and lithology (Janza et al., 1975; Coolbaugh et al., 2000; Calvin et al., 2005). Grain size is one aspect of this, with smaller grained lithologies heating up and cooling down more quickly, having lower thermal inertias (Calvin et al., 2005). Low thermal inertia materials such as shales have large LST amplitudes, being among the warmest in the day and coolest at night. High thermal inertia materials such as basalt and sandstone are much more resistive to LST change and are cooler in the day and warmer at night (Sabins, 1996, Calvin et al., 2005).

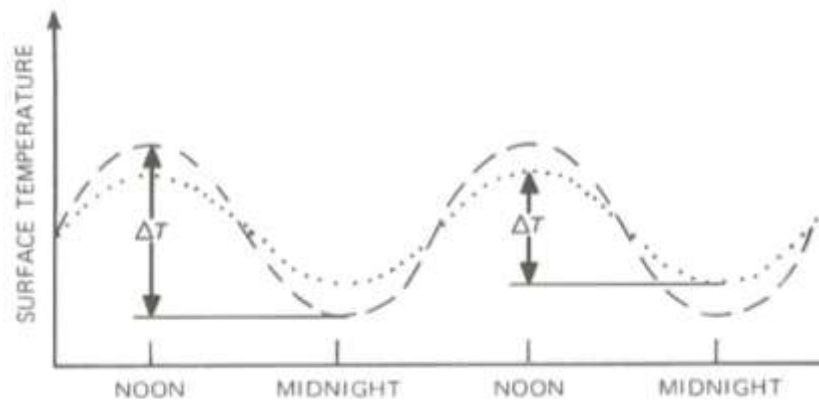


Figure 29: Diurnal cycles where  $\Delta T$  refers to thermal inertia taken from Rees (2013). The dashed line (---) represents a low thermal inertia material such as shale and the dotted line (...) a high thermal inertia material such as basalt and sandstone.

### 2.3.2 Thermal Conductivity

Thermal conductivity is another parameter that influences thermal inertia as described in Eq. 2.5. It refers to the transfer of heat through a medium (Midttømme et al., 1998) and is defined as (Schön, 2015):

$$q = -\lambda (\delta T/\delta x). \text{ (Units: } W m^{-1} K^{-1}\text{)}$$

*Eq. (2.6)*

Where  $q$  is heat flow,  $\lambda$  is thermal conductivity and  $\delta T/\delta x$  the temperature change. It is found to vary by a factor of greater than two for common rock types at the surface (BGS, 2011) (Table 5). Several additional factors control thermal conductivity including porosity, which is a measurement of voids, known as pore spaces, within a medium. It is found that increasing porosity, decreases thermal conductivity (Coolbaugh et al., 2000) (Figure 30); though this is different for unconsolidated sediments\*\* as a result of water and air, that fill pore spaces, being less thermally conductive than rock (BGS, 2011).

*Table 5: Thermal conductivities of common rock types. All values vary depending on porosity, schistosity\*, etc. Data ranges are from Schön (2015). Original references are noted: [1] Rybach and Muffler (1981), [2] Cermak and Rybach (1982), [3] Blackwell and Steele (1989), [4] Jessop (1990) [5] Gong (2005) and [6] Fjaer et al. (2008).*

Lithology	Thermal conductivity ( $W m^{-1} K^{-1}$ )
Basalt	1.12 – 5.33 <sup>[2][4]</sup>
Claystone/Siltstone	0.60 – 4.00 <sup>[2][3][4][5]</sup>
Granite	1.25 – 4.45 <sup>[2][4]</sup>
Gneiss	1.20 – 4.80 <sup>[2]</sup>
Limestone	0.62 – 4.41 <sup>[1][2][3][4][5]</sup>
Marble	1.59 – 4.00 <sup>[2]</sup>
Sandstone	0.90 – 6.50 <sup>[1][2][3][4][5][6]</sup>
Schist	1.40 – 5.20 <sup>[2]</sup>
Shale	0.55 – 4.25 <sup>[1][2][3][6]</sup>

\* Schistosity refers to a geological fabric in which minerals align in a sheet like manner. It forms as a result of pressurisation, i.e. with increasing burial.

\*\* Unconsolidated sediment refers to loose material, varying from sand to clay.

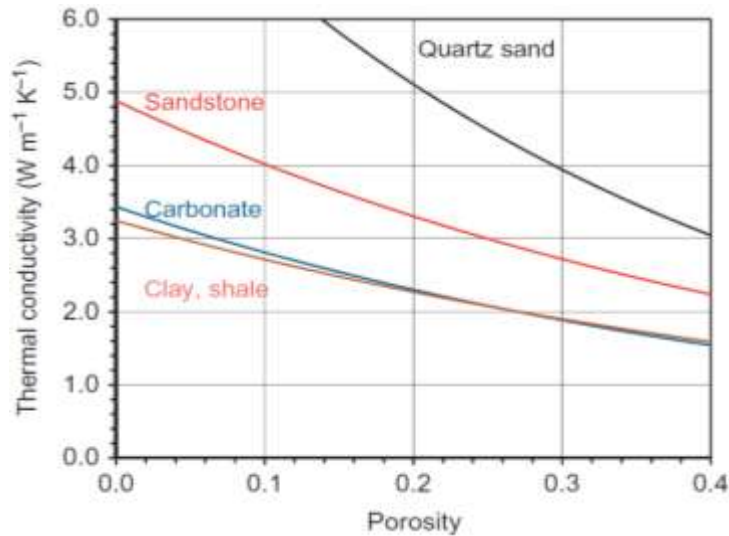


Figure 30: Thermal conductivities varying as a function of porosity and composition as taken from Schön (2015) after Griffiths et al. (1992). Additional lithological parameters including schistosity have not been considered and therefore the ranges differ to those noted in Table 5.

Coolbaugh et al. (2000) confirm the relationship between porosity and thermal conductivity within the geothermally active region of Steamboat Springs, Nevada, USA. Here, deposits of younger, highly porous, opaline-rich\* sinter are seen progressively changing to older, less porous chalcedonic\*\* deposits. It is found that thermal inertias for the younger lithologies are lower than the older lithologies. The lower values arise due to air filled pore spaces. At Steamboat Springs water does not infill pore spaces due to the depth of the water table. Air is a poor thermal conductor at  $0.02 \text{ W m}^{-1} \text{ K}^{-1}$  compared to water at  $0.6 \text{ W m}^{-1} \text{ K}^{-1}$  (BGS, 2011); therefore higher porosities correspond with lower conductivities. If the pore spaces were water filled, thermal conductivity would be higher; though still not as high as the older sinter.

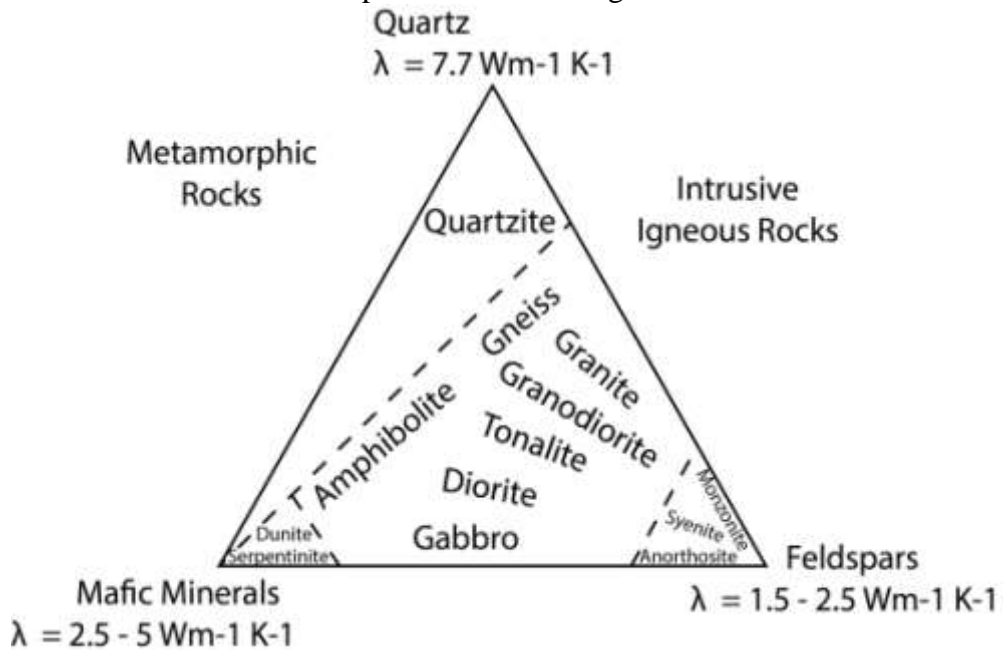
A second factor affecting thermal conductivity is lithological composition. Rock forming minerals have a natural variation in terms of the thermal conductivity and can therefore alter the overall rock (Clauser and Huenges, 1995). From Figure 31 it is evident that quartz has one of the highest conductivities and therefore quartz rich rocks

---

\* Opaline is a hydrous silica rock.

\*\* Chalcedony refers to the compact, microcrystalline structure of silica.

Metamorphic and intrusive igneous rocks



Extrusive igneous (volcanic) and sedimentary rocks

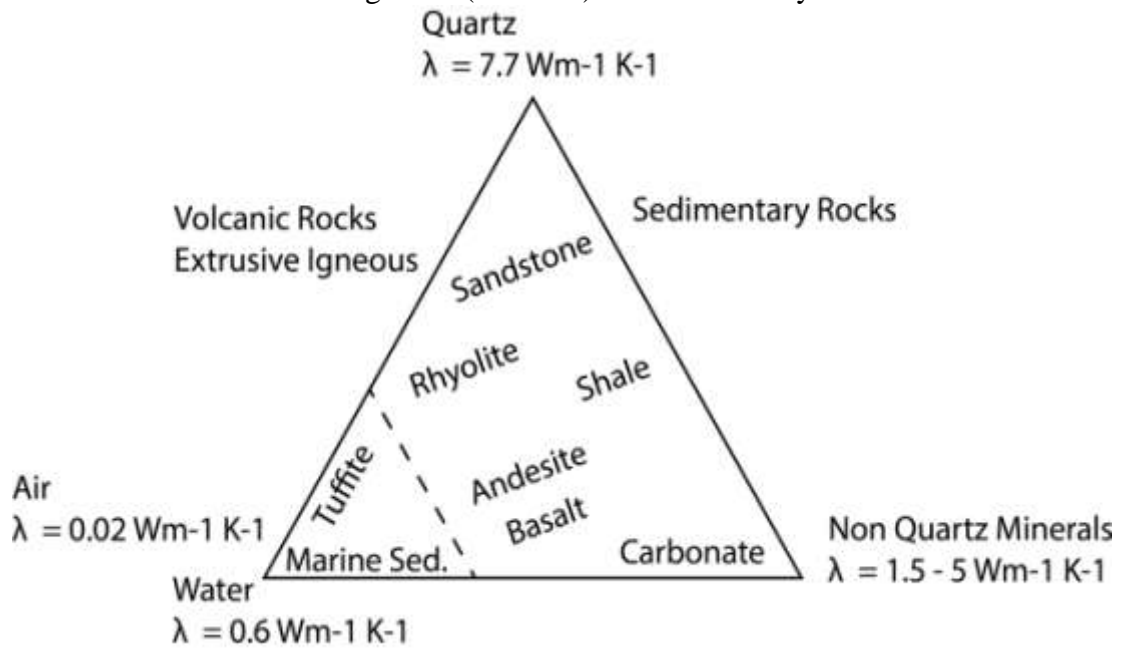


Figure 31: Compositional diagrams showing mineral thermal conductivities as adapted from Clauser and Huenges (1995). The third mineral phase for the lower plot is water/air due to the significance of porosity within these lithologies.

such as granite will also be higher. Rock composition also influences albedo (Calvin et al., 2005) (Figure 32); with lighter, more silicic rocks reflecting more radiation and consequently having lower LSTs during the day time than darker more mafic\* rocks.

Mineral and grain sizes also affect conductivity, as well as thermal inertia. Earlier studies have found that decreasing grain size, decreases thermal conductivity as a result of increasing the number of grain contacts per volume (Schön, 2015). Grain contacts have lower conductivities than solid grains and therefore increasing the number of grains, lowers the conductivity. Degree of induration is also important, with certain cements more conductive than others. In general a cemented rock is always more conductive than the equivalent rock of unfilled pore space (Schön, 2015). Anisotropy, i.e. the mineral alignment, also effects thermal conductivity. This effect is particularly significant for metamorphic rocks (Table 6).

Thermal conductivities of superficial deposits\*\* and soils also vary due to their complex mineral and organic compositions. The conductivity is again reliant upon the nature of the deposit, porosity and degree of saturation (BGS, 2011). Saturation is a measurement of a rock's fluid content and is significant in terms of sedimentary rocks, superficial deposits and soil. This is summarised by Table 7.

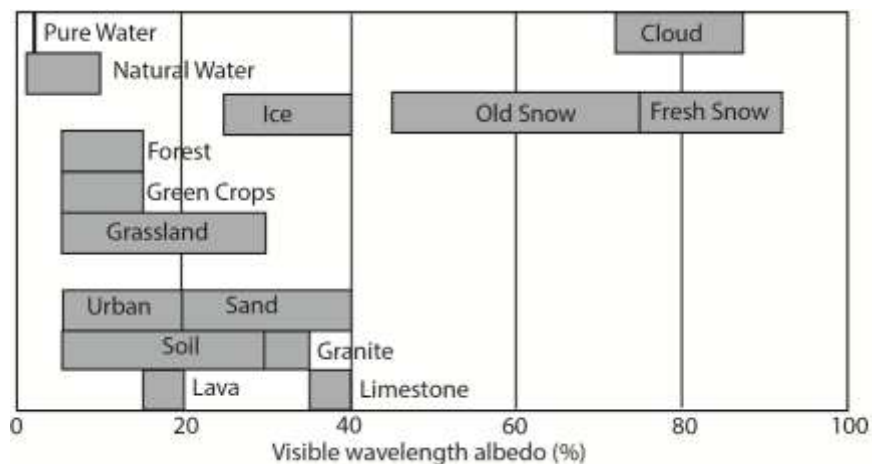


Figure 32: Typical broadband surface albedo, as modified from Rees (2003). Lighter coloured rocks such as granite will have a higher albedo than the more mafic rocks, which will ultimately affect the overall radiation absorbed and thus the LST.

\* Mafic rocks refer to darker rocks that are typically ferromagnesian rich.

\*\* Superficial deposits refer to young deposits, formed in the Quaternary.

Table 6: Thermal conductivities of rock types affected by various schistositities. Data ranges are from Schön (2015) as in Cermak and Rybach (1982).

Lithology	Thermal conductivity ( $\text{W m}^{-1} \text{K}^{-1}$ )
Gneiss - Parallel	1.2 – 4.8
Gneiss - Perpendicular	1.9 – 3.2
Schist - Parallel	2.2 – 5.2
Schist - Perpendicular	1.4 – 3.9

Table 7: Thermal conductivities of superficial deposits, which vary dependent upon the saturation of the sediments (BGS, 2011).

Superficial deposits	Thermal conductivity ( $\text{W m}^{-1} \text{K}^{-1}$ )
Unsaturated clay	1.11
Unsaturated sand	0.77
Unsaturated silt	1.67
Saturated sand	2.50
Saturated silt or clay	1.67

### 2.3.3 Specific Heat Capacity

Specific heat capacity refers to the capability of a medium to store heat. It influences both LST and thermal inertia (Schön, 2015):

$$C_p = \frac{q}{m \cdot \Delta T}. \text{ (Units: } J/(kg \cdot K))$$

Eq. (2.7)

Where  $C_p$  refers to the specific heat capacity,  $q$  to heat flow,  $m$  to the mass and  $\Delta T$  to the temperature change. The specific heat capacity is dependent upon lithology. In terms of sedimentary rocks, the more saturated the higher specific heat capacity. This is due to the increased presence of water which has a relatively high heat capacity at approximately  $4 \text{ kJ kg}^{-1} \text{K}^{-1}$  (Schön, 2015) (Figure 33).

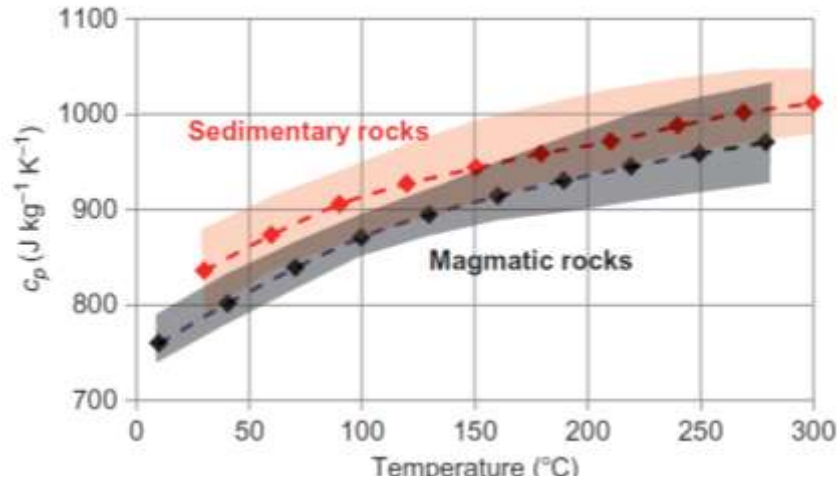


Figure 33: Specific heat capacity for magmatic and sedimentary rocks as taken from Schön (2015). Data originates from Vosteen and Schellschmidt (2003).

### 2.3.4 Thermal Diffusivity

The thermal diffusivity of a given lithology also affects LST and is a measure of the penetration of temperature changes into a material (Schön, 2015):

$$\alpha = \frac{\lambda}{C_p \cdot \rho} \quad (\text{Units: } m^2/s)$$

Eq. (2.8)

Here,  $\alpha$  refers to the thermal diffusivity,  $\lambda$  to thermal conductivity,  $C_p$  to specific heat capacity at constant pressure, given the geological timescale and  $\rho$  to the density. The diffusivity of a typical rock surface is noted as varying from  $0.077 \text{ m}^2 \text{ day}^{-1}$  to  $0.103 \text{ m}^2 \text{ day}^{-1}$  (BGS, 2011), with clays approximately  $0.065 \text{ m}^2 \text{ day}^{-1}$  and metamorphosed quartz around  $0.17 \text{ m}^2 \text{ day}^{-1}$ .

### 2.3.5 Emissivity

Emissivity refers to the ratio of energy radiated from a material's surface to that of the energy radiated from a blackbody (National Physics Laboratory, 2014). It is dependent upon and governed by the surface optical properties, i.e. land cover and all lithological properties, including porosity and colour (Figure 34). Emissivity is defined from zero to one, where one is a perfect blackbody (i.e. a material that perfectly radiates and absorbs energy).

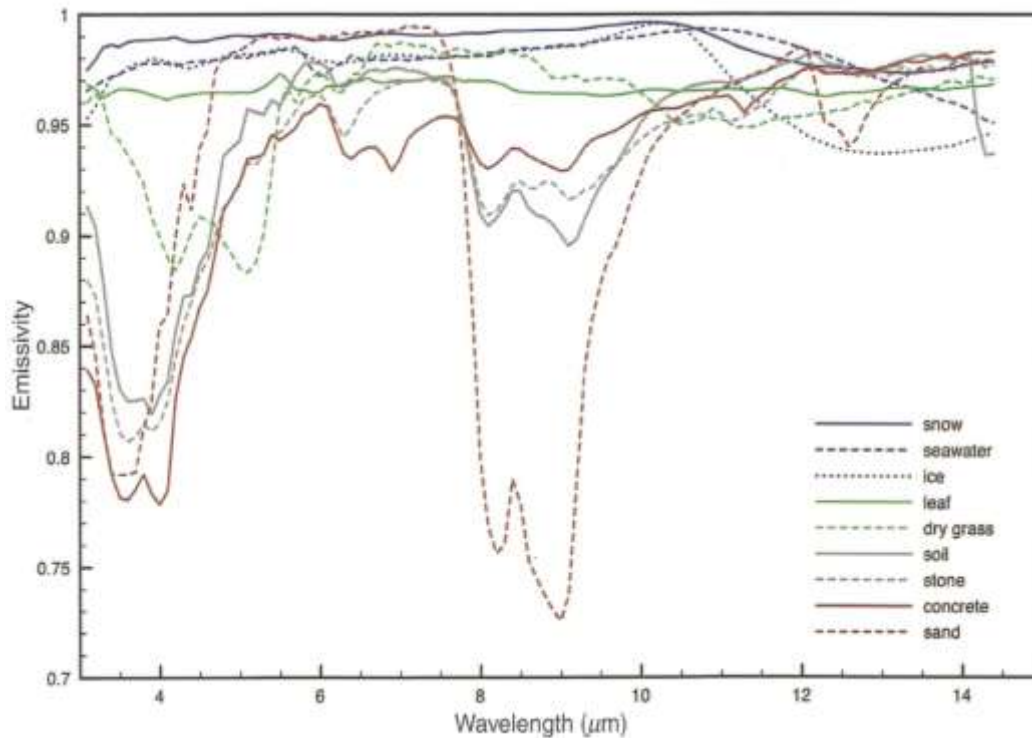


Figure 34: Typical emissivities of materials of normal incidence in the range 3  $\mu\text{m}$  to 15  $\mu\text{m}$  taken from Rees (2013). Data is averaged from a large sample of MODIS datasets.

Soils are found to be most highly variable, which contrasts to forests and rocks which are generally more constant (Tianyu et al., 2012). Emissivity tends to remain fairly constant for short periods, except during periods of increased precipitation (Tianyu et al., 2012).

### 2.3.6 Vegetation and Land Cover

Vegetation is a significant component of the terrestrial environment, modulating ecosystems via soil stability and water retention (Coolbaugh et al., 2000; Calvin et al., 2005; Leilei et al., 2014). Its growth is periodic and reliant upon precipitation and thus root-zone soil moisture (Dorigo et al., 2012). Vegetation is often described in terms of the fraction of the surface covered by green vegetation. This is known as the fractional vegetation ( $f_v$ ) and is reported between zero and one, where highly covered surfaces are one. In addition to this, land cover refers to different biomes varying from forests to ice, and thus it is directly related to the geographical latitude.

Fv and land cover play a significant role in terms of LST by modulating the surface absorption of incoming radiation as a result of surface optical properties and morphological structure (Stroppiana et al., 2014). The effects are therefore more significant during the day as a result of direct solar heating. In arid regions, abundant bare soils absorb more solar radiation than densely vegetated regions (Tianyu et al., 2012). The warmest LSTs on Earth are frequently recorded in such environments, though such regions cool quickly at night. The opposite is observed in densely vegetated areas where less solar radiation is absorbed but more retained (Van De Kerchove et al., 2013).

### **2.3.7 Hydrological Parameters**

Soil moisture is one of the main drivers in the exchange of energy, water and carbon between the land and atmosphere. It has several effects on the surface, including on the partitioning of sensible and latent heat; with wetter soil surfaces having cooler LSTs and losing more latent heat (Ghent et al., 2010). Drier soil surfaces have warmer LSTs and instead lose more sensible heat (Smith et al., 2006). Typically for increases in soil moisture, LSTs decrease (Yao et al., 2013). Soil moisture is also found to affect emissivity, with increases in soil moisture leading to simultaneous increases in surface emissivity. Mira et al. (2007) attributes this relationship to a decrease in soil reflectivity as a result of the water coating the soil particles.

Several studies also report a strong, often negative, correlation between LST and precipitation (Trenberth and Shea, 2005; Wu et al., 2013). This is as dry conditions typically correspond to increased solar radiation and less evaporative cooling; meaning that wetter summers are also cooler. Moreover, increased precipitation is accompanied by increased cloud cover, blocking incoming radiation and thus lowering LSTs. Nunez et al. (2008) additionally report that increasing precipitation, increases surface heat storage capacity, increasing minimum LSTs, reducing maximum LSTs and the overall diurnal difference.

### 2.3.8 Topography and Geolocation

Elevation is recorded throughout literature as having an inversely linear relationship with LST as a result of decreasing atmospheric temperature lapse rates (Calvin et al., 2005; Saraf et al., 2005; Bonan, 2008; Miliareisis, 2009) (Figure 35). Occasionally temperature can increase with elevation, though this is related to local influences, such as cloud (Sabins, 1999). The volume of water vapour present is directly related to this with previous studies reporting that the volume of water vapour decreases with increasing elevation and as a result of this radiation absorption decreases, creating cooler LSTs (Bonan, 2008).

The slope and aspect\* of a region also affect the LST as a result of variations in solar zenith and azimuth angles. Maximum LSTs occur when there is maximum incoming solar radiation, i.e. when a surface is perpendicular to the solar beam. To create the

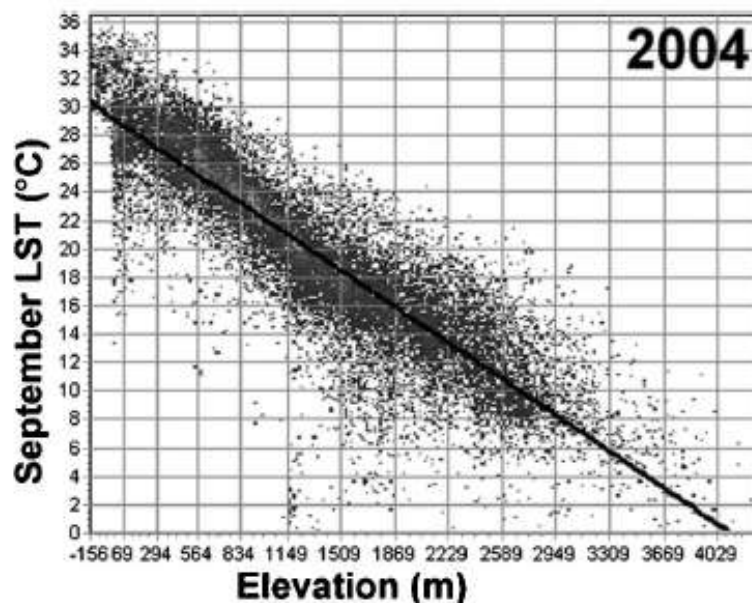


*Figure 35: Elevation versus LST (for September 2004) across the Afar Depression as taken from Miliareisis (2009). Elevation data originates from the GLOBE DEM (Global Land One-km Base Elevation Project Digital Elevation Model) dataset, whilst the LST dataset is from NASA's MODIS instrument that is found aboard it's Terra satellite.*

---

\* Slope refers to geological surfaces that dip in the same direction or the maximum rate of change in downhill descent between a cell and its neighbours. Aspect refers to the greatest downhill descent between a cell and its neighbours. (Environmental Systems Research Institute Inc., 2007).

greatest LSTs therefore requires a different solar zenith angle dependent upon topography, aspect and slope. In addition to this, solar exposure also depends upon geolocation (Bonan, 2008). Typically equatorial regions receive more radiation and have warmer LSTs as a result of maximum incoming solar radiation. Seasonal variations are also related to geolocation and again influence the intensity of incoming solar radiation, with intensity increased during summer.

### **2.3.9 Satellite Viewing Geometry**

LSTs are also found to vary dependent upon the angle of observation, i.e. the satellite zenith angle. This is as when radiation propagates through the atmosphere it interacts with atmospheric constituents such as cloud. These interactions act to attenuate and enhance the intensity of the radiation, thus modifying the top of atmosphere brightness temperature measured by the satellite, as previously explained in Chapter 2.1. Therefore the longer the distance travelled through the atmosphere, the more distorted the measurement may become. Given this, the most accurate results are achieved when the observation angle is nadir, i.e., when the satellite is overhead and the distance that radiation travels through the atmosphere is minimised (Calvin et al., 2005; Joiner and Poli, 2005). In addition to this, surface emissivity can also vary dependent upon the satellite zenith angle. This is significant as it may also incorrectly affect the derived LST.

## **2.4 Targeting Hydrocarbon Basins**

Previous literature is now discussed with respect to rift basins and LST studies. A number of different remote sensing techniques have previously been employed, alongside more traditional geophysical surveys (Aretouyap et al., 2016), to specifically target features hinting at the presence of hydrocarbon rich basins (Sabins, 1999). This includes the use of Landsat MSS, aerial magnetics and gravity surveys in eastern Africa (Miller, 1975), the use of Landsat TM images over the Arabian Peninsula (Wender and Sabins, 1991) and the deployment of airborne radar surveys over Papua New Guinea (Valenti et al., 1996). All of the aforementioned aimed at identifying surface features

that hint at the subsurface structures and are additionally all high resolution datasets (Sabins, 1999).

Following the initial identification, the highlighted features were studied using ground based surveys such as seismics. These surveys were able to confirm that the remote sensing techniques accurately identified the surface expressions and concluded that it is plausible to highlight geological features remotely. The aforementioned exploration studies eventually all yielded commercially viable oil (Sabin, 1999). A combination of these techniques, along with the analysis of more recent datasets, are now applied to the mapping of environmental disasters such as oil spills across the globe (Brekke and Solberg, 2005; Jha et al., 2008).

## **2.5 LST Studies**

In this study LSTs are exploited as a method of delineating hydrocarbon rift basins. Previous studies have applied the use of remotely sensed LSTs worldwide in a variety of geologic and climatic settings to map geothermal anomalies. Geothermal anomalies are often associated with regions of increased tectonic activity, such as Iceland (Einarsson and Kristinsson, 2010), the Great Basin region in Nevada (Coolbaugh et al., 2000) and the EARS itself (Miliareisis, 2012). Additional studies have also considered the presence of geothermal anomalies related to other geological phenomena including earthquakes (Zoran, 2012), though this is often accounted for within the range of normal thermal variation (Blackett et al., 2011). Numerous remotely sensed datasets and techniques have therefore been utilised dependent upon the study and target features. Table 8 summarises the studies that are now discussed throughout this section.

One approach of highlighting geothermal anomalies looks at accounting for the physical variables influencing LSTs. This allows for corrections, eliminating false anomalies and better distinguishing anomalies from their surroundings. An example of this was implemented at Steamboat Springs, Nevada, USA (Coolbaugh et al., 2000). Airborne remote sensing was applied to map an active geothermal area.

*Table 8: LST studies are summarised, detailing datasets used, area of interest and the aim of the study. All are discussed in further detail within the text. Table continues onto next page. Acronyms are as follows; ASTER: Advanced Spaceborne Thermal Emission and Reflection Radiometer, AVHRR: Advanced Very High Resolution Radiometer (sea surface temperature data), AVIRIS: Airborne Visible/Infrared Imaging Spectrometer, CTI: compound topographic index, ETM+: Enhanced Thematic Mapper Plus, FLIR: Forward-Looking Infrared, GLOBE DEM: Global Land One-km Base Elevation Project Digital Elevation Model, MODIS: Moderate Resolution Imaging Spectroradiometer, NDVI: Normalised Difference Vegetation Index, nsnow: number of snow covered days, potSRAD: total yearly potential solar radiation, SEBASS: spatially enhanced broadband array spectrograph system (frequently used in mineral mapping), TIMS: Thermal Infrared Multispectral Scanner, TM: Thematic Mapper, TRMM: Tropical Rainfall Measurement Mission.*

<b>Study</b>	<b>LST dataset</b>	<b>Additional datasets</b>	<b>Area</b>	<b>Aims of Study</b>
Blackett et al. (2011)	MODIS	-	Gujarat, India	Detecting earthquake precursors.
Calvin et al. (2005)	ASTER	SEBASS, DEM, AVIRIS	Nevada, USA	Applying remote sensing to geothermal exploration.
Coolbaugh et al. (2000)	TIMS	AVIRIS	Nevada, USA	Remotely mapping geothermal anomalies.
Coolbaugh et al. (2007)	ASTER	-	USA	Remotely mapping geothermal anomalies.
Einarsson and Kristinsson (2010)	FLIR T360 IR camera	-	Iceland	Thermal imaging in the field – mapping anomalies in soil.

Leilei et al. (2014)	MODIS	NDVI, TRMM	Tibet, China	Evaluating relationship between LST, vegetation and precipitation.
Miliaresis (2009)	MODIS	GLOBE DEM	Afar region, EARS	Thermal and terrain modelling from multi-temporal LSTs.
Miliaresis (2012)	MODIS	GLOBE DEM	EARS	Selective variance reduction of multi-temporal LST.
Miliaresis (2013)	MODIS	GLOBE DEM	Indian Ocean, Persian Gulf and Black Sea areas	Terrain analysis for active tectonic zone characterisation.
Qiuji and Chuting (2015)	Landsat-7 ETM+ and Landsat-5 TM	NDVI	Xi'an, China	Assessing the urban heat environment and LST-vegetation relationship.
Van De Kerchove et al. (2011)	MODIS	SRTM,NDVI, CTI, potSRAD, nsnow	Russia	Studying LST spatiotemporal variability and its relationship with physiographic variables.
Zoran (2012)	MODIS	AVHRR	Tohoku, Japan	Detecting earthquake precursors.
Zouzias et al. (2011)	MODIS	-	Southeast Europe	Geothermal reconnaissance using multi-temporal LST.

Two techniques were applied using NASA's aircraft mounted Thermal Infrared Multispectral Scanner (TIMS) data. The first technique employed the use of the TIMS night time data, which was selected as geothermal anomalies are expected to show higher contrasts to surroundings at this time as result of a reduced solar influence. Initial processing involved the compensation of albedo and topography via the application of a correction derived from the slope and reflectance. Corrections improved the detection of the anomalies, though still did not fully reveal them. This was as different porosities affecting the thermal inertia were not considered.

The second technique used the same datasets but instead focussed on minimising the effects of thermal inertia. To do this TIMS data was averaged over day and night to gain an approximate daily average. Similarly to before, albedo and topography were then corrected. Using the average data, in addition to the previous corrections, led to a more clearly defined anomaly than the first technique; though again this approach could not fully delineate the anomalies present. Additional limitations also existed, of which the most significant was the dependence of the corrected factors on each other.

Derived from the success of the TIMS analysis, a number of studies have applied similar approaches with variations on technique or dataset, including Coolbaugh et al. (2007) and Calvin et al. (2005) that both applied Advanced Spaceborne Thermal Emission and Reflection Radiometer (ASTER) datasets across the Nevada region.

Various LST studies have progressed this approach, by not only correcting but applying further statistical analysis. One example is taken from Miliareisis (2009), which uses MODIS LST night time data across the Afar Depression to identify geothermal anomalies, during the increased volcanic activity of 2005. Night time LSTs were used as it was expected that land affected by geothermal activity would resist LST decreases at night, which are related to the solar influence. The dataset was averaged monthly, from 2004 through to 2006. Initial findings displayed shifts to warmer LSTs in the Afar Depression from April 2005 through to October 2005.

The 2004 monthly LST frequency was then studied to capture the seasonal variability. Digital elevation models (DEMs) revealed that seasonal variation effects the lower elevations more, with higher elevation regions such as the Ethiopian Dome maintaining

more constant LSTs. Frequency distributions from September of each year were also studied to capture regional variations as a result of the volcanic activity. However this was hindered by the localised nature of the 2005 activity, with the regional outlook failing to identify the geothermal anomalies.

Principle Component Analysis (PCA) was then applied to the dataset. PCA is a statistical technique used to identify patterns within data of high dimension (Smith, 2002). This approach is further detailed in Chapter 3.2, though the basic principles are now briefly noted. PCA generates a series of components which each contain component loadings that describe the amount of variance they account for in the dataset, in this case the LST (Mather, 2004). Component loadings vary between  $\pm 1$  and describe the correlation between eigenvectors generated and the initial dataset; where 0 is no correlation and ( $\pm$ ) 1 is complete correlation.

In Miliareisis (2009), PCA is applied to delineate the temporal and spatial variation of the LST time series. The results reveal that the first three components account for 96 % of the LST variation. Figure 36 graphically displays this to better explain the patterns revealed. Principal component 1 (PC1) reveals a significant association with autumn, winter and spring; PC2 with seasonal fluctuations and PC3 with complex annual patterns. From this, the spatial variation is revealed by comparing component loadings across the Afar (Figure 36). The study reveals three sub regions and highlights the central northern part of the depression as having maximised LSTs with respect to the surroundings throughout the year, i.e. a geothermal anomaly is identified.

Miliareisis (2009) furthers this via terrain modelling using GLOBE-derived (Global Land One-kilometre Base Elevation) elevation due to the known LST-elevation relationship (Saraf et al., 2005) (Figure 35). On application of the terrain models to the Afar it was noted that there was a consistent underestimate in the LSTs as a consequence of the surrounding mountains. Terrain classes were therefore established and the LSTs reanalysed. This resulted in warmer LSTs for September of 2005 than the Septembers of 2004 and 2006. It was then concluded that such methods do highlight anomalies, even when localised and that the LST variation is, as expected, highly elevation dependent. Similar such work has since been successfully applied to volcanic regions within Europe (Zouzias et al., 2011).

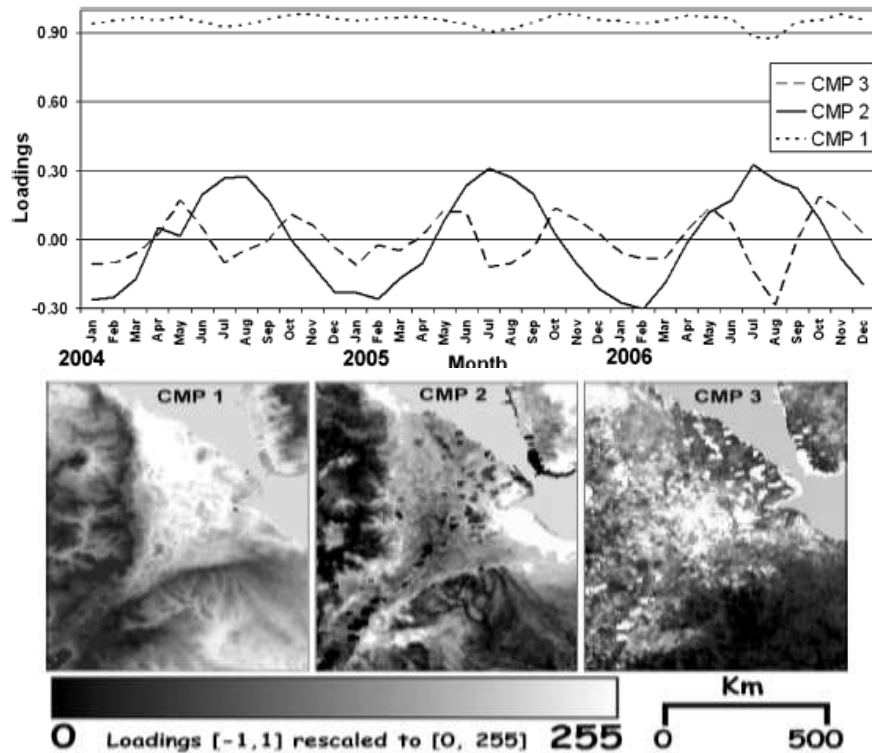


Figure 36: PCA results as taken from Miliareisis (2009). This study aimed to delineate MODIS LST data with respect to elevation and temporal patterns. The upper plot shows the graphical representation of the component loadings that reveal temporal patterns within the dataset. The lower plots show where the correlations between component loadings are observed, i.e. the spatial patterns.

Miliareisis (2012) also invokes the PCA of MODIS LSTs but additionally furthers the analysis by quantifying the independent variables of elevation, latitude and longitude via linear regression analysis. The difference between the PCA and linear regression analysis was calculated revealing unexplained variance. Residual images were then reconstructed accounting for the unexplained variance. This is known as selective variance reduction (SVR). Cluster analysis was applied to the reconstructed images to define the locality of geothermal anomalies which presented themselves as positive in the SVR images. Miliareisis (2013) applies the same approach over the USA and northern Mexico and again is able to successfully define anomalies.

Moving on from PCA, previous literature also looks at the correlation between the LST and the physical parameters driving it. Although such studies do not identify anomalies, they are important for determining the influences on LST. An example of this is Leilei

et al. (2014), whereby MODIS LSTs are correlated with vegetation using the normalised difference vegetation index (NDVI) and precipitation from the Tropical Rainfall Measurement Mission (TRMM). The study successfully highlights the correlation between LST and vegetation and additionally its dependence upon the seasons and the correlation between vegetation and precipitation; hinting at the interconnected nature of the physical parameters influencing LST. Additional studies including Qiuji and Chuting (2015) and Van De Kerchove et al. (2011) have also established correlations between LST and an abundance of variables including vegetation, albedo, topography and solar insolation. All studies conclude similar findings, with correlations dependent upon temporal variations.

In general, previous LST studies within tectonic settings have successfully identified warmer anomalous regions and the variables that influence LST. The spatial extent of the geothermal anomalies is often well mapped. Few earlier studies focus on the use of remotely sensed LSTs to identify rift basins (Miliareisis 2009; Miliareisis 2012) though several studies focus on the locality of faults as an indicator (Miller, 1975, Valenti et al., 1996, Sabins, 1999). Studies concerning LST correlations to variables have been thoroughly considered and demonstrate the interconnected nature of the parameters.

## **2.6 Summary**

LST is a dynamic variable that is influenced by an abundance of interconnected parameters. These parameters include thermal inertia and thermal conductivity which are dependent upon lithology and in turn linked to emissivity, land cover and vegetation. Elevation and geolocation are additional parameters that influence the amount of solar radiation a surface receives. Elevation is particularly notable having an inversely proportional linear relationship with LST (Calvin et al., 2005; Saraf et al., 2005; Miliareisis, 2009). The angle of observation has also been identified as relevant, affecting the measurements of surface emissivity and therefore the retrieval of the LST. This study now attempts to account for several of these factors in order to identify areas of unexplained variance. It is thought that this unexplained variance may be related to subsurface heating, i.e. elevated geothermal gradients, as discussed in Chapter 1.1.6.

Previous work has attempted to use various datasets and techniques to highlight areas of unexplained variance. A number of these studies focus on the EARS but tend to be more concerned with the Afar region. This study differs from previous work by considering a wider area across the EARS on more localised, basin scale. The Turkana region is the focus of several aspects in this thesis and has been mentioned but not extensively studied in previous work. This region is selected based upon its diverse physical parameters, as detailed later in Chapter 3.

Several techniques from previous work have been applied within this study including the application of PCA; which is modified from previous studies, with the LST analysed with respect to physical parameters such as topography as opposed to temporal patterns and additionally to elevation corrected LSTs as well as the absolute LSTs. Correction of elevation has also been applied within previous work such as Miliaris (2009). However, analysis following corrections within this study differs from previous work, with additional analysis on the remaining variance post correction via a restricted PCA.

The following chapter now details the datasets and methods applied within this thesis. Previous studies are referenced where similar techniques are applied. Parameters analysed throughout this thesis are selected based upon the known influences on LST as discussed within this chapter.

## **3. Methods**

### **3.1 Instruments and Data Selection**

A range of datasets from a number of satellites have been used within this study. The datasets are now described with reference to their origin. The main LST dataset is taken from NASA's Moderate Resolution Imaging Spectroradiometer (MODIS) collection 5 and therefore additional satellite and instrument details are provided. Collection 5 is selected as it is noted as substantially refined and considerably improved compared to collection 4 (Wan, 2006). This includes the implementation of procedures to remove cloud contaminated LSTs – a process that is not applied to the collection 4 dataset (Wan, 2006). However, it should be noted that collection 5 is not without its own issues which include the dataset being much cooler than other sensors over similar areas (Liu et al., 2007).

#### **3.1.1 MODIS**

MODIS is an Earth observation instrument flown on both of NASA's Aqua and Terra satellites (NASA, 2016). Its main purpose is to collect visible and infrared multichannel data relevant to the studies of the atmosphere, land and ocean. The four times daily data is produced both day and night, with global coverage achieved every one to two days. Table 9 details the specifications for the both satellites and the MODIS instrument. For this study, MODIS has been selected for its global coverage, high resolution ( $1^\circ$ ) and specific spectral bands designed to accurately monitor LST. The dataset has been obtained from the NASA Land Processes Distributed Active Archive Center (LP DAAC) USGS/Earth Resources Observation and Science (EROS) Center, Sioux Falls, South Dakota (2001).

The pre-processing steps of the selected data are now shown in Figure 37, whereby the product ids and the organisations that generate each product are noted, along with the steps required to produce such datasets. From Figure 37, the point of interception of the data within this thesis is also noted - at the level-3 product, which has been generated

Table 9: Satellite and instrument specifications for the MODIS dataset (NASA, 2016).

Satellites	Terra and Aqua
Organisation	NASA
Launch date	Terra: 18 <sup>th</sup> December 1999, Aqua: 4 <sup>th</sup> May 2002
End date	Unknown
Alternative names	Terra: EOS AM-1, Aqua: EOS PM-1
Data Prefix	Terra: MOD, Aqua: MYD
Instrument	MODIS
Orbital path	705 km, sun-synchronous, near-polar, circular.
Orbital timing	Descending node: 10:30 a.m (Terra), ascending node: 1:30 p.m
Scan rate	20.3 rpm, cross track.
Swath dimensions	2330 km (cross track) by 10 km (along track at nadir).
Spatial resolution	250 m (bands 1-2), 500 m (bands 3-7), 1000 m (bands 8-36).
Spectral bands	36

at the University of Leicester. The remaining part of this section now details aspects of the pre-processing steps in further detail, expanding on the brief overview in Figure 37.

Following receipt of the level-1B calibrated data, pre-processing of the LST dataset includes the application of the generalised split window algorithm developed by Wan and Dozier (1996) and as validated by the MODIS Airborne Simulator (MAS) data and field measurements since 1995 (Wan, 1999). The formula of this algorithm is now provided (Wan and Dozier, 1996; Wan, 1999):

$$T_s = (A_1 + A_2 \frac{1-\varepsilon}{\varepsilon} + A_3 \frac{\Delta\varepsilon}{\varepsilon^2}) \frac{T_{31}+T_{32}}{2} + (B_1 + B_2 \frac{1-\varepsilon}{\varepsilon} + B_3 \frac{\Delta\varepsilon}{\varepsilon^2}) (T_{31} - T_{32}) + C$$

$$\text{Where } \varepsilon = 0.5(\varepsilon_{31} + \varepsilon_{32}) \text{ and } \Delta\varepsilon = \varepsilon_{31} - \varepsilon_{32}$$

Eq. (3.1)

Here,  $T_s$  refers to the retrieved value, i.e. the surface temperature,  $T_{31}$  and  $T_{32}$  refer to top of atmosphere brightness temperatures of MODIS bands 31 and 31 respectively,  $\varepsilon$  to



Figure 37: Flow diagram of the initial pre-processing steps applied to the MODIS dataset prior to the implementation of analyses. For further details of the analysis prior to the interception of data by the University of Leicester, see Justice et al. (2002). For post processing steps, please see Chapter 3.2 (Figure 41).

the emissivity, where  $31$  and  $32$  also denote the respective MODIS bands and  $A_1, A_2, A_3, B_1, B_2, B_3$  and  $C$  to coefficients (Wan and Dozier, 1996; Wan, 1999; Fang et al., 2014).

The split window algorithm differs from others by not requiring precise atmospheric profiles nor pixel by pixel radiative transfer simulations. The accuracy of this algorithm, unlike the alternatives, relies on the knowledge of surface emissivity (Wan, 1999), as well as a number of other variables including viewing angles, cloud cover and water vapour (Wan and Dozier, 1996). For alternative algorithms that can potentially be applied to the MODIS dataset, refer to Wan (1999).

This split window algorithm was selected as it aims to achieve LST accuracy of 1 K at 1 km resolution under the clear sky conditions for which retrieval is possible. It is possible to validate this accuracy via field measurements across flat and uniform land surfaces. An accuracy of 1 K is only achieved, however, with known emissivities for the channels (Wan, 1999). Extensive error analysis shows that viewing angles and atmospheric water vapour must also be considered in order to fulfil the goal of 1 K LST accuracy (Wan, 1999). Considering these additional parameters within the split window algorithm allows for improved accuracy, successfully reducing errors to  $< 1$  K over the entire viewing range (Wan and Dozier, 1996.) Water vapour is significant in terms of the algorithm as it is the most variable absorber within LST spectral windows, thus if this is known then the remainder of atmospheric terms are also known to a high accuracy (Wan, 1999).

Following the application of the split window algorithm, several level products are derived. This is completed at the UK CEMS facility using software developed at the University of Leicester. For this study, level 3 Terra (MOD11) and Aqua (MYD11) products are used for the region indicated in Figure 19. The data streams run from August 2002 to end 2013 for both Aqua and Terra. The LST data is processed together with auxiliary datasets into a common ‘harmonised’ format on an equal latitude-longitude grid of  $10^\circ \times 10^\circ$  tiles of  $0.01^\circ$  resolution (approximately equal to 1 km resolution) (Table 10). The MODIS level 3  $0.01^\circ$  LST data are constructed from the data in the MOD11\_L2 / MYD11\_L2 level 2 products by mapping the level 2 pixels onto equal-angle grids, and averaging the LST values - separately for day and night - of

*Table 10: Longitudes and latitudes that define tiles used within this analysis. Tiles are named according to the most dominant country or geographical feature present.*

Tile id	Region	Minimum Latitude (° N)	Maximum Latitude (° N)	Minimum Longitude (° E)	Maximum Longitude (° E)
H21V08	Lake Kariba	-20	-10	20	30
H21V09	Lake Tanganyika	-10	0	20	30
H21V10	Lake Edward	0	10	20	30
H21V11	Libyan Desert	10	20	20	30
H22V08	Lake Malawi	-20	-10	30	40
H22V09	Lake Victoria	-10	0	30	40
H22V10	Lake Turkana	0	10	30	40
H22V11	Eritrea	10	20	30	40
H23V10	Somalia	0	10	40	50
H23V11	Afar Depression	10	20	40	50

overlapping pixels in each grid using the overlapping areas as weight. At higher latitudes, there may be multiple observations in clear sky conditions for both day and/or night. Daily day time and night time LST values for all grids are derived from single clear-sky MODIS observations. This is done by selecting the clear sky LSTs from the level 2 data with the smallest satellite zenith angles.

The corresponding auxiliary data includes satellite and solar zenith and azimuth angles, cloud cover, aerosol masks and surface emissivity for MODIS channels 31 and 32 between 10.780  $\mu\text{m}$  to 11.280  $\mu\text{m}$  and 11.770  $\mu\text{m}$  to 12.270  $\mu\text{m}$ , respectively.

Independent variables of total column water vapour (tcwv) and fractional vegetation (fv) are also provided within the MODIS auxiliary data but do not originate from the MODIS retrieval itself. Instead total column water vapour is derived from the European Centre for Medium-Range Weather Forecasts (ECMWF) ERA-Interim reanalysis (Dee

et al, 2011). Whilst,  $f_v$  is based on the Geoland-2 FCOVER dataset, which is available globally at the desired near 1 km resolution of  $1/112^\circ$  every 10 days from 1999 and acquired from a moving temporal window of approximately 30 day composites of observations (Baret et al, 2013). Analysis of this data is later discussed in Chapter 3.2.

### **3.1.2 Shuttle Radar Topography Mission**

Elevation is obtained from the Shuttle Radar Topography Mission (SRTM). The SRTM was a joint project between NASA, the National Geospatial-Intelligence Agency, and the German and Italian Space Agencies (Farr et al., 2007). It was deployed in February 2000, with the goal of creating the highest resolution DEM of the Earth to date and a globally consistent dataset. The data has a resolution of 90 m that has been averaged to 1 km. The absolute horizontal and vertical accuracies of the SRTM dataset are noted at 20 m and 10 m, respectively (Farr et al., 2007). In this study, the elevation is considered on the same grid as the MODIS dataset of  $0.01^\circ$  (1 km equivalent) (Figure 9). Elevation does not significantly vary temporally and therefore this dimension is not considered further, with the dataset static.

### **3.1.3 ATSR LST Biome V2: GlobCover Derivative**

The land cover classification scheme used within this study is the ATSR (Along Track Scanning Radiometers) LST Biome V2 (ALB2) scheme generated at the University of Leicester (Ghent et al., 2012). The biome auxiliary data is a variant of the Globcover classification (Arino et al. 2007), with the original  $1/360^\circ$  spatial resolution product having been re-gridded to  $1/120^\circ$ , i.e. approximately 1 km resolution. In addition, the original Globcover bare soil class has been divided into six separate classes, taking the total number of land and inland water classes to 27 (Figure 38 and Table 11). GlobCover is an ESA project that was commissioned in 2005 in collaboration with a number of international scientific partners (UCLouvain and ESA, 2011). Its aim was to produce the first 300 m global land cover maps using observations recorded by the

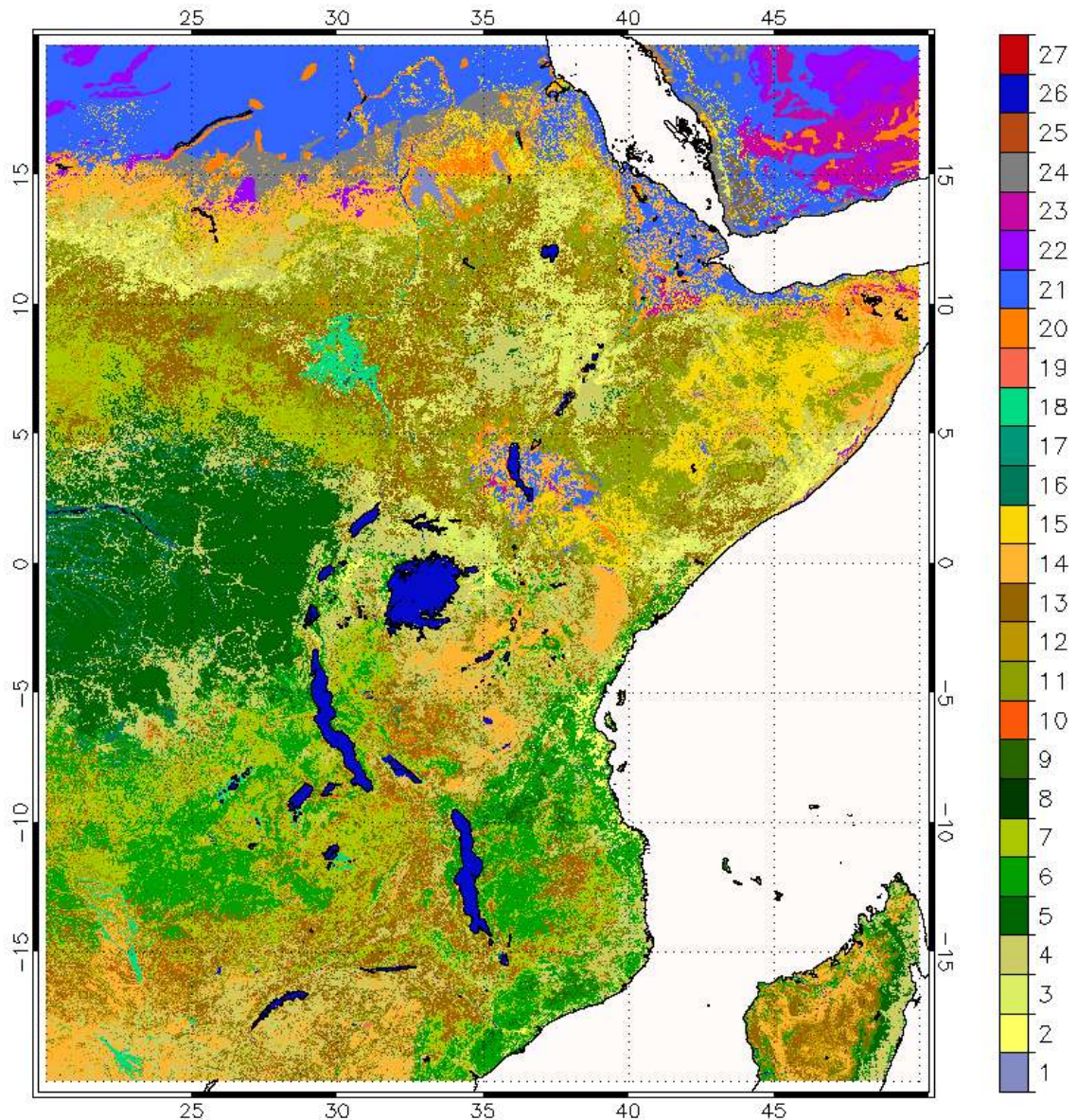


Figure 38: ALB2 land cover as generated at the University of Leicester; for the EARS mapped on a  $0.01^\circ \times 0.01^\circ$  resolution grid ((NASA LP DAAC USGS EROS, 2001; Ghent, 2012). Temporal resolution is not applicable for this dataset and accuracy has not been provided.

MEDium Resolution Imaging Spectrometer (MERIS) instrument on board the ENVISAT mission. Land cover and thus the biomes present across the EARS are not considered on a temporal basis within this study, as they are not expected to vary significantly. The dataset considered here is therefore temporally static. For this land cover product, accuracy is not provided and is thus a limiting factor to be considered.

*Table 11: ALB2 land cover classification, detailing the biome that each ALB2 number describes (NASA LP DAAC. USGS EROS, 2001; Ghent, 2012). This data is shown spatially across the EARS in Figure 38.*

ALB2 number	Land cover classification
1	Post-flooding/irrigated croplands
2	Rainfed croplands
3	Mosaic Cropland / Vegetation
4	Mosaic Vegetation / Cropland
5	Closed to open broadleaved evergreen and/or semi-deciduous forest
6	Closed broadleaved deciduous forest
7	Open broadleaved deciduous forest
8	Closed needleleaved evergreen forest
9	Open needleleaved deciduous or evergreen forest
10	Closed to open mixed broadleaved and needleleaved forest
11	Mosaic Forest/Shrubland / Grassland
12	Mosaic Grassland / Forest/Shrubland
13	Closed to open shrubland
14	Closed to open grassland
15	Sparse vegetation
16	Closed broadleaved forest regularly flooded -Fresh
17	Closed broadleaved semi-deciduous and/or evergreen forest regularly flooded -Saline
18	Closed to open vegetation on regularly flooded or waterlogged soil
19	Artificial surfaces and associated areas
20	Bare soil General
21	Bare soil Entisols – Orthents
22	Bare soil Shifting sand
23	Bare soil Aridisols - Calcids
24	Bare soil Aridisols - Cambids
25	Bare soil Gelisols - Orthels
26	Water bodies
27	Permanent snow and ice

To minimise this limitation, the most Climate Change Initiative land cover dataset should be studied. This dataset has addressed the issue of land cover, but was not available for analysis within this thesis.

### **3.1.4 USGS ESRI Shape Files**

Additional datasets also used in the analysis are ESRI shape files sourced from Tullow Oil plc (Figure 39 and Figure 40). These shape files include basin outlines, water body outlines and lithological units as outlined by the USGS (Section 2.4). The ESRI shape files have been regridded into the MODIS product format of  $10^{\circ} \times 10^{\circ}$  grids of  $0.01^{\circ}$  resolution (1 km equivalent) to allow for easier comparison. Some loss of detail has been incurred with the translation to the MODIS grid format but this is not thought to have hindered analysis of the USGS datasets. Once again lithological data and basin outlines are not expected to vary significantly over the timescales within this study. Both lithology and basin outline datasets are thus temporally static.

### **3.1.5 Tropical Rainfall Measurement Mission**

Precipitation data has been gathered from the joint NASA and Japan Aerospace Exploration (JAXA) Tropical Rainfall Measurement Mission (TRMM) deployment in 1997. The TRMM was commissioned to monitor rainfall rates over the tropical and subtropical regions, where it is reported that approximately two-thirds of global rainfall occurs (NASA Precipitation Measurement Missions, 2015). The dataset is now the standard for measuring precipitation.

Derived from the TRMM raw data, TRMM-based precipitation estimates have been generated (Huffman and Bolvin, 2014). In this report, the version 7 TRMM data is used in which precipitation and subsequent errors are provided via Algorithm 3B43. Algorithm 3B43 is executed. This algorithm is executed once per month by combining 3-hourly merged IR estimates with monthly data from the accumulated Global Precipitation Climatology Centre rain gauge. This result of this is a single, best-estimate precipitation rate and root mean square (RMS) precipitation-error estimate fields (Huffman and Bolvin, 2014). The temporal resolution is for TRMM dataset is therefore monthly.

Spatially, the TRMM dataset is provided globally between latitudes  $50^{\circ}$  N and  $50^{\circ}$  S, on a  $0.25^{\circ} \times 0.25^{\circ}$  resolution grid (Huffman and Bolvin, 2014), making it coarser than the

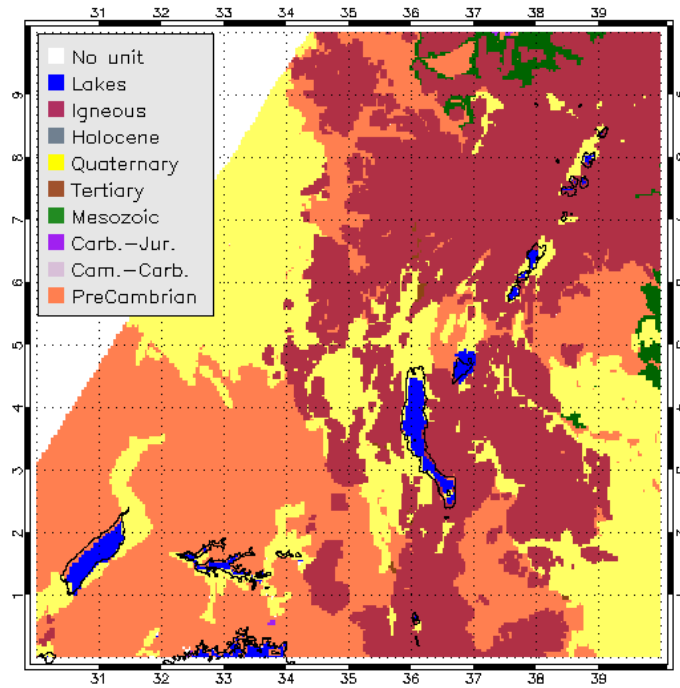


Figure 39: Lithology for the Turkana region, regridded from Tullow Oil plc ESRI ArcGIS shape files to a  $10^{\circ} \times 10^{\circ}$  grid of  $0.01^{\circ}$  resolution. Temporal resolution is not applicable here. No unit refers to a lack of data. Carb.-Jur. refers to Carboniferous-Jurassic and Cam.-Carb. to Cambrian-Carboniferous.

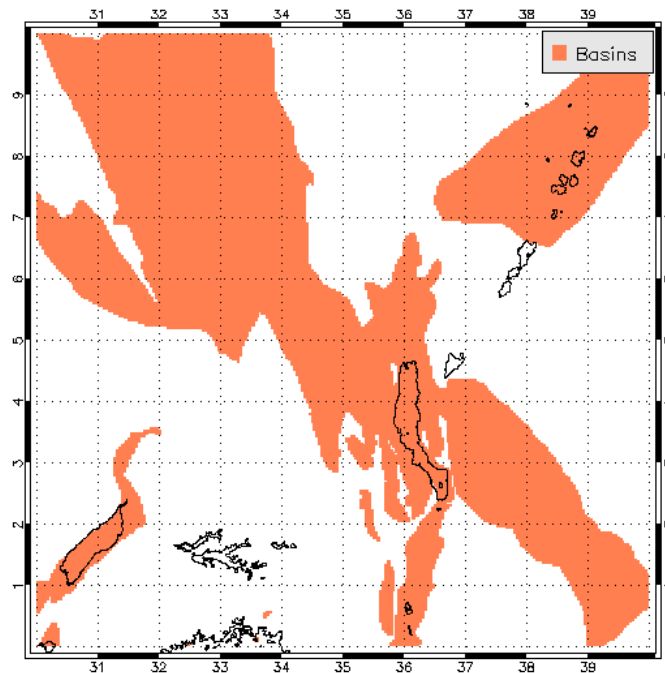


Figure 40: Basin outlines derived from the shape files in Figure 5 as provided by Tullow Oil plc. This figure shows the data regridded onto a  $10^{\circ} \times 10^{\circ}$  grid of  $0.01^{\circ}$  resolution.

previous datasets discussed within this thesis. In light of this, the TRMM dataset has been regrided onto the MODIS product format of the  $10^\circ \times 10^\circ$  harmonised grids. Some loss of information within this regriding is likely to have occurred, though it is not thought that the overall average for the given  $10^\circ \times 10^\circ$  region tiles has been significantly affected.

The accuracy of the TRMM version 7 data is reported by several studies as varying seasonally and with altitude (Huffman and Bolvin, 2014; Cai et al., 2014; Cai et al., 2015). For example, increasing altitude is reported to decrease the absolute error in precipitation recorded and also decrease the ability of the satellite to detect rain events (Cai et al., 2014). Given this, no specific quantity can be given for the overall accuracy of the TRMM dataset however; overestimations in the precipitation rates are regularly noted, with the most significant absolute bias calculated for the equivalent, daily TRMM dataset at 103.54 % (Cai et al., 2015). This should be considered throughout this thesis when analysing the results attained.

### **3.1.6 Climate Change Initiative Soil Moisture**

The version 02.2 soil moisture data is used within this study as taken from the multi-sensor global Soil Moisture CCI project (Liu et al., 2011; Liu et al., 2012; Wagner et al., 2012). This project is part of the 2010 ESA Programme on Global Monitoring of Essential Climate Variables (ECV), otherwise known as the Climate Change Initiative (CCI) that was commissioned for a period of 6 years. The main aim of the CCI Soil Moisture project was to create the most comprehensive and consistent soil moisture record to date. Both active and passive microwave sensors were deployed, with three resultant soil moisture products (active-only, passive-only, merged active-passive). In this study only the merged passive volumetric soil moisture product has been analysed.

The spatial resolution of this dataset is  $0.25^\circ \times 0.25^\circ$  (Dorigo et al., 2010), which is again coarser than the MODIS product format. This has again required regriding of the data onto the  $10^\circ \times 10^\circ$  harmonised grids used within this thesis. This dataset is provided on a daily basis but has been averaged to monthly means for use within this thesis, as with the MODIS LST product to increase the data coverage observed. Several areas

within the EARS, including areas of extreme desert and dense vegetation, have been masked by ESA as meaningful soil moisture retrievals are not possible in such areas (Dorigo et al., 2010). This affects several areas within the EARS particularly heavily, included the extensive desert towards the Afar region, in the north.

Noise estimation files are also provided with the dataset and describe the random uncertainty of the retrieval and thus the quality of the dataset for night time only. Error propagation methods have not been applied to day time observations within this version of the CCI soil moisture dataset. The uncertainty for night time is estimated as the standard deviation of the observation (Liu et al., 2012). Uncertainty of the CCI soil moisture data has not been quantitatively considered within this thesis.

## **3.2 Analysis**

Following initial pre-processing outlined in Figure 37, several techniques were applied to identify the anomalies (Figure 41). The following details the methods and reasoning behind such analyses. The full range of available MODIS data has been used to confirm potential anomalies with the greatest certainty possible (Wan, 1999). Both day and night datasets are utilised to provide estimates of thermal inertia (Coolbaugh, 2000; Calvin et al., 2005). However, night time data is expected to be most suitable for the identification of geothermal anomalies (Miliareisis, 2013), with such features expected to remain warm at night, regardless of the effects of direct solar influence. When discussing basins and the surroundings throughout this thesis, the basins are defined by USGS outlines (Figure 5) and the remainder of the rock is from here on referred to as the host. Results are given in Section 4.

### **3.2.1 Absolute LSTs**

For this thesis, it is desirable to work with monthly data to reduce the effects of cloud cover and to help determine whether identified anomalous regions are attributable to a physical anomaly or simply the result of climatic fluctuations. The results from this analysis will also prove useful as values for input LST parameters during basin modelling as discussed in Chapter 1.1.5.

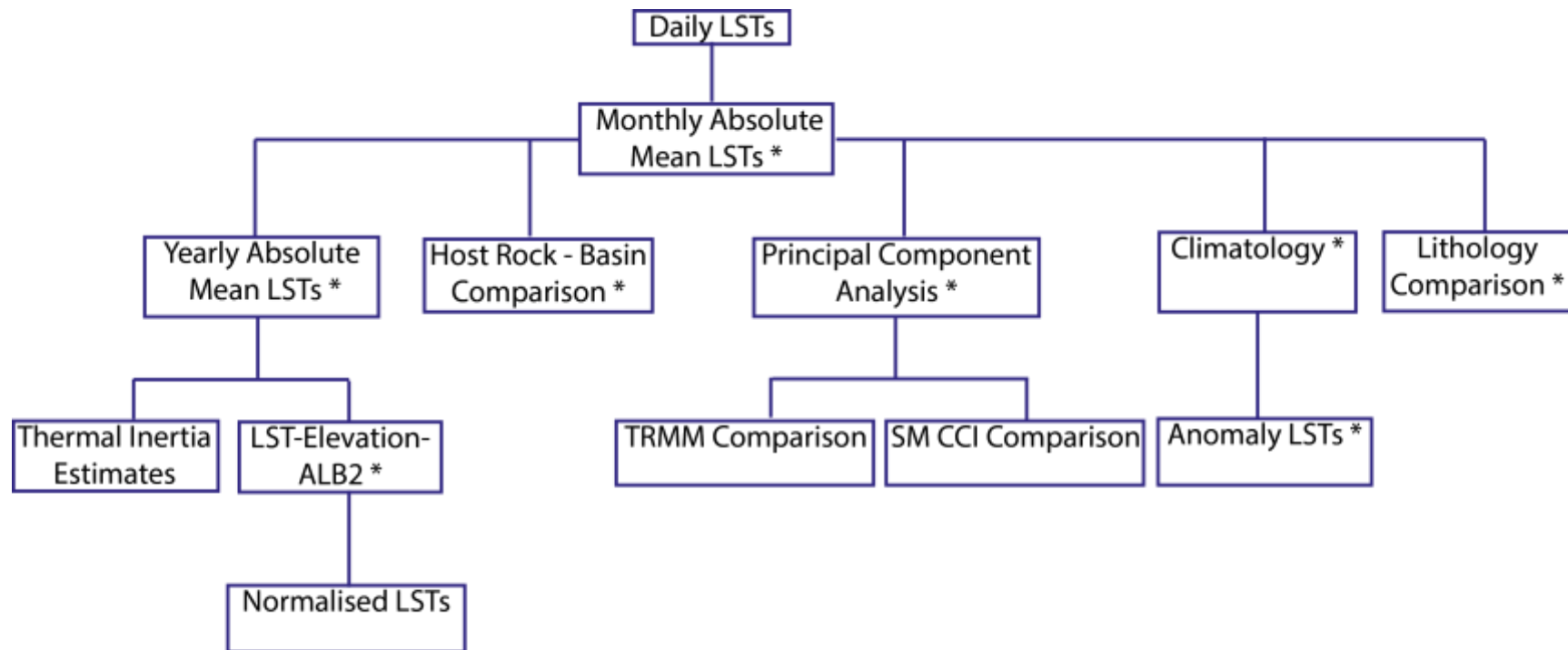
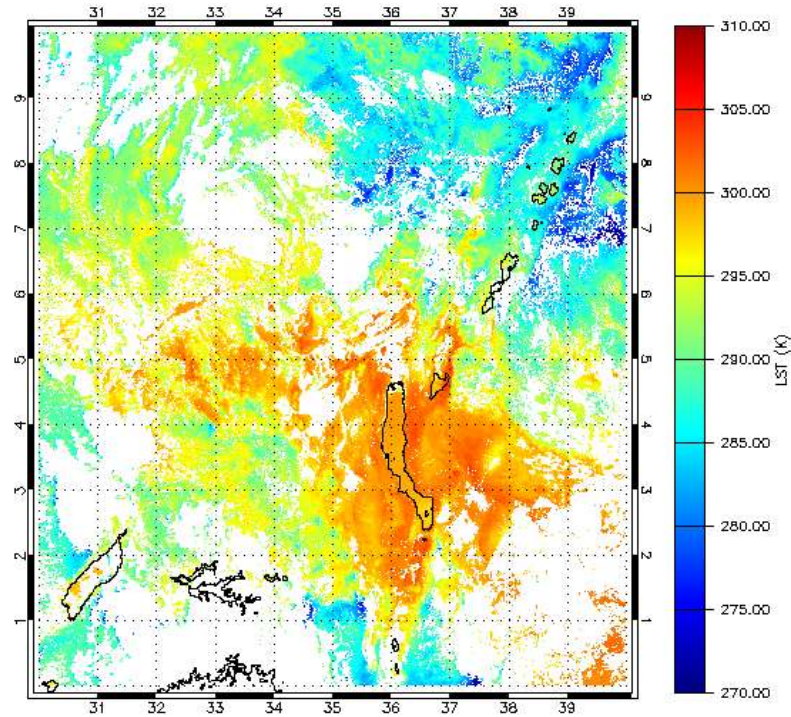


Figure 41: Flow diagram showing main sequence of analysis. \* refers to analysis that are rerun following the generation of a normalised LST dataset. CCI SM refers to the CCI soil moisture and TRMM to the TRMM precipitation dataset. Note that PCA, LST-Elevation-ALB2 comparisons, normalised LSTs, lithology and host rock-basin comparisons can be generated via monthly and yearly absolute LSTs.



*Figure 42: Night time MODIS LST from Aqua for 1<sup>st</sup> January 2006 over the Turkana region on a 10° x 10° grid of 0.01° resolution.*

Here, monthly mean LSTs have been generated from the daily MODIS LST products running from January 2003 through to December 2013 (Figure 42). The year 2002 has been excluded from analysis due to a lack of data at the start of the year, related to the timing of satellite deployments. Means are generated on both a 0.01° per grid point and by calculating a tile wide mean (i.e. a whole tile approach) for day and night over the region of interest. Missing values that arise from cloud cover are discarded in the calculation of the means and therefore clear sky biases may occur. Pixels were considered as cloudy, where there was an absence of cloud free throughout the entire month.

Histograms of LST frequency are also generated to show the diurnal shift in LSTs and thus the solar influence. Histogram bins are set at 1 K for LST. The histogram density refers to the number of pixels recorded at a given temperature.

Absolute yearly mean LSTs are also produced for day and night from 2003 to 2013. The means per pixel of each monthly tile, as previously calculated, are used to generate the overall yearly mean. For these means, all pixels tend to have values thus increasing

coverage and reducing cloud cover effects. Seasonal effects are also negligible, with the means spanning all months throughout the year. Spatial plots, whole tile means and histograms of LST frequency are again all considered, as with the monthly dataset.

LST uncertainty has not been extensively analysed but consideration is given to the auxiliary uncertainty data provided with the MODIS LST. This dataset is once again daily, on a  $10^\circ \times 10^\circ$  grid with a spatial resolution of  $0.01^\circ$ . Though the uncertainties are scientifically important, the most useful values in terms of industry are maximum and minimum LSTs. This is as a range of LSTs are useful within basin models to provide the best and worst case scenarios. Therefore these values are provided throughout the study with further detail given when necessary.

### **3.2.1.1 Turkana Region**

The Turkana region has been selected as a case study throughout this thesis (Figure 42). This region has been selected due to its diverse geographic setting, with dynamic elevation and land cover varying from dense vegetation to abundant bare soils. An additional reason for the tile selection is that several techniques are not expected to work well across regions of dense forest such as to the west of Lake Albert (Figure 38). This is as the LST signals retrieved from these regions are for the forest canopy and not the land surface itself. Moreover, forests tend to be regions of increased cloud cover which would decrease the volume of available data. Turkana has therefore been selected as it is the tile composed of the most abundant bare soils. This is with the exception of tiles further north that lie outside the main rift region.

### **3.2.1.2 Diurnal Differences**

Thermal inertia, as noted in Chapter 2.3.1, is the amplitude of the fluctuations in diurnal shifts and seasonal cycles (Rees, 2013). In this thesis, the time intervals of the MODIS LSTs does not allow for an accurate determination of this inertia. However, the diurnal LST difference between day and night can be used to hint at the potential thermal inertia. This is important as it necessary to understand the rate at which different surfaces absorb and emit heat. By understanding the thermal inertia, it is possible to

identify false anomalies. For example, areas of dense forest may be highlighted as thermally anomalous at night due to high thermal inertia. However, this is not geothermally associated and would therefore be considered a false geothermal anomaly.

In this study, the diurnal shifts are studied on monthly and yearly time scales using tile mean and LST frequencies. The results of which are discussed throughout. Special consideration is given to the Turkana region, whereby the diurnal difference has been calculated per pixel. This has provided a more detailed outlook of the temperature shifts and has allowed for diurnal LST differences to be compared to different physical parameters including vegetation.

### **3.2.2 Host Rock-Basin Comparisons**

Following the generation of the absolute means, comparisons between the warmth of basins and surrounding host rock are made. In this study, basins are defined according to USGS outlines (Figure 5 and Figure 40). Host rock is therefore defined as the rock surrounding the basins. Distinguishing between host rock and basins is important as this is the basis to which areas of interest can be determined using satellite data. Here, a number of analyses now look at whether a contrast in LSTs exists between the host rock and basins. The first approach uses yearly mean LSTs, to spatially observe the LSTs within basins. It employs the use of night time data as this is where the greatest contrast between geothermal anomalies and their surroundings is expected, as previously explained (Miliareisis, 2009).

Histograms recording absolute LST frequency are also generated to show the shift with respect to basins and host rock. For the Turkana region, mean, maximum and minimum LSTs for the host and basin rock are also calculated to gain a temporal outlook. This is shown for both day and night to provide estimates on thermal inertia. This analysis is additionally rerun following normalisation of the LST with respect to the effects of elevation, as described later in Chapter 3.2.4.

Specific basins are also considered with respect to the absolute LSTs and the host rock average. Basins analysed here are selected due to known presence of geothermal

activity or hydrocarbons. In all cases, water bodies are excluded from the analysis as not to skew results.

### 3.2.3 Principal Component Analysis

PCA is a statistical technique used to find patterns within data of high dimension (Smith, 2002). It is an approach that is widely employed across the remote sensing community as a means of data compaction since it is often the first two or three principal components that account for the majority of variability (Mather, 2004). Once patterns are identified, the PCA is able to reduce the dimensions without great loss of information (Smith, 2002; Miliareisis, 2012; De Almeida et al., 2015). This method allows the principal causes of variation in the LST to be highlighted. Component loadings values refer to the correlation between the eigenvectors and the variable means. These loadings vary between  $\pm 1$ . Greater component loadings, irrelevant of sign, correspond to a greater contribution in terms of the LST variance.

Several steps are required to complete the PCA (Figure 43). The specifics concerning the steps alter depending on the number of input variables. For example for a five variable PCA there is a 5 x 5 covariance matrix that produces five eigenvectors, each with five eigenvalues. Each eigenvalue can then be segregated into five component loadings, with each representative of an input variable. This procedure would vary slightly for a four variable PCA, having a 4 x 4 covariance matrix and so on. The formula used to calculate the principal components within this study is as follows:

The following now details the mathematics behind the flow diagram found in Figure 43. Here,  $x, y, z, a, b$  are vectors containing physical parameters as taken from the MODIS auxiliary files. For each vector, the data is normalised using the following equations:

$$\bar{x}_i = x_i - \langle x \rangle \tag{Eq. (3.2)}$$

$$\tilde{x}_i = \frac{\bar{x}_i}{\sigma(\bar{x})} \quad \text{where } \sigma(\bar{x}) = \sqrt{\text{variance}(\bar{x})} \tag{Eq. (3.3)}$$

Where  $x_i$  refers to the vector components, i.e. individual pixel values from a given tile,  $\bar{x}$  to the pixel mean,  $\langle x \rangle$  to the mean value of  $x$ , i.e. the tile mean and  $\tilde{x}$  to the normalised data vector. In order to then successfully calculate the covariance between the normalised vectors, a common index of cloud free pixels is generated.

$$D = [\tilde{x}, \tilde{y}, \tilde{z}, \tilde{a}, \tilde{b}] \quad Eq. (3.4)$$

The covariance between two parameters is given as follows, where by  $n$  refers to the index of common, cloud free pixels, i.e. the vector size.

$$cov(\tilde{x}, \tilde{y}) = \sum_{i=1}^n \frac{(\tilde{x} - \langle \tilde{x} \rangle) (\tilde{y} - \langle \tilde{y} \rangle)}{n} \quad Eq (3.5)$$

The covariance matrix of  $D$  is then calculated using the covariance defined above in Eq. 3.5:

$$covMatrix(D) = \begin{bmatrix} cov(\tilde{x}, \tilde{x}) & \cdots & cov(\tilde{b}, \tilde{x}) \\ \vdots & \ddots & \vdots \\ cov(\tilde{x}, \tilde{b}) & \cdots & cov(\tilde{b}, \tilde{b}) \end{bmatrix} \quad Eq. (3.6)$$

Following the generation of this square covariance matrix, eigenvectors and corresponding eigenvalues are calculated. This is completed using an idl function that computes such values for an  $n \times n$  matrix, using the Householder reduction algorithm and the QL method. The Householder reduction algorithm reduces the covariance matrix to a tridiagonal form\*, which is then diagonalised by the QL procedure with implicit shifts; as is further detailed in Press et al. (1987). The eigenvectors can then be used to generate the principal components ( $PC$ ) as follows:

$$PC = Eigenvectors \times \langle \tilde{x} \rangle \quad Eq. (3.7)$$

---

\* A tridiagonal matrix refers to a matrix that only has non-zero elements on its main diagonal and two diagonals directly adjacent to it (Chen, 2014).

The below then describes how to generate the corresponding component loadings ( $CL$ ):

$$CL = PC \times \langle x \rangle$$

*Eq. (3.8)*

Following the above, plots can then be generated for each principal component, with respect to the mean LST ( $\overline{LST}$ ) data of a given month, as follows:

$$Rotated\ data = \overline{LST} \times CL$$

*Eq. (3.9)*

The rotated data is then plotted spatially as a result of fitting and then a temporal picture is built analysing each month independently. In this case, the  $10^\circ \times 10^\circ$  grid of the Turkana region is selected as an area of focus for this analysis due to its diverse geographical setting, varying from high altitudes dominated by vegetation to areas of soil rich, lower relief, as explained in Chapter 3.2.1.1.

A number of factors were selected as the input variables for the PCA with respect to the LST, based on their known influences on the LST. The factors selected are elevation,  $f_v$ , emissivities at two wavelengths within the infrared region and  $tcwv$ . Satellite and solar angles were also considered but later discarded due to uncertainties in the monthly means. This is not thought to have affected the outcome of the PCA. A five variable PCA with respect to the absolute LST was henceforth produced (Figure 44). From here on, this is referred to as the full PCA.

Once the temporal variation is potentially understood, other factors were invoked to explain variations within the component loadings via simple comparisons. The datasets employed for this were TRMM precipitation and CCI soil moisture. The TRMM precipitation has been chosen due to the known inverse relationship with LST (Trenthberth and Shea, 2005; Wu et al., 2013). CCI soil moisture data is additionally analysed due to its relationship with LST, whereby increases in soil moisture result in cooler LSTs (Ghent et al., 2010, Yao et al., 2013). Note that future work on this analysis should strive to remove the temporal variation prior to the PCA being applied to the LST data. This would help remove seasonal influence and thus allow a better spatial understanding of the physical variables.

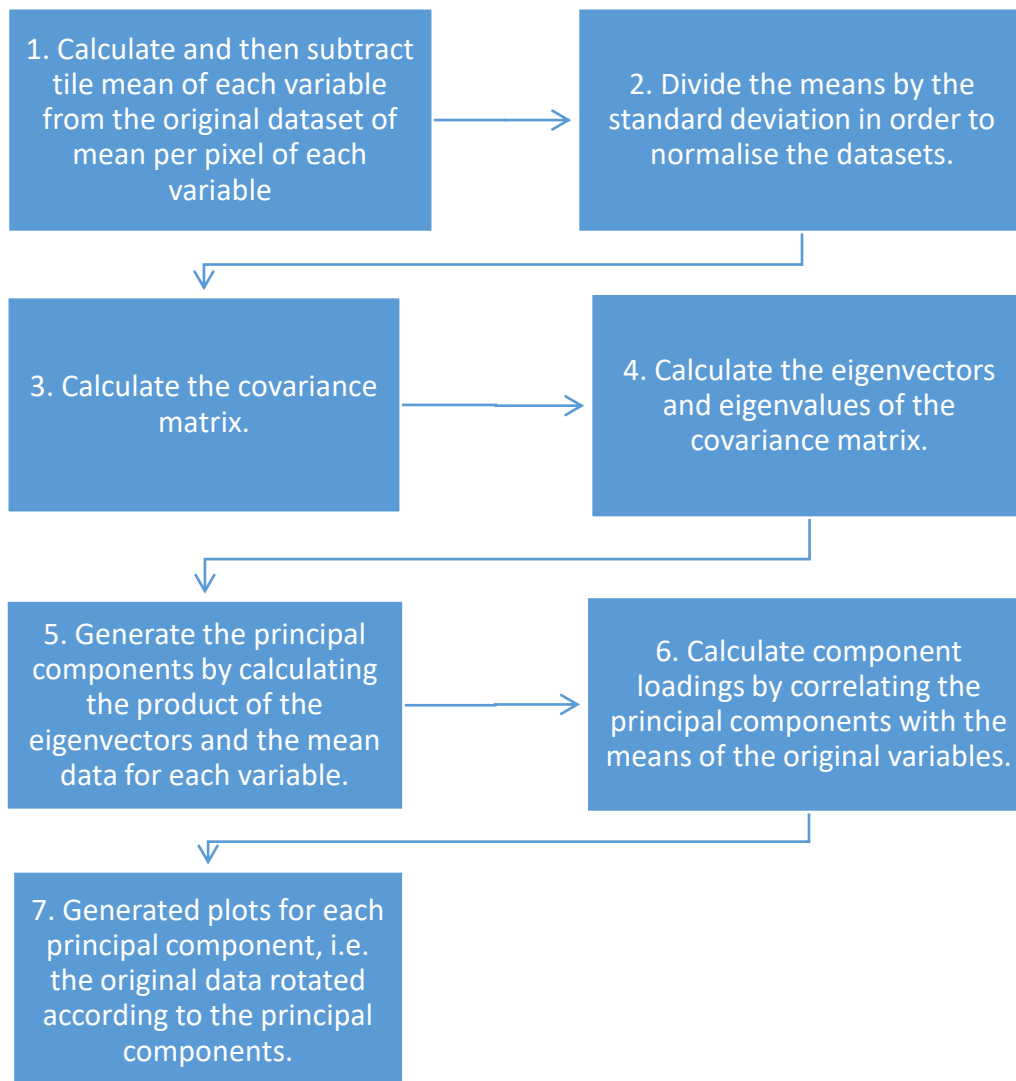


*Figure 43: Flow diagram outlining the steps taken within this study's PCA. Specifics including the size of the covariance matrix will vary dependent upon the number of input variables, as mentioned within the text.*

In addition to the full PCA, a four variable PCA, referred to as the restricted PCA, has also been generated. This has been applied following the application of an elevation correction, as is detailed later in Chapter 3.2.4 and thus this parameter is additionally removed as an input variable within the restricted PCA. It is hoped by rerunning this analysis; the LST in normalised space will be delineated further to allow for a better understanding of the parameters influencing LST, beyond elevation.

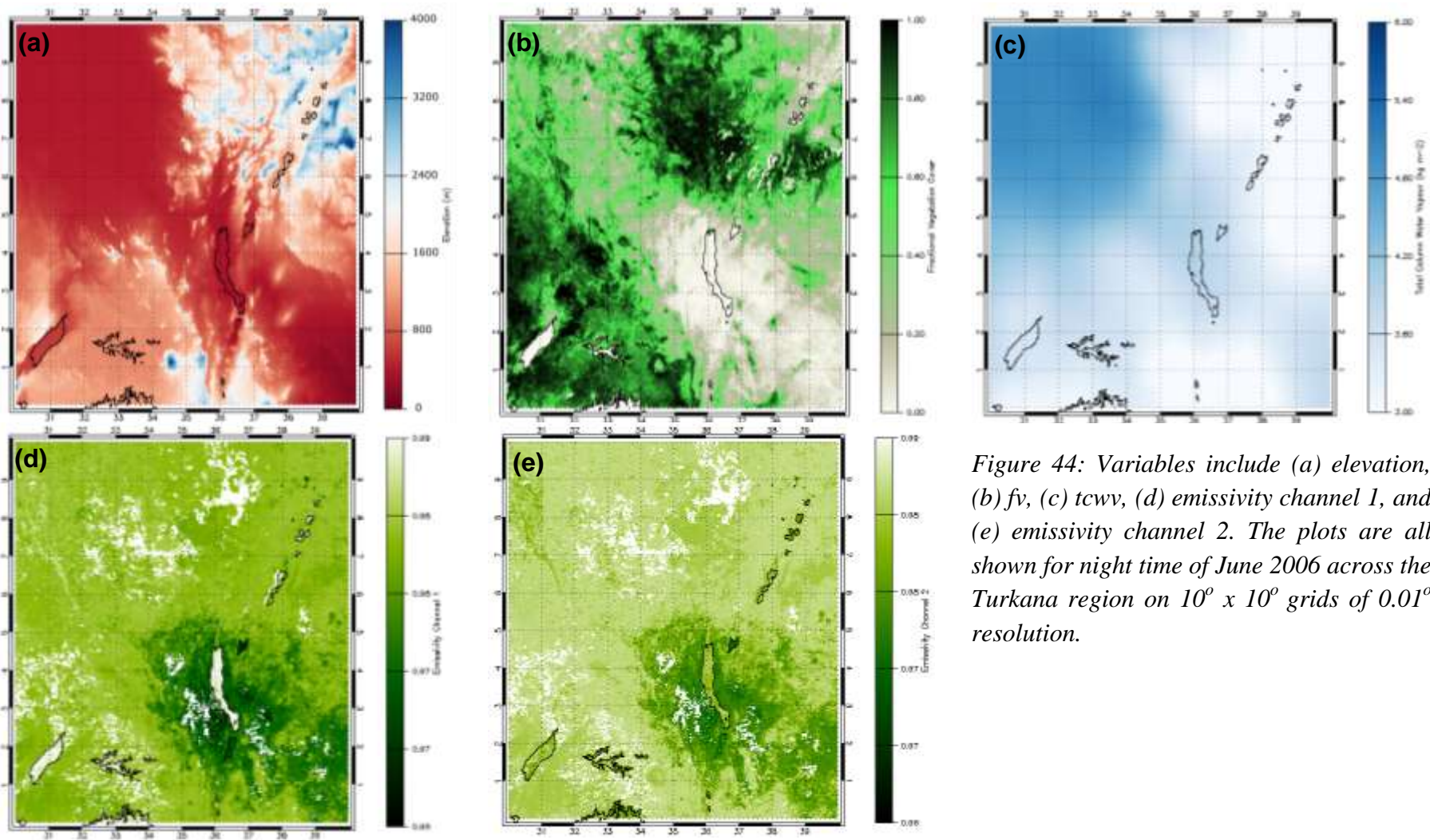


Figure 44: Variables include (a) elevation, (b) fv, (c) tcwv, (d) emissivity channel 1, and (e) emissivity channel 2. The plots are all shown for night time of June 2006 across the Turkana region on  $10^\circ \times 10^\circ$  grids of  $0.01^\circ$  resolution.

### **3.2.4 Normalised LSTs with respect to elevation**

From previous studies, elevation has been identified as a consistent contributor in terms of the LST signal recorded (Coolbaugh et al., 2000; Saraf et al., 2005). It has additionally been proven to significantly affect LSTs observed across the EARS (Miliaresis, 2009) (Figure 35). Elevation has therefore been accounted for within this study, whereby linear regression analysis is used to determine the elevation correction. Additional consideration is given to land cover, though this is not extensively covered in this thesis.

#### **3.2.4.1 Land Cover-Elevation-LST Analysis**

Linear regression analysis has been applied to highlight correlations between three datasets: SRTM elevation, ALB2 land cover and mean LSTs per pixel. This was completed to determine whether an expected near linear relationship exists (Calvin et al., 2005; Miliaresis, 2009; Miliaresis, 2012). Both day and night data of the monthly and yearly pixel mean LSTs across the Turkana region were analysed. This was initially applied to all land covers.

Pearson correlation coefficients and gradients are generated for the night time monthly means of 2006 and the night time yearly means from 2003 through to 2013 across the Turkana region. Pearson correlation coefficients have been chosen as the most appropriate way of evaluating the relationship as the elevation and LST datasets are both continuous and expected to be linearly related. The gradients provide the rate of change in LST with elevation. A number of pre-set idl functions were applied to the datasets to calculate such values and determine the most appropriate function. These functions included LINFIT which fits the data to a linear model of equation  $y = mx + c$  (by minimising the chi-square error statistic). The second function was the LINFIT with errors function, which is much the same as LINFIT but also accounts for errors in the y values which in this case is the LST. The final function was LADFIT, which also attempts to fit the data to a linear model but via different means (i.e. using a “robust” least absolute deviation method).

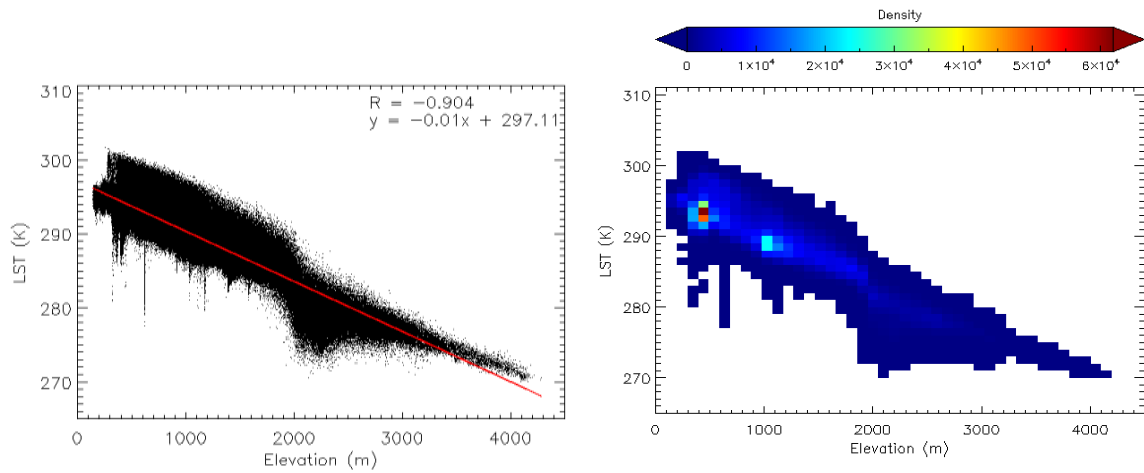


*Figure 45: Examples figures of the elevation-LST analysis. Left: Scatter plot showing how the gradient and intercepts were calculated, which are later required for normalisation as discussed within Chapter 3.2.4.2. Right: Density plot of elevation-LST, with LST bins set to 1 K and elevation to 100 m. From this plot, the number of pixels at a given LST and elevation is more clearly observed, explaining the locality of the corresponding line of best.*

Density plots were produced to explain the locality of the lines of best fit generated, where shifts occur as a result of increased density affect linearity. Density plots display the elevation, LST and the third dimension of pixel density. Pixel density refers to the frequency of specific LSTs occurring at a given elevation. For the density plot to be generated histogram bins are specified, with LST bins set to 1 K and elevation bins to 100 m. An example density plot and corresponding scatter plot is provided in Figure 45.

Linear regression analysis of elevation and LST was also generated with respect to land covers to determine the influence on LSTs, potentially acting as a filter to narrow the region of search for geothermal anomalies. Four land cover subgroups that are expected to display different LSTs were considered (Figure 46 and Table 12). Simple comparisons of land cover with both elevation and LST are also provided as supporting plots, detailing the range over which all land covers span. This will hopefully highlight whether warmer land cover is real or a result of preferred elevation.

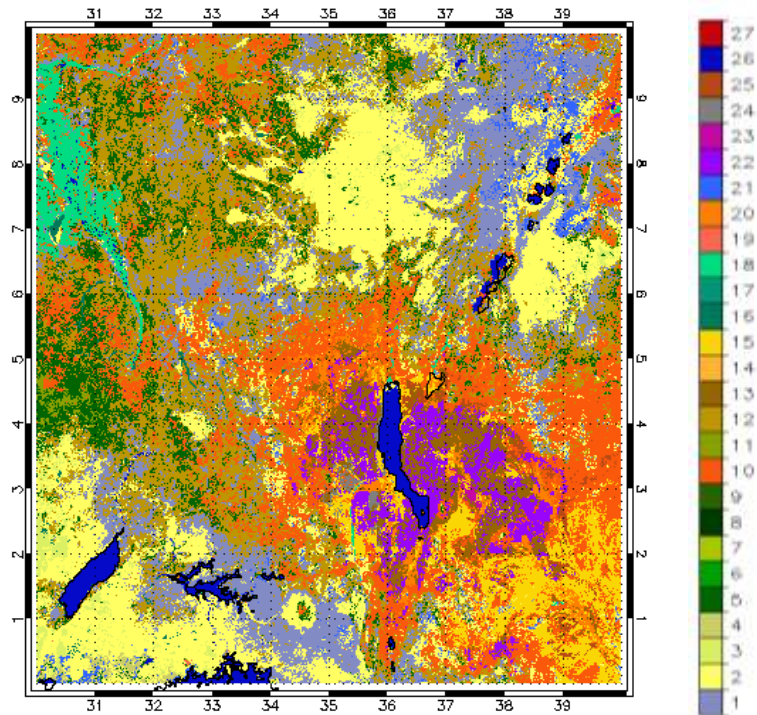


Figure 46: ALB2 land cover classification for the Turkana region on a  $10^{\circ} \times 10^{\circ}$  grid of  $0.01^{\circ}$  resolution.

### 3.2.4.2 Normalising LST with respect to elevation

Given the known linear relationship between LST and elevation, it is important to account for this in order to delineate the LST signal further; thus revealing more of the unexplained variance that may relate to geothermal anomalies. Accounting for this relationship will also reveal the next most dominant parameters driving the LST, which in turn can then be corrected for, again delineating the signal even further.

In order to account for the LST-elevation relationship in this study, linear regression analysis of elevation and LST is used to provide approximate gradients to which the two variables relate. These values can be used to normalise the LST dataset with respect to the elevation. All LST values are recalculated to be the equivalent LST as if all elevations were reduced to sea level at 0 m. This is useful as it identifies the dependence of LST on the elevation and accounts for it; as within studies such as Coolbaugh et al. (2000). From this, regions of warmer and cooler LSTs are observed at 0 m, with notable differences to the original LSTs within the area. This approach is applied to yearly means, with tile means, maximums and minimums contrasted to corresponding values

*Table 12: Land cover groups used within the Land cover- Elevation-LST analysis are now shown. Land cover groups have been selected from the University of Leicester ALB2 dataset, as explained previously in chapter 3.1.3.*

Group	ALB2 number	Description of land cover
Vegetation/Cropland	1	Post-flooding/irrigated croplands
Vegetation/Cropland	2	Rainfed croplands
Vegetation/Cropland	3	Mosaic Cropland / Vegetation
Vegetation/Cropland	4	Mosaic Vegetation / Cropland
Vegetation/Cropland	15	Sparse vegetation
Vegetation/Cropland	18	Closed to open vegetation on regularly flooded or waterlogged soil
Grass/Shrubland	11	Mosaic Forest/Shrubland / Grassland
Grass/Shrubland	12	Mosaic Grassland / Forest/Shrubland
Grass/Shrubland	13	Closed to open shrubland
Grass/Shrubland	14	Closed to open grassland
Forest	5	Closed to open broadleaved evergreen and/or semi-deciduous forest
Forest	6	Closed broadleaved deciduous forest
Forest	7	Open broadleaved deciduous forest
Forest	8	Closed needleleaved evergreen forest
Forest	9	Open needleleaved deciduous or evergreen forest
Forest	10	Closed to open mixed broadleaved and needleleaved forest
Forest	16	Closed broadleaved forest regularly flooded - Fresh
Forest	17	Closed broadleaved semi-deciduous and/or evergreen forest regularly flooded -Saline
Bare soils	20	Bare soil General
Bare soils	21	Bare soil Entisols – Orthents
Bare soils	22	Bare soil Shifting sand
Bare soils	23	Bare soil Aridisols – Calcids
Bare soils	24	Bare soil Aridisols – Cambids
Bare soils	25	Bare soil Gelisols – Orthels

of the absolute datasets. Histograms of LST frequency are also provided as a means of observing the shift in thermal inertia associated with the normalisation. The overall change following normalisation is also highlighted by various diagnostic cross sections that have been selected to further study features of interest.

### **3.2.5 Climatology and Anomalies**

Climatology plots have been generated to progress the understanding of features identified in the datasets. The climatology is expected to reveal the locality of persistent features. This is important as geothermal anomalies are expected to coincide with consistently warmer features if present, as elevated geothermal gradients are not influenced by seasonal or climatic factors. Corresponding anomaly plots are therefore expected to highlight transient features, including volcanic activity and weather events, such as heat waves. It is necessary to highlight such features as to avoid the false identification of warm regions due to transient anomalies instead of real persistent features.

The climatology is established from 2003 through to 2013 for both the absolute and normalised datasets. This time period is thought to be sufficient for this study as any changes in geothermal gradient are expected to occur over a geological timescale, i.e. much longer timescales than any satellite datasets currently available. The climatology has been produced by creating a time series using the monthly mean LSTs, whereby a single per pixel average is calculated for a specific month using the given month from all years. Both day and night LSTs are considered to gain an overview to the diurnal contrasts. LST anomalies are also produced from 2003 through to 2013 on a day and night monthly basis. The anomalies are calculated by removing the climatology of a given month away from the mean of the same month for a given year, i.e. June (2003 mean) – June (climatology mean).

### **3.2.6 Lithological Comparison**

A number of analyses have been conducted comparing the lithological units shown in Figure 39 with LSTs and auxiliary variables. These analyses have been produced to determine whether lithology is correlated to specific LSTs or variables such as emissivity. This approach is applied as thermal inertia is known to significantly vary with rock type (Janza et al., 1975; Coolbaugh et al., 2000; Calvin et al., 2005; Tianyu et al., 2012). Therefore it is thought that such a difference may also arise in the LSTs observed. Lithologies are also expected to have characteristic emissivities which are

related to the land cover and therefore in turn the LSTs (Rees, 2003; Tianyu et al., 2012).

### **3.2.7 Summary**

MODIS LST data is the main dataset analysed in this thesis and is retrieved using the generalised split window algorithm developed by Wan and Dozier (1996). It is expected that this dataset will achieve an LST accuracy of 1 K at 1 km resolution under the clear sky conditions for which retrieval is possible and surface emissivities known (Wan, 1999). Several additional datasets have also been used and include auxiliary MODIS data processed alongside the LST product and data taken from other sources including fv and tcwv.

Figure 41 outlines the approaches applied. The first step involves the generation of mean LSTs from January 2003 through to December 2013, which are produced with the aim of reducing cloud effects. From these datasets, estimates of the thermal inertia are obtained from studying the diurnal shift. In addition to this, comparisons are made between host rock and basins to determine whether remote sensing is a suitable approach to delineating geothermal features.

Following averaging, two main approaches have been applied to the datasets – PCA and normalisation with respect to the data. PCA is first used to identify the most dominant variables contributing to the LST in terms of both spatial and temporal variation. Elevation, emissivities at two wavelengths within the infrared region, fv and tcwv are considered as input parameters. Subsequent study of the PCA results with the additional datasets of soil moisture and precipitation is also applied, in order to understand the periodicity of the components.

Following this, the second approach uses linear regression analysis to further understand the variation between LST and elevation. The results of this are used to generate an elevation correction, whereby LSTs are recalculated to the equivalent LSTs as if elevation were reduced to 0 m. It is hoped that this will reveal structure in the LST previously masked by elevation. PCA was later rerun using the normalised data to understand the remaining variation within the LST signal.

All analyses were implemented on the basis that they would enhance the identification of areas that are geothermally associated and aid in the delineation of the LST signal. The following chapter now displays the results attained. Specific references are made throughout to geological and physiographical features, as discussed in Chapter 1 and as highlighted by the individual analyses.

## 4. Results and Discussion: Part 1

The following two chapters now display and discuss the results from the implementation of the methods described in Chapter 3. Within this chapter, the generation of absolute LSTs is first shown after which key geological features are identified. PCA has then been applied to the newly generated dataset in order to delineate the physical parameters contributing to the LST. Following this, Chapter 5 then goes onto to discuss how such parameters can be accounted for within the LST dataset.

Below, a Google Earth image is provided, with country boundaries outlined to better aid the locality of features and areas within the following discussions (Figure 47). The Turkana region is additionally highlighted (red) as the region of focus within this study, spanning Kenya, Ethiopia, Uganda, South Sudan and the most eastern extent of the Democratic Republic of the Congo.



*Figure 47: Google Earth (2016) image with country boundaries highlighted across the EARS. The dashed red line refers to the Turkana tile – a region of interest throughout this study.*

## **4.1 Absolute LSTs**

Given the volume of cloud cover in daily LSTs, it is desirable within this thesis to work with averaged LSTs as to minimise cloud effects. Here, absolute means are generated on monthly and yearly time scales for both per pixel and whole tile approaches. The full dataset of absolute mean LSTs from 2003 through to 2013 is generated but not shown. LSTs are reported in Kelvin. Both day and night LSTs are provided. Scales vary throughout this chapter as to best illuminate the results. Pixels shown in white refer to a lack of available data due to limitations including cloud cover. For all plots, where clouds are present the pixel for that given day is not included in the mean LST calculation and therefore it is likely that there is an element of clear sky biases within the results presented.

### **4.1.1 Monthly Mean LSTs**

Absolute monthly LSTs are now displayed on a per pixel basis from June and December 2006. An overview of the area is first provided via two regions stretching from the Afar in the north to Tanzania in the south, spanning the full range of tiles. Further work then focuses on the Turkana region. Figure 48 displays monthly means for June and December across the Afar region (tiles H21V10, H21V11, H22V10, H22V11, H23V10 and H23V11 (Table 10)). The full 2006 dataset for the Afar region is found in Appendix 3. Figure 49 displays the June and December 2006 LSTs for the main EARS (tiles H21V08, H21V09, H21V10, H21V11, H22V08, H22V09, H22V10, H22V11 (Table 10)). See Appendix 4 for the full 2006 EARS dataset.

From the monthly LSTs, key features are noted including the depressed Turkana Trough and Afar Triangle that are warmer than the more elevated areas (Figure 48 and Figure 49). This is observed throughout and is consistent with previous literature, whereby LSTs decrease with increasing elevation (Saraf et al., 2005; Miliareisis, 2009). Moreover the Afar region is mainly composed of dark volcanics that exhibit higher emissivities (Figure 10). All variables within this region appear to favour warmer LSTs, which is not surprising given the Afar region's geological setting, as discussed in Section 1. From

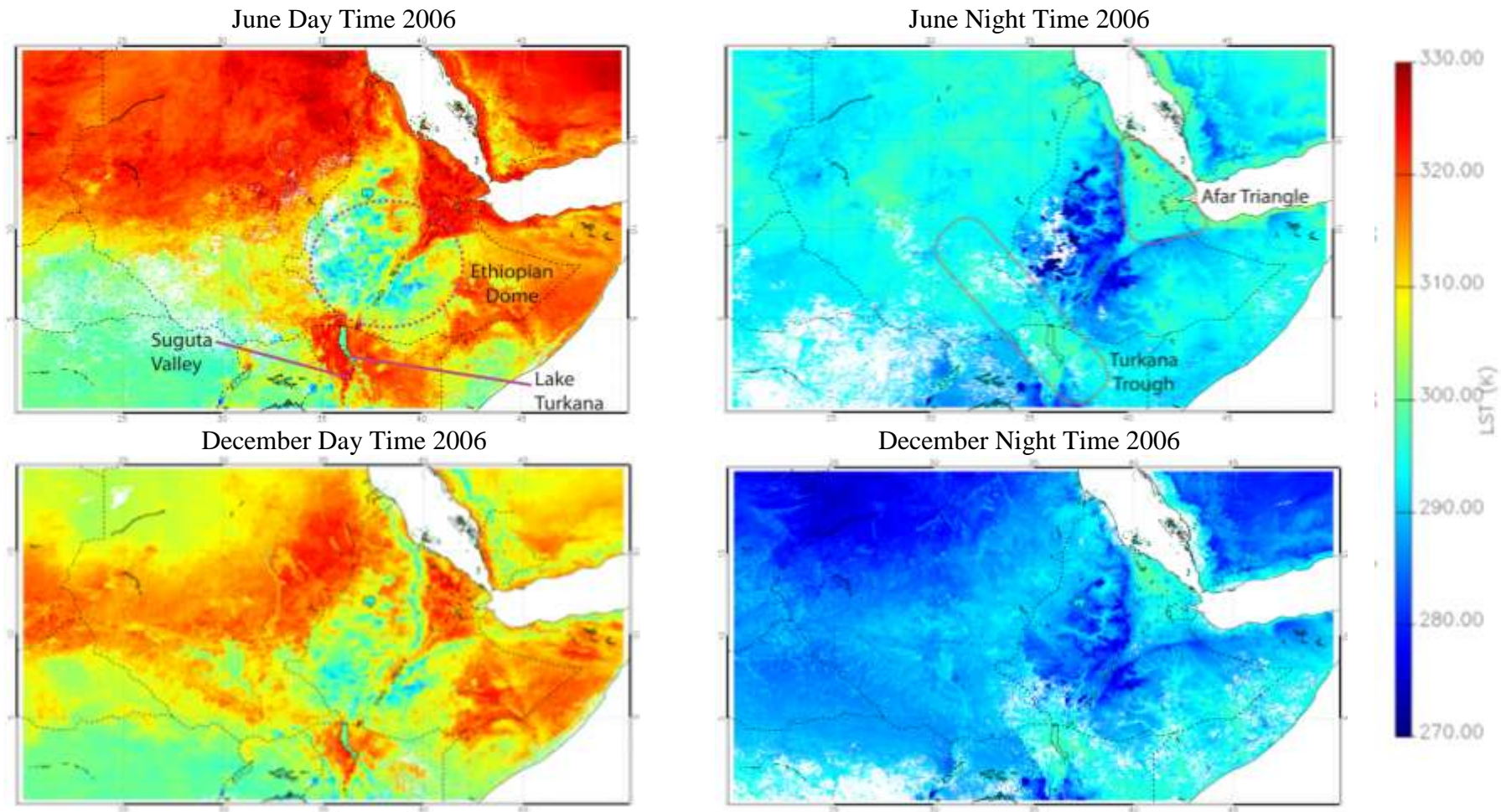


Figure 48: Absolute monthly mean MODIS LSTs, taken from the Aqua dataset, across the Afar region, on  $30^\circ \times 20^\circ$  grids of  $0.01^\circ$  resolution. Black dashed lines refer to country boundaries, as shown in Figure 47.

the Afar, the approximate location of the rift prior to bifurcation at 5° N is clearly visible. It is shown to track southwards through the Ethiopian Dome, before re-emerging near Lake Turkana (Figure 48). It is not clear as to whether this is a geothermal anomaly or simply associated with elevation.

To the south, the area of lower relief surrounding Lake Turkana shows consistently warmer LSTs, regardless of temporal variation. Again a singular factor driving the LSTs is not apparent; though LST patterns correspond to lower elevations as a result of rift associated subsidence. A higher abundance of sediments are also noted which is significant given they are known to have higher specific heat capacities than more indurated rock. The presence of numerous factors therefore requires further analysis.

Warmer LSTs are observed continuing southwards, with the rift migrating from Lake Turkana into the Suguta Valley. This region is also the locality of a numerous factors that favour warmer LSTs, including low elevation and bare soils. The valley is also the site of extensive geothermal activity, as is discussed in Chapter 1.1.6 (Omenda, 2008). Therefore if it is possible to delineate geothermal anomalies using satellite-derived LSTs, then this region is a likely candidate for this.

Within the eastern branch, cooler regions also exist and show apparent association with higher elevations including Mount Kilimanjaro. Several of these regions are volcanic though few have been recently active and thus the expectation of warmer LSTs is diminished. Any warmer LSTs present would likely be distorted by the effects of elevation. On all occasions there is an absence of warmer LSTs and instead some of the coolest LSTs within the area are observed.

To the west, Lake Albert (Figure 49) is illuminated by seasonally warmer LSTs. It is clear that this warmer area is not limited to the lake itself but instead the entire basin. Here, the effects of vegetation must be considered with significant cover surrounding the shoreline. Further south, warmer lake filled basins are seen bending around the central craton (Figure 7) and are punctuated by a serious of cooler, uplifted regions, including the Rwenzori Mountains (Figure 9). This is the typical pattern seen throughout the rift.

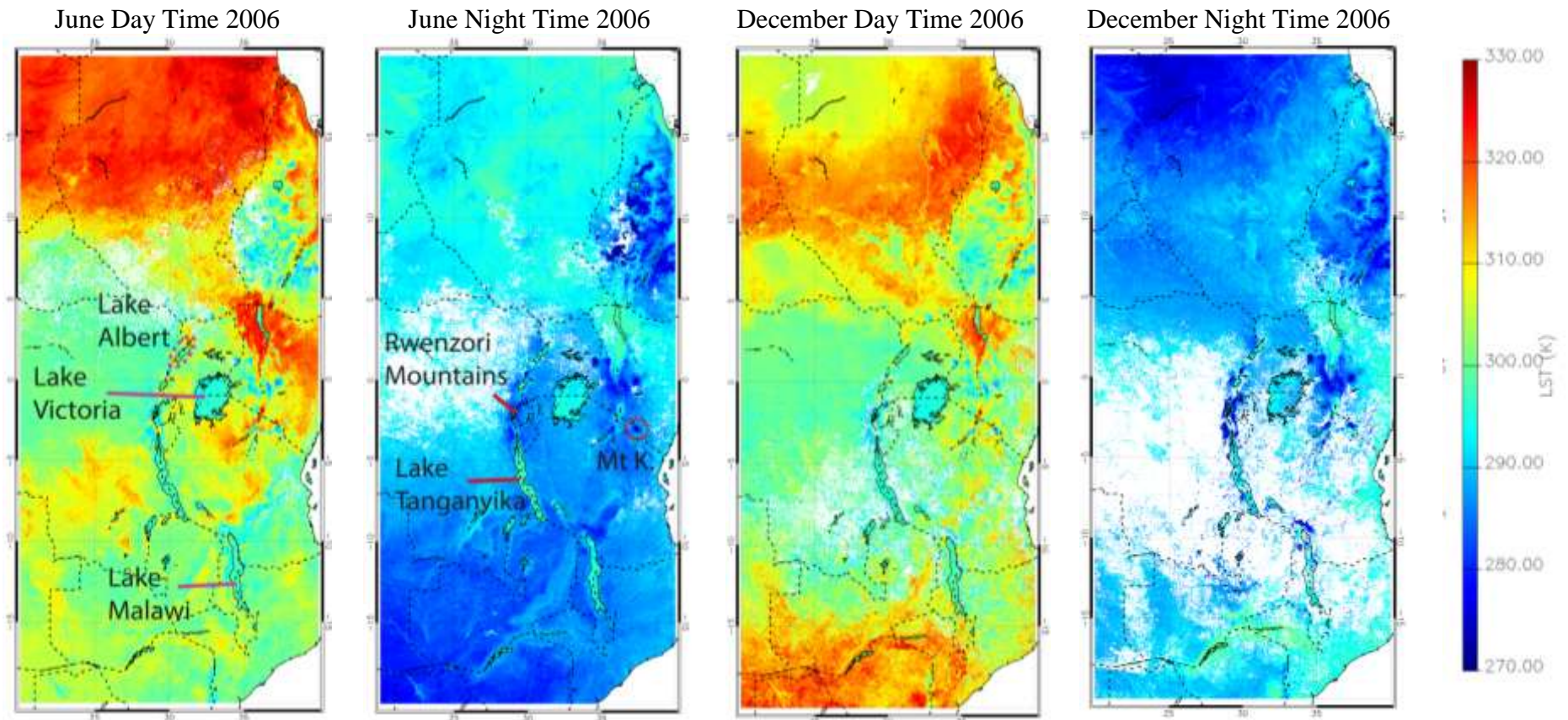


Figure 49: Absolute monthly mean MODIS LSTs, taken from the Aqua dataset, across the EARs region, on  $20^\circ \times 40^\circ$  grids of  $0.01^\circ$  resolution. Mt K refers to Mount Kilimanjaro. Black dashed lines refer to country boundaries as shown in Figure 47. Note the significant loss of data towards the west during December night time 2006, which is likely the result of increased cloud cover corresponding to the migration of the ITCZ as previously discussed in Chapter 1.3.

Lying between the regions, the LST of Lake Victoria fluctuates seasonally. This however is not necessarily representative of the LST but rather the surface water of the lake. Surface waters are affected by the factors mentioned in Chapter 2 and additionally by currents and winds that are not accounted for when considering the land surface. This variation of water bodies is observed across the region but should be interpreted with caution; though the contrast with the land surface is evident. LST variation of smaller drainage features, such as the Turkwel River, is also observed.

Looking south towards the termination point of the EARS, absolute LSTs again tend to be warmer for basins, including Lake Malawi and Lake Tanganyika. During these latter months of 2006, these warmer LSTs are of a comparable magnitude to the warmer region of Lake Turkana. Once again the similar pattern of cooler rift flanks and warmer basins is noted, though basin perimeters are not always obvious.

LST frequency histograms are now provided to show the diurnal shift across the Afar and the main EARS regions for June and December 2006 (Figure 50). The total number of pixels varies between day and night for a given month due to cloud. From the LST distributions it is apparent that the Afar region is warmer than the main EARS regardless of diurnal effects. However, it is not clear whether this is the region as a whole or simply part of the region, skewing the results.

The Afar region shows a significant diurnal shift with minimal overlap between day and night LSTs. The overlap occurs within a narrow window between 290 K and 300 K for both months. Day time LSTs for both months show a broad spread of results. Day time of June shows a bimodal distribution, peaking at approximately 300 K and 320 K, whilst December is unimodal peaking just below 310 K. This bimodal distribution of the June data may occur for a number of potentially physical reasons including the effects of sampling, i.e. missing data or possible distortion by cloud cover; however the reasons for this cannot be conclusively confirmed. Night time LSTs for both months show narrower spreads with unimodal distributions, peaking at approximately 294 K and 288 K respectively.

The main EARS differs from the Afar by displaying a greater overlap in LSTs between day and night for both June and December, suggesting that solar radiation has less of an

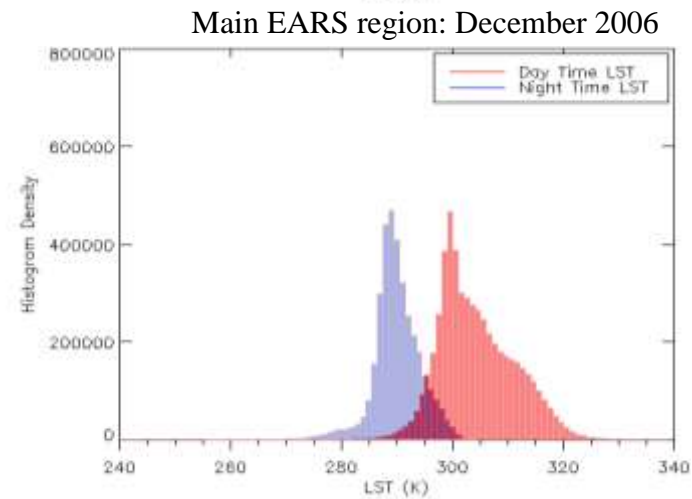
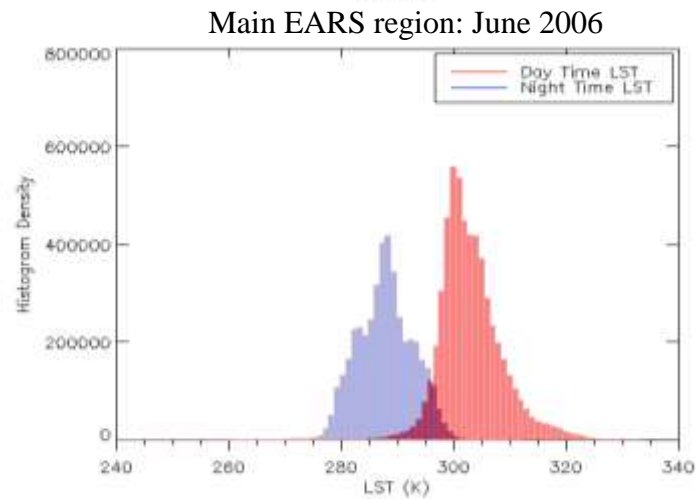
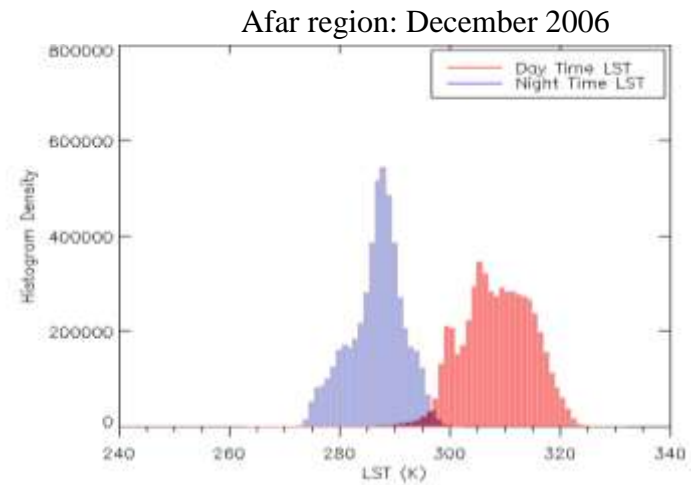
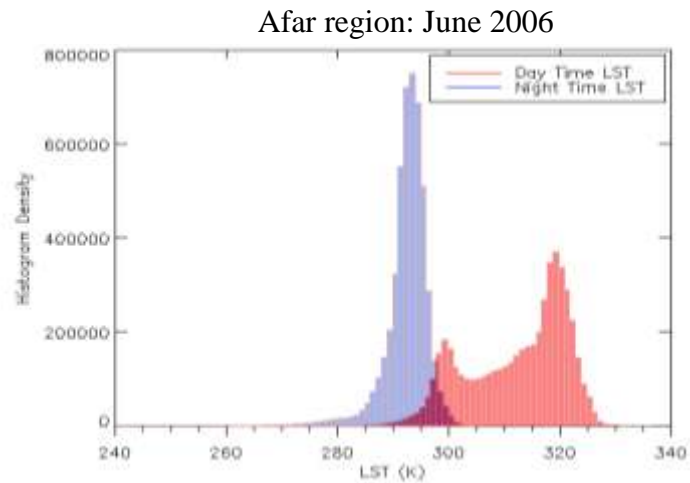
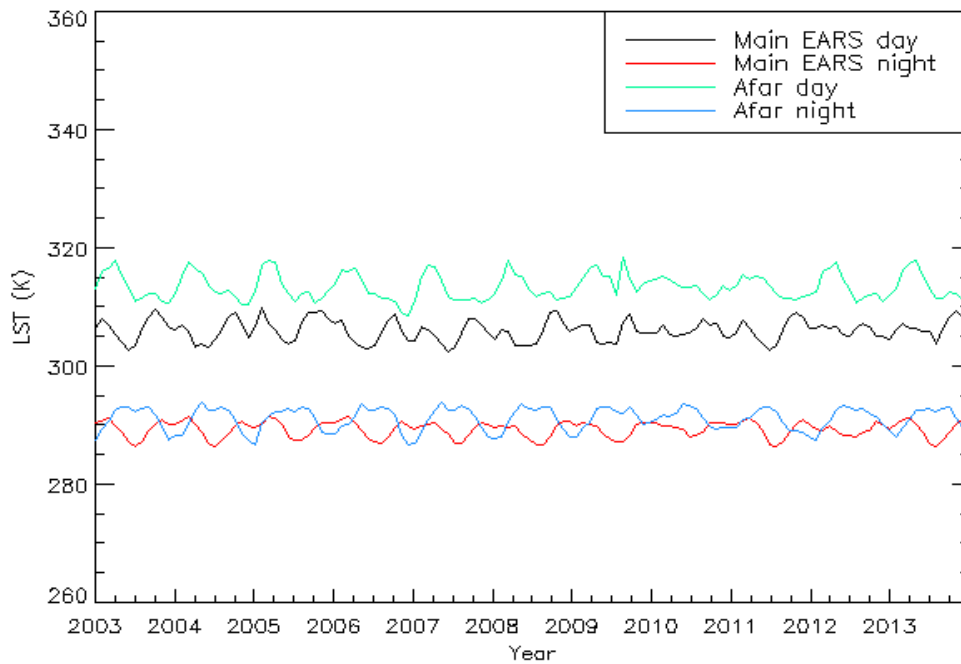


Figure 50: MODIS LST frequencies, as taken derived from the Aqua dataset for the Afar ( $30^{\circ} \times 20^{\circ}$  areal extent) and main EARS ( $20^{\circ} \times 40^{\circ}$  areal extent) regions. Note that pixels number will vary due to both the regions and cloud cover, as discussed further within the text.



*Figure 51: Monthly absolute MODIS LSTs derived from the Aqua dataset, across the Afar ( $30^{\circ} \times 20^{\circ}$  areal extent) and main EARS ( $20^{\circ} \times 40^{\circ}$  areal extent) regions; for day and night, January 2003 to December 2013. Note the intensified feature during the day time Afar region dataset between 2009 and 2010. This is discussed in further detail within the text.*

influence. The majority of the overlap exists between 285 K and 300 K. Both day and night show unimodal distributions. The day and night peaks are approximately 300 K and 288 K for June and approximately 300 K and 290 K for December, respectively.

Further to this, a temporal outlook on the whole tile is presented (Figure 51). For this a mean is calculated by averaging all pixels. A period of 10 years between 2003 and 2013 has been analysed by month for day and night. Initial findings support earlier histograms with a diurnal shift of approximately 20 K noted (Figure 51). During the day the Afar region remains consistently warmer than the main EARS regardless of season. This is seen to be less so at night, though the Afar still records the greatest LSTs. A seasonal cycle is also observed, with the regions mirroring each other. A higher intensity feature has also been noted between 2009 and 2010. The physical reasons for this may include potential weather events; alternatively this feature may once again arise as a result of sampling, with cloud coverage skewing the dataset.

Maximum and minimum LSTs have also been provided (Figure 52). Here, the values refer to the maximum and minimum LSTs used to calculate the tile mean LST. This data is important, providing a guide to the best and worst case scenarios in terms of basin modelling. It is particularly significant within the EARS given that relatively small LST changes have significant impacts on modelling results. The values for the maximums and minimums appear to show similar peaks and troughs to the mean LST data. The minimum values, however, consistently deviate further from the mean than the maximums. This deviation has been attributed to persistent cloud cover issues and potential instrumental errors.

#### **4.1.1.1 Turkana Region**

The Turkana region is now studied further, for the reasons provided in Chapter 3.2.1.1 (Figure 53). Here, features observed within the Turkana tile have been previously discussed and are not commented on further. Histograms of the region differ from the Afar and main EARS tiles (Figure 54); though some similarities exist, including the distribution of the datasets. The broad, more even distribution of day time LSTs is again observed, as is the narrower spread of night time LSTs. For June, day time LSTs show a bimodal distribution akin to June in the Afar region. This may once again be the result of data sampling, with cloud cover skewing the results. In contrast to this, June night time LSTs show a less well defined unimodal peak than is typical but are similar to the main EARS (Figure 50).

Both day and night for December 2006 act as expected and are most similar to the main EARS with little deviation away from a singular peak. For both day and night the peaks in LST frequency are of a similar range to regional outlook tiles. Once again, it should be noted that the LST distributions here, both unimodal and bimodal, could potentially be the result of sampling effects, i.e. the distributions observed may arise from the number of cloudy and this discarded pixels within the region. Thus further work is required to determine the accuracy of these histograms. To do this an index pertaining to the number of cloudy pixels would be required.

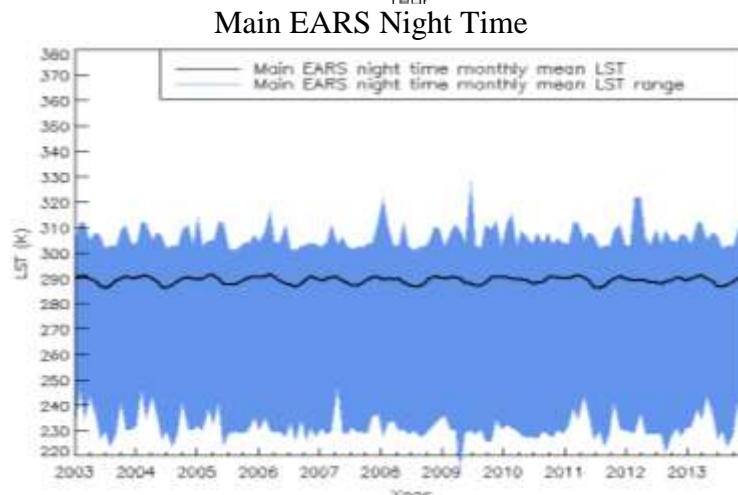
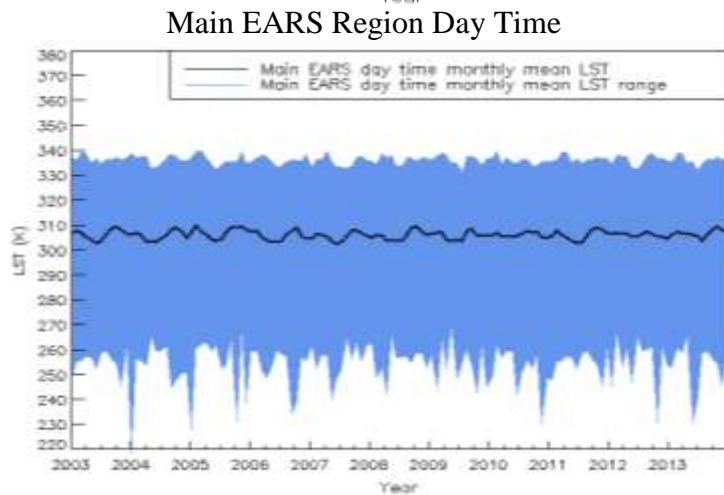
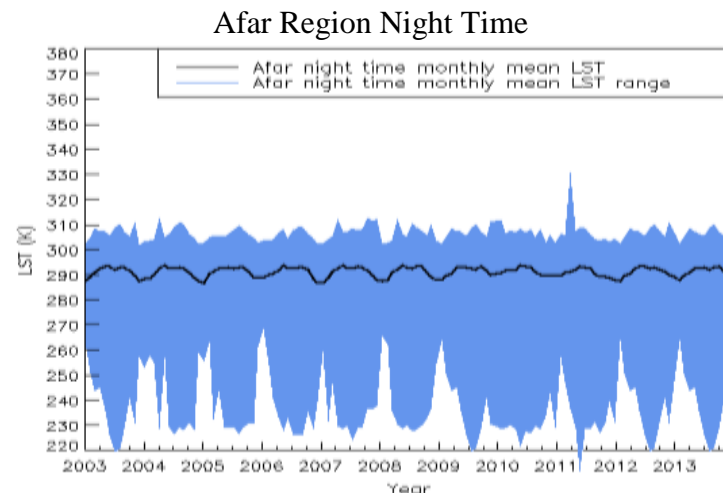
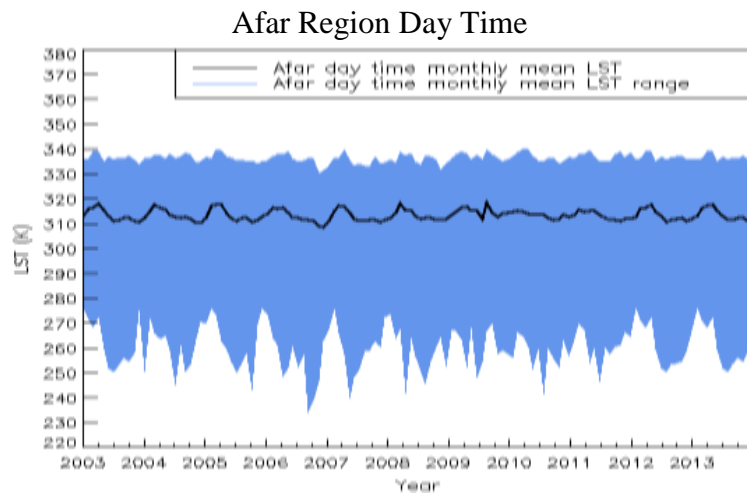


Figure 52: Maximum and minimum ranges of monthly MODIS LSTs, taken from the Aqua dataset, across the Afar and EARS regions of  $0.01^\circ$  resolution.

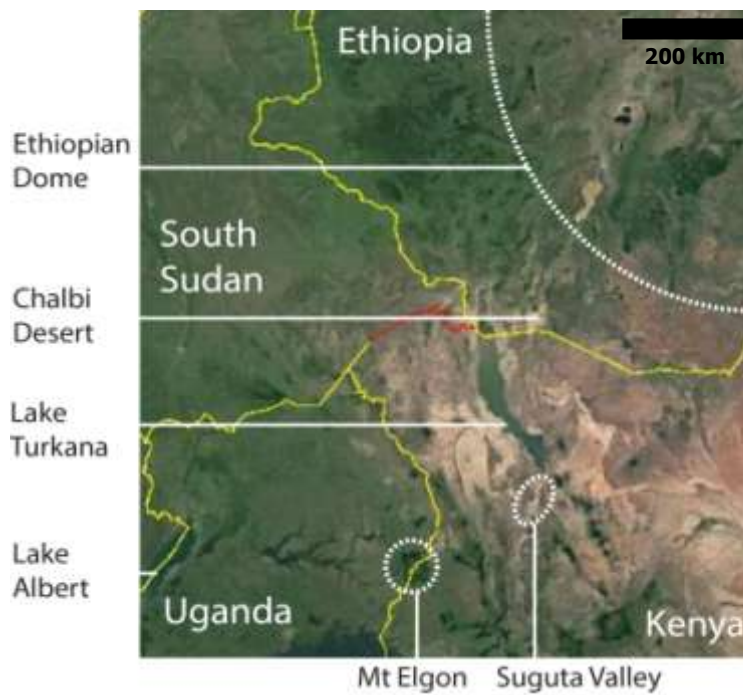
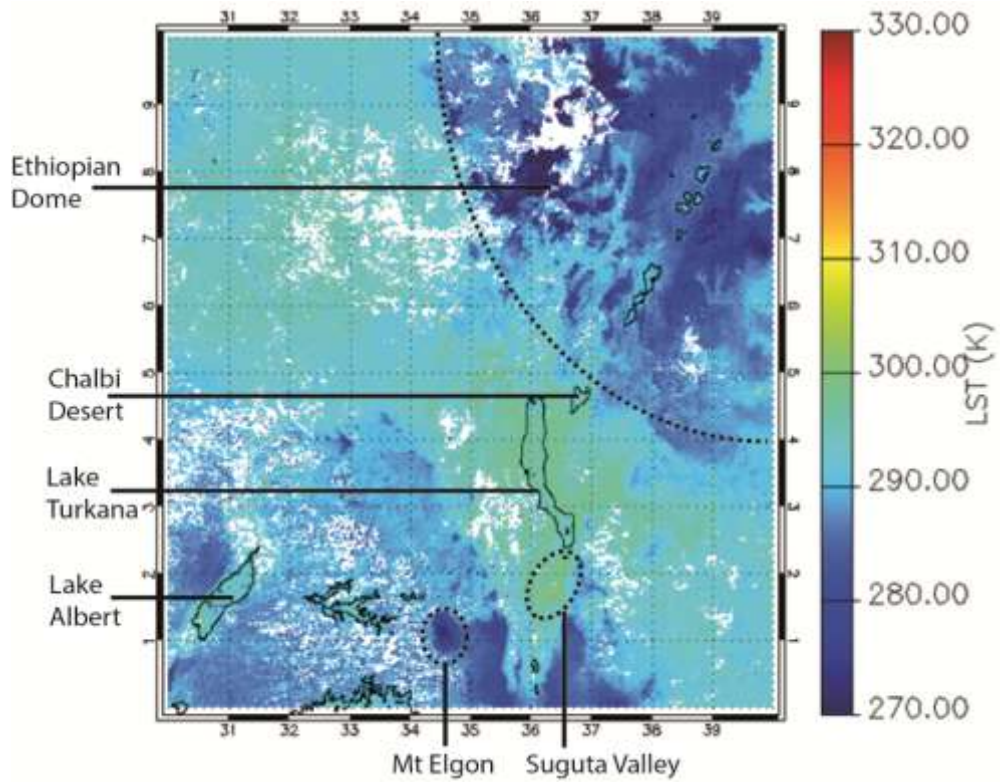
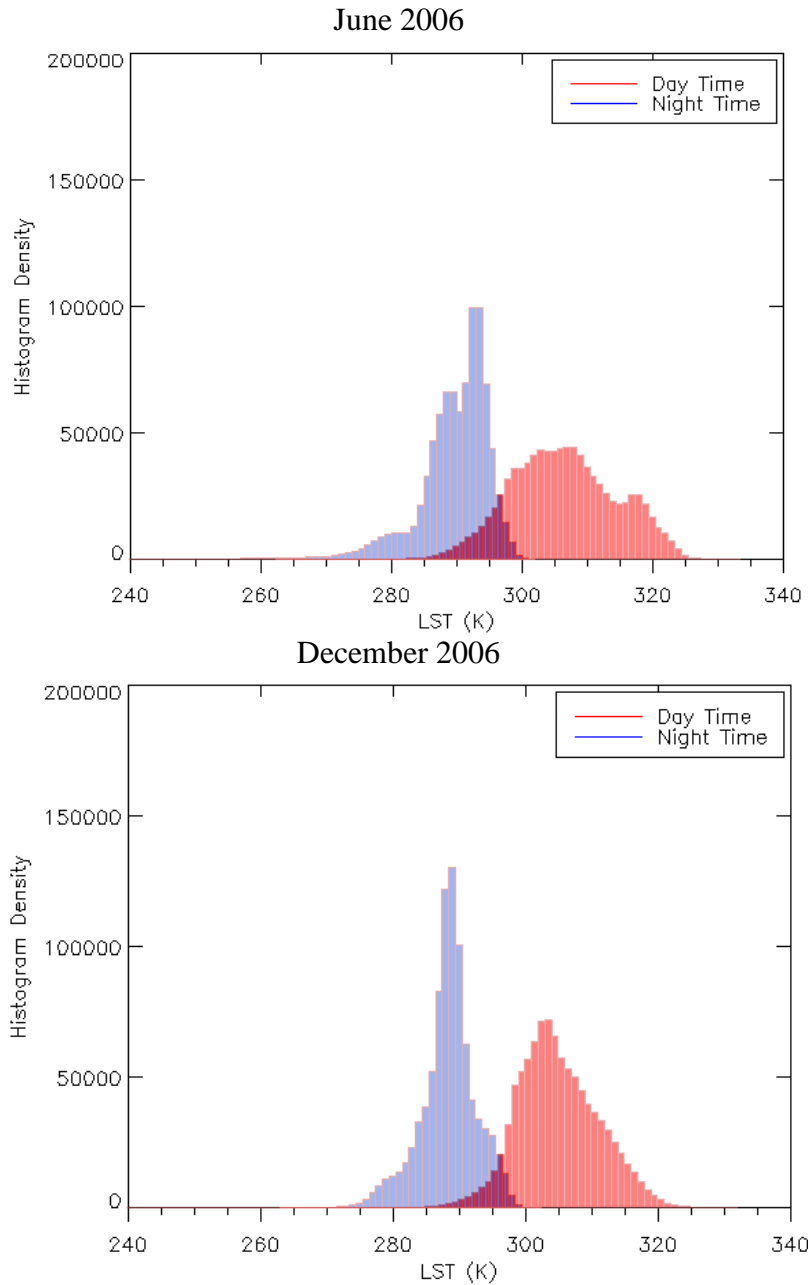
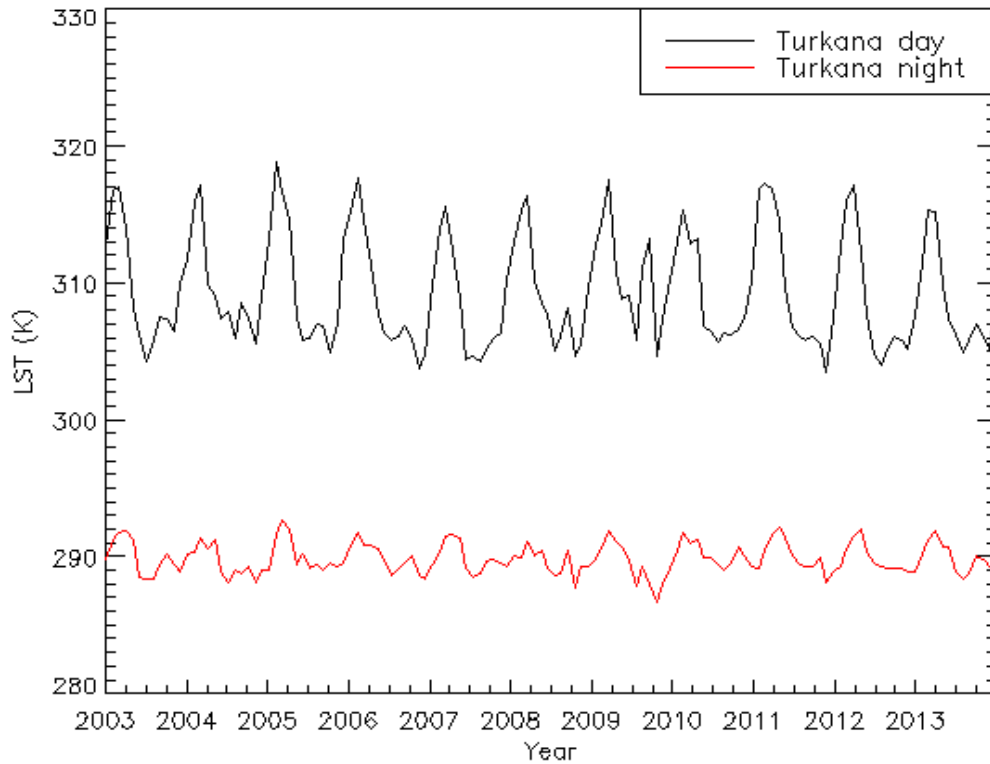


Figure 53: Absolute night time monthly MODIS LSTs, from the Aqua dataset, across the Turkana area for June 2006 on a  $10^\circ \times 10^\circ$  grid of  $0.01^\circ$  resolution and corresponding Google Earth (2016) image. White pixels within the MODIS absolute data refer to a lack of data as a result of cloud coverage. Yellow lines on the Google Earth image refer to country boundaries.



*Figure 54: Absolute monthly MODIS LST frequencies, derived from the Aqua dataset, for the Turkana region tile that is a  $10^{\circ} \times 10^{\circ}$  grid of  $0.01^{\circ}$  resolution.*

A temporal plot of whole tile monthly LSTs is now presented from 2003 to 2013 (Figure 55). On this timescale, diurnal and seasonal effects are visible. Seasonal variation is less significant at night with smaller fluctuations. Periodic peaks in LST are observed between January and March of each year and dips in LST between September



*Figure 55: Temporal variation of whole tile monthly mean MODIS LSTs, derived from the Aqua dataset, across the Turkana region that is a  $10^{\circ} \times 10^{\circ}$  grid of  $0.01^{\circ}$  resolution.*

and December. The period 2009 to 2010 fits the typical period pattern but also has an anomalous second peak within mid-2009. The reason behind which is unknown however, the anomaly may potentially arise from instrumental errors or an anomalous physical event, such as increased volcanism. The day time LSTs typically fluctuate about 310 K and the night around 290 K.

Maximum and minimum LSTs follow a similar pattern to the mean LST and are again provide valuable inputs for basin modelling best and worst case scenarios (Figure 56). For example, when LSTs are warmer, maximum and minimum values are also likely to increase. Similarly to the previous maximum and minimums, values should be viewed critically due to persistent cloud issues.

Auxiliary variables over the Turkana region are now studied to gain an insight into their variation. Variables here are used later within the PCA and thus only the time period from 2005 to 2008 has been focussed on, in accordance with this analysis. Analysing both channels of emissivity reveals that emissivity 2 has consistently higher values than

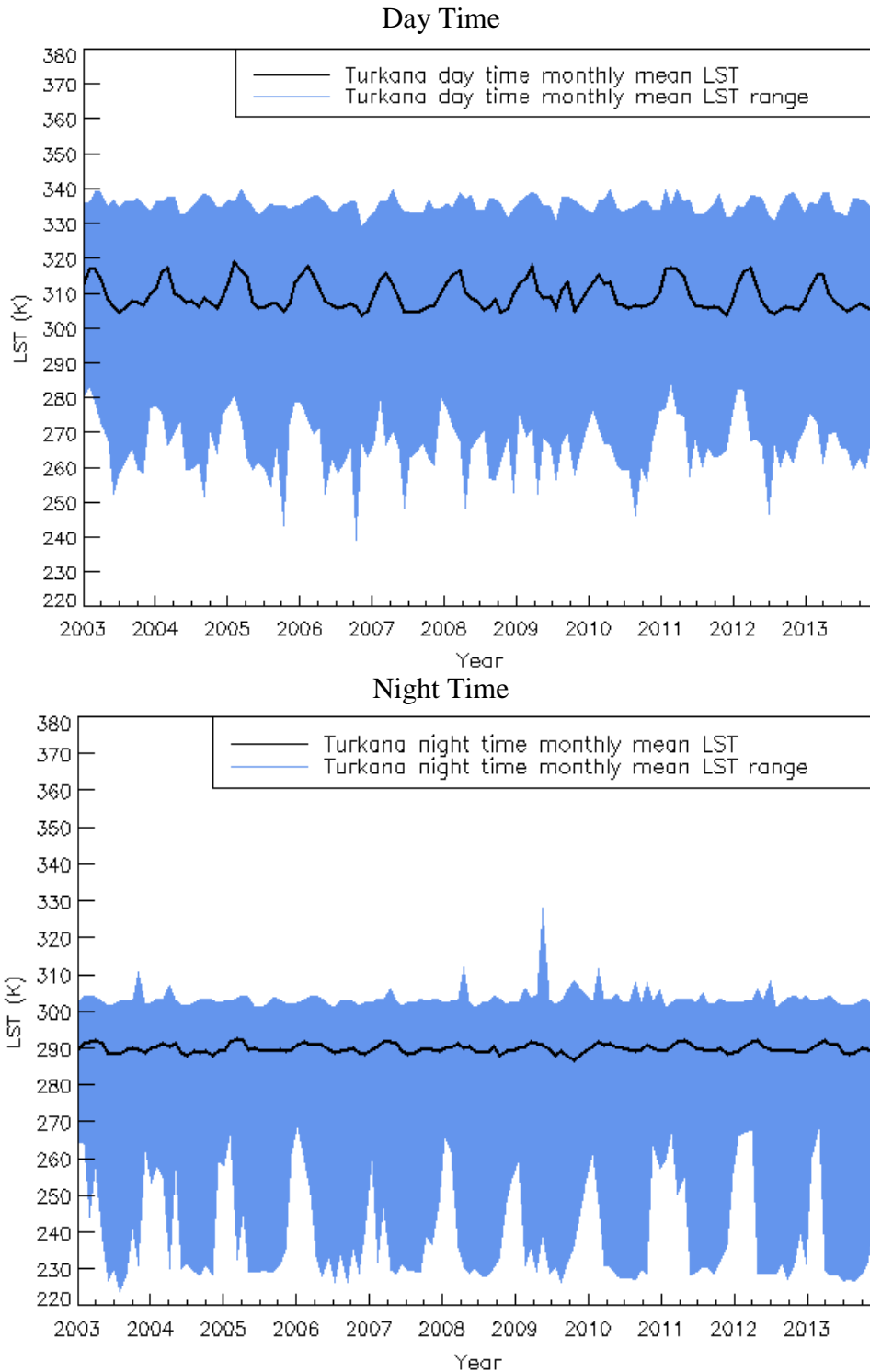


*Figure 56: Maximum and minimum absolute MODIS LSTs, taken from the Aqua dataset, from January 2003 to December 2013 for the Turkana region that is a  $10^{\circ} \times 10^{\circ}$  grid of  $0.01^{\circ}$  resolution. The approximate temperature difference observed between the maximum and minimum LSTs for the day time is 80 K, whilst for night time this is lower at 70 K.*

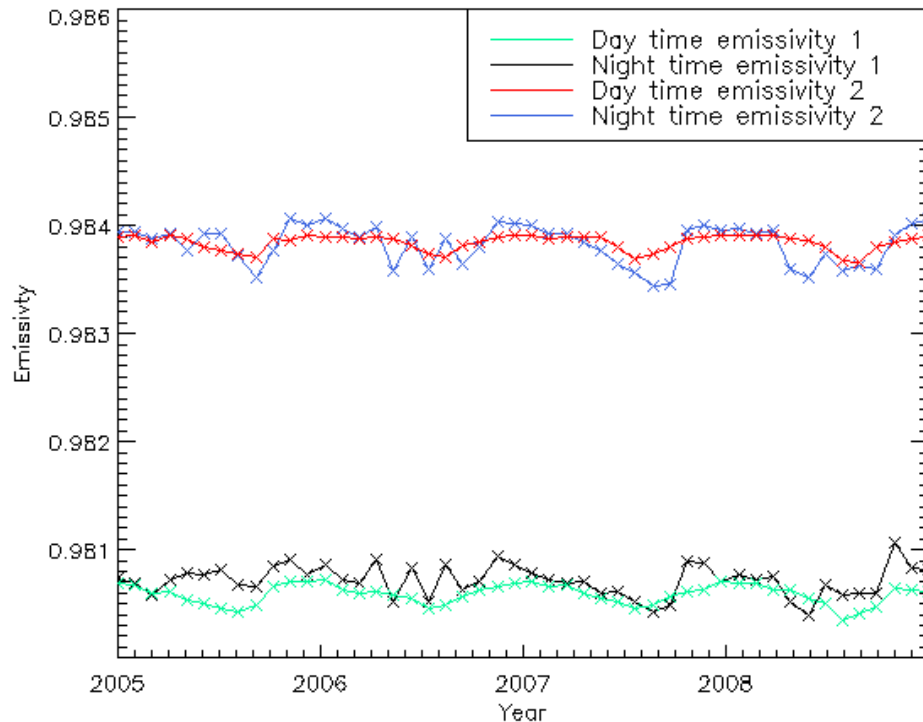
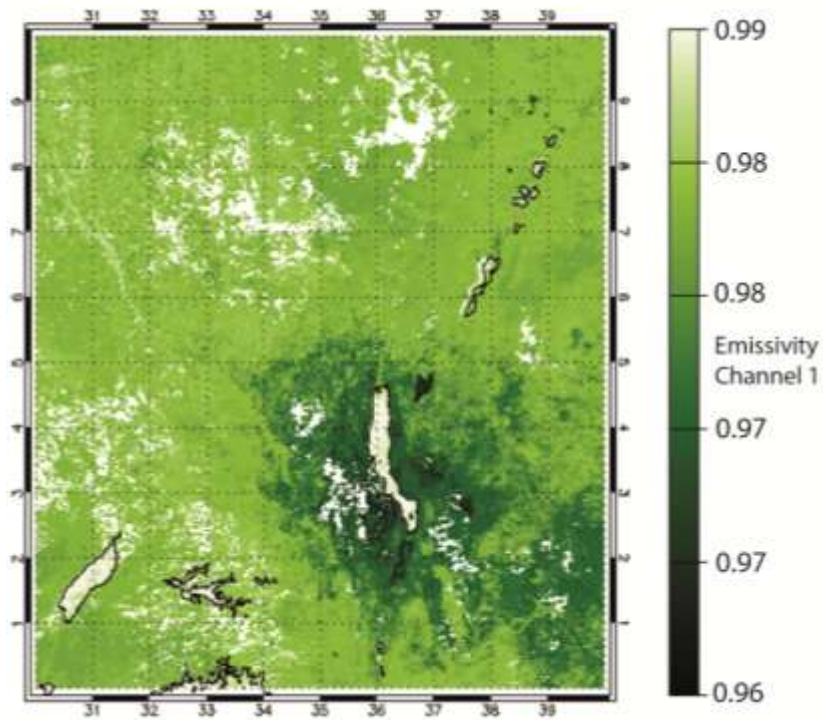


Figure 57: Monthly mean emissivities in both channel 1 and channel 2 from January 2005 through to December 2008 across the Turkana region that is a  $10^{\circ} \times 10^{\circ}$  grid of  $0.01^{\circ}$  resolution. Emissivity data is from the MODIS auxiliary variables, i.e. the emissivity measured by MODIS channels 31 and 32 as described in Chapter 3.1.1.

that emissivity 1 (Figure 57). Both night time emissivities are more variable than the day and synchronous with each other. Day time magnitudes remain similar throughout with synchronous periodicities.

Figure 58 additionally provides spatial plots of the respective emissivity channels. The differences in emissivity values may arise from the uncertainty between the channels, with channel 1 (MODIS band 31) between  $10.780 \mu\text{m}$  to  $11.280 \mu\text{m}$  and emissivity channel 2 (MODIS band 32) between  $11.770 \mu\text{m}$  to  $12.270 \mu\text{m}$ . Such uncertainties are enhanced given the locality of the study, with greater emissivity variability in arid regions, where bare soil and rock surfaces are exposed, displaying the widest range of emissivity (Schmugge et al., 2007). The day-night variability could potentially arise from the overall stability of the atmosphere and the amount of cloud cover, which will ultimately determine how quickly the Earth's surface cools in the absence of solar heating.

Emissivity MODIS channel 31



Emissivity MODIS channel 32

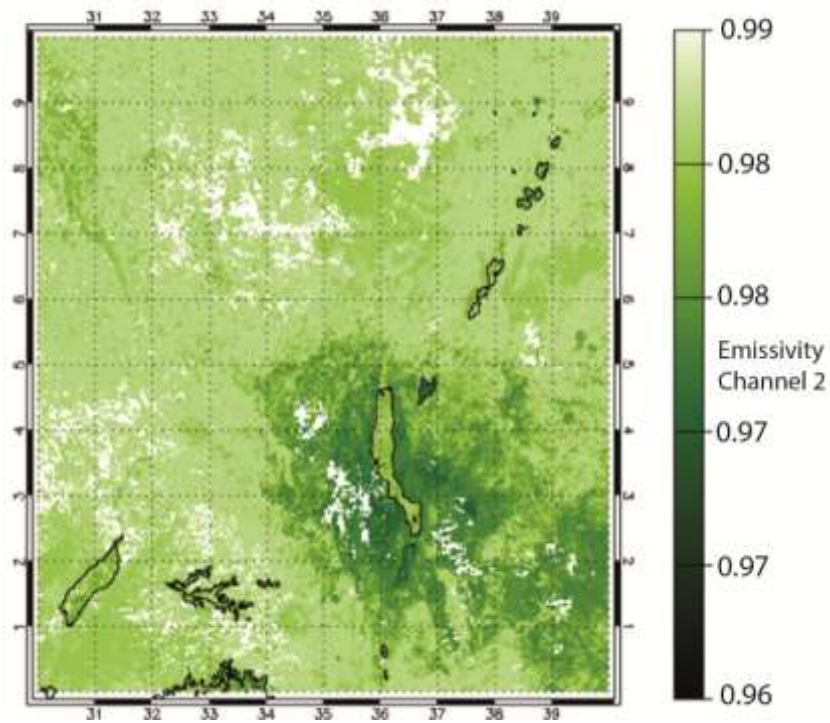


Figure 58: Monthly mean emissivities from MODIS channels 1 and 2, as described in Chapter 3.1.1; for June 2006 across the Turkana region on  $10^\circ \times 10^\circ$  grids of  $0.01^\circ$  resolution.

Unlike emissivity,  $f_v$  does not show significant diurnal variation but does vary seasonally, likely as a result of the growing seasons (Figure 59). Peaks in  $f_v$  should be noted, with a two stepped transition to the highest  $f_v$  of each year before a sharp drop to the lowest.  $tc_{wv}$  also shows periodic patterns and little diurnal variation. Two rapid changes are noted within each year, with a three stepped transition downward from peak  $tc_{wv}$  to the lowest  $tc_{wv}$  (Figure 60).

#### **4.1.2 Absolute Yearly Means**

Given that cloud cover is still persistent in monthly means, yearly LSTs have also been generated. It is also desirable to have such a dataset as to average for seasonal variation. Yearly means are therefore generated from 2003 to 2013. Compared to monthly LSTs, the yearly means have reduced cloud effects, proving a more complete overview. The seasonal influence should be negligible in the yearly LSTs due the averaging across the seasons. Figure 61 and Figure 63 display the yearly LSTs for night time 2006 across the main EARS and Afar region. Minimum and maximum LSTs are also provided for day and night (Figure 62 and Figure 64, respectively).

Minimum and maximum values here refer to the minimum and maximums throughout the year and therefore it should be noted that neighbouring pixels may be from the beginning and ending of the year. Once again, these values are important for basin modelling, providing most likely and least likely scenarios in terms of basin evaluation and hence identification of new exploration sites.

The warmer and cooler areas highlighted via the monthly means are also observed within the yearly means. In the yearly means such features are more consistent and distinct, including the Ethiopian Dome, Afar Depression and Lake Turkana area. Several areas also appear more homogenous across the yearly means. This is particularly the case for water bodies, though as previously noted the water body LSTs are likely invalid due to the additional influence of currents and winds not accounted for when considering the land surface. One disadvantage with the yearly means is the loss of finer features including the Turkwel River.

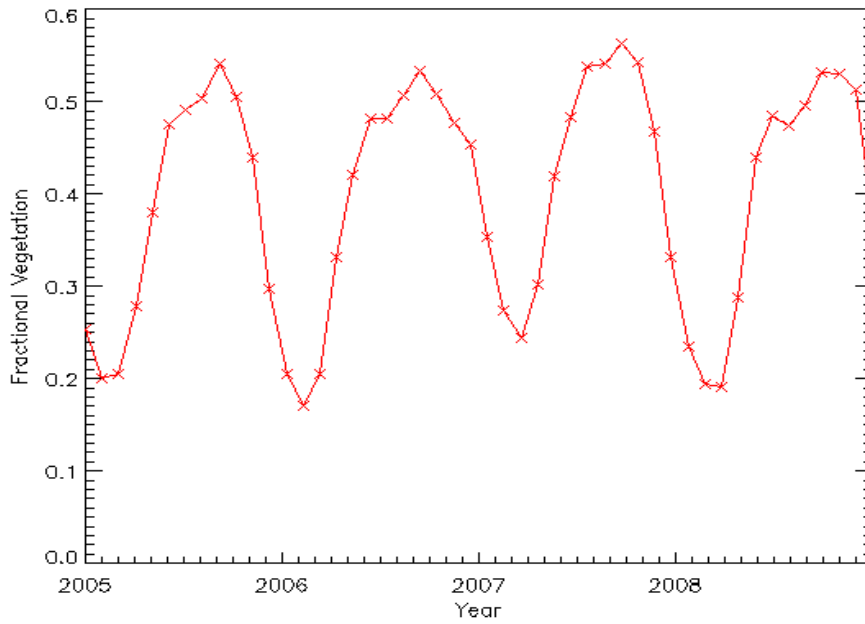


Figure 59: Monthly mean fv from January 2005 through to December 2008 across the Turkana region that is a  $10^{\circ} \times 10^{\circ}$  grid of  $0.01^{\circ}$  resolution. The fv data is based on the Geoland-2 FCOVER dataset (Baret et al, 2013), as explained in Chapter 3.1.1.

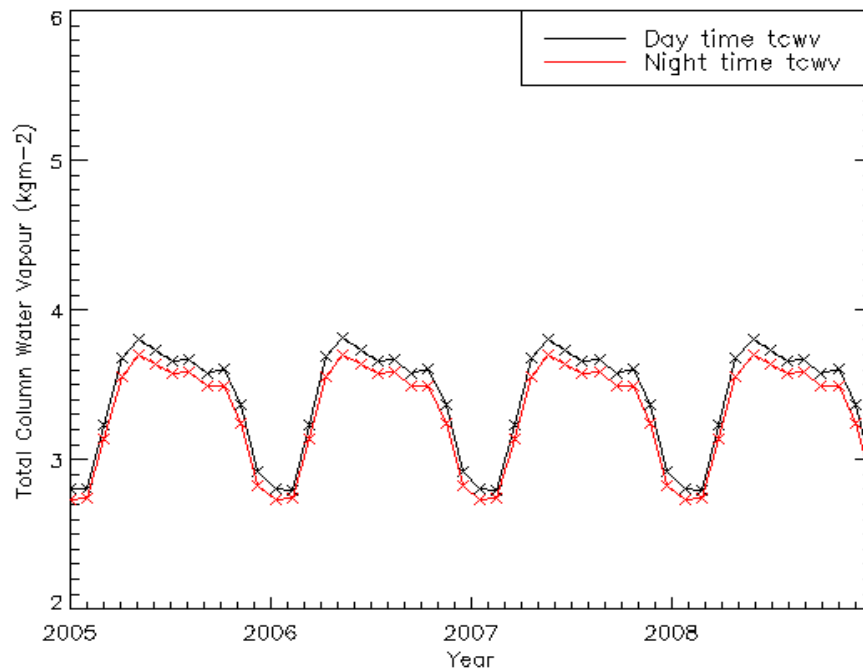


Figure 60: Monthly mean tcwv from January 2005 through to December 2008 across the Turkana region that is a  $10^{\circ} \times 10^{\circ}$  grid of  $0.01^{\circ}$  resolution. Tcwv data is taken from the European Centre for Medium-Range Weather Forecasts (ECMWF) ERA-Interim reanalysis (Dee et al, 2011), as explained in Chapter 3.1.1.

In terms of the overall LSTs, the north of the region is typically warmer than the south and the east generally warmer than the west. This can be explained by various factors including desert conditions towards the north and more vegetated regions further south, i.e. it can be explained by the typical climatologies of the regions.

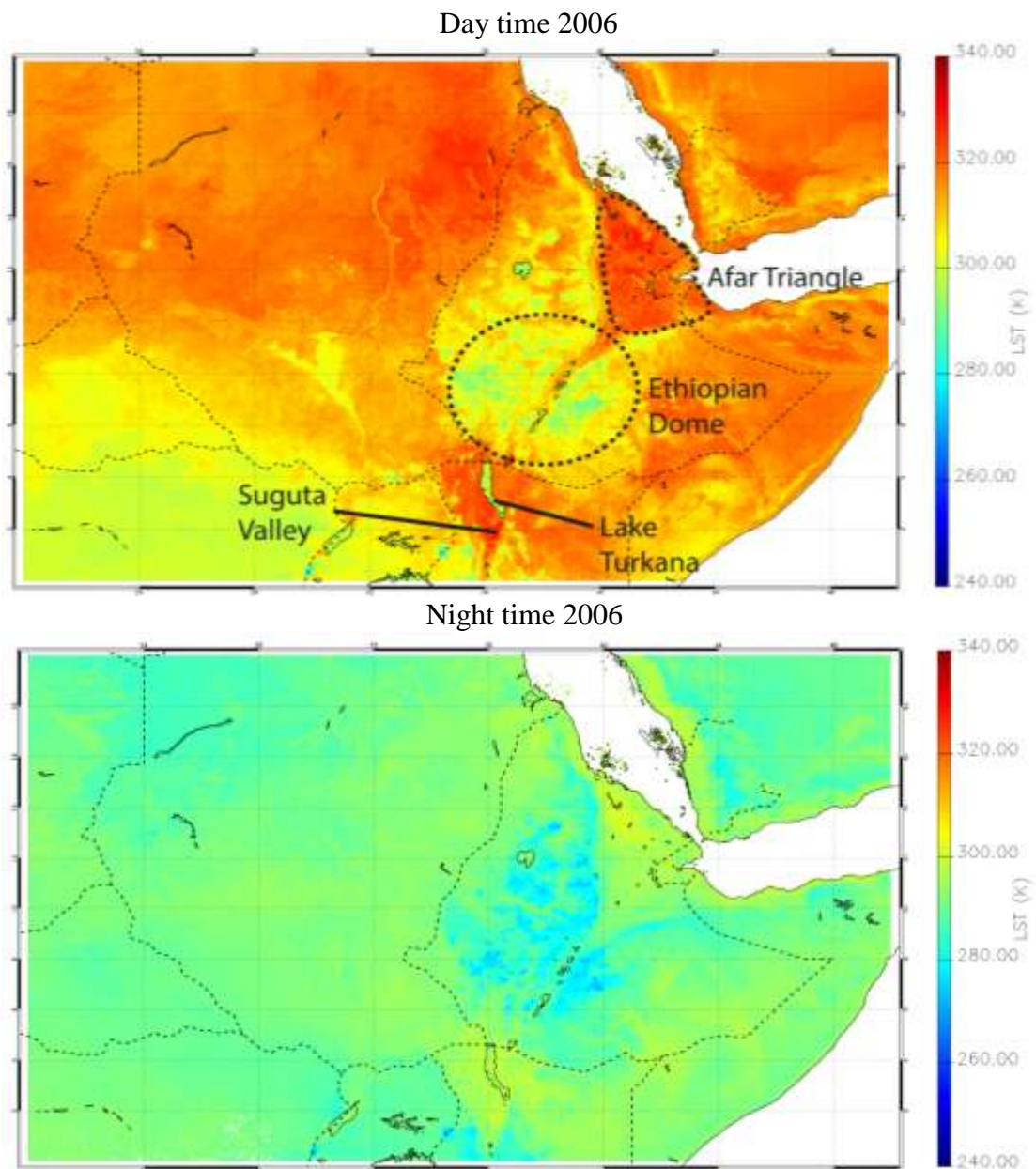


Figure 61: 2006 yearly mean MODIS LSTs, for the Aqua dataset, across the Afar region that is a  $30^{\circ} \times 20^{\circ}$  grid of  $0.01^{\circ}$  resolution. Dashed lines, with the exception of the Ethiopian Dome, refer to country boundaries previously noted in Figure 47.

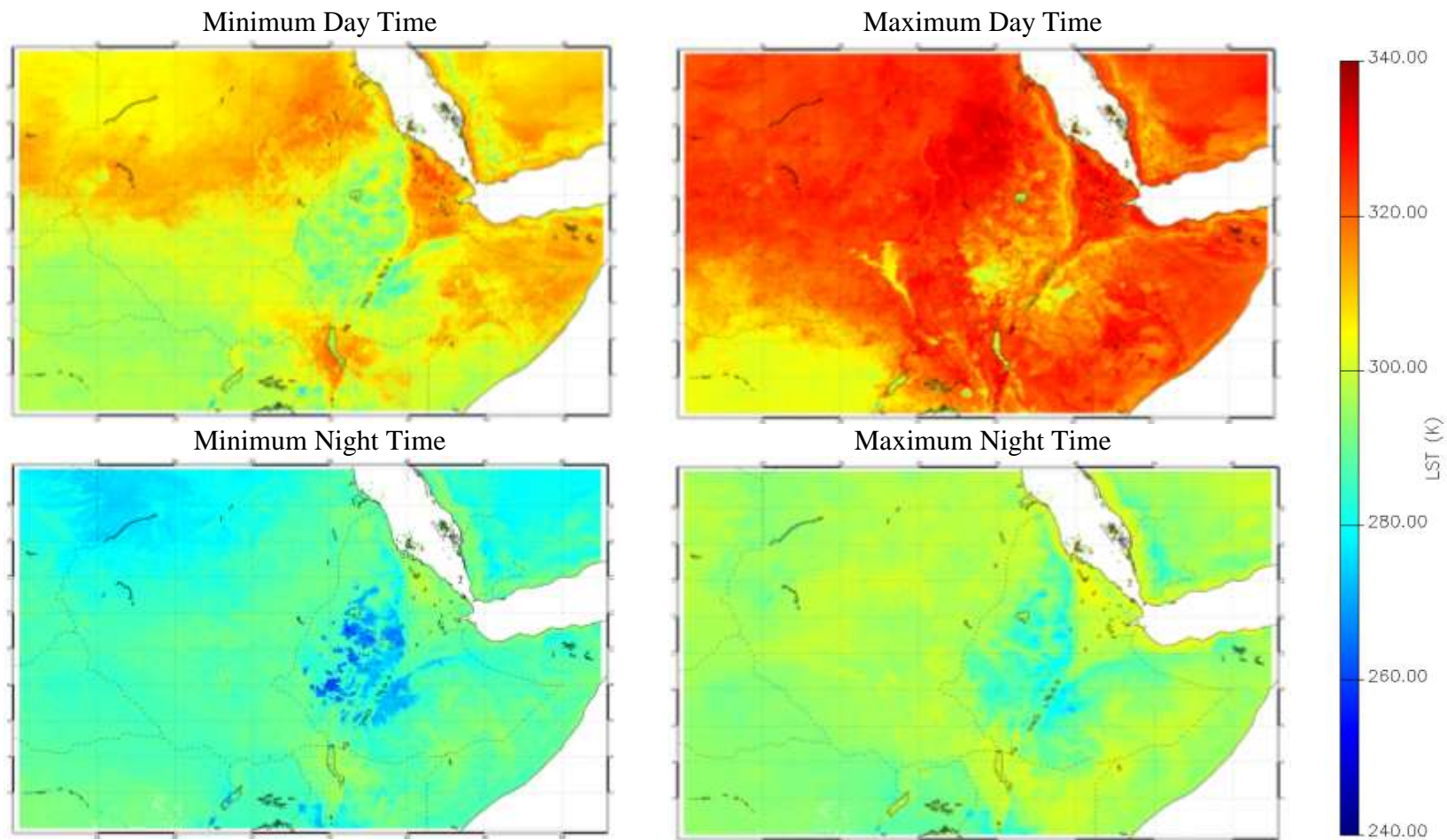
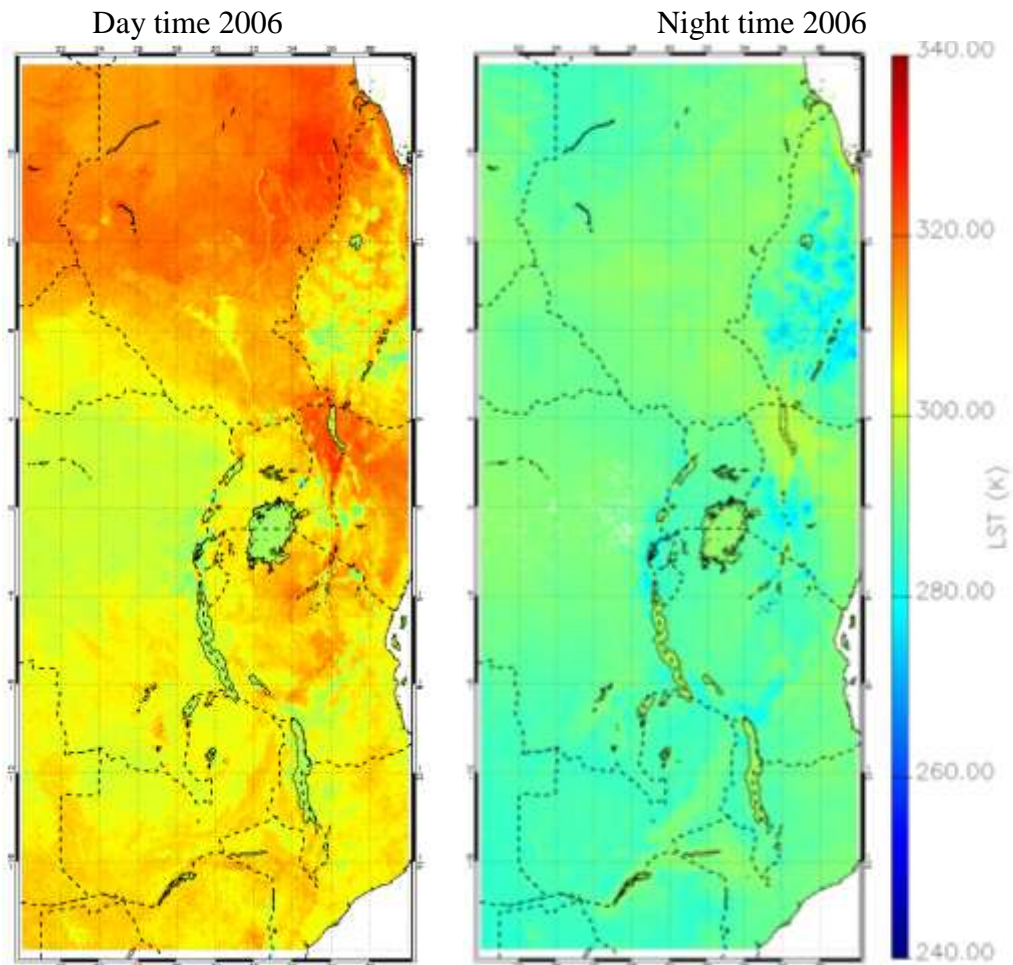


Figure 62: Maximum and minimum 2006 MODIS LSTs, for the Aqua dataset, across the Afar region that is a  $30^\circ \times 20^\circ$  grid of  $0.01^\circ$  resolution. Dashed lines refer to country boundaries as further detailed in Figure 47.



*Figure 63: 2006 yearly mean MODIS LSTs, for the Aqua dataset, across the main EARS region that is a  $20^{\circ} \times 40^{\circ}$  grid of  $0.01^{\circ}$  resolution. Dashed lines refer to country boundaries as outlined earlier in the chapter in Figure 47.*

There is a similar east-west distinction in land cover type with the east composed of bare soils and the west, more heavily vegetated. Elevation is also found to significantly vary between the distinct sub-regions. Maximum and minimums LSTs reveal a greater range for the day, supporting previous analyses (Figure 64).

Yearly mean histograms of LST frequency remain consistent with the monthly means, with a clear diurnal shift (Figure 65). The day time datasets for both the Afar and EARS show more variation with numerous peaks and a broader data spreads. The night time LSTs have narrower ranges and a unimodal distribution, peaking at approximately 290 K in both the main EARS and the Afar region.

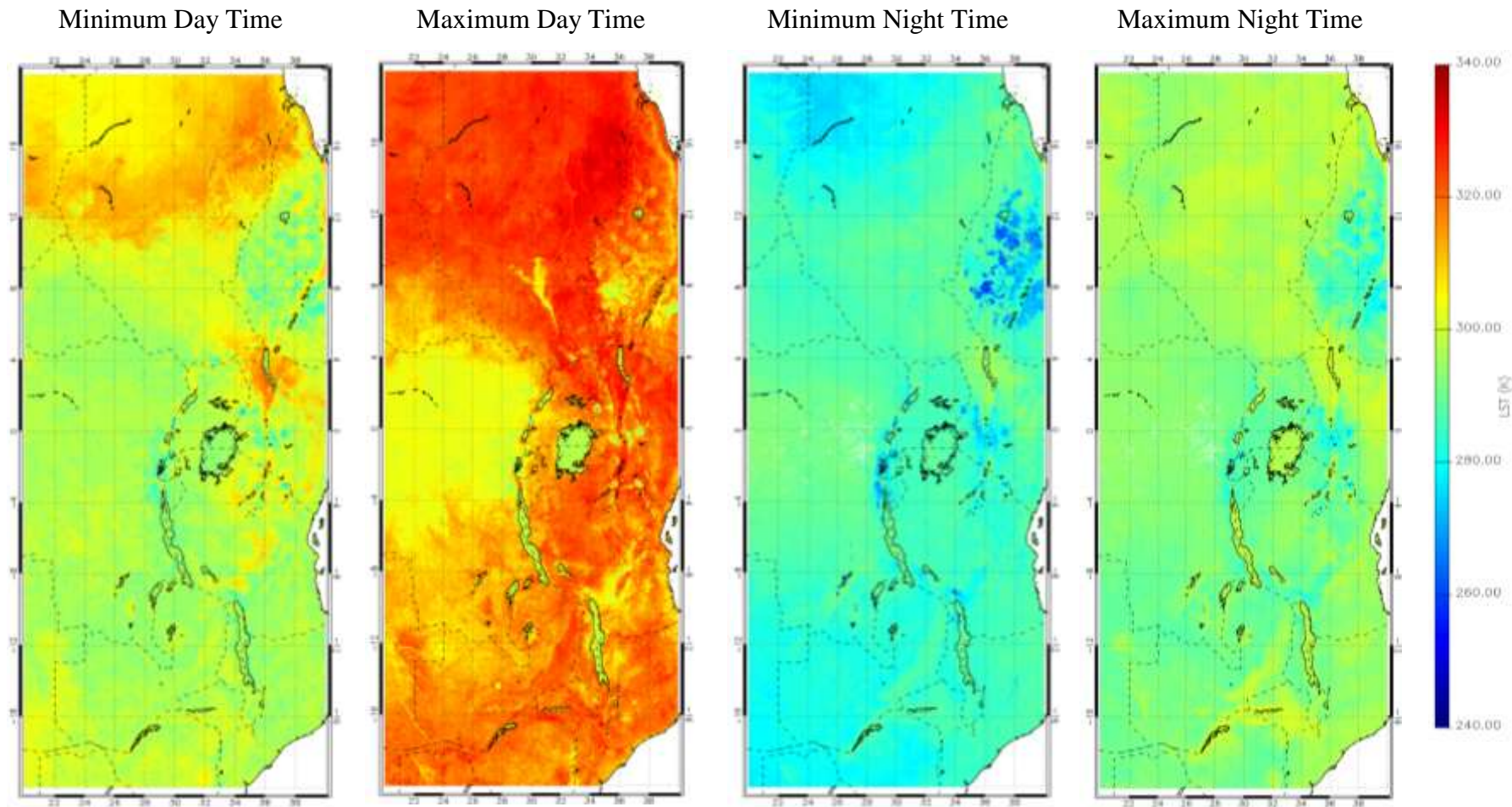


Figure 64: Maximum and minimum 2006 MODIS LSTs, for the Aqua dataset, for the Aqua dataset, across the main EARS region that is a 20° x 40° grid of 0.01° resolution. Dashed lines refer to country boundaries as further detailed in Figure 47.

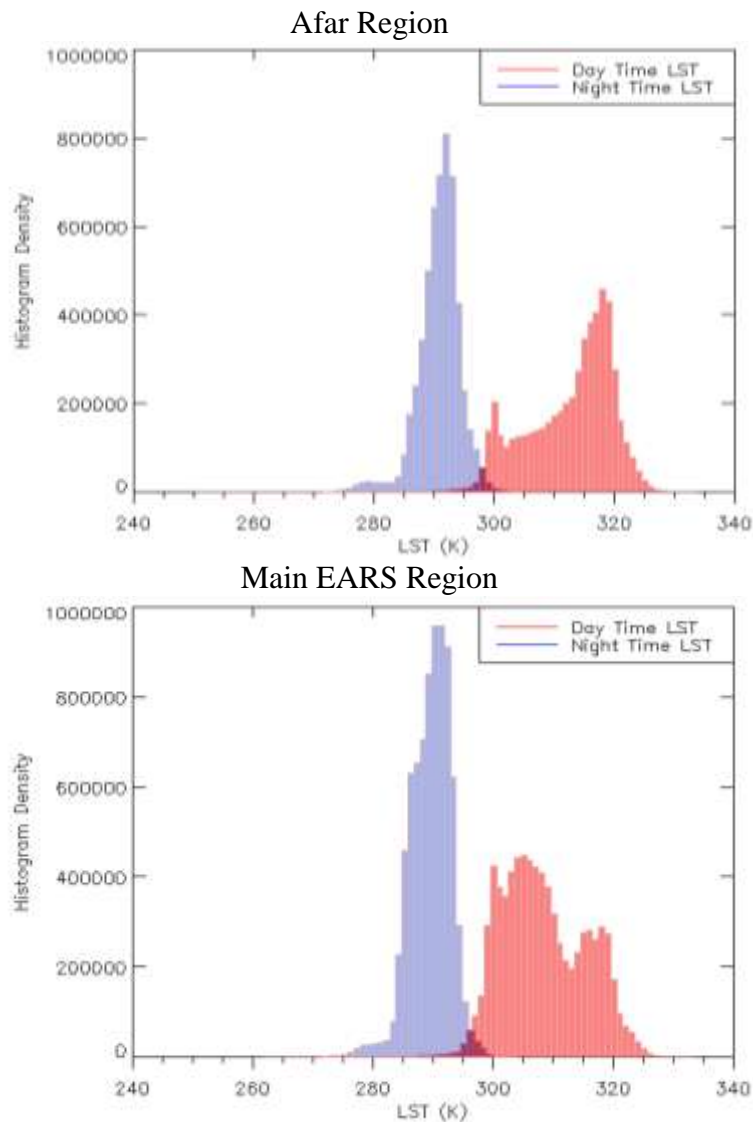
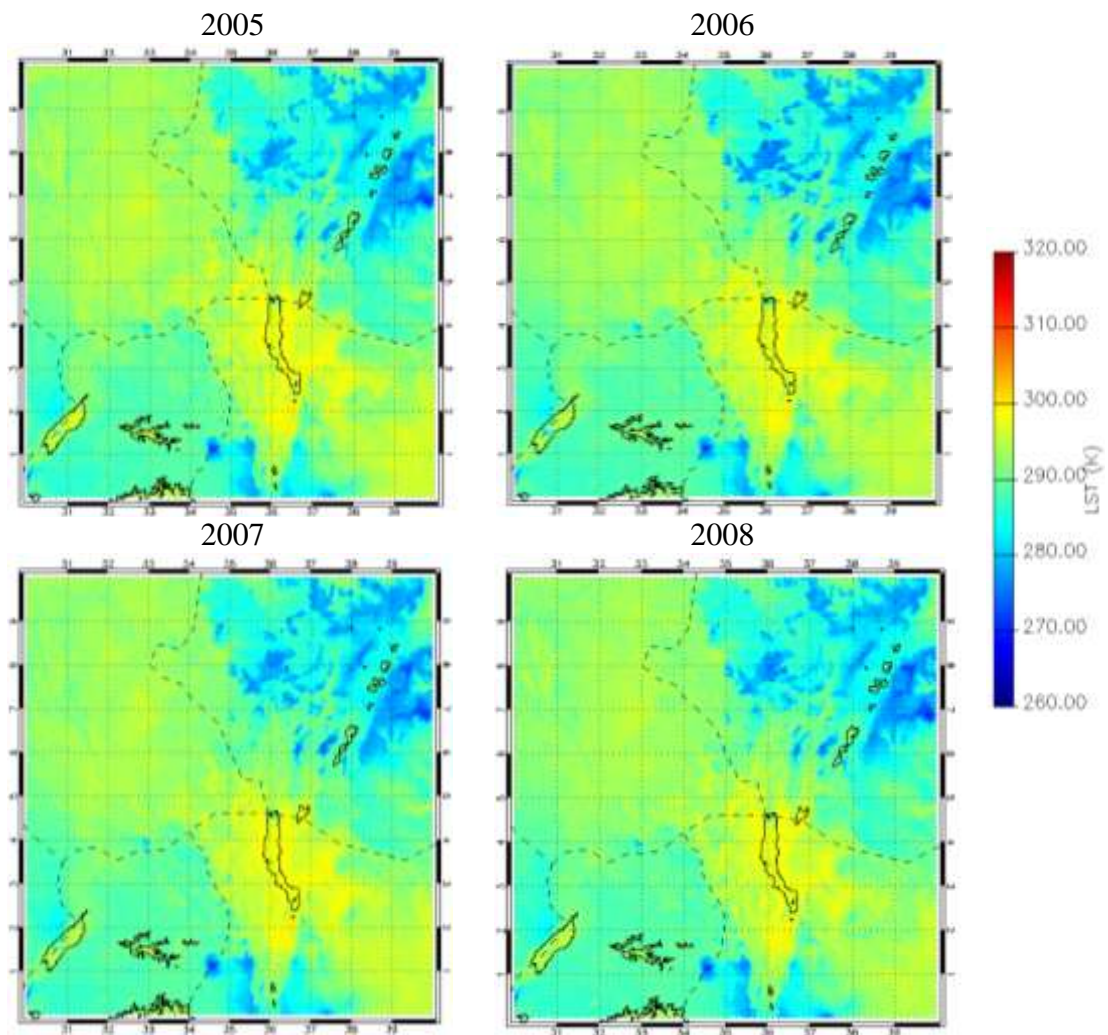


Figure 65: MODIS LST frequencies, from the Aqua dataset, for the 2006 yearly means across the Afar and main EARS regions. Once again pixel numbers between the regions vary due to the tile areas and additionally as a result of cloud cover.

#### 4.1.2.1 Turkana Region

Focus for the yearly means now returns to the  $10^{\circ} \times 10^{\circ}$  grid of the Turkana region. Figure 66 shows the night time yearly LSTs. From this it is clear that yearly means vary as a result of climatic variations. For 2003, 2004 and 2009 through to 2013 similar LSTs are also observed. Notable features are identified, as previously discussed, with respect to the whole region. At this scale smaller features such as the Turkwel River are unresolved.



*Figure 66: Night time MODIS LSTs, for the Aqua dataset, from 2005 to 2008 across the Turkana region that is a  $10^{\circ} \times 10^{\circ}$  grid of  $0.01^{\circ}$  resolution.*

LST frequency is generated across the Turkana region for the 2006 means. Similarly to previous plots, a broad day time range is observed as is a narrower night time range. The data displayed in Figure 67 is a near but not exact replica of the single monthly means tile of June 2006 LSTs across the Turkana region (Figure 54). From the LST frequencies, several features can be readily identified. This includes the first peak of the night time LSTs at approximately 270 K which is likely to be associated with the Ethiopian Dome.

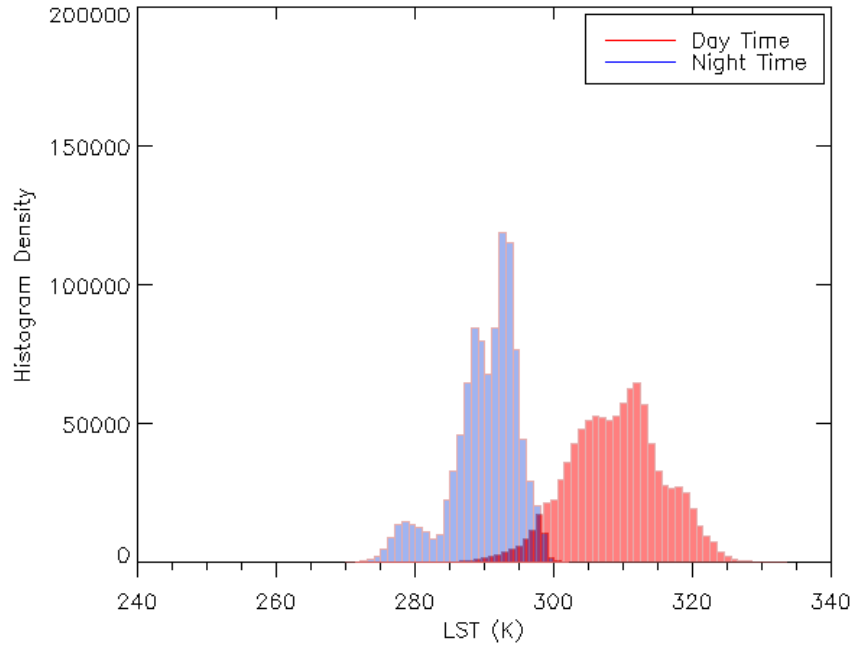


*Figure 67: MODIS LST frequencies for the 2006 yearly means of the Aqua dataset, across Turkana tile that is a  $10^{\circ} \times 10^{\circ}$  grid of  $0.01^{\circ}$  resolution.*

Table 13 and Figure 68 detail the maximum and minimum yearly LSTs for the Turkana region. Here, mean LSTs refer to a whole tile mean taken from the per pixel yearly means (Figure 66). Plots showing minimum and maximum LSTs per pixel have been generated with the values taken from the mean per pixel values throughout the twelvemonths. The minimum and maximums stated in Table 13 refer to means taken from the respective plots. Maximum day LST remains constant throughout, whilst minimum LSTs are more variable. Similarly night time maximums are more consistent compared to the minimums. One exception to this is in 2011, which is anomalously low and potentially an artefact of cloud cover issues, though further work is required to confirm this.

#### **4.1.2.2 Diurnal Differences**

Thermal inertia estimates describe the fluctuation in LST amplitude between day and night. This is important to consider within this study as to not identify false anomalies. In this study, thermal inertia cannot be accurately calculated due to the sampling

Table 13: Yearly MODIS LSTs for the Aqua dataset, across the Turkana region that is  $10^{\circ} \times 10^{\circ}$  grid of  $0.01^{\circ}$  resolution.

Year	Day Time Mean			Night Time Mean			Day/ Night
	Mean LST (K)	Maximum LST (K)	Minimum LST (K)	Mean LST (K)	Maximum LST (K)	Minimum LST (K)	Mean Temperature Difference (K)
2003	309.9	334.1	282.9	290.4	301.4	269.9	19.5
2004	309.6	333.4	279.3	290.1	301.4	268.8	19.5
2005	310.3	333.6	282.7	290.4	301.5	269.4	19.9
2006	308.9	332.7	271.5	290.2	301.7	270.1	18.7
2007	308.6	333.2	282.3	290.2	301.6	270.1	18.4
2008	309.2	333.3	281.1	290.0	301.7	269.5	19.2
2009	311.1	335.2	270.3	290.6	302.5	265.3	20.5
2010	309.2	332.9	277.2	290.5	302.1	267.2	18.7
2011	306.7	332.5	268.3	290.1	302.2	229.1	16.6
2012	308.9	332.4	282.4	290.2	301.4	269.6	18.7
2013	308.7	333.0	280.6	290.2	301.7	269.0	18.5

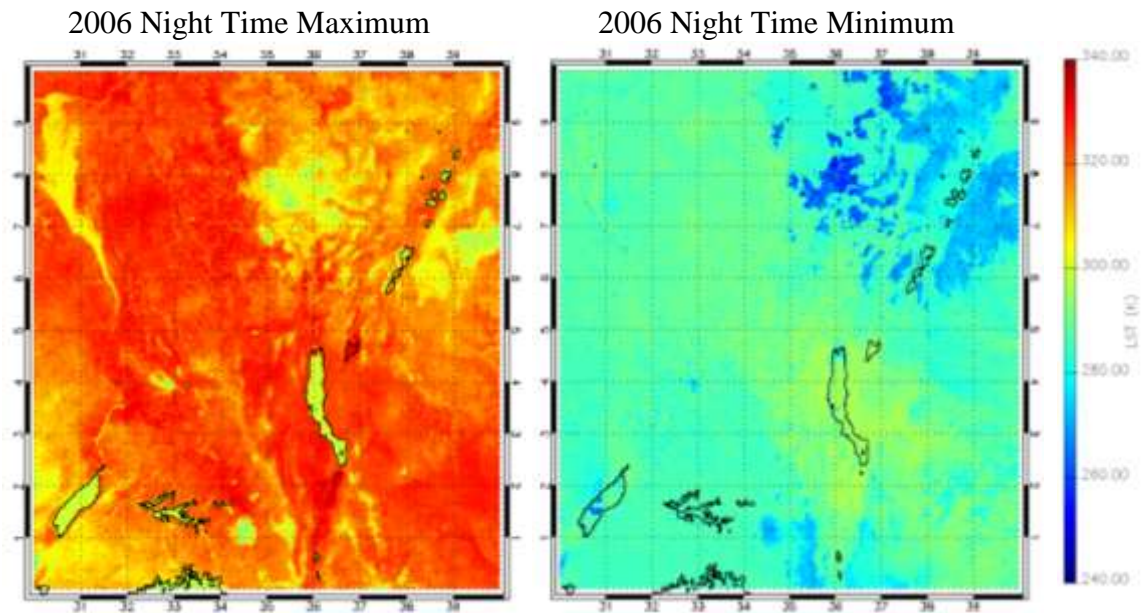


Figure 68: Minimum and maximum mean MODIS LSTs per pixel, for the night time 2006 Aqua dataset, across the Turkana region on a  $10^{\circ} \times 10^{\circ}$  grid of  $0.01^{\circ}$  resolution. The equivalent day time plots are found in Appendix 5.

periodicity of the MODIS data; however the diurnal LST differences can indicate potential thermal inertias. Table 13 shows the day-night difference as a mean across the entire Turkana region, calculated by removing the tile mean day time LST away from the tile mean night time LST. The difference is found to vary between 16.6 K and 20.5 K dependent upon year. This is likely the result of climatic fluctuations that are considered later.

Figure 69 now displays the spatial distribution of diurnal differences for the years 2005 through to 2008. The region surrounding Lake Turkana and parts of the Ethiopian Dome are visible via high diurnal temperature shifts throughout. This indicates that such regions are much warmer during the day time than the night time, i.e. they have lower thermal inertias. Additional areas of lower thermal inertia estimates include Mount Elgon, the more southerly part of the Ethiopian Dome and numerous rift flanks, particularly around the Suguta Valley. These lower thermal inertias contrast to the lakes across the region, which tend to display smaller diurnal temperatures differences and therefore have higher thermal inertias. Rivers are additionally found to have higher thermal inertias, though less so than lakes. This is a likely result of the water depth.

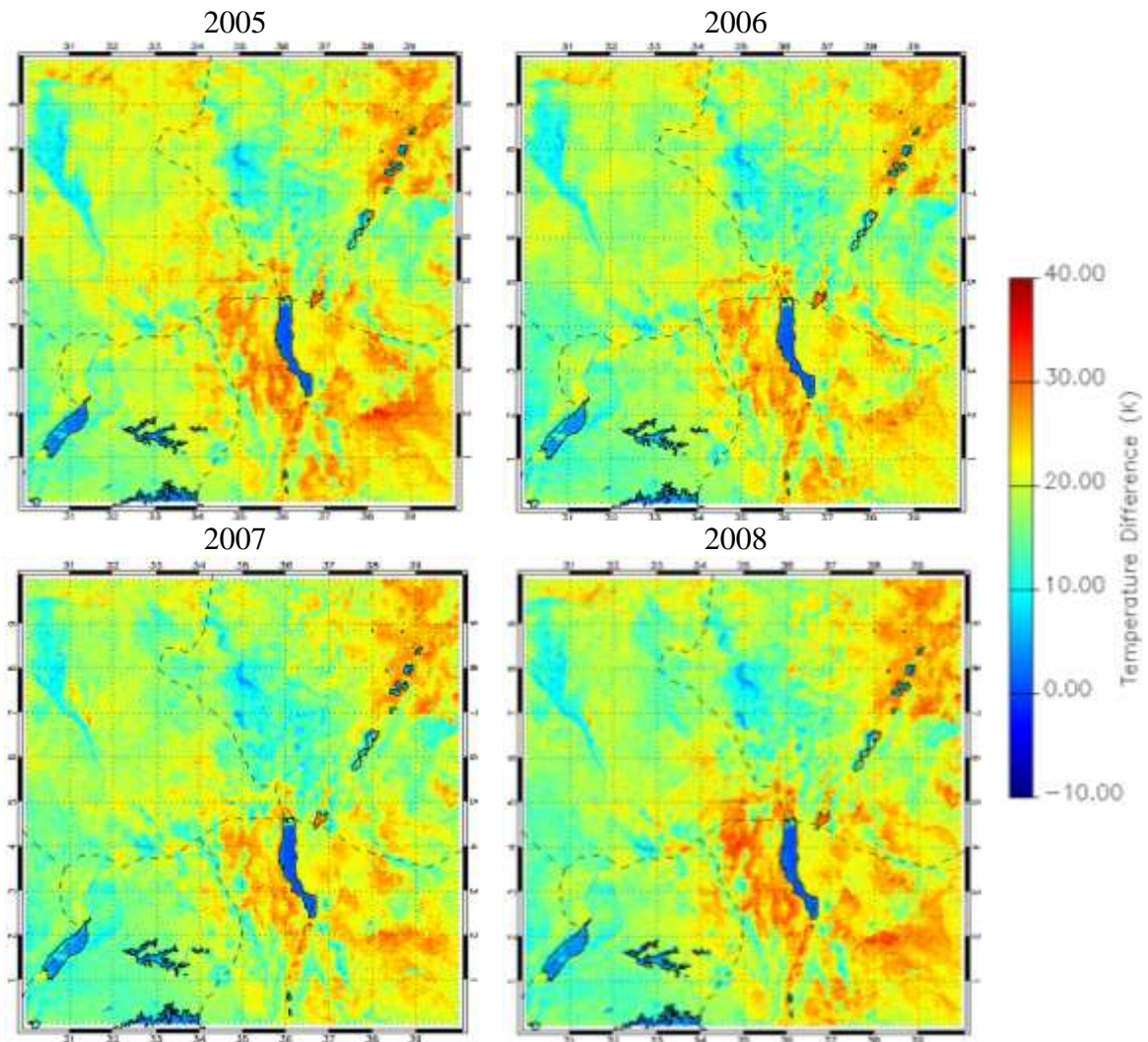


Figure 69: Diurnal differences for mean MODIS LSTs of the Aqua dataset, across the Turkana region that is  $10^{\circ} \times 10^{\circ}$  grid of  $0.01^{\circ}$  resolution. Dashed lines refer to country boundaries.

#### 4.1.3 Discussion

The MODIS derived dataset successfully provides a constant spatial and temporal sampling of LSTs across the EARS. Spatially, the dataset spans a large segment of the African continent from the Afar Depression in the north to Malawi in the south. This broad region is composed of  $1 \text{ km}^2$  pixels, which are found to be of sufficient resolution to identify basin scale features and geographic aspects of the landscape. However, the identification of finer features such as the Turkwel River is not always possible for the yearly LSTs. Temporally, the datasets are available for both day and night, monthly and

yearly, spanning from 2003 to 2013. This is deemed to be sufficient allowing for the determination of diurnal shifts, seasonal cycles and climatic patterns.

The maximisation of the LSTs both spatially and temporally to the surroundings is reported by a number of previous studies as a criteria for a thermal anomaly (Miliaresis, 2009; Zouzias et al., 2011). The Afar Depression, as discussed in Chapter 1, fits the criteria and could therefore be confirmed as thermally anomalous with respect to the surrounding. This is as expected given the active sea floor spreading within the region; that is additionally known to correspond to the termination of the Red Sea Rift (Miliaresis, 2009). However, the criteria fails to distinguish between a thermal anomaly and geothermal anomaly. Therefore further analysis is necessary to confirm whether the thermally anomalous Afar is geothermally associated. However with respect to the geology of the area, it is likely that the Afar region is geothermally associated and it would be unexpected that such a significant heat source would not contribute to the LST.

To the south, the thermally anomalous area surrounding Lake Turkana is more obviously affected by the influence of external variables on LST than the Afar. This is as the Turkana area sharply contrasts to its surroundings in terms of elevation, land cover and emissivity. The physical variables present in the region all appear to act in favour of warmer LSTs and must therefore be considered in order to identify the unexplained variation. Unless the unexplained variance is identified, it is difficult to understand whether geothermal activity contributes to the anomaly. Given the locality of the basins and the approximate orientation of the known rift, the presence of warmer LSTs in this area is most likely the third arm of the triple junction exhibiting itself at the surface and therefore the likelihood of a geothermal association is high. Miliaresis (2012) also identifies this area as one of higher LSTs.

The warmer western and eastern branches have also been identified as thermally anomalous by previous work (Miliaresis, 2012). Given the locality of the rift, this is again no surprise. The contrast in LSTs of the branches and the central cratonic region is also expected with the thick body inhibiting upwards mantle movement and therefore suppressing the geothermal gradient (Figure 16). This contrast is most significant at the south-western edge of the Turkana region at night (Figure 61 and Figure 63).

Overall the generation of a mean LST dataset, whether it be monthly or yearly, is a useful tool for energy companies. It not only provides an alternative way of mapping broad and inaccessible regions prior to field work but also provides input values for basin modelling, as discussed in Chapter 1.1.5 (Kuper, 2016). Estimates of thermal inertia also prove useful for mapping land cover and lithology across extensive areas in attempts to narrow down the region of interest. In terms of the scientific understanding, the mean LST maps have hinted at the dynamic variables that influence the LST and allow a number of regions to be identified for further study. Seasonal fluctuations in the variables allow growing seasons (Leilei et al., 2014), periods of increased rainfall due to the ITCZ migration (Danley et al., 2012) and other cyclical events to be identified and then considered during analysis as is discussed in Chapter 2.3.

#### **4.1.4 LST Means: Limitations and Uncertainties**

The dataset on the whole is well resolved as previously discussed, nevertheless a number of limitations exist. This includes the presence of empty pixels arising due to cloud issues which reduce the overall availability of data; particularly during the night time when optical instruments are not additionally available to improve the data. The persistent cloud issues are further highlighted within this thesis by the lower than expected minimum LSTs (Table 13). Cloud cover is reduced by averaging LSTs, though monthly plots still display cloud as a result of the ITCZ migration (Danley et al., 2012) (Figure 22). Yearly LSTs show further reductions in cloud cover as a result of seasonal averaging, though this does not entirely resolve such issues. To fully understand the limitations here, an index pertaining to the number of cloudy pixels would be beneficial. This would be a useful indication to the potential uncertainty in the means derived from the original LST dataset. The development of this as further work is discussed later in Chapter 6.

Other limitations concern water body LSTs. These LSTs are likely affected by additional processes such as winds and currents, which are not accounted for when considering the parameters affecting the land surface as discussed in Chapter 2. It is therefore likely that the LSTs are inaccurate and potentially skew results. This is

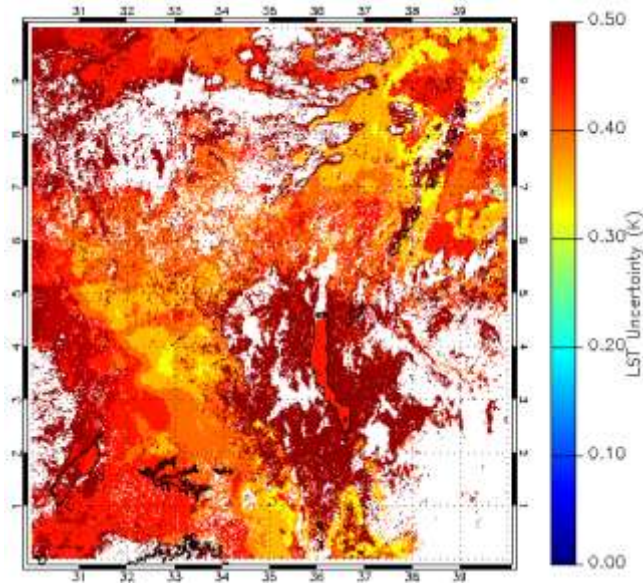


*Figure 70: Night time MODIS LST uncertainty for the 5th February 2006, as obtained from the Aqua MODIS Level 3 auxiliary product on a  $10^{\circ} \times 10^{\circ}$  grid of  $0.01^{\circ}$  resolution across the Turkana region.*

particularly evident along the western branch of the rift where a number of deep lake filled basins exist. This therefore requires further work, though as noted earlier determining the surface temperatures of offshore areas is easier for oil companies, whereby the water temperature is often used as an indicator (Kuper, 2016). Further work is likely to focus on implementing the tile average as a mask for the lakes, which is again later noted in Chapter 6.

The aforementioned limitations require uncertainty analysis that is not extensively covered within this study. The daily MODIS LST product employed in LST averaging contains auxiliary uncertainty data (Figure 70). LST uncertainties from this dataset typically vary between 0 K and 1 K for daily LSTs, however this is likely to be higher when propagated through the analysis. The 1K uncertainty for daily data is however, in line with the expected uncertainties that the split window algorithm, used to generate the LST, aims to achieve at 1 km resolution under clear sky conditions with known surface emissivities (Wan, 1999). The range of 0 K to 1 K is significant in terms of geothermal anomalies as  $\pm 1$  K may be sufficient to mask an anomaly; though this is not discussed in previous literature. This uncertainty is critical for this thesis as the intensity of the geothermal anomalies associated with basins is unknown, however it is expected

that for areas of increased volcanism, where geothermal power plants are situated, such geothermal anomalies would be significantly higher than the surroundings.

Propagation of this uncertainty is not applied to the absolute LSTs, though it is expected that uncertainties of similar magnitude will exist. Though not directly applicable, studying the daily LST products with respect to the monthly and yearly LSTs provides an indication to the certainty of such regions. For example, from Figure 70 it is clear that the LSTs across the area surrounding Lake Turkana are of greater uncertainty at approximately 0.5 K than those to the immediate west at around 0.3 K to 0.4 K. This therefore suggests that LSTs to the west of the lake are likely to be more accurate than those in the lake's immediate vicinity. Furthermore, it should be noted that LST validation via other geophysical methods, as discussed by Aretouyap et al. (2016), is necessary to fully understand the uncertainty in the data. This is discussed later within Chapter 6.

## **4.2 Host Rock-Basin Comparison**

For this study, it is important to distinguish between basin and host rock in an attempt to identify areas that may be of interest geothermally and in turn commercially in terms of hydrocarbon prospects. Host rock and basins across the EARS are therefore now contrasted in terms of LSTs. The first area to be considered is the Turkana region for the night time period of 2006 (Figure 71). Basin outlines within this area show both concordance and discordance with the distribution of warmer and cooler absolute LSTs. It should be noted that where basins are adjoined the outline is not observed.

From Figure 71, a number of distinctly warmer LST regions coincide with basins. This includes the broad, low lying Turkana Trough, whereby the majority of warmer LSTs lie within the basin boundaries; from Melut, Melut West, Melut East, Mongalla and Pibor Post in the northwest to the Anza Basin in the southeast. The warmer LSTs observed in this depression intensify around Lake Turkana, where an abundance of basins are situated (Figure 40). One additional area that should be noted here is the region of warmer LSTs to the northeast of the Turkana Basin. This area is in fact

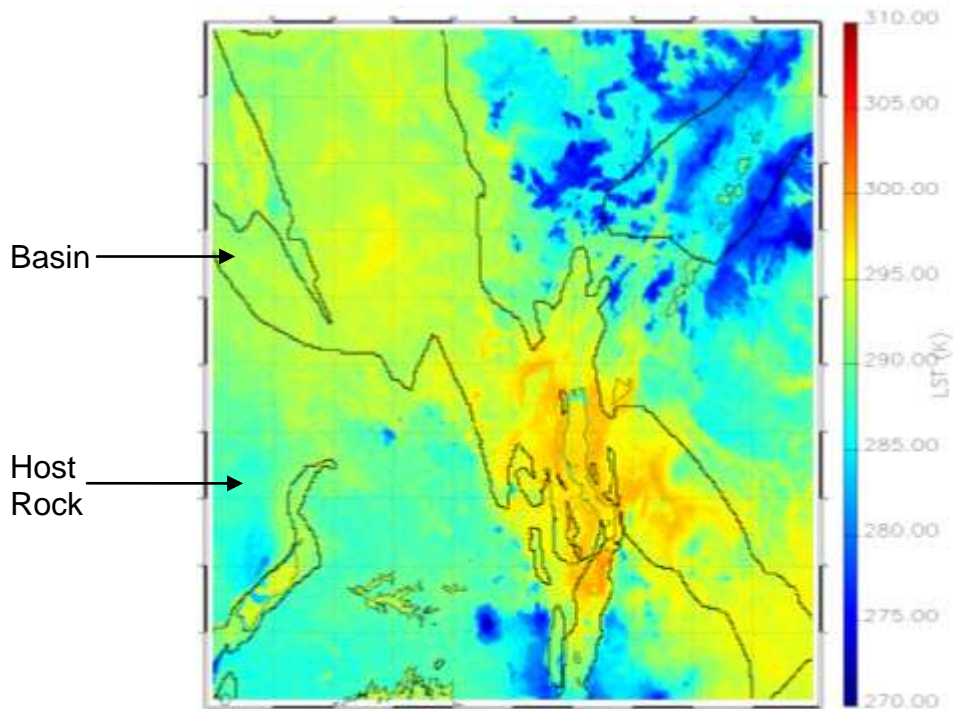


*Figure 71: Night time MODIS LSTs of 2006 for the Turkana region on  $10^\circ \times 10^\circ$  grid of  $0.01^\circ$  resolution. Basin outlines are overlain (thicker black lines), as supplied from Tullow Oil plc and as described previously in Chapter 3.1.4.*

another basin, known as Chew Bahir, which is not mapped by USGS outlines. Just south of Lake Turkana lies the Suguta Basin that is of particular interest due to its known geothermal activity. This basin displays consistent and strong LSTs throughout the dataset; particularly within the narrow, lower lying Suguta Valley. To the immediate west lies the South Kerio Basin that also continues to display warmer LSTs regardless of diurnal shifts or seasonal patterns. In contrast to this, the coolest LSTs are generally found outside of basins with the exception of the Afar. Here, the distinct LST-basin boundary is not present and the basin cross cuts the cooler LSTs; although marginally warmer LSTs are recorded trending in the same orientation as the rift.

LST frequency histograms are now generated for day and night with respect to the host rock and basins (Figure 72). The comparisons reveal that overall the two entities span a similar LST range; however the basins are consistently warmer. Mean, maximum and minimum LSTs across the Turkana tile for basin and host rocks are also shown in Table 14. Here, means are for the tile mean of the yearly per pixel plot. Maximums and

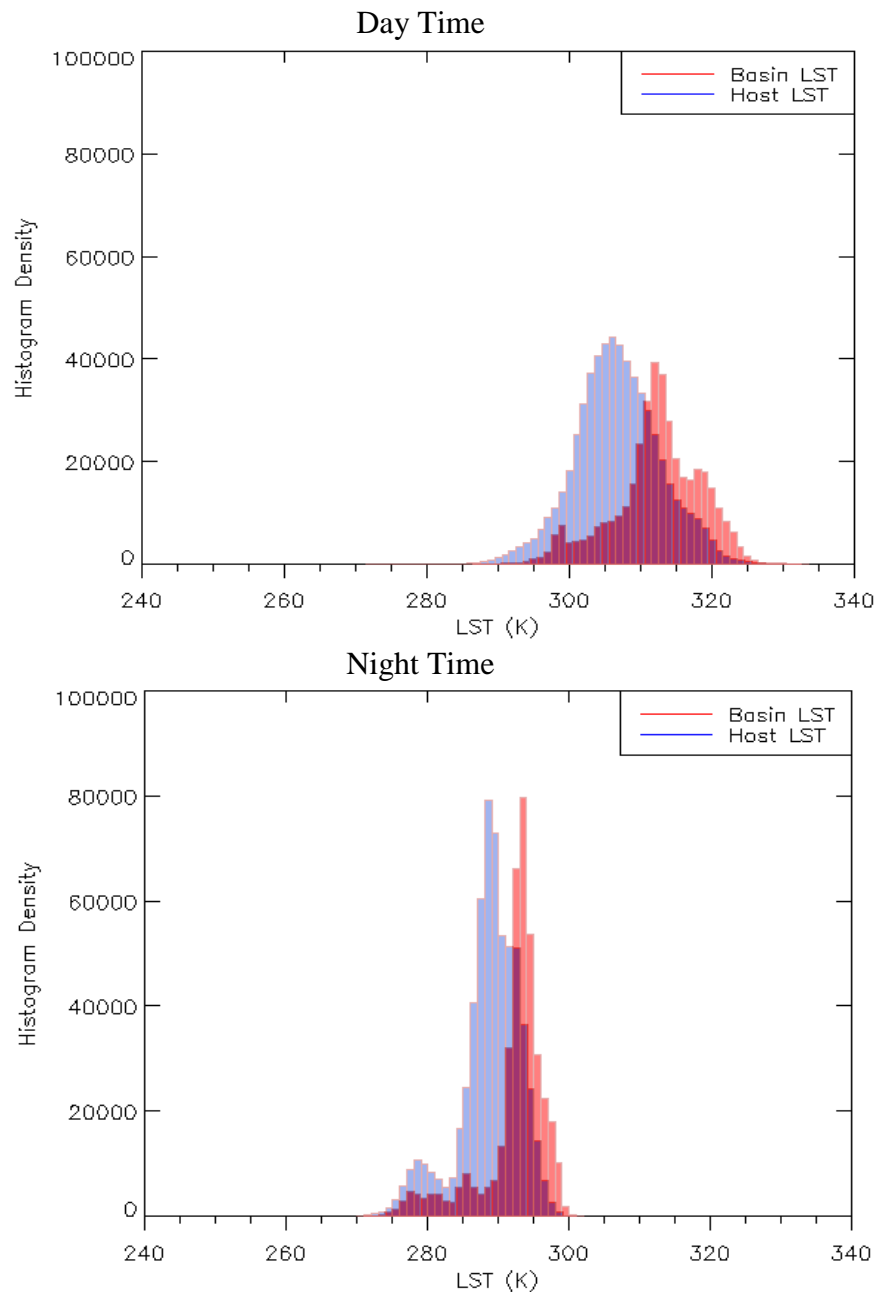


*Figure 72: MODIS LST frequencies of the host rock and basins for the Aqua 2006 night time dataset, across the Turkana region, on a  $10^{\circ} \times 10^{\circ}$  grid of  $0.01^{\circ}$  resolution.*

minimums are the means of the corresponding maximum and minimum yearly LSTs. Values are provided for night time only as it is expected that the contrast between basins and host will be best observed at this point in time. Data for the year of 2011 has been identified as anomalous, lying beyond the physical limits of LST. Thus this data is likely associated with persistent cloud issues (Table 14).

*Table 14: Mean, maximum and minimum night time yearly MODIS LSTs for the absolute Aqua dataset for host rock to basins, across the Turkana region tile that is a  $10^\circ \times 10^\circ$  grid of  $0.01^\circ$  resolution.*

Year	Host Rock			Basin Rock		
	Mean LST (K)	Maximum LST (K)	Minimum LST (K)	Mean LST (K)	Maximum LST (K)	Minimum LST (K)
2003	289.1	300.6	269.9	292.4	301.4	270.9
2004	288.8	300.5	268.8	292.2	301.4	271.2
2005	289.0	300.6	269.4	292.5	301.5	270.7
2006	288.8	300.3	270.1	292.2	301.7	271.0
2007	288.8	301.0	270.1	292.2	301.6	270.6
2008	288.7	300.5	269.7	292.0	301.7	269.5
2009	289.3	301.8	265.3	292.7	302.5	270.9
2010	289.1	301.7	267.2	292.7	302.1	271.3
2011	288.4	301.4	229.1	292.5	302.2	247.6
2012	288.8	301.1	269.6	292.2	301.4	270.7
2013	288.9	301.2	269.0	292.3	301.7	270.3

The LST data displays a difference between host rock and basin LST means; though this is often subtle. For the absolute LSTs, the host rock ranges between 288 K and 289 K whilst the basin rock is approximately 292 K throughout, resulting in a difference of 3 K to 4 K dependent upon the year. The accuracy of this however, is not known and further uncertainty analysis is required to be propagated to the LST averages from the daily uncertainty product. Given however, that the LST retrieval aims for an accuracy of 1 K, it could be possible that this basin-host rock difference is reduced, making them less distinguishable than present.

Additional tiles have also been analysed to determine whether basins and host rock are distinguishable elsewhere. All show that basins are distinguishable with respect to the host rock. The Lake Victoria tile is now presented as an example (Figure 73). Plots of the remaining tiles are found in Appendix 6, with corresponding normalised plots discussed later in Chapter 4. In the Lake Victoria tile, the warmest absolute LSTs are observed immediately east of Lake Victoria; in the Magadi Trough. LSTs of a similar

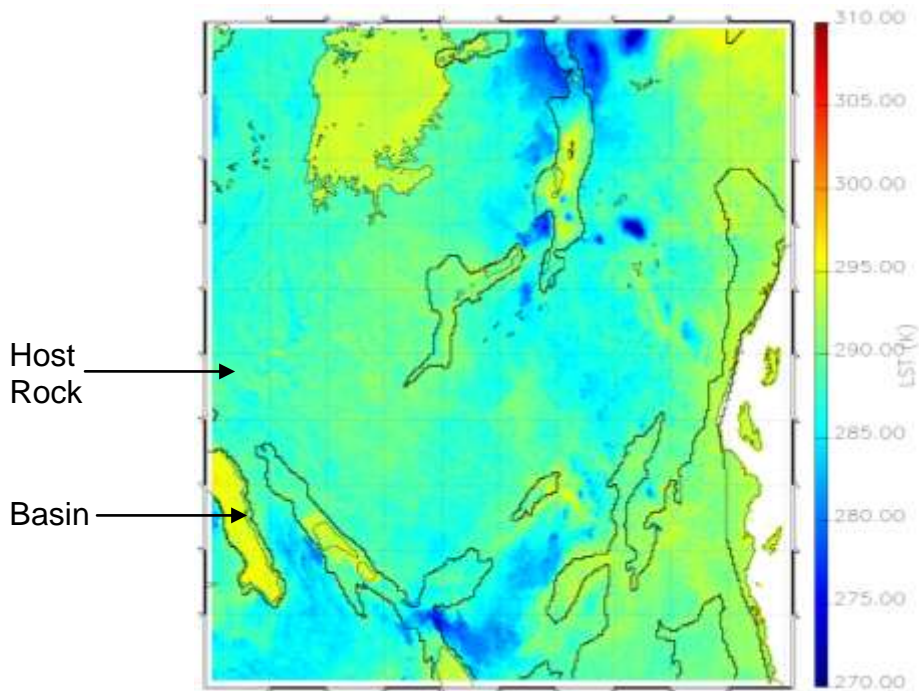


*Figure 73: The 10° x 10° Lake Victoria tile of 0.01° resolution, for 2006 night time MODIS LSTs for the Aqua dataset. Basin outlines are overlain (thicker black lines), as supplied from Tullow Oil plc and as described previously in Chapter 3.1.4.*

magnitude are also found within the southernmost extent of the Suguta Valley, where cooler regions mark the basin outline. To the southwest, basin boundaries are evident from the LSTs, particularly so for the lake filled based of Rukwa and Tanganyika. An anomaly with respect to the surroundings is noted to exist at the intersection between the Rukwa, Usangu and northern Malawi basins. This is a likely the effect of higher elevations at the intersection of the basins. LSTs of this magnitude are not typically observed within basins; although where they are, such as the Afar region, they are often elevation associated.

LST frequencies for the Lake Victoria tile and all additional tiles included in the Appendix 6 were also considered. The results from these histograms display similar trends to Turkana region. Marginal positive shifts in the peak of the absolute LST distribution of basin rock are noted. This suggests that the basin LSTs for the absolute dataset are warmer than the host rock.

### 4.2.1 Specific Basins

Having identified the correspondence of basins and warmer LSTs, a more localised approach is now taken. This is important to determine the warmth of specific basins with respect to the host rock. Moreover, initial analysis of LST influencing parameters is considered, by studying the relative altitude dependence of the host rock and basins. This is important as it will be necessary to understand the LST components in order to highlight the variance that may be attributable to geothermal activity.

Individual basins are now compared relative to each other and the host rock average, looking at the relative altitude dependence. Figure 74 displays the absolute LSTs of host rock in the Turkana tile. Pearson correlation coefficients and gradients of the night time yearly host rock and basins LSTs within the Turkana tile are found in Table 15. Initial results reveal the known inverse relationship between elevation and LST (Saraf et al., 2005; Miliareisis, 2009), which is discussed in more detail later in Chapter 5.

The first basins analysed are the West Lokichar, Lokichar and Turkana, which are located southwest of Lake Turkana (Figure 75) and have been selected due to known

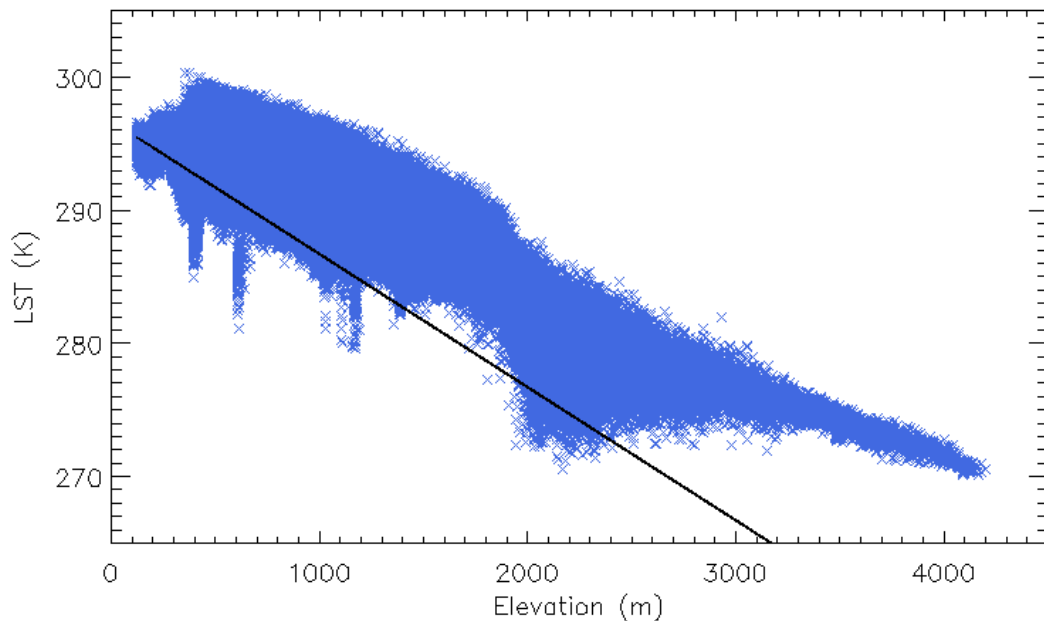


*Figure 74: Absolute host rock MODIS LSTs with respect to original elevation for the 2006 Aqua night time yearly mean. Data is taken from the Turkana region tile, which is  $10^{\circ} \times 10^{\circ}$  grid of  $0.01^{\circ}$  resolution. The line of best is fitted according to the density distribution of the pixels.*

Table 15: Pearson correlation coefficients and gradients for the Turkana tile basins. MODIS LSTs are from the Aqua dataset for night time 2006. The intercept shows the mean of the rock at 0 m elevation.

Region	Central coordinates of basin		Absolute LSTs ( $y = mx + c$ )		R
	Latitude ( $^{\circ}$ N)	Longitude ( $^{\circ}$ E)	Gradient	Intercept	
Adama	8.86	39.84	0.00	293.49	-0.50
Afar	10.06	39.84	-0.01	299.17	-0.94
Albertine	1.75	30.86	0.00	292.13	-0.06
Anza	2.27	38.22	0.00	295.98	-0.01
Gatome	4.38	35.30	0.02	283.29	0.65
Host	-	-	-0.01	296.71	-0.09
Lake Edward	-0.38	29.73	0.01	281.90	0.31
Lokichar	2.71	35.77	0.00	299.71	-0.35
Lotikipi East	3.20	35.24	0.05	260.46	0.08
Lokichar West	2.19	35.39	0.00	294.91	-0.66
Melut	8.93	33.27	-0.02	301.32	-0.26
Melut East	9.55	33.58	0.00	294.51	-0.10
Melut West	7.26	32.72	0.00	291.61	0.29
Mongalla	5.50	32.18	0.00	294.29	-0.13
Pibor Post	6.90	33.56	-0.08	327.90	-0.31
Remnant Bugiri	0.56	33.73	-0.01	296.39	-0.23
Remnant Dagusi	0.15	33.57	0.02	283.31	0.65
Remnant Entebbe	0.06	32.45	-0.01	296.42	-0.23
South Kerio	0.81	35.69	-0.01	304.93	-0.95
Suguta	0.91	36.17	-0.01	302.91	-0.94
Turkana	4.55	36.08	-0.01	297.31	-0.32

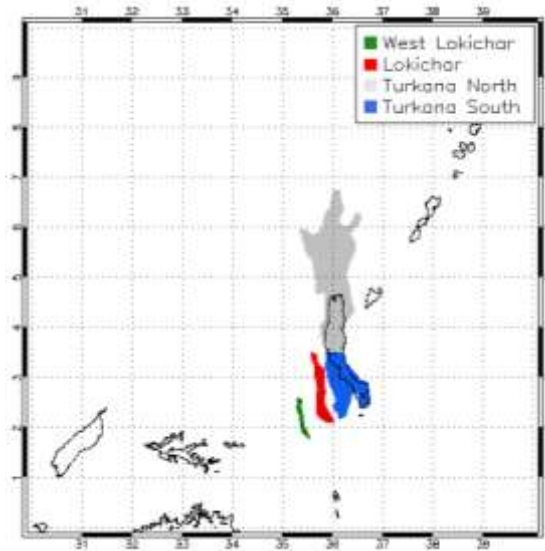


Figure 75: West Lokichar, Lokichar and Turkana basins are highlighted, as taken from the basin outlines supplied by Tullow Oil plc, as described in Chapter 3.1.4.

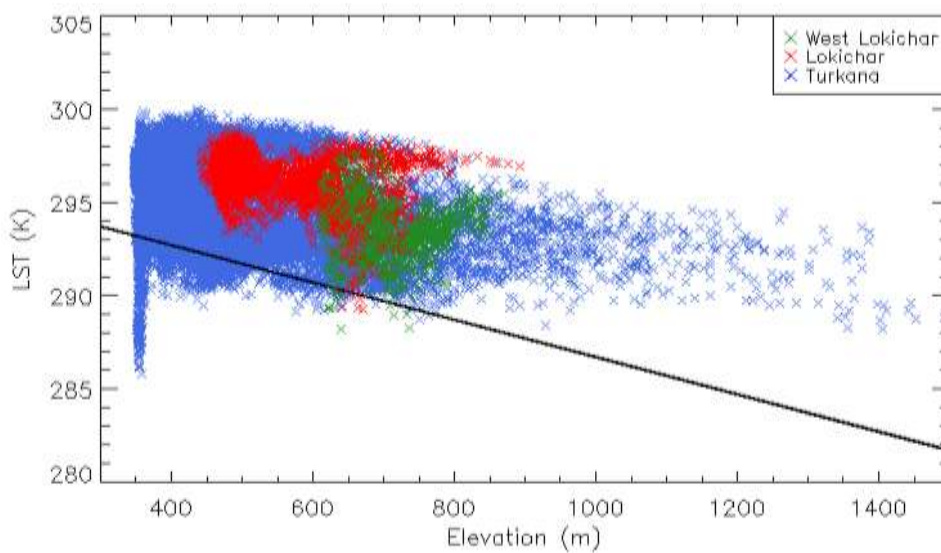


Figure 76: West Lokichar, Lokichar and Turkana basins: Elevation versus absolute MODIS, 2006 night time LSTs from the Aqua dataset. The black line refers to the host rock average. Data is taken from within the Turkana region tile, which is  $10^{\circ} \times 10^{\circ}$  grid of  $0.01^{\circ}$  resolution.

hydrocarbon prospects and geothermal activity within the area (Omenda, 1998) (Figure 12). From Table 15, the West Lokichar Basin shows moderate to strong correlations between LST and elevation, indicating strong elevation dependence. Lokichar and Turkana instead display moderate to weak correlations, suggesting lower elevation

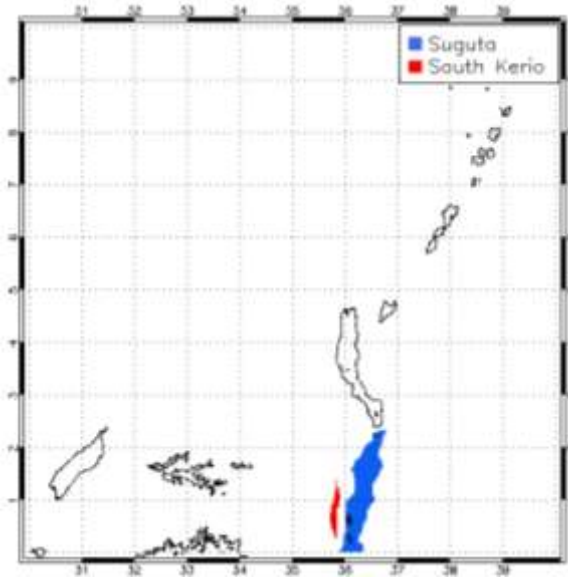


Figure 77: Locality of Suguta and South Kerio basins within the Turkana region tile, supplied by Tullow Oil plc as detailed in Chapter 3.1.4.

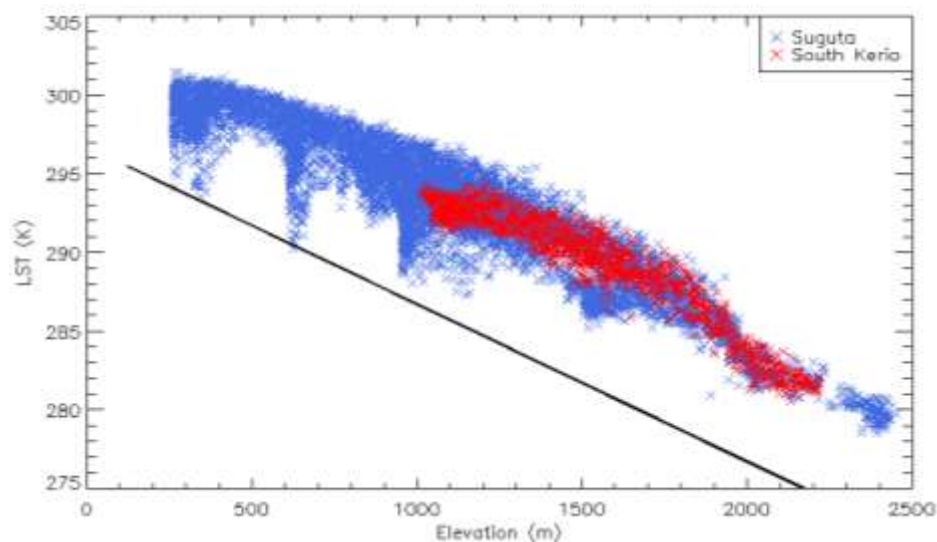


Figure 78: Absolute Aqua 2006 night time MODIS LSTs for the Suguta and South Kerio basins. The black line refers to the host rock average. Data is taken from within the Turkana region tile, which is  $10^\circ \times 10^\circ$  grid of  $0.01^\circ$  resolution.

dependence. LSTs of the West Lokichar, Lokichar and Turkana basins are found to lie above the host rock average (Figure 76).

Additional basins studied include the Suguta and South Kerio basins (Figure 77), again due to known geothermal activity and hydrocarbon prospects, as discussed in Chapter 1 (Figure 12 and Figure 17). In line with expectations, both basins lie above the host rock

average (Figure 78). Both basins show strong, negative Pearson correlations. These strong correlations are the greatest observed throughout the basins (along with the Afar). This is not surprising given the Suguta Basin contains the Suguta Valley which lies at less than 500 m. The Afar Depression has also been analysed and is expected to be one of the warmest regions due to active sea floor spreading (Figure 79). From Figure 80, it is clear that the data matches expectations with the Afar lying above the host rock average. In terms of its Pearson correlation coefficient, the Afar LST is strongly associated with elevation.

Further to the basins displayed, the Albertine and Edward basins have also been analysed (Figure 81). Both basins are found to straddle the average of the host rock, suggesting little overall difference. This is unexpected given the known hydrocarbon prospects within the Albertine rift (Figure 12). This is potentially the result of only parts of the basins analysed and as a consequence of data being skewed by the water bodies present. Pearson correlation coefficients for the two basins reveal little elevation dependence, which is again unexpected.

Figure 81 now displays the average of the basins discussed within this section. From this plot, it is clear that the Afar is warmer than the Turkana Basin but cooler than the Suguta and South Kerio basins. In addition to the Albertine and Edward basins, the Lokichar and West Lokichar are also found to depend little on elevation effects. This may arise from potential edge effects within the dataset; alternatively this may also be the result of ineffectively masked water bodies. When the entirety of the region is accounted for in terms of basins and host rock, as in Table 15, it is clear that only the five basins observed as warmer in Figure 81 along with the Melut Basin, are warmer than the average of the host rock.

#### **4.2.2 Discussion**

Host rock-basin comparisons return the focus of this study to the geology of the area. Absolute LSTs show concordance with basin perimeters, hinting at LST elevation

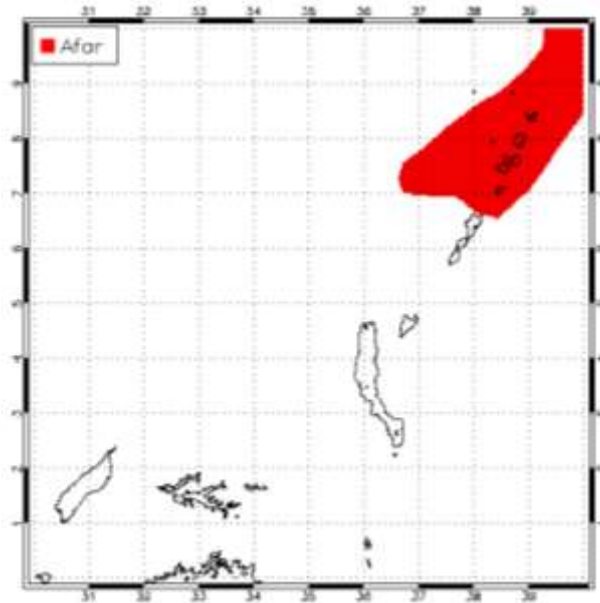


Figure 79: Locality of the Afar Basin highlighted within the Turkana region tile. Basin outlines have been supplied from Tullow Oil plc, as described in Chapter 3.1.4.

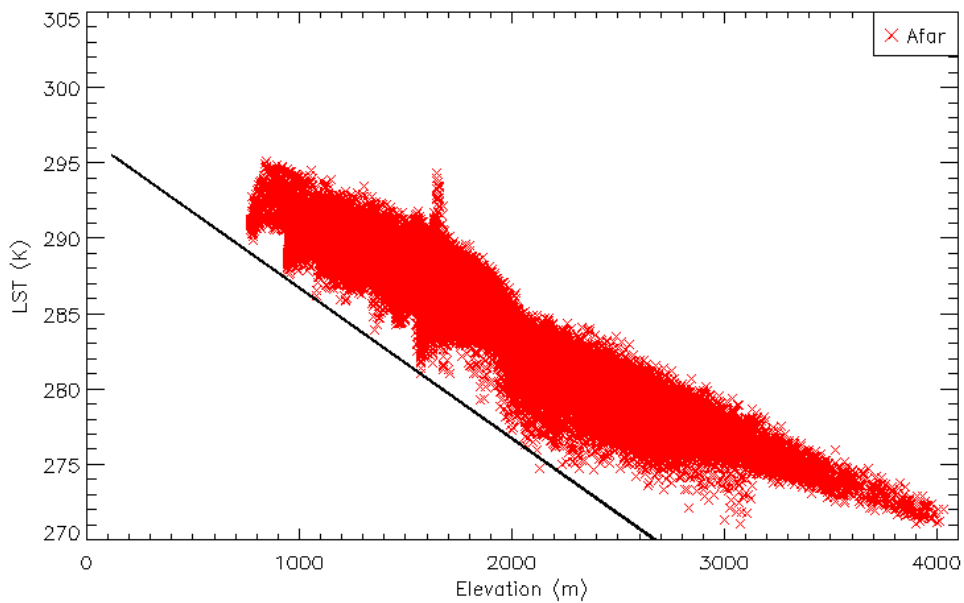


Figure 80: Absolute 2006 night time MODIS LSTs, taken from the Aqua dataset, for the Afar Basin. The black line refers to the host rock average. Data is taken from within the Turkana region tile, which is  $10^{\circ} \times 10^{\circ}$  grid of  $0.01^{\circ}$  resolution.

relationships. The presence of this relationship suggests that the absolute LSTs may in fact not image geothermally associated anomalies but simply reflect the elevation driven thermal anomalies as a consequence of low lying basin topography due to rift associated subsidence. Although this is not of use for the identification of geothermal anomalies,

the analysis with respect to the host rock does provide a means of highlighting basins remotely from satellite-derived data; which is particularly useful for mapping broad and extensive regions, such as the EARS, whereby basins are not always outlined, such as the Chew Bahir Basin, northeast of Lake Turkana.

The six basins noted as warmer than the average host rock across the entire Turkana tile are as follows in descending order: South Kerio, Suguta, Melut, Lokichar, Afar and Turkana. This is particularly pleasing to see the warmer LSTs of the South Kerio, Suguta, Lokichar and Turkana basins, given the previously noted geothermal activity and hydrocarbon prospects (Dunkley et al. 1993; Lagat, 2010) (Figure 12 and Figure 17).

The Afar region is again warmer, as expected; although given that the region is a current site of active sea floor spreading, the LSTs recorded may in fact be lower than the 'real' maximum LSTs. This is potentially the result of only the southernmost extent of the basin lying within the Turkana tile. Had this been applied to the entire basin, spanning the Afar Triangle, it is likely that LSTs would be warmer.

The presence of the Melut Basin as warmer than the host rock, is perhaps surprising given all other adjacent basins are much cooler. However, this can be explained by the known presence of hydrocarbons within the region (Dou et al., 2007), which ultimately require increased geothermal gradients as discussed in Chapter 1.1.4.

A number of limitations exist within this study and include the presence of lake filled basins. Masking of the water bodies has been applied when studying specific basins, though this does not fully resolve the issue, as is likely the case for the Albertine Basin. All lake filled basins should thus be viewed with caution due to the additional parameters that affect the water surface temperature. Additional limitations also include the potential absence of data, with several basins including Edward and the Afar Depression lying only partially within the Turkana tile. Results are likely to be skewed as a consequence of this. Within the Turkana region, basin coverage is 39.5 % of the total  $10^{\circ} \times 10^{\circ}$  grid tile.

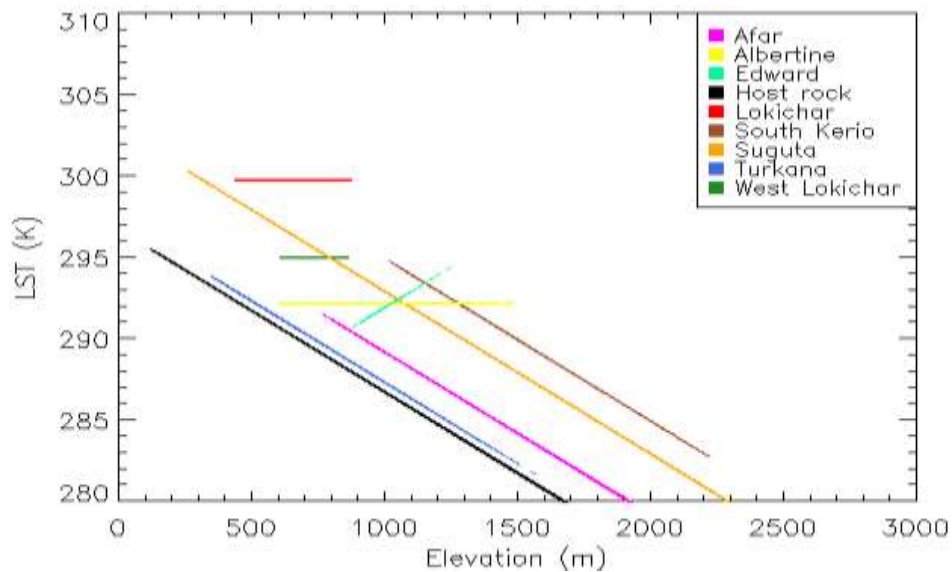


*Figure 81: Average 2006 night time, MODIS LSTs versus elevation for the host rock and basins of interest as discussed within the text. Data is taken from within the  $10^{\circ} \times 10^{\circ}$  grid of the Turkana region tile of  $0.01^{\circ}$  resolution. MODIS LSTs originate from the Aqua dataset. Above shows a Google Earth (2016) image identifying the locality of the basins noted.*

In summary of this section, it can be concluded that this approach fully confirms that basins can be remotely sensed by satellite-derived absolute LSTs. This therefore fulfils one of the main objectives of this thesis: to remotely identify the locality of hydrocarbon basins within the East African Rift system. However caution must be taken when determining the variables behind the LST signal as it is likely that basin are identified based upon topography, rather than the presence of elevated geothermal gradients. The study is now advanced by analysing and thus delineating several variables thought to contribute to the LST signal.

### **4.3 Full Principal Component Analysis**

Full PCA, using five variables, is now applied to the LST dataset on a monthly basis via the steps described in Figure 43. This is completed with the aim of delineating several of the known variables that impact LST, such as the effects of elevation that were noted in the previous section. The five variables applied include elevation, emissivity in two infrared channels, tcwv and fv (Figure 44).

#### **4.3.1 Spatial Variation**

The following display two day and night examples of the five variables PCA as applied to the absolute LSTs across the Turkana for June and December 2006. The magnitudes of PC scales vary to best illuminate the features. This is dependent upon time of day and month. All principal components, from PC1 to PC5, are considered. The smaller principal components are expected to be the PCs in which geothermal anomalies are most visible due to the lesser effects of other variables. Several features including the Turkana Depression and Ethiopian Dome are persistent throughout as in the absolute LSTs. The PCA is additionally still capable of resolving finer features such as the Turkwel River.

For the LSTs the majority of variability (94 % in all cases) is accounted for within the first three components (Figure 82 to Figure 85 and Table 16 to Table 19). A number of patterns are identified across the PCs, regardless of diurnal effects; though this is not confirmed for all years. One recurring pattern is that emissivity channels 1 and 2 are generally simultaneous and strongly associated with PC1. Fv is typically associated with PC3 and tcwv with PC4. Tcwv is often of a similar magnitude to elevation for PC4. The effects of elevation are strongly associated with PC2, PC4 and PC5 and are clearly significant. Component loadings temporal variation is discussed later.

Table 16: PCA results for the Turkana region of MODIS LST Aqua data for June 2006 day time. The Turkana region is a  $10^{\circ} \times 10^{\circ}$  grid of  $0.01^{\circ}$  resolution.

Component	Eigenvalue	Variance (%)	Cumulative (%)	Component Loadings				
				Elevation	Emissivity 1	Emissivity 2	tcwv	fv
1	2.50	49.32	49.32	0.01	0.87	0.82	0.53	0.55
2	1.72	33.89	83.20	0.76	-0.17	-0.10	-0.61	0.51
3	0.58	11.41	94.61	0.29	-0.62	-0.66	-0.55	-0.76
4	0.18	3.54	98.14	-0.75	-0.60	-0.51	0.73	-0.23
5	0.09	1.86	100.00	0.76	0.72	0.82	-0.42	0.57

Table 17: PCA results for the Turkana region of MODIS LST Aqua data for June 2006 night time. The Turkana region is a  $10^{\circ} \times 10^{\circ}$  grid of  $0.01^{\circ}$  resolution.

Component	Eigenvalue	Variance (%)	Cumulative (%)	Component Loadings				
				Elevation	Emissivity 1	Emissivity 2	tcwv	fv
1	2.42	47.55	47.55	-0.01	0.87	0.82	0.57	0.54
2	1.75	34.47	82.02	0.76	-0.17	-0.09	-0.59	0.53
3	0.62	12.10	94.12	0.35	-0.57	-0.61	-0.60	-0.75
4	0.20	3.88	98.00	-0.69	-0.58	-0.48	0.71	-0.17
5	0.10	2.00	100.00	0.76	0.68	0.81	-0.40	0.54

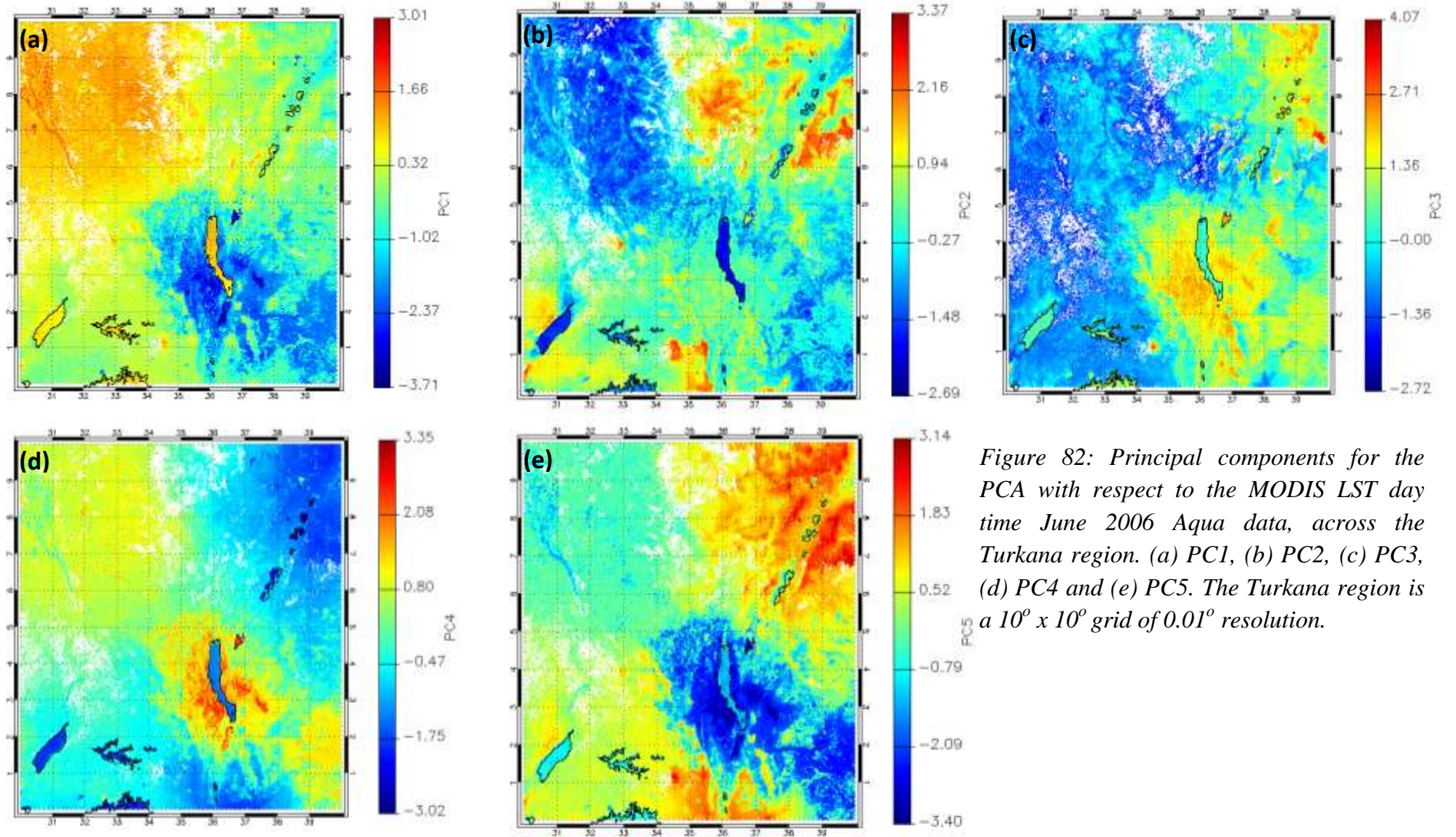


Figure 82: Principal components for the PCA with respect to the MODIS LST day time June 2006 Aqua data, across the Turkana region. (a) PC1, (b) PC2, (c) PC3, (d) PC4 and (e) PC5. The Turkana region is a  $10^{\circ} \times 10^{\circ}$  grid of  $0.01^{\circ}$  resolution.

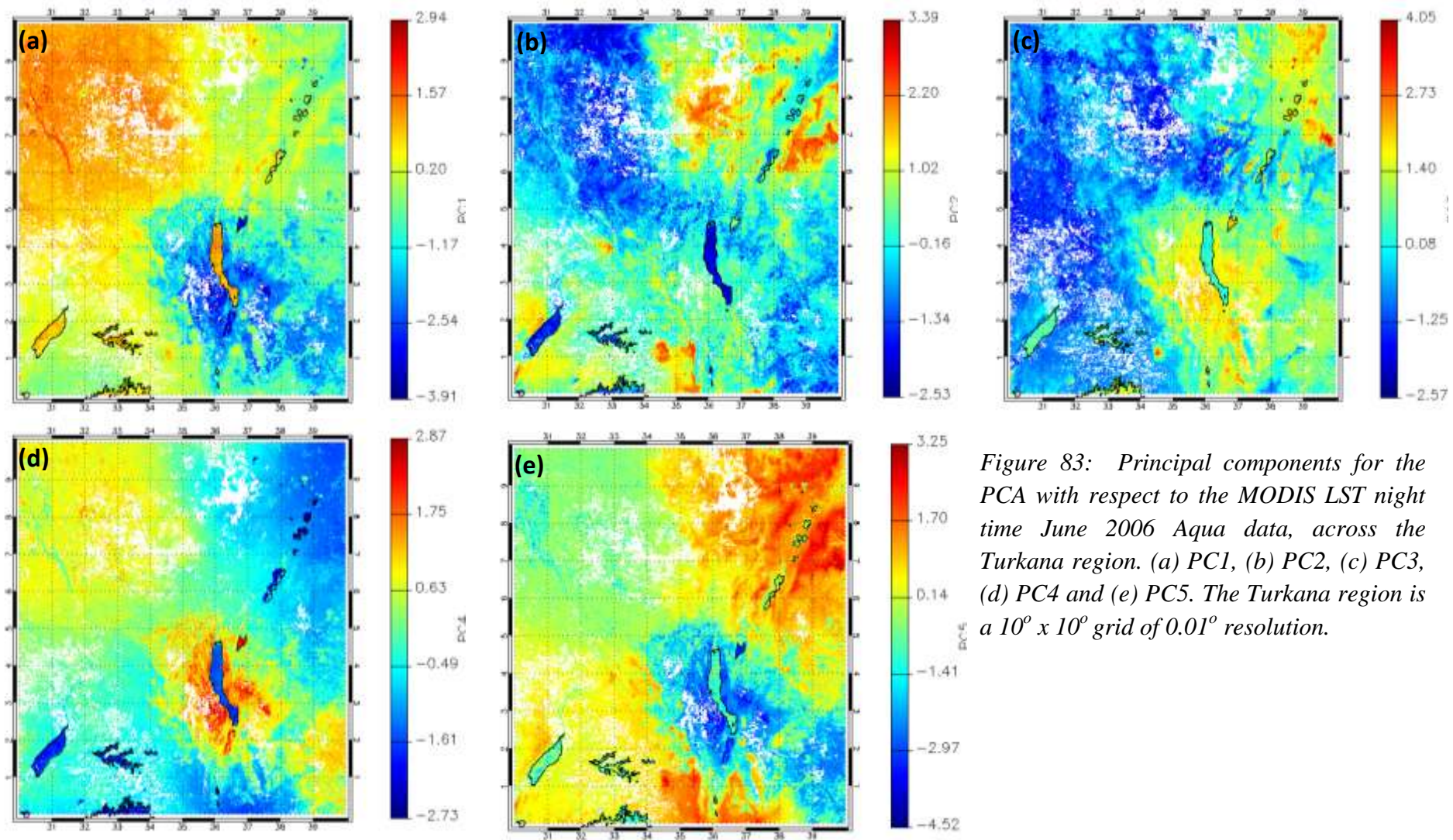


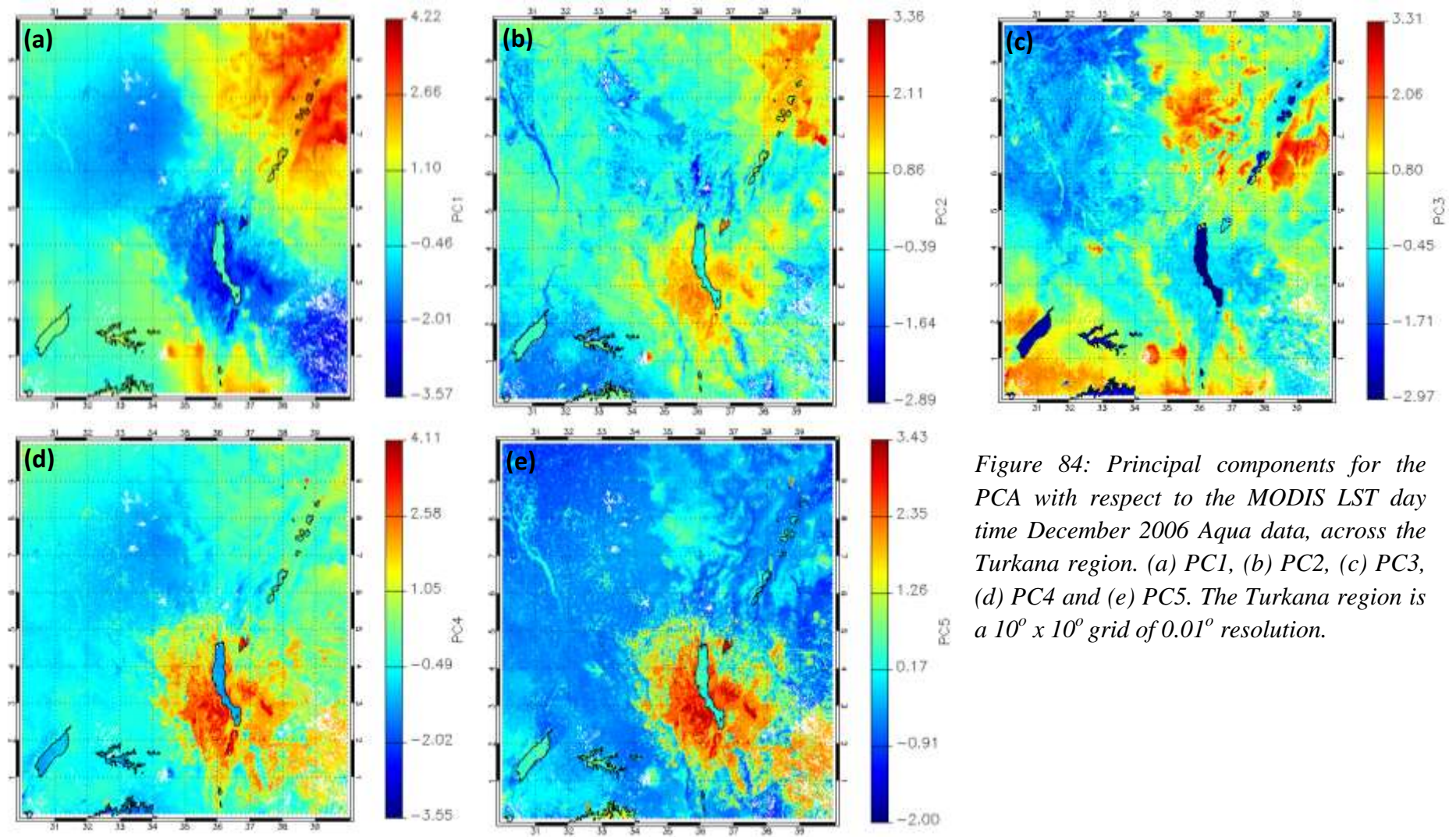
Figure 83: Principal components for the PCA with respect to the MODIS LST night time June 2006 Aqua data, across the Turkana region. (a) PC1, (b) PC2, (c) PC3, (d) PC4 and (e) PC5. The Turkana region is a  $10^\circ \times 10^\circ$  grid of  $0.01^\circ$  resolution.

Table 18: PCA results for the Turkana region of MODIS LST Aqua data for December 2006 day time. The Turkana region is a  $10^{\circ} \times 10^{\circ}$  grid of  $0.01^{\circ}$  resolution.

Component	Eigenvalue	Variance (%)	Cumulative (%)	Component Loadings				
				Elevation	Emissivity 1	Emissivity 2	tcwv	fv
1	2.31	47.03	47.03	0.88	0.49	0.49	-0.88	0.29
2	1.49	30.30	77.33	0.30	-0.42	-0.37	-0.47	-0.70
3	0.86	17.48	94.82	0.69	-0.07	0.08	-0.37	0.86
4	0.17	3.42	98.24	-0.06	-0.90	-0.87	-0.25	-0.28
5	0.09	1.76	100.00	-0.10	-0.88	-0.98	0.12	-0.27

Table 19: PCA results for the Turkana region of MODIS LST Aqua data for December 2006 night time. The Turkana region is a  $10^{\circ} \times 10^{\circ}$  grid of  $0.01^{\circ}$  resolution.

Component	Eigenvalue	Variance (%)	Cumulative (%)	Component Loadings				
				Elevation	Emissivity 1	Emissivity 2	tcwv	fv
1	2.30	45.82	45.82	-0.21	-0.69	-0.60	0.59	0.03
2	1.53	30.48	76.31	0.69	0.49	0.50	-0.34	0.85
3	0.90	17.92	94.23	0.46	0.41	0.29	-0.56	-0.56
4	0.19	3.67	97.90	-0.62	0.58	0.52	0.72	-0.07
5	0.11	2.10	100.00	0.65	0.75	0.87	-0.54	0.39



*Figure 84: Principal components for the PCA with respect to the MODIS LST day time December 2006 Aqua data, across the Turkana region. (a) PC1, (b) PC2, (c) PC3, (d) PC4 and (e) PC5. The Turkana region is a 10° x 10° grid of 0.01° resolution.*

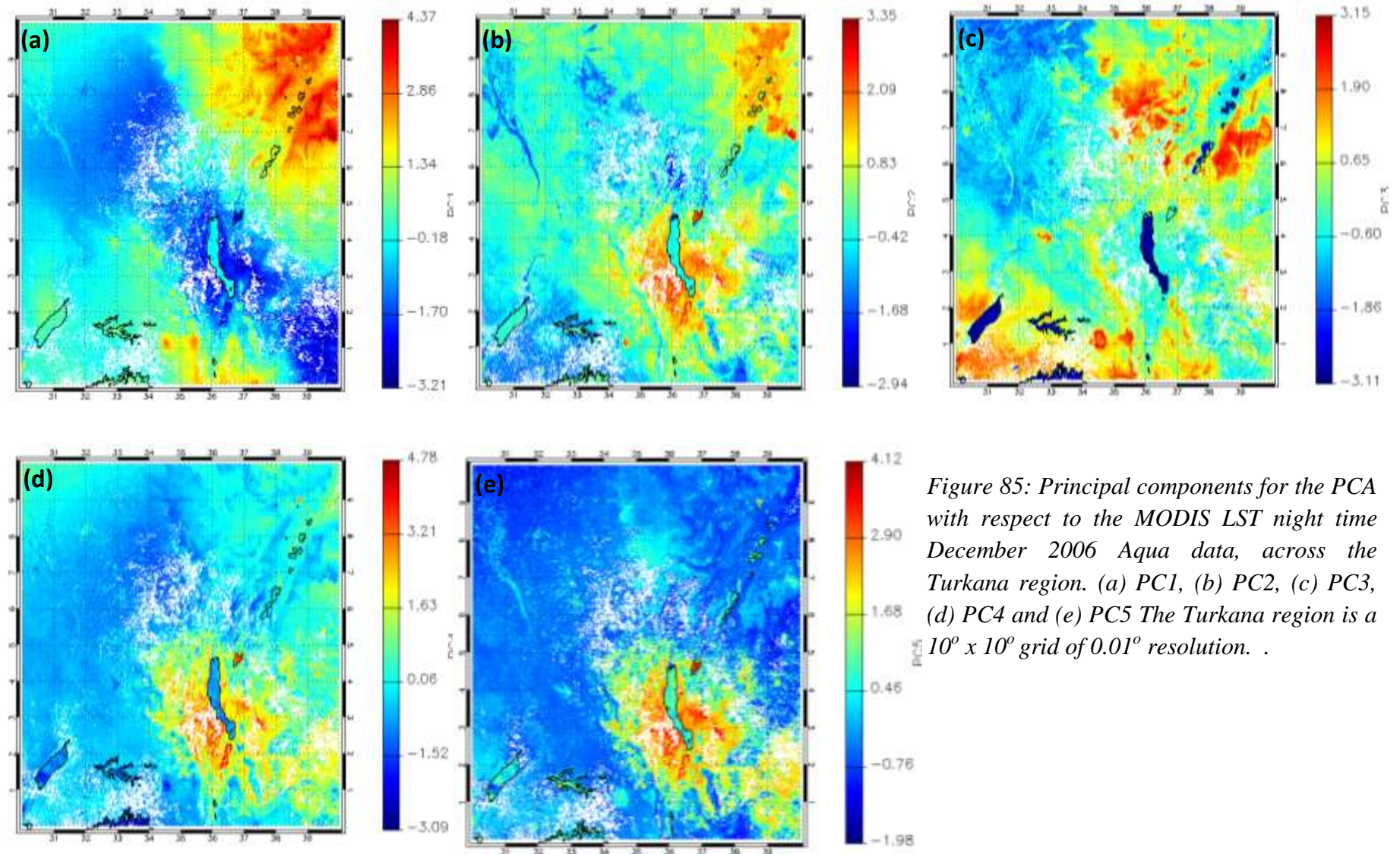
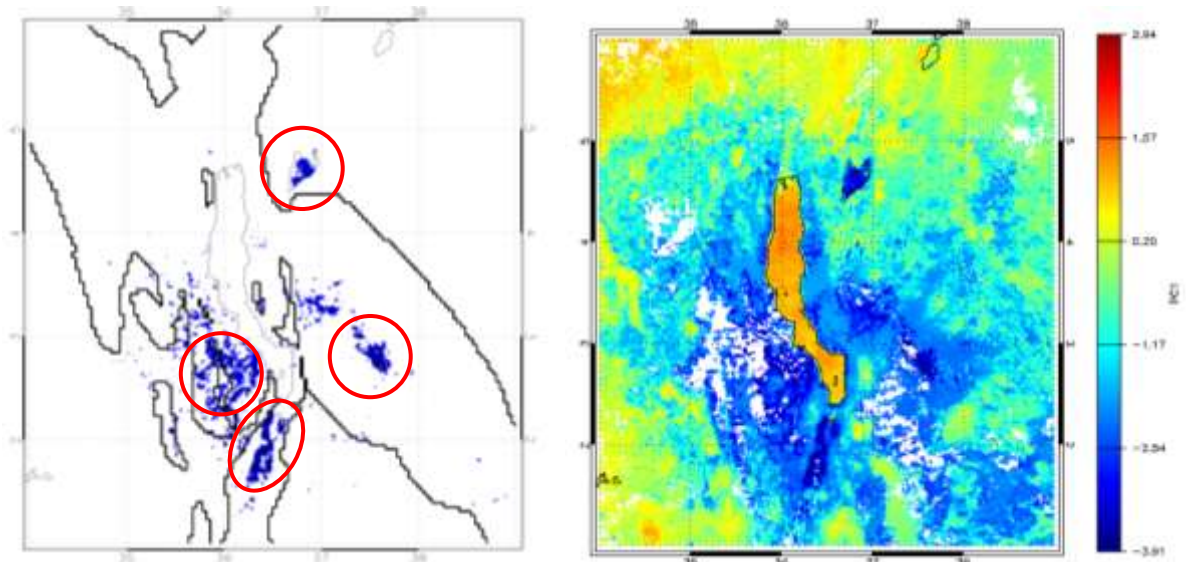


Figure 85: Principal components for the PCA with respect to the MODIS LST night time December 2006 Aqua data, across the Turkana region. (a) PC1, (b) PC2, (c) PC3, (d) PC4 and (e) PC5 The Turkana region is a  $10^\circ \times 10^\circ$  grid of  $0.01^\circ$  resolution. .



*Figure 86: Example of anomalies in PCI night time June 2006 as highlighted by low component loadings representing the emissivity channels 1 and 2 is shown to the right. The component loadings here are generated with respect to the MODIS LST 2006 June night time data as taken from the Aqua dataset, across the  $10^{\circ} \times 10^{\circ}$  grid of the Turkana region at  $0.01^{\circ}$  resolution. The four main anomalous areas, where by the PC is less than -3 are isolated and displayed to the left.*

Spatially, several points of interest are consistent with regions of warmer and cooler LSTs are observed in the PCA (Figure 86), of which the most consistent is the geothermally active Suguta Valley. A second anomalous area is located to the west, crossing over basin the Lokichar and Turkana basins. A third anomaly is situated in south of Turkana in the low lying Chalbi Desert and a fourth within in the Chew Bahir Basin to the northeast. Similar features are identified via various component loadings throughout the PCAs from January 2003 to December 2013.

The anomalous features are now isolated into four sub groups (Figure 86), which from clockwise starting in the north are the Chew Bahir Basin, Chalbi Desert, Suguta Valley and Lokichar-Turkana basin areas. Considering elevation to be a potentially key factor, the anomalies are further analysed by via linear regression analysis of 2006 night time yearly LSTs and elevation for the regions of the anomaly (Table 20). Strong, negative Pearson correlation coefficients are noted for all. Gradients are as previous when studying the whole Turkana region. For all subgroups LST at 0 m is higher for basins

Table 20: Gradients and Pearson correlation correlations for anomalous areas as identified from PCA. Absolute LSTs are from the Aqua MODIS dataset for the night time of 2006 across the region indicated in blue within Figure 86.

Region identified from PCA	Absolute LSTs (i.e. LSTs with elevation) ( $y = mx + c$ )		R
	Gradient ( $\text{Km}^{-1}$ )	Intercept (K)	
Chalbi Desert	-0.01	301.93	-0.99
Chew Bahir Basin	-0.01	303.47	-0.99
Host	-0.01	296.71	-0.09
Lokichar-Turkana Basin Area	-0.01	303.36	-0.98
Suguta Valley	-0.01	301.21	-0.99

than the host rock (Figure 87). The deviations of the anomalies away from the host rock average are of a similar magnitude to warmer basins that are similarly elevation dependent (Figure 81). In essence, mapping LSTs as a function of elevation reveals some regions which are significantly warm, whilst highlighting elevation as a factor to be taken into account. Elevation effects may thus obscure geothermal (or other) anomalies. This therefore highlights the importance of delineating the LST signal and consequently, correcting for the contributing variables to reveal the unexplained variance that may be related to geothermal anomalies, as opposed to thermal anomalies.

#### 4.3.2 Temporal Variation

Having identified that much of the LST variance can be explained by the known factors, it was interesting to understand the temporal explanation of the PCA factors. Such variations are applied across the Turkana region for the years starting January 2005 and ending December 2008 (Figure 88). A number of periodic patterns are noted and are found to vary across the principal components. Overall the patterns between day and night remain consistent, though distinct disparity is visible at times. In all datasets patterns are less distinct between end 2007 and start 2008.

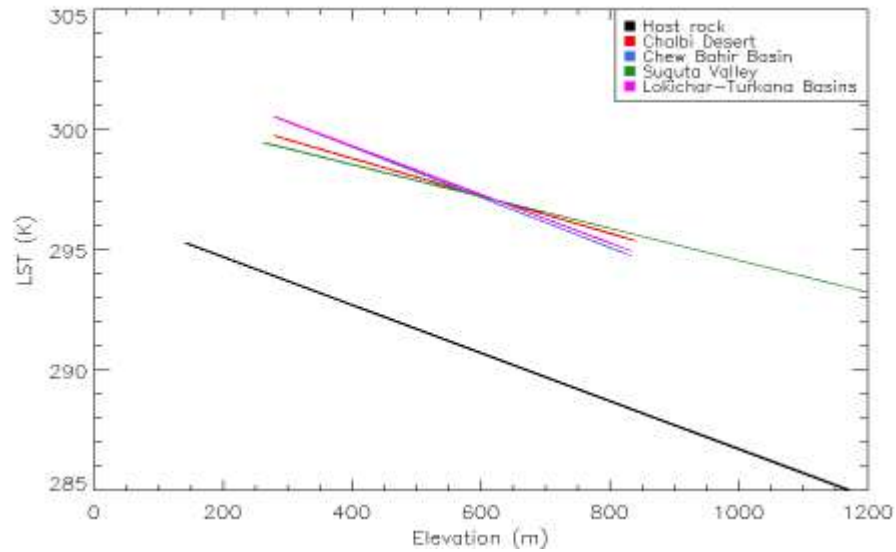


Figure 87: Elevation versus MODIS LSTs for night 2006, as taken from the Aqua dataset, for anomalies highlighted by PCA. The host rock line is generated from the host rock average LSTs within the  $10^{\circ} \times 10^{\circ}$  grid of the Turkana region at  $0.01^{\circ}$  resolution.

For the absolute PC1 dataset the timing of peaks to positive component loadings and dips to negative component loadings are dependent upon variable. All variables are shown to display similar but not identical periodicities, with the exception of the two channels of emissivities which appear to mirror each other throughout. Closely related to the emissivities is the fv which follows a similar cycle, though never reaching the same extremes. Elevation also follows the same approximate cycle but exhibits several additional fluctuations and again never reaches the same extremes as the emissivities. Tcww on the other hand follows the same periodicity in terms of significant changes but does not follow the same cycle of peaks and troughs; acting as a somewhat inverse to elevation.

For PC1, the changes in emissivities and fv occur between April and June, after which the variables peak and then once again change between December and January. For tcww rapid changes typically occur in the November of each year, prior to the changes in emissivity and fv. The tcww change is not consistent throughout. The elevation is almost the inverse of tcww, though not to the same magnitude.

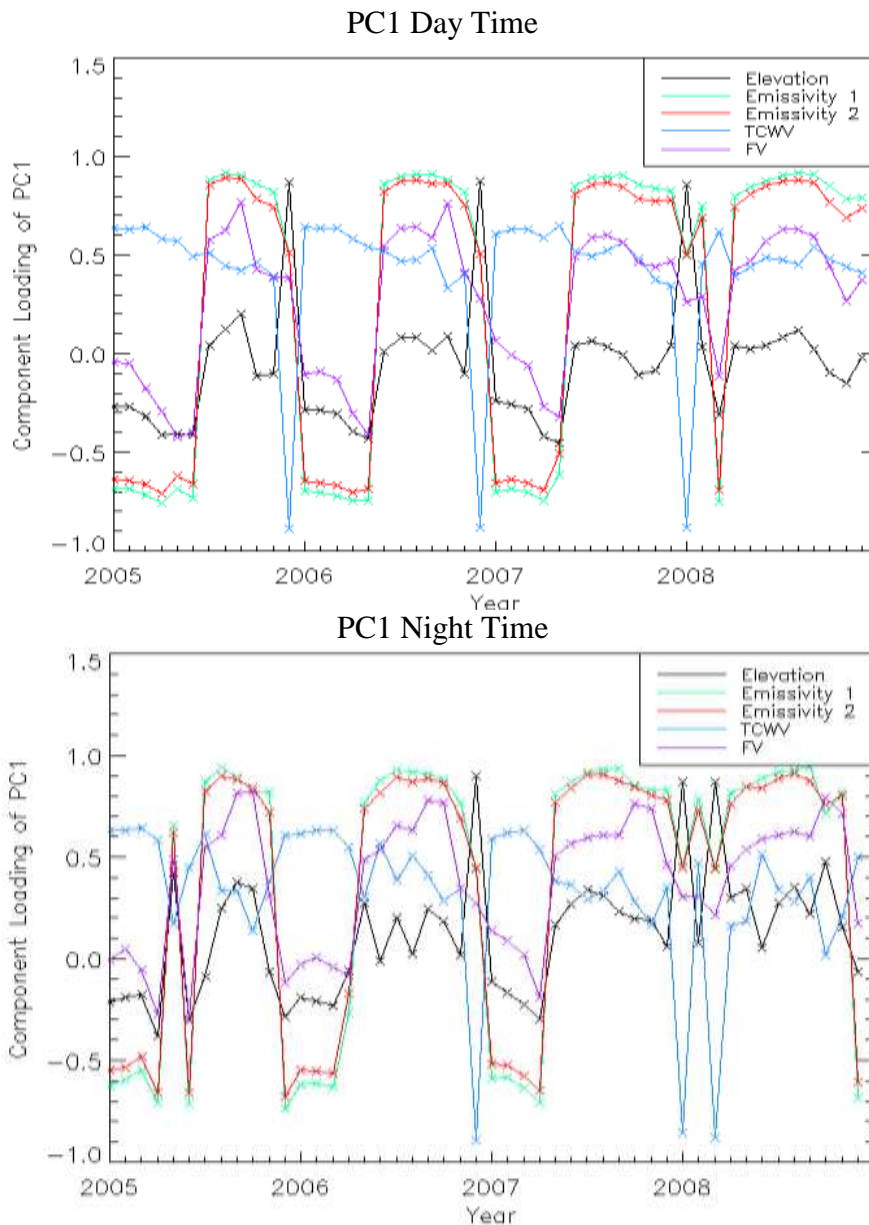


Figure 88: Absolute MODIS LST PC1 component loadings across the Turkana region for the period 2005 to 2008 from the Aqua dataset. The Turkana region is a  $10^{\circ} \times 10^{\circ}$  grid with the EARS of  $0.01^{\circ}$  resolution.

For day and night PC2 through to PC5 similar periodicities are observed (PC2 to PC5 night time are found in Appendix 7). Emissivities throughout mirror each other with fv closely related, with the exception of 2005, 2006 and 2007 for PC2. Elevation shows similarities to emissivity throughout. Tcww is again, inverse to elevation, appearing almost the exact positive mirror of elevation in PC4. Significant decreases in emissivity, fv and elevation component loadings occur between September and November for PC2

and between April and June and then November and January for PC3. For PC4 decreases are not as clear. For PC5 rapid changes in the components loadings occur less periodically but often between December and January of the next year and occasionally between March and April.

### **4.3.3 Understanding the Temporal Variation**

The focus of this PCA now turns to understanding the variables that contribute to the periodicity observed by the component loadings outside of those applied in the PCA. Precipitation from the TRMM dataset is first considered. For both day and night, only tenuous correlations can be drawn between PC1 and precipitation (Figure 89). Potential links exist between peaks in rainfall and decreases in the component loadings of both channels of emissivity, elevation and fv, whilst tcwv increases. However, this is not consistent throughout.

Once again for both day and night, potential relationships are noted throughout PC2 to PC5, though never conclusive. In PC2, peaks in the emissivities appear concurrent with increases in rainfall, whilst elevation and fv continue to display decreases in loadings. The links between precipitation and tcwv are less distinct, though there is an apparent increase in tcwv just preceding increases in rainfall. Further work is necessary to determine whether this potential lag is real. For PC3, the emissivities, elevation and fv show rapid decreases following rainfall peaks. Tcwv displays a similar periodicity to rainfall. For PC4, emissivity and fv show potential increases with increasing precipitation. It is unclear what link, if any, elevation has to the rainfall. Tcwv does not show a distinct link, with a consistent pattern observed throughout the years, whereby it fluctuates at positive loadings before rapidly decreasing at the end of each year. Further work is required to generate specific statistics on the potential relationships, such as the Pearson correlation coefficients between the variables.

Soil moisture content taken from ESA's CCI project is now compared to the component loadings. For PC1 loadings, correlations with soil moisture are identified for both day and night (Figure 89). Periodically rapid transitions in the variables correspond

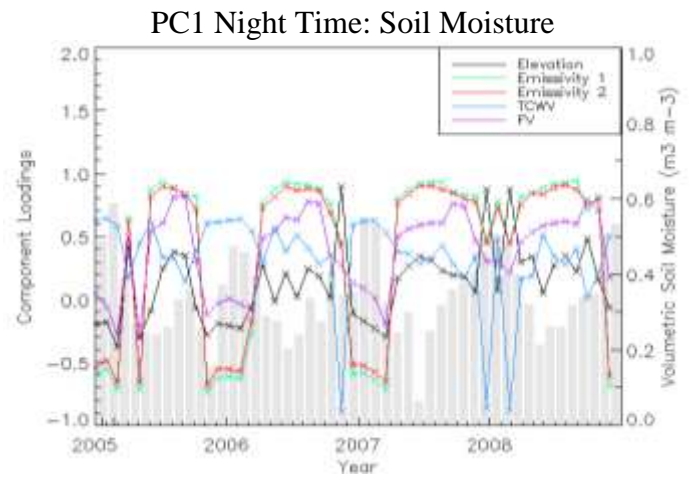
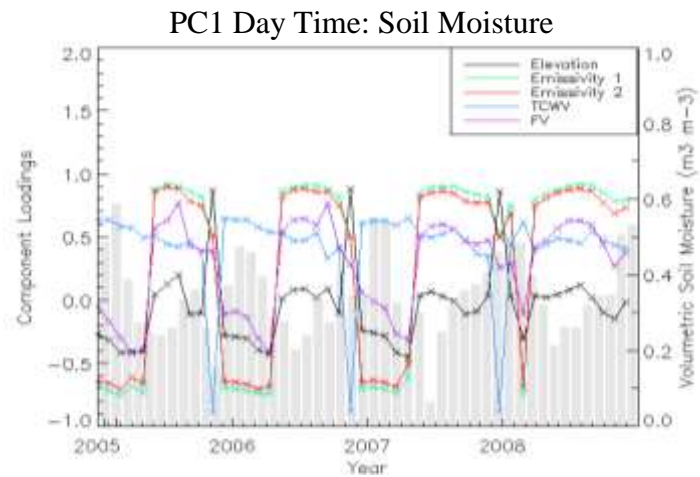
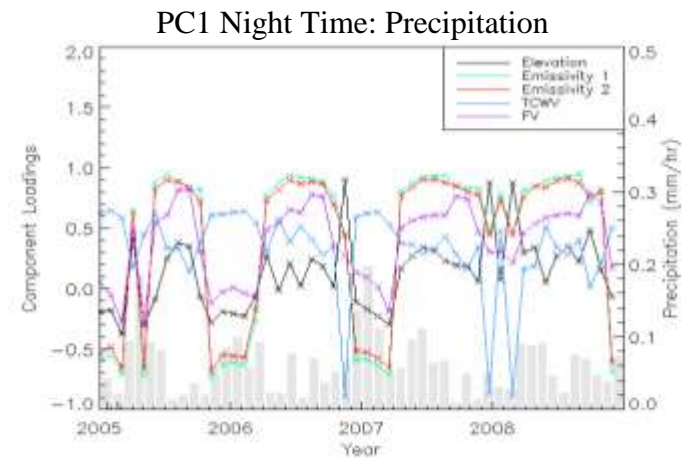
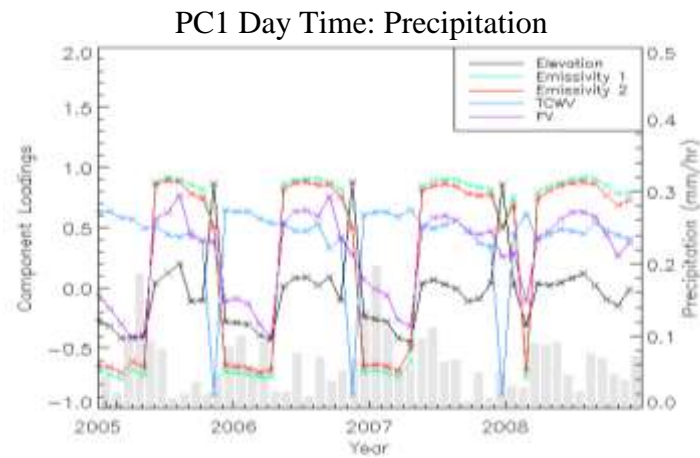


Figure 89: Absolute MODIS LST PC1 component loadings and corresponding TRMM precipitation data and CCI soil moisture data (grey bars) Data is for the  $10^{\circ} \times 10^{\circ}$  grid of Turkana region at  $0.01^{\circ}$  resolution, running from 2005 through to 2008.

to changes in soil moisture. The lag in data should be noted, with transitions in component loadings occurring after changes in the soil moisture. The transitions for PC1 tend to occur between April and June of each year, where the emissivities, fv and elevation increase and then again between November and January, where the variables decrease. Tcwg does not follow this trend but instead follows a consistent periodicity of fluctuating throughout the year before rapid decrease towards the end of year that is consistent with the greatest decrease in soil moisture. The lags identified have not however, been studied in detail. A number of inconsistent features are also noted throughout, including the previously identified end 2007/start 2008 for PC1 loadings of emissivity, fv and elevation.

For day and night time PC2s through to PC5s relationships between component loadings and soil moisture are also observed, as are several anomalies. For PC2, the relationship between emissivities, fv and elevation is the same as PC1, with decreases in component loadings preceding decreases in soil moisture. A lag in data is also observed between changes in soil moisture and emissivity, fractional vegetation and elevation. A lag in the tcwg is also noted for day and night. For PC3, all variables appear once again appear to correspond to soil moisture with the exception of tcwg, for which an apparent lag and inverse relationship is observed. For PC4 similar relationships are observed again; though tcwg shows additional decreases towards the end of each year that are more visible at night and appear to correlate to low soil moistures. For PC5 a lag is observed with emissivities, elevation and fv increases preceding soil moisture increases. Tcwg once again follows the same trend as soil moisture; although a number of anomalies are observed at night. In all cases further analysis of the correlations is necessary to confirm the apparent relationship and to allow for understanding the data lag.

#### **4.3.4 Discussion**

PCA of the Turkana region successfully proves that elevation, both channels of emissivity, fv and tcwg all contribute to the absolute LST signal. The dominance of elevation on the LST signal throughout the PCA suggests that this is the main driver on LST in terms of the variables considered. This is closely followed by the effects of

surface emissivity, which in turn is linked to a number of parameters including land cover and lithology as noted in Chapter 2 (Janza et al., 1975; Coolbaugh et al., 2000; Calvin et al., 2005). The dominance of elevation and emissivity over  $f_v$  and  $t_{cwv}$  has been observed by the identification of several anomalous regions that correspond to warmer absolute LSTs. All anomalies (Figure 86) are found to be low lying (Figure 19) and of Quaternary or Holocene lithology (Dunkley et al., 1993) (Figure 10).

However, the PCA fails to identify the unexplained variance with respect to the anomalous regions; which may be related to geothermal anomalies and additional complex parameters that are not easily input into the PCA. This is significant given that all identified anomalies are additionally of known geothermal activity (Dunkley et al., 1993; Lagat, 2010) (Figure 17) or sites undergoing or considered for hydrocarbon exploration (Rop, 2013; Tullow Oil plc, 2014) (Figure 12). This suggests that it is also plausible that elevated geothermal gradients may be present within the region as is supported by the presence of warmer LSTs in these areas compared to the average of the host rock.

In terms of the temporal variation, the full PCA successfully reveals the changes in the most dominant drivers of LST throughout the year, with the periodic variations coinciding with seasonal fluctuations. Overall the periodicities identified with both the precipitation and soil moisture datasets hint additional factors that influence LST that are not accounted for here. From simple observations it is difficult to determine the full extent to which the additional datasets are related. Further statistical analysis is required to calculate correlation and offsets in the corresponding datasets.

A number of limitations are now discussed in relation to the PCA. This includes the number of input variables analysed. The PCA in this study is simplified with respect to the abundance of potential input variables. Therefore even unexplained variance can never fully be concluded as geothermal; with the unknown effects of precipitation, soil moisture, slope, aspect, coastal proximity, viewing angle and atmospheric circulation all modulating LST. Issues also arise where geothermally anomalous regions may not be identified due to overriding factors. This is a real possibility in the geothermally active Suguta Valley which is a region of relatively low elevation. From the PCA, it would therefore be easy to conclude that the elevation is responsible for LST variation here,

neglecting the potentially elevated geotherms and thus disregarding the area as a false geothermal anomaly. In addition to this, LST and auxiliary variable uncertainties are a major limitation and require propagation to the averages.

To summarise this section, the variability of the LST in terms of the five input variables in PCA is now understood to an extent, though further work is necessary to incorporate additional contributing variables such as slope, aspect, soil moisture and so forth, as discussed in Chapter 2. It is found that the most significant variables influencing LST in this region are elevation and emissivity. The following section now attempts to correct for the effects of elevation to reveal the influence of other parameters on the LST signal.

#### **4.4 Summary of Results**

The techniques applied within this chapter have generated a series of informative results. Absolute LSTs have revealed that it is possible to remotely distinguish between host rock and basins. However, they fail to determine whether thermal anomalies identified are geothermally associated. PCA has successfully delineated the LST and finds that elevation is most dominant, closely followed by surface emissivity. Further steps are now applied within Chapter 5 to further delineate the LST, particularly with respect to the elevation.

## **5. Results and Discussion: Part 2**

Elevation is now considered in more detail, having been identified as the most significant contributor to the LST signal in Chapter 4. The following sections thus identify the typical LST-elevation relationship by linear regression analysis and subsequently apply the derived correction to generate an equivalent normalised LST dataset. Following this, the normalised results have also been analysed, with respect to the remaining input variables of fractional vegetation, the two channels of emissivity and water vapour. This therefore expands the research within this thesis beyond the scope of previous work noted in Chapter 2.5. This work includes the generation of a climatology and the reapplication of a more restricted PCA, whereby elevation has been excluded.

### **5.1 Normalised LSTs with respect to elevation**

Normalisation of LSTs with respect to elevation is now applied due to the known dominance of elevation as identified by the PCA. It is necessary to account for this variable in order to better understand the remaining variance in the LST. The first step towards normalisation has been to mathematically determine the linear relationship between LST and elevation for day and night, monthly and yearly datasets. The result of this has then been used to recalculate absolute LSTs equivalent to the LSTs at 0 m. Comparisons have then been generated between the absolute and normalised datasets using a number of transects across the Turkana region, which have been selected based upon a number of features identified and as previously discussed in the absolute LSTs.

#### **5.1.1 Land Cover-Elevation-LST Analysis**

In order to correct for the effects of several parameters, the relationship between them must first be understood. Initial linear regression has therefore been applied with respect to the elevation and mean LSTs as generated for all ALB2 land cover types. This was produced across the Turkana region for both day and night of June 2006. From this a number of pre-set idl functions: LINFIT, LINFIT with errors and LADFIT, as detailed

in Chapter 3, were applied to determine the relationship gradient (Figure 90). There is minimal difference observed between the gradients of all three functions with all recording the gradient at  $-0.01 \text{ K m}^{-1}$  (Table 21). The most notable difference is the intercept of the lines at 0 m, though again the difference is minor. It has therefore been concluded that LINFIT with errors is to be applied to the datasets as it is the only function to additionally account for uncertainty.

The selection of this function has been further confirmed as suitable by the generation of a density plot (Figure 91). From the density plot, clusters are observed around 290 K and 295 K. Moving to higher elevation, density reduces as a result of a smaller area at such altitudes. Thus the densities explain the positioning of the lines of best fit that are shifted as a result of LST frequency. Nonetheless, initial studies of elevation versus LST for all land cover types within the Turkana region reveal a linear relationship. This linearity is most clear for night time, with narrower data spreads observed.

The Lake Turkana and Lake Edward tiles are now considered to determine whether this relationship varies spatially and temporally (Figure 92). The Lake Edward tile has been selected for its more vegetated land cover (Figure 38) and it's more consistent, mid-

*Table 21: Gradients and correlations coefficients between MODIS LST and elevation, as calculated by IDL functions referred to in the text for June 2006.*

Time of day	idl function	y=mx+c	
		Gradient ( $\text{K m}^{-1}$ )	Intercept (K)
Day	LINFIT	-0.01	316.79
Night	LINFIT	-0.01	297.10
Day	LINFIT with errors	-0.01	316.67
Night	LINFIT with errors	-0.01	297.09
Day	LADFIT	-0.01	316.70
Night	LADFIT	-0.01	296.55

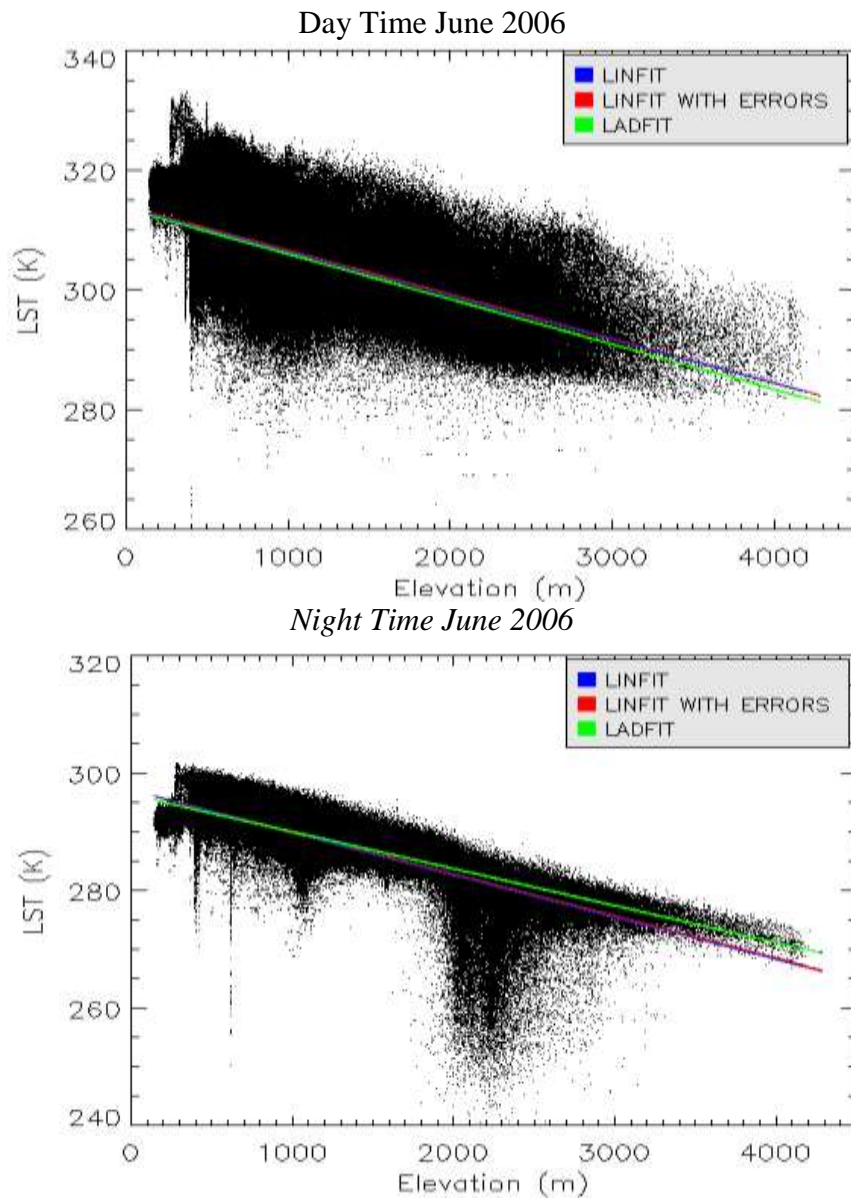
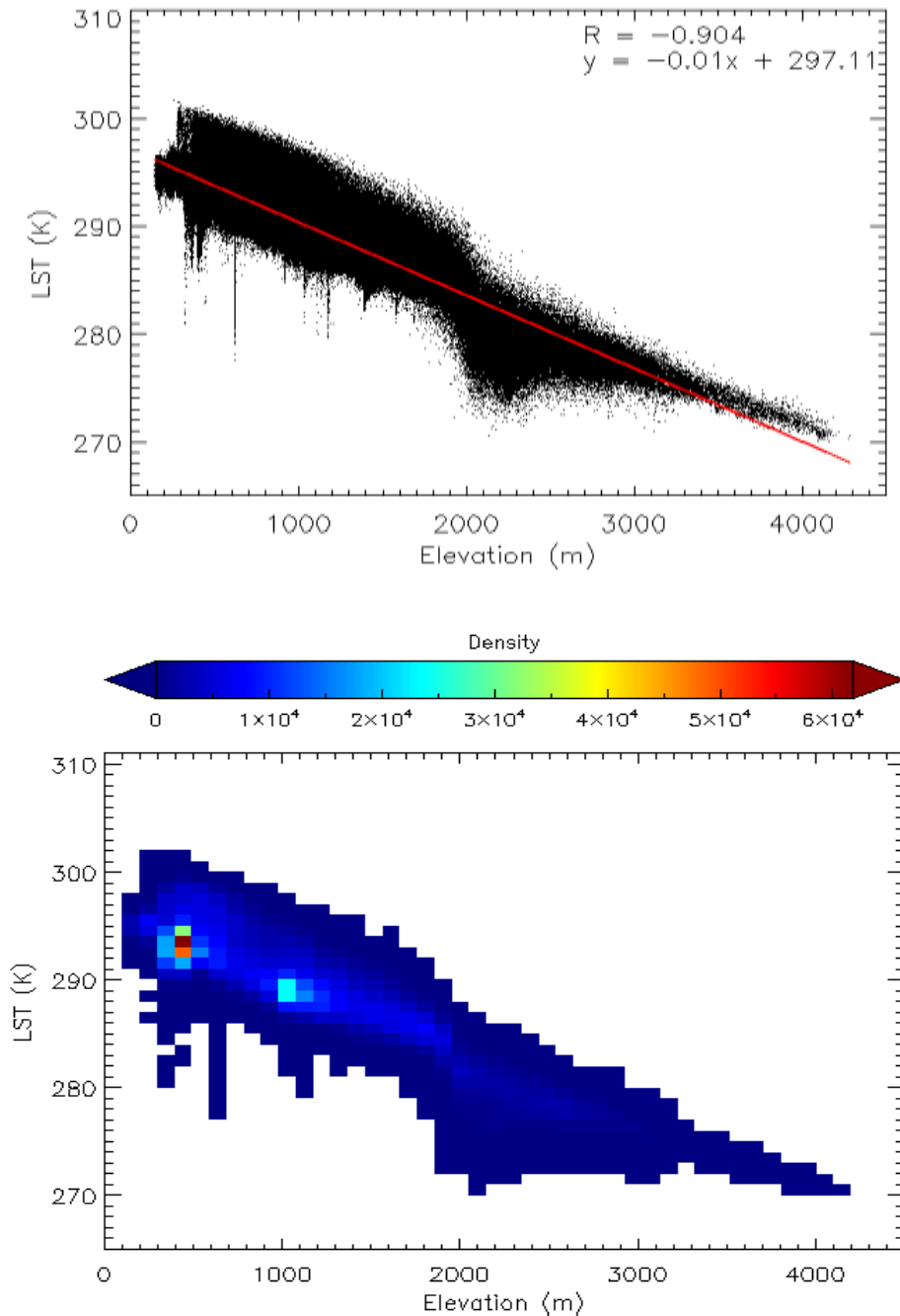


Figure 90: Elevation versus monthly MODIS LST gradients as generated from the idl functions: LINFIT, LINFIT with errors and LADFIT across the  $10^{\circ} \times 10^{\circ}$  grid of Turkana region at  $0.01^{\circ}$  resolution.

range elevations with an absence of low troughs and higher domes as found in Turkana (Figure 19). A clear linear relationship is noted for both tiles, though at several elevations LSTs diverge from the main sequence. This creates a number of plateaus and clusters which are more visible at night. The most obvious divergence occurs at 2000 m



*Figure 91: Density plot and scatter plot comparison for elevation versus the 2006 night time yearly MODIS LST means across the  $10^\circ \times 10^\circ$  grid of Turkana region at  $0.01^\circ$  resolution. Density refers to the number of pixels within the given region.*

for the Turkana region which is likely associated with the Ethiopian Dome. There are also numerous plateaus below this elevation that are potentially linked to lakes, basins and valley floors. For the Lake Edward area there is no divergence at 2000 m but instead less distinct plateaus below 1000 m that are once again thought to be related to lakes, basins and valleys.

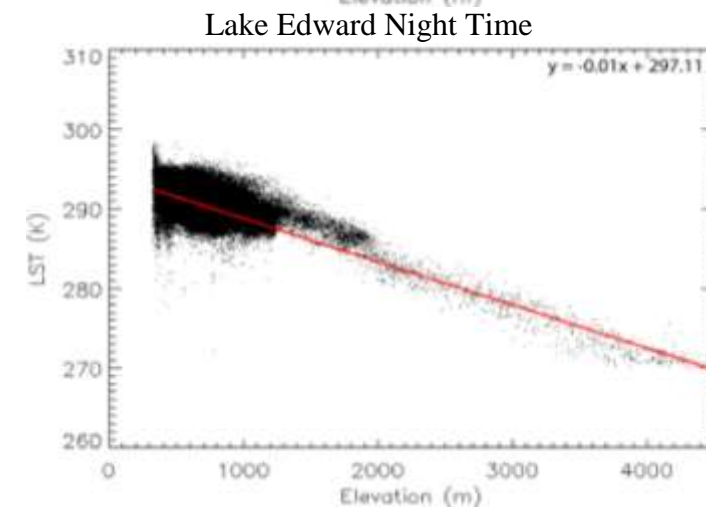
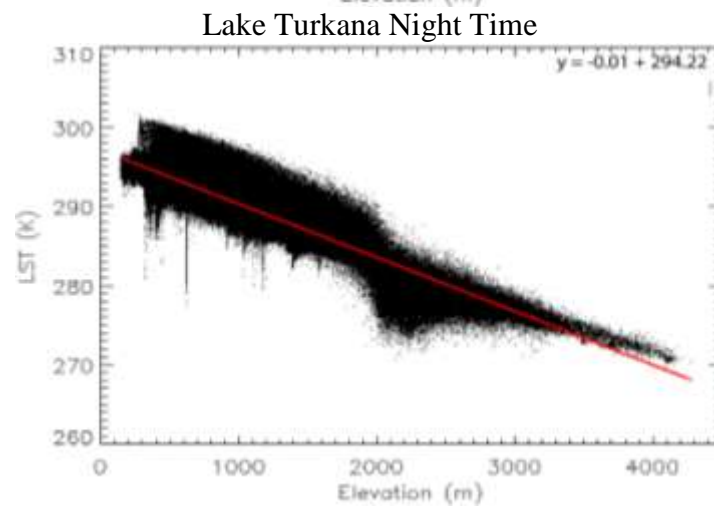
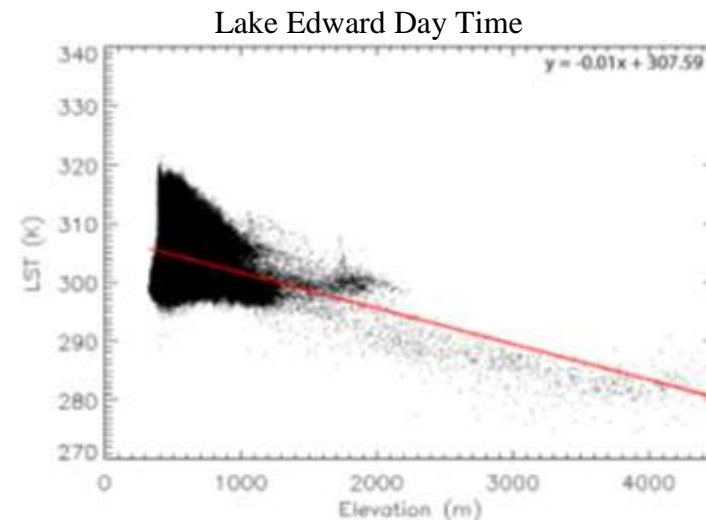
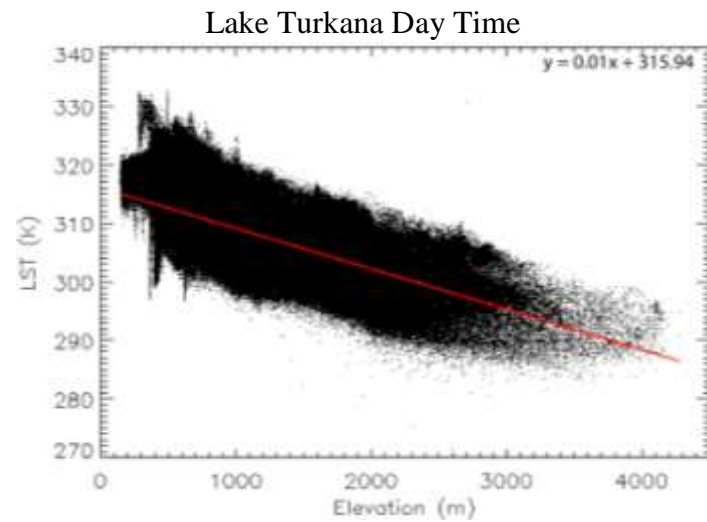


Figure 92: Elevation versus the 2006 yearly MODIS LST means for the Lake Turkana and Lake Edward tiles. Both tiles are on  $10^\circ \times 10^\circ$  grids of  $0.01^\circ$  resolution.

The gradient and Pearson correlations are now provided for each month throughout 2006 (Table 22) and yearly from 2003 to 2013 (Table 23). Pearson correlation coefficients are reported as values between  $\pm 1$  and describe the linearity of the relationships between the variables. The values given solely represent the Turkana region. For day time data, correlations coefficients are within the range of -0.50 and -0.70 which suggests moderate to strong correlations. For night correlations the values range from -0.80 to -0.90 and therefore show a stronger correlation than during the day. Most derived gradients have values of  $-0.01 \text{ K m}^{-1}$  which are consistent with the expected inverse relationship that exists. Exceptions to this gradient are found within the monthly files for November and December where gradients are  $0.04 \text{ K m}^{-1}$ . The LSTs recorded at 0 m for the monthly files vary more than those recorded for the yearly. Standard deviations are also provided and detail the deviation when the average line of best fit is removed from all data points. Again, monthly deviations are greater and fluctuate more than the yearly equivalents.

Elevation-LST relationships are now considered in terms of four land cover groups (Figure 93). Initial findings show that the three vegetated groups occur at all elevations, whilst the bare soils are restricted to elevations lower than 2000 m. These findings are further supported by the plot of elevation versus land cover, where the LST range over which specific land cover span is recorded (Figure 94).

The linear elevation-LST relationship is distinct for all land cover groups, though once again plateaus and clusters are observed. In all groups the gradients are recorded at  $-0.01 \text{ K m}^{-1}$ . However, the gradient for the bare soils does not fit all data points perfectly. Two parallel regions are apparent, with the gradient concordant with the lower elevations but not the higher elevations.

The LSTs at 0 m for all groups are within a similar range varying from approximately 296 K for the three vegetated groups to 298 K for the bare soils. The increase of 2 K for the bare soils is likely the result of their higher heat capacities and lower thermal inertia. From Figure 95, it becomes clear that all land cover groups can reach 298 K, though only the vegetated groups reach as low as 270 K.

Table 22: Gradients and Pearson correlation coefficients ( $R$ ) between elevation and the 2006 yearly MODIS LST means across the  $10^\circ \times 10^\circ$  grid of Turkana region at  $0.01^\circ$  resolution.

2006								
Month	Day time				Night time			
	Gradient (K m <sup>-1</sup> )	Intercept (K)	Standard Deviation (K)	R	Gradient (K m <sup>-1</sup> )	Intercept (K)	Standard Deviation (K)	R
January	-0.01	321.60	7.02	-0.57	-0.01	297.40	6.07	-0.81
February	-0.01	324.24	8.86	-0.56	-0.01	298.60	6.53	-0.83
March	-0.01	322.39	8.37	-0.60	-0.01	297.79	6.49	-0.84
April	-0.01	319.91	10.46	-0.60	-0.01	299.19	7.85	-0.87
May	-0.01	314.67	9.12	-0.56	-0.01	298.43	7.06	-0.87
June	-0.01	313.82	8.96	-0.60	-0.01	297.13	6.86	-0.85
July	-0.01	313.59	9.24	-0.60	-0.01	297.02	6.61	-0.82
August	-0.01	313.88	9.33	-0.56	-0.01	297.69	7.07	-0.86
September	-0.01	314.25	9.78	-0.50	-0.01	298.36	7.08	-0.84
October	-0.01	312.23	8.80	-0.50	-0.01	298.26	7.34	-0.86
November	-0.004	308.29	6.53	-0.50	-0.01	294.25	6.47	-0.77
December	-0.004	309.72	6.82	-0.51	-0.004	293.40	4.81	-0.78

Table 23: Gradients and Pearson correlation coefficients (*R*) for 2003 through to 2013 between elevation and the yearly MODIS LST means across the 10° x 10° grid of Turkana region at 0.01° resolution.

Year	Day time				Night time			
	Gradient (K m <sup>-1</sup> )	Intercept (K)	Standard Deviation (K)	R	Gradient (K m <sup>-1</sup> )	Intercept (K)	Standard Deviation (K)	R
2003	-0.01	316.67	5.14	-0.64	-0.01	297.09	2.13	-0.89
2004	-0.01	316.44	5.38	-0.63	-0.01	296.96	3.78	-0.89
2005	-0.01	317.59	5.01	-0.68	-0.01	297.18	2.50	-0.90
2006	-0.01	315.94	4.96	-0.67	-0.01	297.11	2.85	-0.90
2007	-0.01	315.10	5.00	-0.64	-0.01	296.96	2.09	-0.90
2008	-0.01	315.22	5.32	-0.58	-0.01	296.52	3.36	-0.90
2009	-0.01	317.57	5.50	-0.60	-0.01	297.23	6.97	-0.87
2010	-0.01	316.73	5.11	-0.69	-0.01	297.64	4.43	-0.90
2011	-0.01	314.57	8.96	-0.65	-0.01	297.44	6.93	-0.85
2012	-0.01	314.95	4.93	-0.61	-0.01	296.90	1.91	-0.91
2013	-0.01	315.28	5.19	-0.63	-0.01	297.12	2.60	-0.91

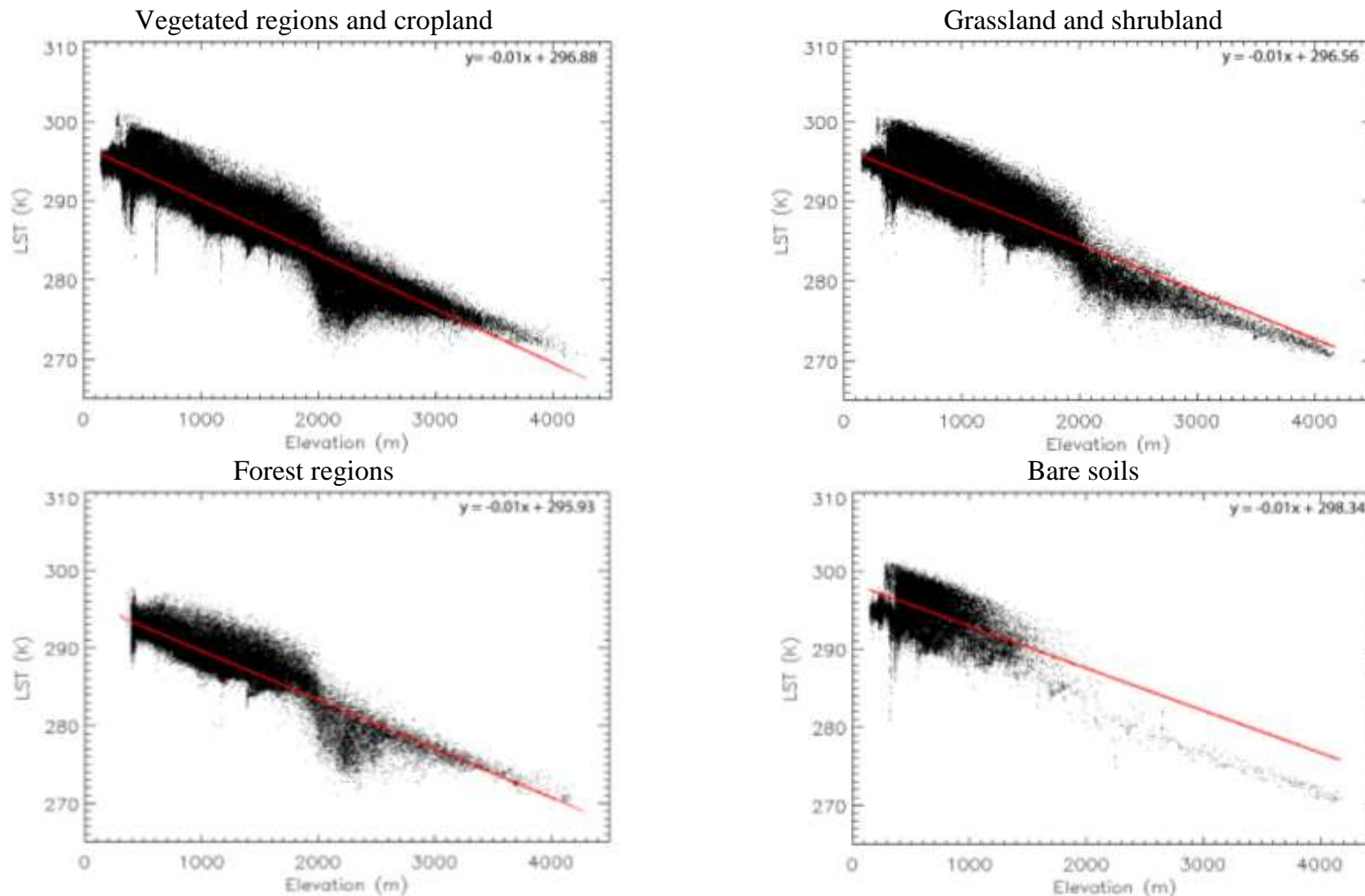


Figure 93: Elevation versus 2006 night time MODIS LSTs across the  $10^\circ \times 10^\circ$  grid of Turkana region at  $0.01^\circ$  resolution for selected land cover types.

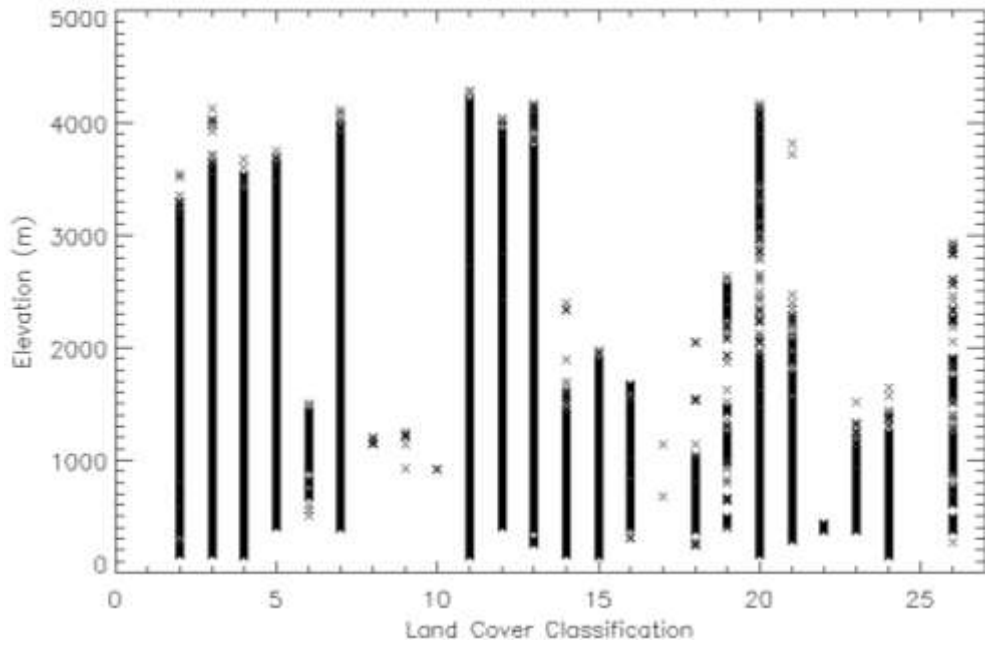


Figure 94: Elevation versus land cover across the  $10^{\circ} \times 10^{\circ}$  grid of Turkana region at  $0.01^{\circ}$  resolution. Elevation data has been taken from the SRTM dataset and land cover from the University of Leicester ALB2 dataset, as described in Chapter 3.

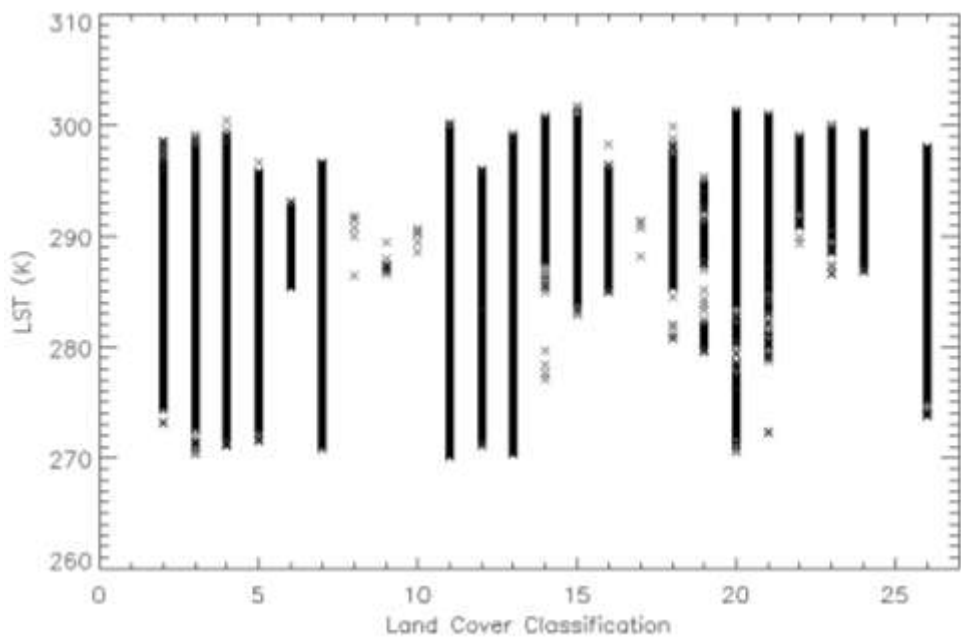


Figure 95: Night time 2006 MODIS LST means versus land cover type the  $10^{\circ} \times 10^{\circ}$  grid of Turkana region at  $0.01^{\circ}$  resolution. Land cover data has been taken from the University of Leicester ALB2 dataset, as described in Chapter 3.

### 5.1.2 Normalisation for 2006 Yearly Means

Given the known inversely linear relationship between elevation and LST, it is now necessary to correct for this in order to better understand the contribution of less dominant parameters. An example of normalising LSTs with respect to elevation is thus provided for 2006. Table 23 provides the gradients that are invoked to reduce LSTs to an elevation of 0 m (sea level). Figure 96 shows the contrast between the 2006 night time absolute LSTs and normalised LSTs. Table 24 contrasts all points in the absolute and normalised datasets from which the distinct shift in LSTs is evident.

Significant warming is noted for several of the elevated regions including Mount Elgon that stands at approximately 4000 m. Originally at LSTs of 270 K, the volcano has increased approximately by 40 K at LSTs of 0 m to 310 K. This increase is consistent with the gradient of  $-0.01 \text{ K m}^{-1}$  that equates to an increase of 10 K for each 1 km decrease in altitude. Other features including the uplifted Ethiopian Dome also display increases in LSTs. Increases in LSTs are also noted for lower relief areas such as the Turkana Trough, Turkana Basin and Suguta Valley. The changes in LSTs are however minor in comparison to the more elevated regions and Suguta Valley. Increases across all of the Turkana region is a result of elevations all originally lying above 0 m. Decreases in LSTs would have been expected if values were below this altitude.

Table 24 contrasts the overall LSTs, with shifts noted in the datasets. The means here refer to a tile mean of the yearly per pixel data. Minimum and maximum values refer to the lowest value per pixel throughout the year, as selected from monthly means. For the mean LSTs a shift of approximately 11 K is noted increasing from an original 290 K to a normalised 301 K. Note that the data associated with 2011 has been ignored due to inconsistencies within the results.

Overall, there is a large shift in perception. In absolute LSTs, the highest values were concentrated within the Turkana Trough. In normalised LST space, the thermally anomalous regions are now the volcanoes and are additionally shown to flow up from the Turkana region towards the Afar region. Considerable structure is now seen.

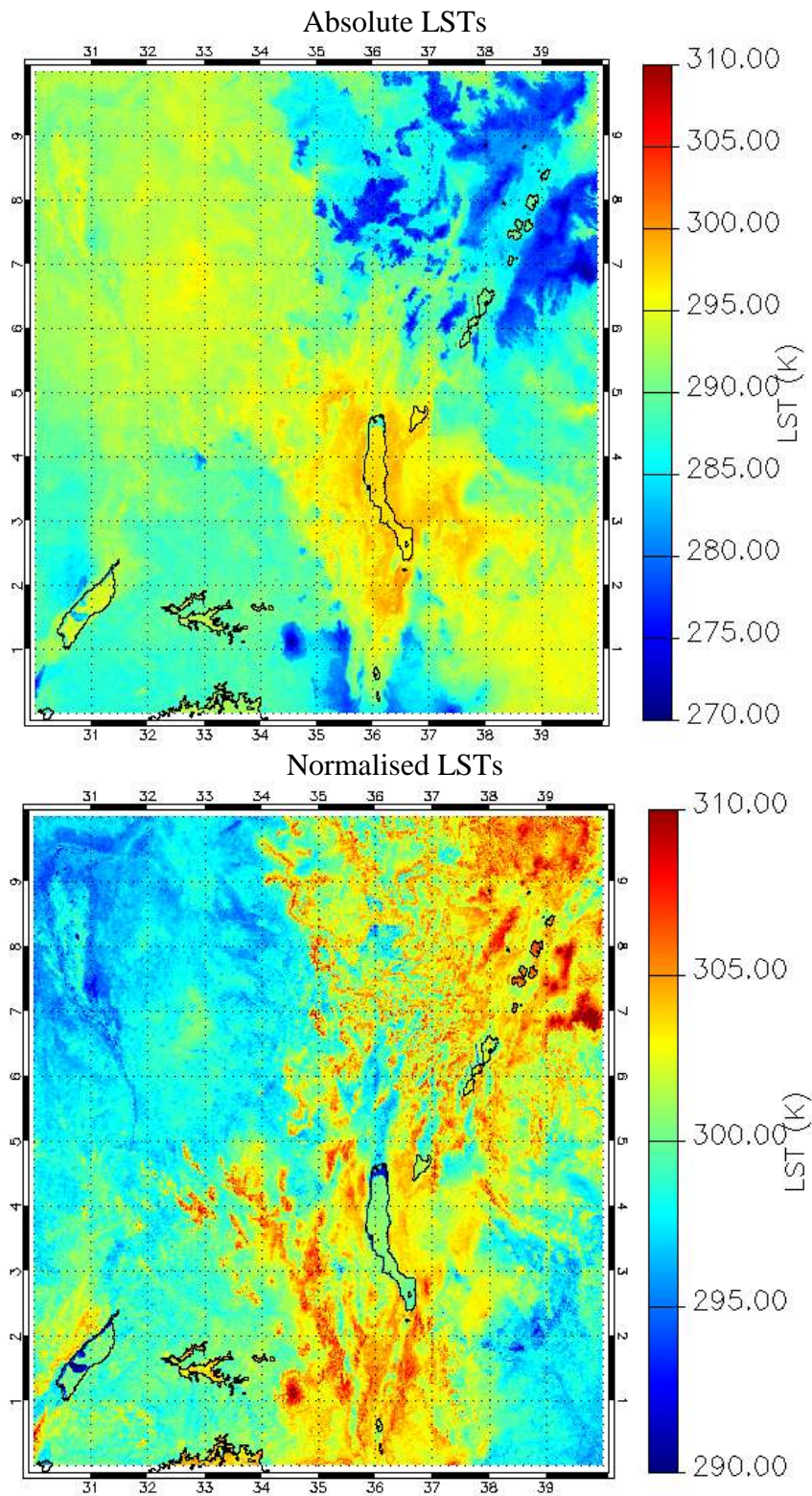


Figure 96: Absolute and normalised MODIS LST means for night time 2006 across the  $10^{\circ} \times 10^{\circ}$  grid of Turkana region at  $0.01^{\circ}$  resolution. Mean LSTs have been calculated using NASA's Aqua dataset.

Table 24: Maximum and minimums for the absolute, yearly MODIS LST means and the normalised, yearly MODIS LST means with respect to the SRTM elevation across the  $10^{\circ} \times 10^{\circ}$  grid of Turkana region at  $0.01^{\circ}$  resolution. LSTs are again calculated from the Aqua dataset.

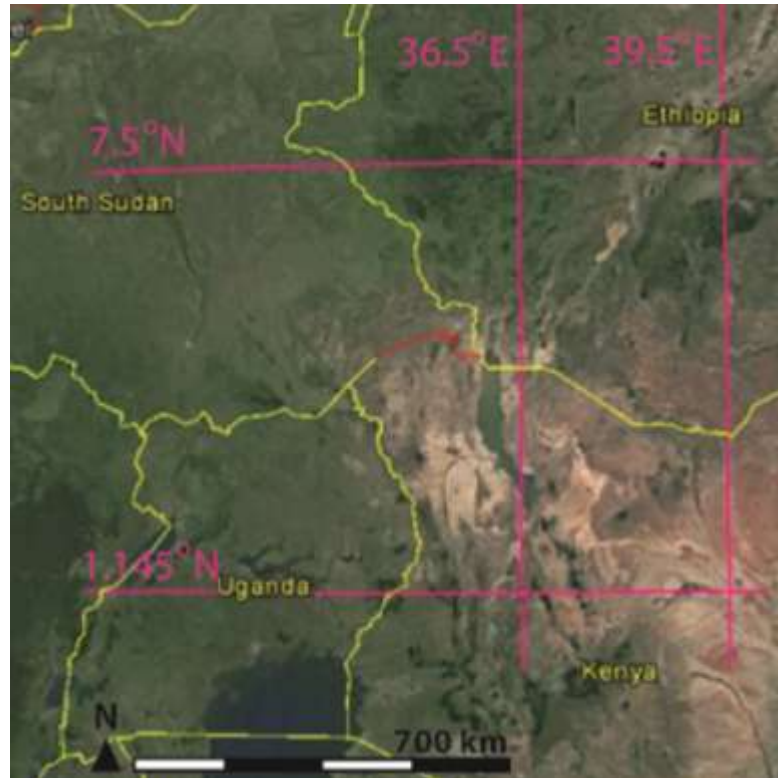
Year	Night Time Yearly Mean LST (K)			Night Time Yearly Normalised Mean LST (K)		
	Mean	Maximum	Minimum	Mean	Maximum	Minimum
2003	290.4	301.4	269.9	301.5	315.2	281.5
2004	290.1	301.4	268.8	301.1	314.3	281.0
2005	290.4	301.5	269.4	301.4	314.6	287.1
2006	290.2	301.7	270.1	301.2	314.1	283.7
2007	290.2	301.6	270.1	301.2	314.2	284.4
2008	290.0	301.7	269.5	301.0	314.0	287.3
2009	290.6	302.5	265.3	301.5	314.7	280.7
2010	290.5	302.1	267.2	301.5	313.6	281.7
2011	290.1	302.2	229.1	301.4	315.7	249.5
2012	290.2	301.4	269.6	301.2	315.0	284.8
2013	290.2	301.7	269.0	301.3	314.5	284.9

Night Time Yearly Elevation (m)			Night Time Yearly Normalised Elevation (m)		
Mean	Maximum	Minimum	Mean	Maximum	Minimum
1027.7	4286.0	142.0	0.0	0.0	0.0

### 5.1.3 Absolute-Normalised Transects

Selected cross sections are shown to compare the absolute and normalised datasets (Figure 98 to Figure 101). The locality of these lines can be seen in Figure 97. Additional transects can be found in Appendix 8. From Figure 98, at  $34.5^{\circ}$  E longitude, warmer LSTs are observed post normalisation for the volcanic Mount Elgon region. Heat flux, that is most likely volcanic in nature, is additionally observed to increase towards a central peak, which coincides with the locality of the volcanic centre. The presence of these increases in LST suggests that additional parameters favouring warmer LSTs are likely to be present in this area.



*Figure 97: Google Earth (2016) terrain map showing locality of absolute-normalised LST transects, as discussed within Chapter 5.1.3. All transects span the Turkana region tile that is a  $10^\circ \times 10^\circ$  grid of  $0.01^\circ$  resolution.*

To the east at a range of longitudes from  $34^\circ$  E to  $38^\circ$  E five additional peaks of warmer LSTs are encountered post normalisation; though not to the same extent as the LSTs of Mount Elgon. These peaks all correspond to a number of uplifted, rift flanks as follows; the Cherangani Hills at  $35.5^\circ$  E longitude (Foster and Gleadow, 1996), rift flanks separating the South Kerio and Suguta basins thought to be part of the Tirioko Platform at  $36^\circ$  E longitude (Dunkley et al., 1993), the uplifted Samburu Hills at  $36.5^\circ$  E longitude (Dunkley et al., 1993), eastern rift flanks of the Suguta Basin and parts of the uplifted Turr plateau at  $36.9^\circ$  E longitude (Dunkley et al., 1993) and finally, the Mathew's mountain range at  $37.4^\circ$  E longitude (Foster and Gleadow, 1992).

The identification of these uplifted rift flanks and plateaus as now warmer with respect to the surrounding is pleasing as elevated geothermal gradients would be predicted here. The rift flanks present separating the South Kerio and Suguta basins are particularly

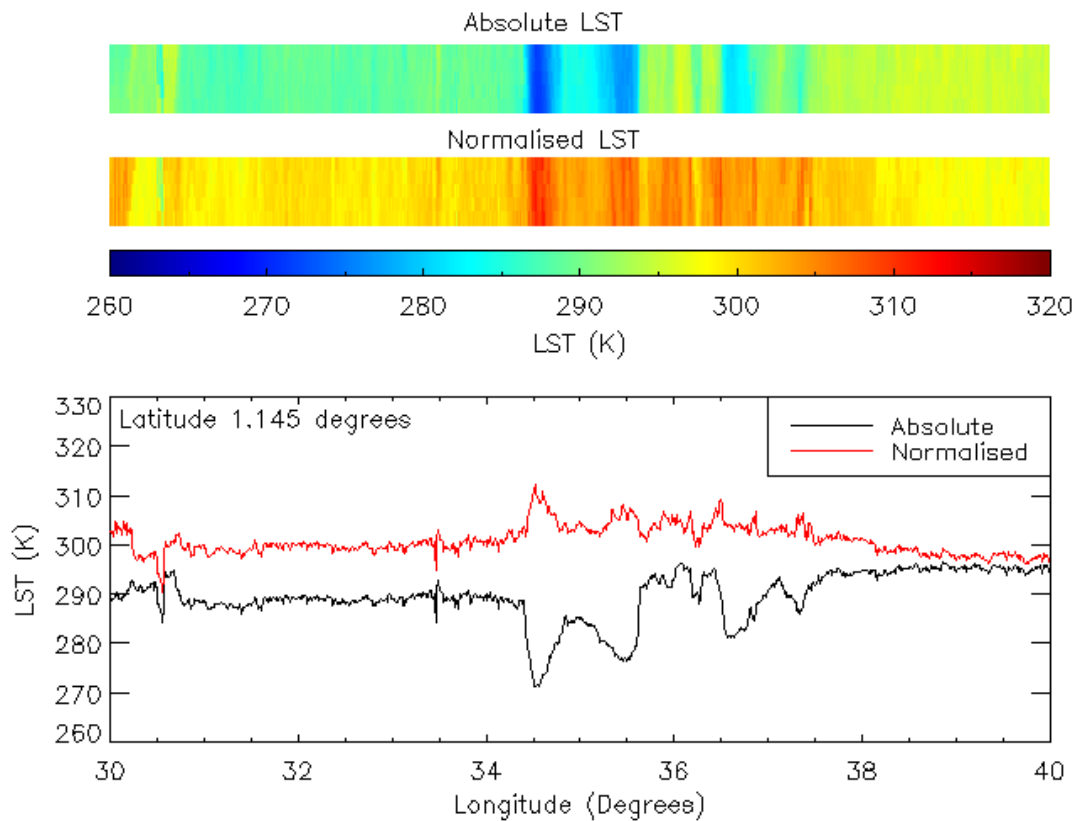
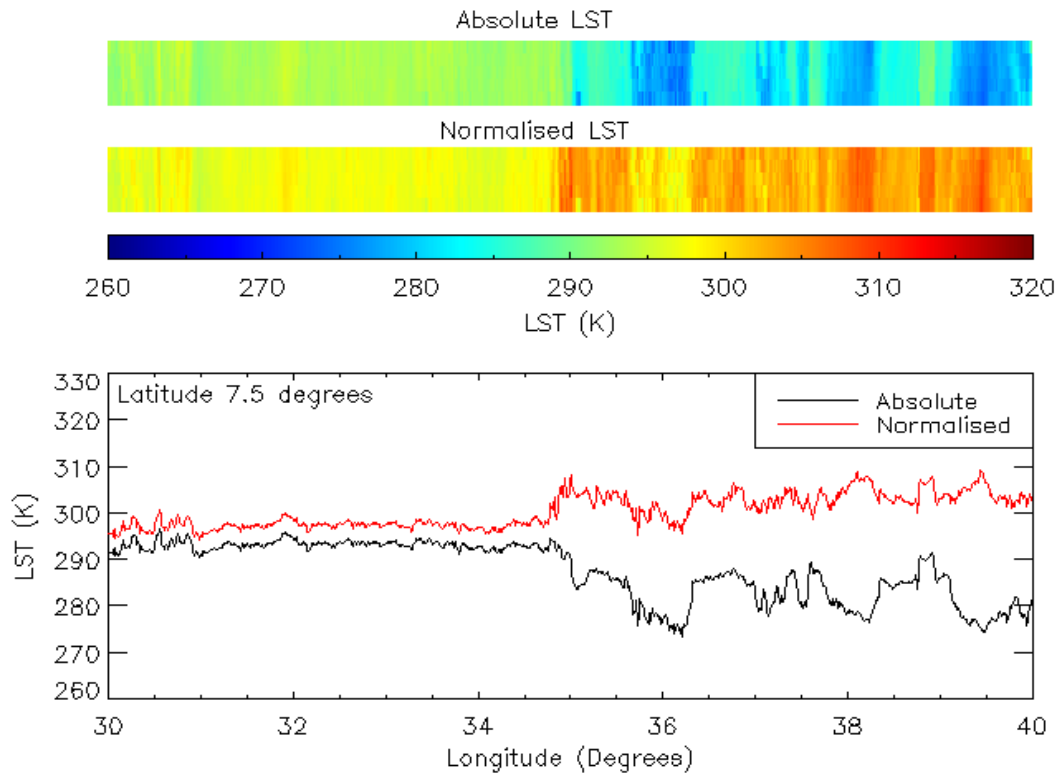


Figure 98: Cross section along  $1.145^{\circ}$  N latitude. LSTs shown are for the absolute and normalised MODIS LST means for night time 2006, which are displayed previously in Figure 96. See Figure 97 for the locality of the transect.

interesting, given that the flanks now appear marginally warmer than the basins themselves which are reportedly the regions of the most extensive, known geothermal activity (Omenda, 1998; Lagat, 2010) (Figure 17).

Moreover, to the west of  $34^{\circ}$  E and to the east of  $38^{\circ}$  E, the tapering of LSTs to lower values is consistent with increasing distance from the main rift. For the west of the region, this is further enhanced by the presence of lakes at  $30.5^{\circ}$  E longitude. However, tapering of the LSTs is perhaps unexpected for the east extent given that from approximately  $38.6^{\circ}$  E longitude, the rifted Anza Basin is located. From Figure 98, it is now evident that this basin's warmth does not exist post normalisation, particularly so for increasing proximity to the coast; which is a factor not considered in this study.



*Figure 99: Cross section along 7.5° N latitude. LSTs shown are for the absolute and normalised MODIS LST means for night time 2006, which are displayed previously in Figure 96. See Figure 97 for the locality of the transect.*

Figure 99 shows an elevation associated boundary at approximately 34.7° E longitude, between the broad plains in the west and the Ethiopian Dome in the east. Here, the topography shows an apparent steep gradient rapidly increasing from around 500 m up to over 1000 m (Figure 19). In terms of the LST, elevation has little effect on the western side, with only minor increases on correction. To the east, a broad range of longitudes show elevated normalised LSTs which make additional factors influencing warmth likely.

Fluctuations within the dome correspond to a number of geographic features, including the presence of lakes at 38.7° E longitude, which are found to be located within an area of lower elevation that separates the Ethiopian Dome in two. This region is likely to be consistent with the rift locality, migrating from the Afar region to Lake Turkana, as discussed in Chapter 1. Given, that much warmer LSTs are recorded for this region,

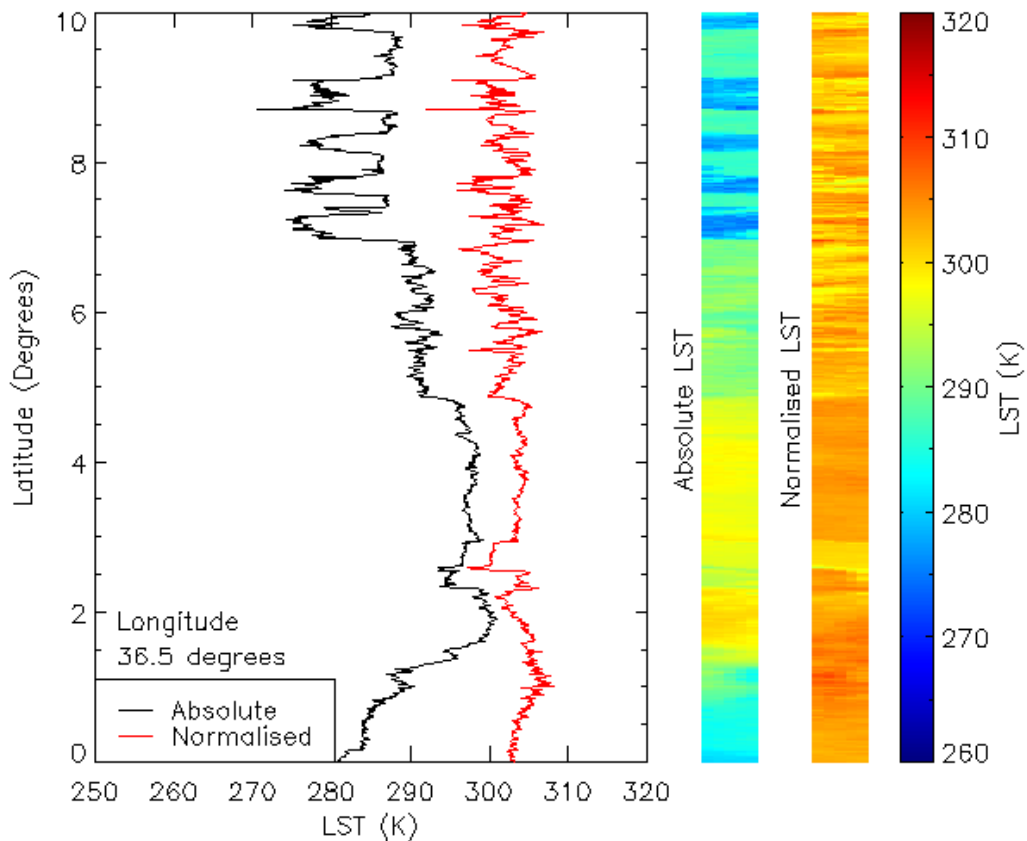


Figure 100: Cross section along longitude 36.5° E. LSTs shown are for the absolute and normalised MODIS LST means for night time 2006, which are displayed previously in Figure 96. See Figure 97 for the locality of the transect.

regardless of absolute and normalised dataset, the transect appears to agree. Additionally, a number of warmer peaks within the dome are also found to correspond to various volcanic cones, which are again expected to have larger heat fluxes; especially as this is a region of current sea floor spreading (Dunkley et al., 1993).

Figure 100 shows a cross section encountering rifts flanks from 0° N to 1.5° N latitude that have increased in warmth post normalisation, similarly to those observed in Figure 98. North of this, between 1.5° N and 2° N latitude, the Suguta Basin is located and now observed as cooler than the surrounding rift flanks. The slight peak in LSTs between 0.5° N and 1.5° N latitude shows apparent correspondence with the transition between the basins and the flanks, where faulting is likely to be abundant.

It is therefore plausible that the increased heat flux is volcanic in nature and thus a direct result of increased migration pathways to the surface. However, this is simply speculative and requires more work to fully prove.

Northwards of the Suguta Basin, at approximately 2.5° N latitude, a notable peak in the LSTs is found to correspond to a lake filled segment of the Turkana Basin. This data should therefore be treated as suspicious due to the known uncertainties in using LST measurements across water bodies. However, to the north of this at between 3° N and 5° N latitude, a sediment filled segment of the Turkana Basin is observed. Within this region a slight gradient of increasing LSTs towards the north is noted. This is consistent with the southern propagation of the rift, which means that the crust of regions further north is more extended and thus the mantle is closer to the surface, resulting in increased geothermal gradients (Ebinger, 2005). Above 5° N latitude, no mapped basins are encountered. A more erratic LST signal is observed; whereby various plateaus and lakes are found scattered across the Ethiopian Dome. This is much the same as discussed for Figure 99.

In Figure 101, a LST gradient of increasing warmth is again observed towards the north as within the Turkana Basin in Figure 100. This gradient is however, more distinct than previous spanning the entire range of latitudes from 0° N to 10° N. This is consistent with basin distribution and the known geology, with an absence of basins towards the south at 39.5° N latitude, transitioning northwards to the currently active Afar Basin where sea floor spreading is occurring.

In addition to the gradient, a singular larger peak in LSTs is observed at approximately 7° N latitude. This area is found to coincide with the Bale Mountains that are composed of a numerous volcanic cones. The presence of volcanoes and the uplift of the dome itself are likely associated with elevated geotherms and increased geothermal activity. Moreover, the region is known for its diverse soils, which affect specific heat capacity and therefore the LSTs and corresponding diurnal shifts (Mohr et al., 1963; Yiniger et al., 2007). Thus it is equally likely that land cover or elevated geotherms drive the warmer LSTs.

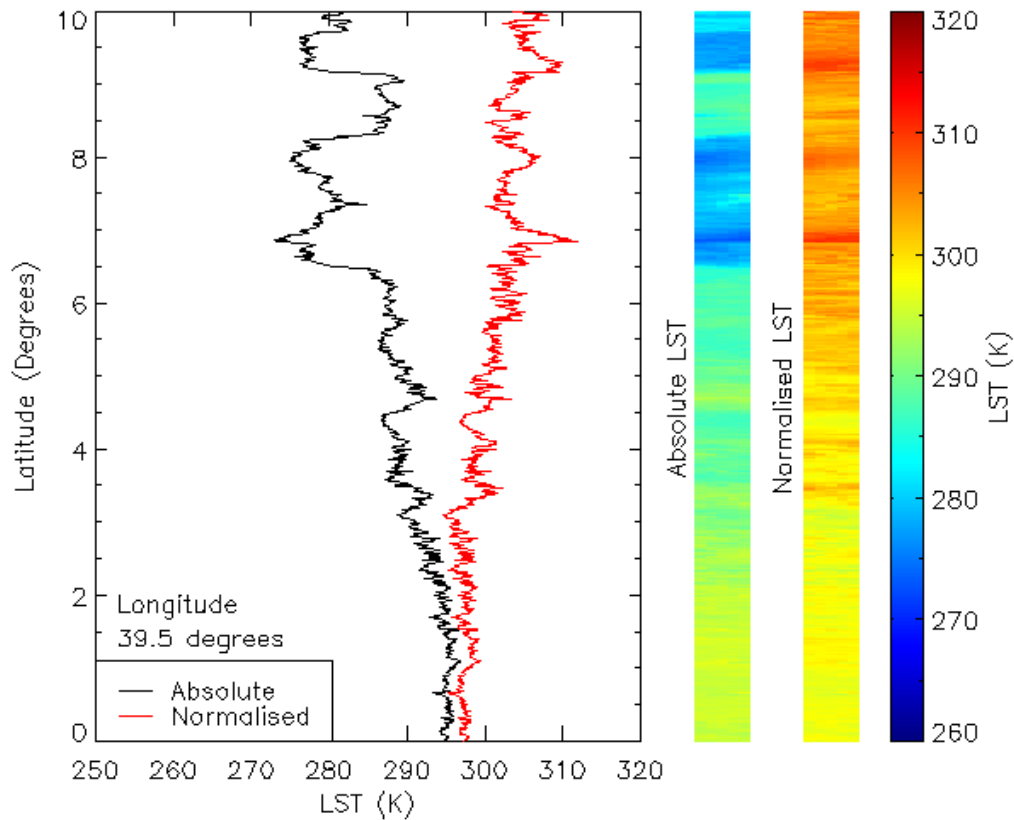


*Figure 101: Cross section along longitude 39.5° E. LSTs shown are for the absolute and normalised MODIS LST means for night time 2006, which are displayed previously in Figure 96. See Figure 97 for the locality of the transect.*

From Figure 98 through to Figure 101, it seems plausible that the normalisation process gives a whole new insight into places that could be explored. The identification of warmer LSTs reveals a number of rift associated features, including uplifted flanks and plateaus, as well both rift axis volcanics such as Bale Mountains and off axis volcanics, such as Mount Elgon. Additionally a number of basins are also found to remain warmer, including that of Turkana, which is of known geothermal activity. Moreover, the gradients highlighted within basins, predominantly within the Afar, provide an additional means of understanding the potential influence of geothermal gradients on the LST.

#### **5.1.4 Host Rock-Basin Comparison**

Similarly to the absolute data in Chapter 4.2, comparisons between basins and host rock are now discussed with respect to the normalised data. Immediately from Figure 102, the Turkana region is observed to show much greater discordance to basin boundaries than the absolute data due to a directional shift in the warmer LSTs. This supports the theory that elevation is a major factor in the identification of basins as warmer in the absolute LSTs. Therefore users of absolute LSTs must take with the interpretation of such data. Similar such discordance is also observed by the additional tiles including Lake Victoria (Figure 102), with discordance more notable for basins of increasing coastal proximity. Appendix 6 includes all normalised and absolute LST tiles.

Frequencies of the normalised LSTs have also been analysed with respect to host rock and basins (Figure 103). Basins are shown to have less warmth in normalised space and therefore there is now no overall distinction in terms of LST frequency between the basin and host rock. Further analysis of tiles, included in Appendix 6, also supports this conclusion. This lack of distinction once again supports the theory of basin elevation dependence with respect to LSTs. However, the basins in normalised space show a more distinct bimodal distribution, unlike the absolute dataset. This contrasts to the unimodal distribution of host rock LSTs post normalisation. It is therefore suggested that the additional peak in the basins could represent a group that are in fact warmer than the host rock in normalised space. Further work was applied to study specific basins as with the absolute dataset in Chapter 4.2.1. The six basins previously noted as warmer were again found to have higher LSTs than the average of the host rock in normalised space, whilst all other basins clearly did not.

Similarly to the absolute dataset, the mean, maximum and minimum LSTs with respect to the basins and host rock are provided (Table 25) and then additionally plotted with respect to the absolute dataset (Figure 104). From this, the known increase in LST post normalisation is observed. The year of 2011 is again identified as anomalous due to cloud issues. Unlike the absolute LSTs, the normalised dataset does not show an increase in mean LSTs for the basins when contrasted to the host rock. Similar LSTs of between 299 K and 301 K are recorded for the host rock and basins, with host rocks

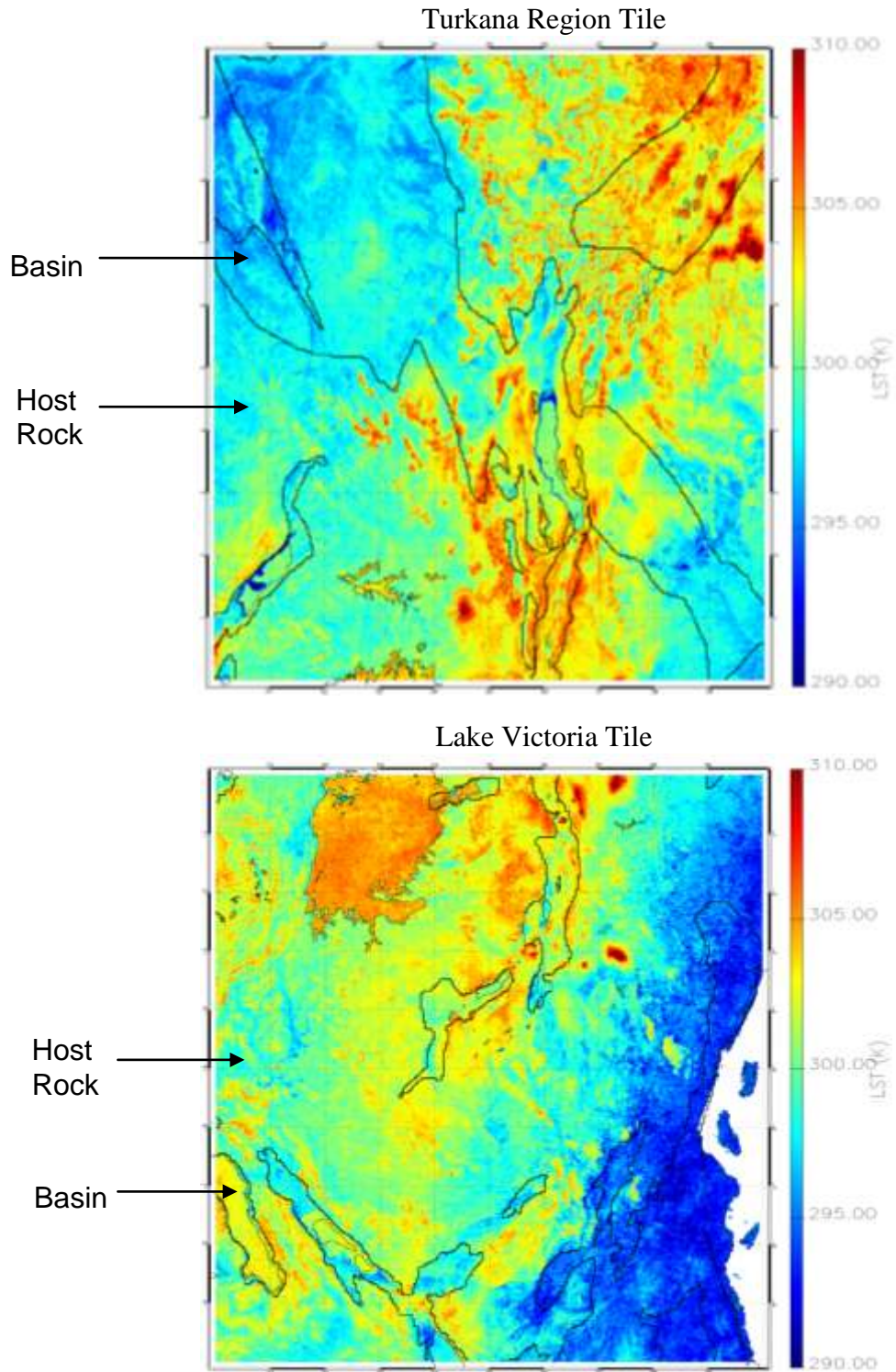


*Figure 102: The Turkana and Lake Victoria tiles with basin outlines as supplied by Tullow Oil plc (thicker black lines). LSTs are for the night time, 2006 yearly, MODIS LST means. Equivalent absolute LST-basin comparisons can be found in Chapter 4.2. Both the Turkana and Lake Victoria regions are  $10^{\circ} \times 10^{\circ}$  grids of  $0.01^{\circ}$  resolution.*

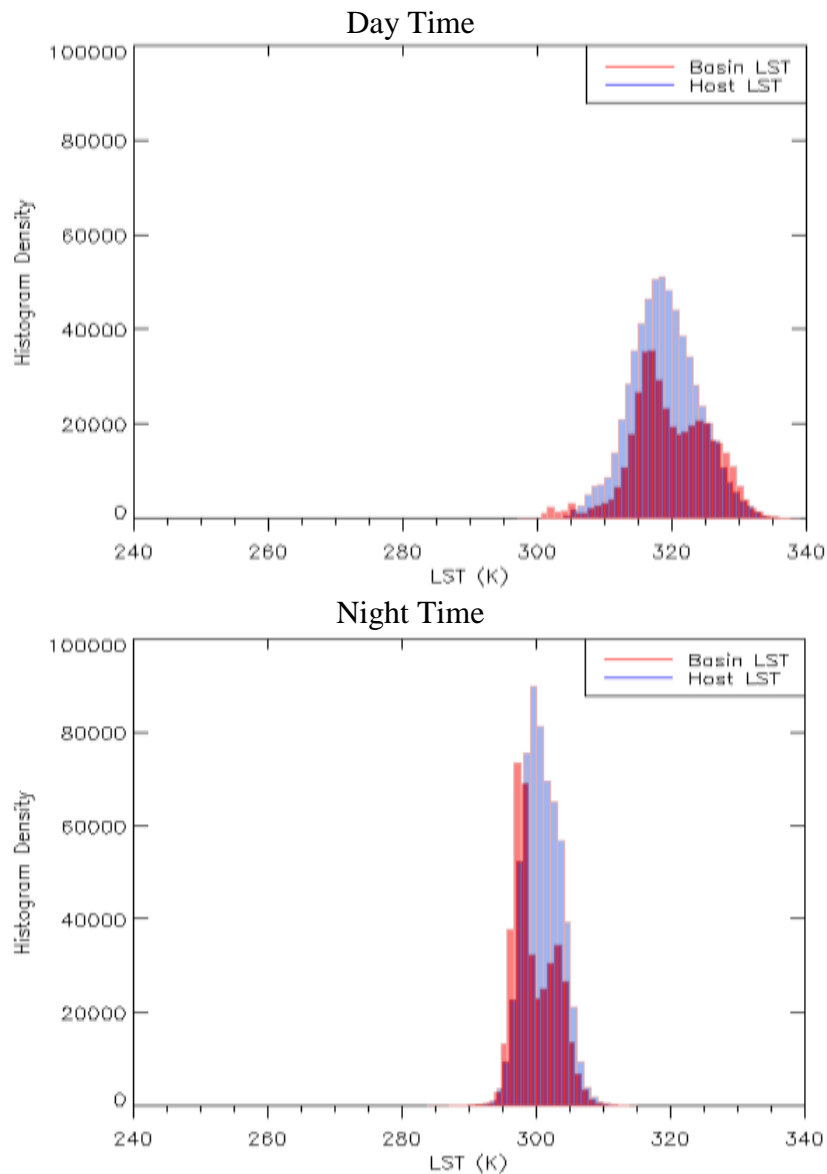


*Figure 103: 2006 MODIS LST frequencies of the host rock and basins, from the Aqua dataset, across the  $10^{\circ} \times 10^{\circ}$  grid of the Turkana region at  $0.01^{\circ}$  resolution.*

slightly warmer (Table 25). It can therefore be concluded that overall the normalised dataset does not indicate an average difference for all basins versus host rock.

In conclusion of this comparison, the discordance between normalised LSTs and basin outlines suggests on elevation correction, basins and host rock are indistinguishable on a regional basis. However, more localised studies, considering specific basins and the bimodal peak of basin LST frequency indicate that it still plausible that some basins may be warmer than the host rock average and thus distinguishable.

Table 25: Mean, maximum and minimum night time yearly MODIS LSTs, for the Aqua normalised dataset, across the  $10^{\circ} \times 10^{\circ}$  grid of the Turkana region at  $0.01^{\circ}$  resolution, for host rock and basins.

Year	Host Rock			Basin Rock		
	Mean LST (K)	Maximum LST (K)	Minimum LST (K)	Mean LST (K)	Maximum LST (K)	Minimum LST (K)
2003	301.18	315.23	288.71	299.83	314.09	281.45
2004	300.89	314.29	287.70	299.67	313.70	280.95
2005	301.16	314.60	287.99	299.91	313.70	287.12
2006	300.91	314.14	287.31	299.69	313.18	283.71
2007	300.93	314.16	288.30	299.67	313.39	284.42
2008	300.79	313.99	287.27	299.43	312.77	287.55
2009	301.43	314.72	282.39	300.17	314.49	280.66
2010	301.25	313.62	284.19	300.16	313.63	281.68
2011	300.63	315.42	249.47	300.25	315.66	267.48
2012	300.93	315.02	287.79	299.67	313.80	284.80
2013	300.97	314.51	289.05	299.72	314.01	284.95

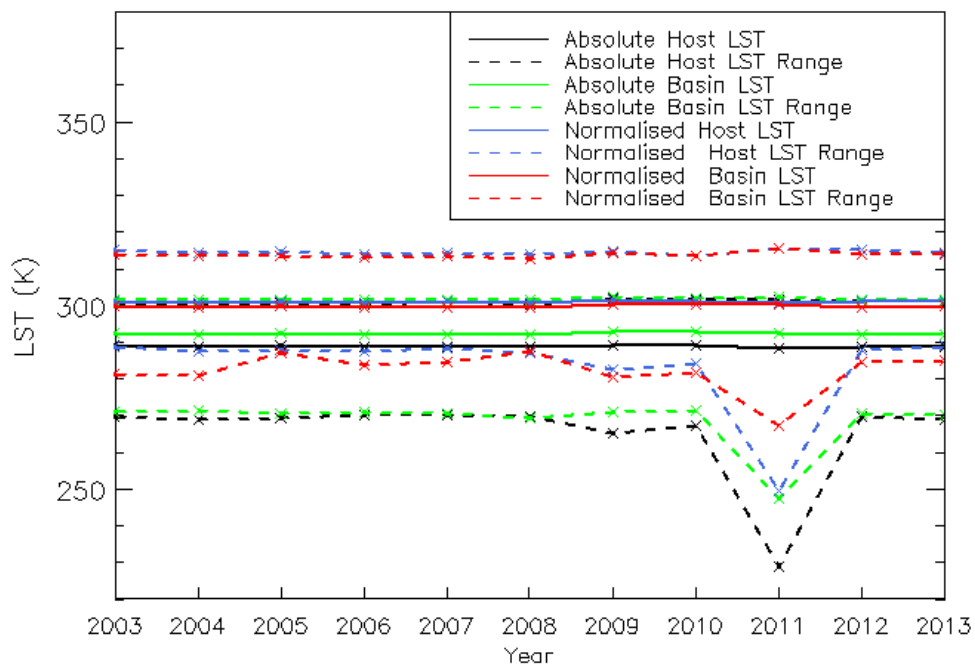


Figure 104: Absolute and normalised MODIS LST yearly means, as calculated from the Aqua dataset, from 2003 through to 2013 for the basin and host rock across the  $10^{\circ} \times 10^{\circ}$  grid of the Turkana region at  $0.01^{\circ}$  resolution.

### 5.1.5 Discussion

Linear regression analysis of LST and elevation is consistent with previous literature by identifying an inverse relationship (Coolbaugh et al., 2000; Calvin et al., 2005; Saraf et al., 2005; Miliareisis, 2009; Stroppiana et al., 2014). The greater distinction of this relationship at night has also been noted by additional studies (Fu and Rich, 2002; Pouteau et al., 2011; Van De Kerchove et al., 2013). The greater consistency of the relationship at night allows for improved correlations during this time and supports the use of such datasets over the day time equivalents at several points throughout this thesis. The improved night time relationship is useful when considering geothermal anomalies as it is suggested that the greatest contrast is to the surroundings at night due to the absence of direct solar influence (Coolbaugh et al., 2000; Miliareisis, 2009). Touched upon within this study, but not fully considered is the seasonal variation with respect to the LST dependence on elevation, which has been proven to be a significant factor in previous work (Stroppiana et al., 2013). Not fully accounting for this variation is potentially a major limitation in this study.

In terms of additional variation accounted for, the presence of the inverse linear relationship, regardless of biome; suggests that although land cover does play a role in modulating LST, that elevation is perhaps more dominant. The greater LSTs of bare soils on the extrapolation of data to 0 m elevation is, as expected during the day with the bare soils absorbing more radiation. However, this is unexpected at night as bare soils emit heat more rapidly. Further work is required to determine whether these findings are restricted to 2006 only and to whether the uncertainties within the datasets may affect the overall results and thus affect the disparity between the vegetated groups and bare soils.

Limitations within the linear regression analysis are now considered and include the presence of numerous plateaus within the datasets. These features are potentially associated to data skewing water bodies as discussed earlier. Masking to exclude lakes has been applied though is not always successful due to the discordance between shape files provided and the LST data. Furthermore, not all plateaus relate to lakes, with several appearing consistent with regions of higher elevation such as the Ethiopian Dome, making it difficult to distinguish between real and poorly filtered data plateaus.

Standard deviations do however provide a robust understanding of the variability within the datasets, with geothermal anomalies more likely to be identified when deviations are lower, i.e. during yearly and night time datasets. Such limitations may be overcome by applying the average tile LST mean to the lakes as opposed to making them. This is later discussed in further detail within Chapter 6.

Consideration should also be given to the assumed near constant nature of elevation. On the timescales within this study it is fully suitable but for applications of basin modelling along a geological time series, it is necessary to consider the elevation with respect to the active tectonic environment. For the ALB2 classification scheme, the effects of pixel mixing must be noted with a 1 km<sup>2</sup> area likely to be heterogeneous in terms land cover and therefore not fully represented by a singular classification.

Normalising the elevation via data provided from linear regression analysis has proven successful in correcting for its influence on LST. It has shown that elevation is responsible for masking the effects of other physical parameters; of which the extent is not fully recognised by additional analyses in this thesis, including PCA. The application of the elevation reduction has caused the significance of several features to diminish, though the overall surface structure across the dataset has been enhanced.

This has led to better identification of numerous features, including the Chew Bahir Basin and the locality of several volcanoes and calderas including Mount Elgon and the Bale Mountain volcanics of the Ethiopian Dome that were not previously considered as areas of warmer LSTs (Figure 98 through to Figure 101). However, it should be noted that this technique better identifies the more visible physiographic features such as Mount Elgon and the Ethiopian Dome as opposed to the more subtle distinction between basin and host rocks, which is more easily identified by absolute LSTs.

The plausibility of a geothermal anomaly is now considered with respect to the Mount Elgon transect (Figure 98). Here, the timing of the last volcanic activity is unknown; however, geothermal activity is still expected within the volcano's vicinity. This indicates the presence of upwelling magma, i.e. increased geothermal activity which will affect the LST as discussed in Chapter 1.1.6. Similar such activity can also account for the increasing LSTs towards the north throughout the region, as is consistent with

increasing age and therefore increasing crustal extension and mantle upwelling within the rift (Omenda, 1998). This is however not conclusive, with it entirely plausible that variables including surface emissivity are instead responsible for the LST variation.

This lack of ability to identify the additional factors driving increased heat flux is limiting within this analysis. A clear indication of the expected heat flux or predicted LST where geothermal anomalies are present is required. Throughout this thesis several parameters have been considered and it is now thought that the emissivity and the effects of elevated geothermal gradients are likely to be responsible for a number of increases in LST observed across the diagnostic transects, though once again this cannot be fully confirmed.

Emissivity has previously been identified as a dominant parameter during the PCA. It is closely linked to vegetation cover, land type and lithology (Rees, 2013) (Figure 34). Increased geothermal gradients are also linked to lithology, corresponding to upwelling mantle which in turn triggers volcanism (Ebinger, 2005) (Figure 3) Volcanics in this region are likely to be basaltic and therefore dark and thus of a lower albedo, which itself will influence emissivity (Dunkley et al., 1993). Therefore it is difficult to consider the variables in isolation. Moreover, it is difficult to determine whether the presence of such factors creates higher absolute LSTs than would otherwise be observed.

To summarise this section, application of the elevation correction has been successful. A number of previously masked features are now visible, though cannot be confirmed as geothermally associated due to the abundance of parameters that can be invoked to explain the variation. The following sections attempt to understand the features now identified as thermally anomalous by means of establishing a climatology to highlight persistent features and via a restricted PCA to understand the remaining variation within the LST.

## **5.2 Absolute and Normalised Climatology**

It is likely that geothermal anomalies are reasonably stationary, at least away from volcanic activity. Therefore, it makes sense to consider a climatology of data which

reduces the year to year variance. The climatology is now established monthly from 2003 to 2013 across the Turkana region (Figure 105 and Figure 106). The equivalent day time plots can be found in Appendix 9A and Appendix 9B. An example of the monthly means from each year for night time December 2003 through to December 2013 is additionally given in Appendix 9C to allow for better understanding of the variation within a given month across different years that contribute to the overall climatology. Day time and night time examples of anomaly plots are additionally provided in Appendix 10. Persistent features within the climatology and transient features within the anomalies are noted throughout. Here, only night time climatology plots are provided as the features are best illuminated at this time; without the influence of direct solar heating.

For both the absolute and normalised datasets, the same seasonal variation across the Turkana region is observed. It is found that the warmer months typically occur at the beginning and end of each year and the cooler months towards the middle of the year as has been noted previously (Danley et al., 2012).

Persistent features across the year, regardless of seasonal variation, are now noted. Disparity in these features is observed between the absolute and normalised datasets. This is not surprising given the dominance of elevation over the LST as identified by a number of previous studies (Coolbaugh et al., 2000; Saraf et al., 2005; Miliareisis, 2009).

From the absolute datasets it becomes clear that the northwest-southeast trending feature of warmer LSTs is dominant throughout (Figure 105). This consists of the low lying Turkana Trough and more specifically the immediate area surrounding Lake Turkana; which are persistently warm, regardless of seasonal effects. Moreover, a number of persistently cooler features are recognised including the uplifted Ethiopian Dome and Mount Elgon towards the south of the region. On normalisation, there is an apparent shift in the trend of warmer LSTs from the northwest-southeast trending Turkana Trough to the northeast-southwest trending area of Ethiopian Dome, Lake Turkana, Suguta Basin and Mount Elgon (Figure 106). This suggests that the features identified earlier for 2006 in the normalised LSTs are persistent.

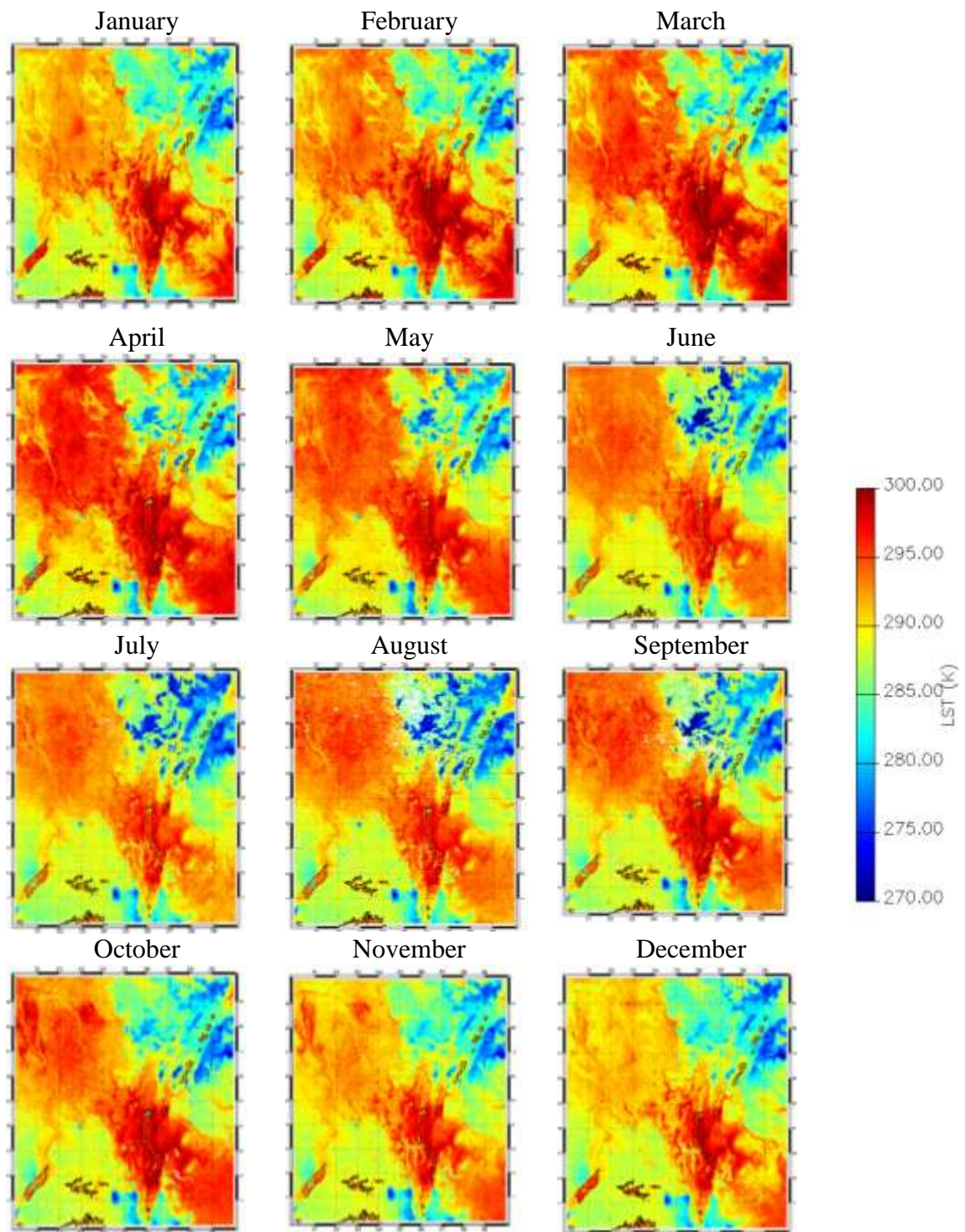


*Figure 105: Absolute, night time climatology, derived from the Aqua MODIS LST dataset for 2003 through to 2013, across the  $10^{\circ} \times 10^{\circ}$  grid of the Turkana region at  $0.01^{\circ}$  resolution.*

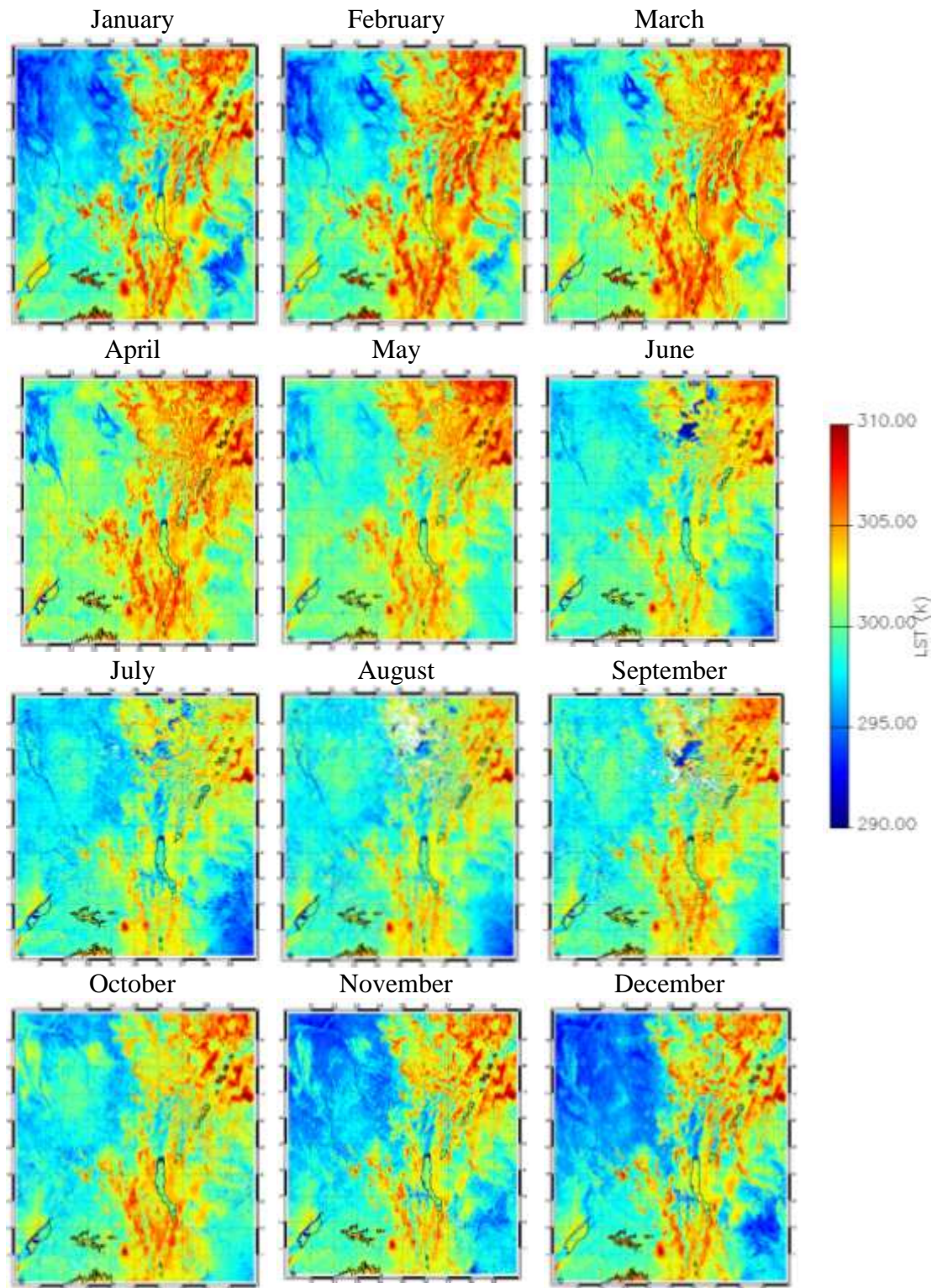


*Figure 106: Normalised, night time climatology, derived from the Aqua MODIS LST dataset for 2003 through to 2013, across the  $10^{\circ} \times 10^{\circ}$  grid of the Turkana region at  $0.01^{\circ}$  resolution.*

### 5.2.1 Discussion

The climatology has successfully identified regions of persistent LSTs throughout the dataset. The identification of these features, which include the Afar and Lake Turkana regions, are consistent with areas of thermal anomalies highlighted by previous research (Miliareisis, 2009; Miliareisis, 2012). The causes of such persistent features have also been addressed by earlier studies; with results suggesting but not conclusively confirming that geothermal activity within the region is one such parameter responsible for the increased LSTs. In addition to this, anomaly plots have highlighted transient features throughout the data. The causes of the transient features have not been extensively considered within this thesis; although it thought that such features may relate to weather events or volcanic eruptions.

The climatology and supporting anomalies have thus provided a means of assessing the plausibility of areas highlighted as thermal anomalies. Moreover, the features highlighted additionally act as a way to identify periods in which potential thermal anomalies may be minimised, for example as a result of the presence of a cooler, transient features. However, at this point it is important to consider the timescale of geothermal heat fluxes, which will determine what is considered anomalous. Where there is active sea floor spreading and volcanics, such as in the Afar region, the timescale are likely to be short and heat fluxes large, varying dependent on eruptive cycles. In contrast to this, where volcanoes are dormant, heat fluxes are unlikely to be large and the time over which they change is likely to be longer than more active regions.

Limitations within the climatology again concern the propagation of LST uncertainty that is not fully addressed within this thesis, as discussed earlier in Chapter 4. The approach of considering the plausibility of thermal anomalies is however helped by establishing the climatology and LST anomalies. However, validation in terms of ground measurements is still required as discussed in further detail in Chapter 5 (Aretouyap et al., 2016).

Climatology can therefore be concluded as a way of understanding the plausibility of geothermal anomalies. The following two sections now begin to delineate the normalised data further. Additional testing with respect to lithology is first considered

as this cannot be quantified within the PCA. A restricted PCA is then applied to the normalised dataset.

### **5.3 Lithological Comparison**

Lithology is expected to correlate to LSTs given it influences a number of surface parameters including thermal conductivity, thermal inertia and thermal diffusivity as described in Chapter 2. It now therefore considered with respect to LST to establish whether such a link is observed. Additionally, lithology is expected to correlate to surface emissivity, via influences on the land cover and albedo. Therefore lithology and emissivity are also contrasted. Given the identification of emissivity as a major component of the full PCA, it will also be interesting to understand whether this variance can be further delineated. Absolute and normalised LSTs and surface emissivity data is now compared to the USGS lithology files across the Turkana area (Figure 39).

From Figure 107 there is no apparent relationship between LST and lithology. The shift in LSTs when normalised is however evident for all rock types. The diurnal differences as a result of solar influence are also observed regardless of normalisation. Though distinct relationships are not observed between the LST and lithology, the maximum values of the normalised LSTs provide hints to what are the warmest lithological units. Here, it is found that igneous units are the warmest, followed by Quaternary and then Pre-Cambrian units. However, this must be viewed with caution as the plots only provide the range of LSTs and do not explain this data in terms of LST frequency nor the spatial distribution, which are required to progress this further.

For comparisons of lithology and emissivities, diurnal shifts are minimal (Figure 108). The magnitude of the emissivities varies dependent upon rock with emissivity channel 1 displaying higher values for lakes, igneous, Quaternary, Carboniferous-Jurassic, and Pre Cambrian units. Emissivity 2 instead displays higher values for Holocene, Mesozoic and Tertiary units. Conclusions cannot be made for the Cambrian-Carboniferous unit due to its absence. There are also a significant number of unmapped units which can also not be accounted for.

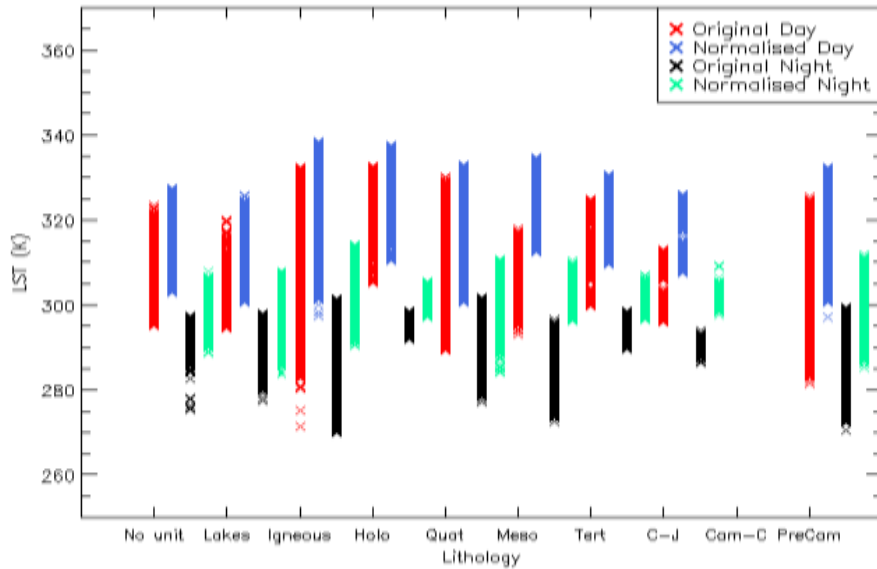


Figure 107: Lithology versus Aqua MODIS, mean LSTs for 2006, across the  $10^{\circ} \times 10^{\circ}$  grid of the Turkana region at  $0.01^{\circ}$  resolution. Lithology data has been supplied by Tullow Oil plc, as described in Chapter 3. No unit refers to a lack of mapped data. Abbreviations are as follows: Holo: Holocene, Quat: Quaternary, Meso: Mesozoic, Tert: Tertiary, C-J: Carboniferous-Jurassic, Cam-C: Cambrian-Carboniferous ad PreCam: PreCambrian.

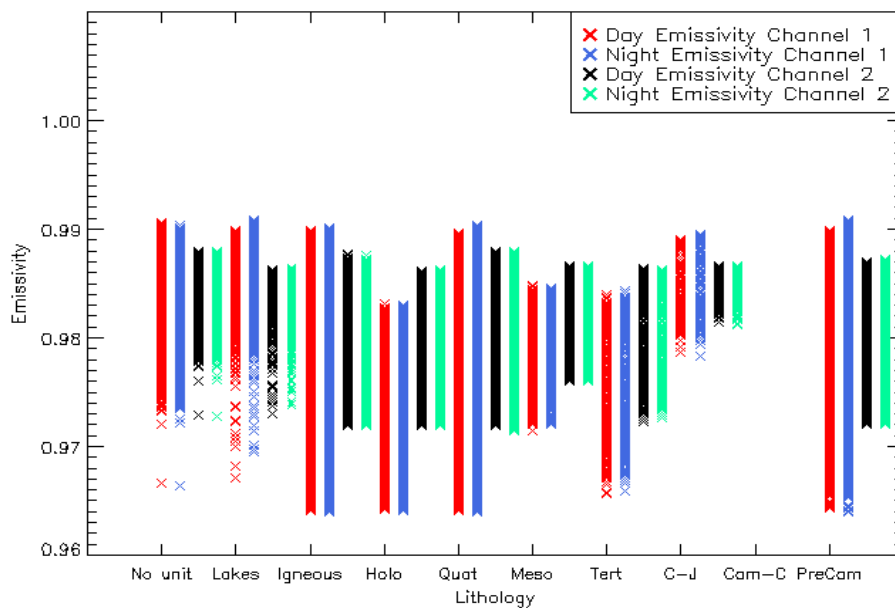


Figure 108: Comparison of lithology and Aqua MODIS, mean channel 1 and channel 2 emissivities for 2006, across the  $10^{\circ} \times 10^{\circ}$  grid of the Turkana region at  $0.01^{\circ}$  resolution. Lithology data has been supplied by Tullow Oil plc, as described in Chapter 3.

### 5.3.1 Discussion

Comparisons of LSTs and auxiliary variables to additional datasets have yielded few conclusive correlations. For lithology this is unexpected given that rock properties including porosity, grain size and composition directly influence LST. The study of maximum LSTs, does however, allow for some interpretation; though this should be done so with caution.

For example, the warmth of igneous rocks is pleasing given that such units will have originated from rift associated volcanism (Dunkley et al., 1993). When studying the lithology map outlined by the USGS (Figure 39), it is also apparent that a large proportion of the Turkana region is composed of such rocks. It is therefore plausible that the rocks contribute to the warmer LSTs. However, without identifying direct relationships, the discussion here is speculative at best. The normalisation of LSTs does not appear to have aided in establishing such links. It might therefore be that lithology is a lesser factor in terms of the overall LST signal.

Limitations within this study include the scale of the regridded lithology map (Figure 39) which is known to be coarser than the ESRI shape files outlined by the USGS (Figure 10). Therefore, the effects of pixel mixing will influence results. The abundance of only certain lithological units and the lack of both spatial and LST frequency considerations are also a hindrance in the identification of links between the auxiliary variables and lithology.

In addition to the parameters considered in this chapter, the TRMM precipitation dataset and the CCI soil moisture were also analysed with respect to LST and auxiliary variables but again yielded no additional information. For precipitation, this is surprising given the known inverse relationship with LST (Trenberth and Shea, 2005; Nunez et al., 2008; Wu et al., 2013) and additionally  $f_v$  (Leilei et al., 2014). The lack of conclusive links was also unexpected for soil moisture where an inverse relationship with LST exists (Smith et al., 2006; Ghent et al., 2010; Yao et al., 2013). An absence in links to emissivity and  $f_v$  are also inconsistent with the known relationships identified by previous studies (Mira et al., 2007; Dorigo et al., 2012).

From this analysis, none of the information retrieved is currently beneficial in the delineation of the LST signal. Given, that the variance within the restricted dataset has not been improved by this analysis, a restricted PCA is now run with the normalised dataset to improve the understanding of variance in the normalised LST signal.

#### **5.4 Restricted Principal Component Analysis**

Given that the application of the normalisation in Chapter 5 reveals considerable structure within the LST dataset, it is important to now delineate the remaining variance. It is hoped that by better understanding the reduced signal, further enhancements can be made to the identification of regions of unexplained variance that potentially correlate to geothermal anomalies.

PCA is now therefore rerun using the normalised data. The elevation variable has been removed as an input from the PCA as a result of the correction applied. The PCA is thus now generated from the four variables of emissivity channel 1, emissivity channel 2, fv and tcwv. This is once again completed on a monthly basis, as described in Figure 43. The magnitudes of PC scales once again vary as to best illuminate the features. This is dependent upon time of day and month as within the full PCA. Several features previously identified in the full PCA are still visible including parts of the Ethiopian Dome and the area around Lake Turkana. However, a number of features appear to have diminished post normalisation, including the Turkana Trough. However, the restricted PCA remains capable of resolving finer features such as rivers.

##### **5.4.1 Spatial Variation**

The normalised PCA results are shown for December 2006 only (Figure 109 to Figure 110 and Table 26 to Table 27). December has been chosen over the June dataset as less cloud cover is observed due to seasonal effects. Once again the majority of variation is accounted for within the first three principal components at 97 % to 98 % dependent upon month, regardless of diurnal effects. Variation of 97 % to 98 % is higher than the 94 % variation recorded by the first three components of the absolute PCA.

The two emissivities of different wavelengths are most consistently associated with PCs 2 and 3 for the normalised data; although dependent upon month, emissivities also show dominance in the first principal component. This contrasts to the absolute PCA where emissivity is strongly associated with PC1. The two emissivities at different wavelengths remain simultaneous for both PCAs. PC1 appears highly dependent upon month with either the pairs of emissivity channels or tcwv and fv displaying dominant. Fv is generally dominant in PC2, though this is less so when fv is most significant in PC1. This is unlike the absolute PCA, where fv is typically associated with PC3. Tcwv is typically the most associated in PC4, as consistent with the absolute PCA.

A number of features are also noted with the normalised PCA and again include the Suguta Valley, Chalbi Desert and the Chew Bahir Basin as previously analysed via linear regression analysis. The area of abundant bare soils around Lake Turkana continues to be highlighted throughout via emissivity and fv dominated components. Less obvious in the normalised PCA is the Turkana Trough and the Ethiopian Dome, as to be expected. However, the Ethiopian Dome and additionally Mount Elgon are partially highlighted by certain principal components. This includes the day PC1 of June for the Ethiopian Dome where tcwv and fv are dominant and the day PC3 of June for Mount Elgon where both emissivities dominate. Similar observations are made throughout the dataset.

#### **5.4.2 Discussion**

The restricted PCA is shown to still successfully identify variation within the LST signal. This is most obvious for the Turkana region, where emissivity varies (Figure 44). This can be seen when contrasted to the normalised climatology (Figure 106). However, it is not possible to conclude whether this is emissivity related or a result of unexplained variance, not accounted for within the PCA. Moreover, it is also difficult to distinguish between the host rock and basins in terms of emissivity and therefore the PCA fails to distinguish between such regions; although, the area of basins surrounding Lake Turkana is particularly well-defined, with this likely associated to biome and vegetation.

Table 26: Normalised PCA results for the Turkana region of MODIS LST Aqua data for December 2006 day time. The Turkana region is a  $10^\circ \times 10^\circ$  grid of  $0.01^\circ$  resolution.

Component	Eigenvalue	Variance (%)	Cumulative (%)	Component Loadings			
				Emissivity 1	Emissivity 2	tcwv	fv
1	2.04	51.49	51.49	0.79	0.81	-0.33	0.72
2	0.97	24.47	75.96	0.68	0.57	-0.21	-0.55
3	0.87	21.86	97.82	0.68	0.57	0.21	0.55
4	0.09	2.18	100.00	0.17	0.10	0.96	0.04

Table 27: Normalised PCA results for the Turkana region of MODIS LST Aqua data for December 2006 night time. The Turkana region is a  $10^\circ \times 10^\circ$  grid of  $0.01^\circ$  resolution.

Component	Eigenvalue	Variance (%)	Cumulative (%)	Component Loadings			
				Emissivity 1	Emissivity 2	tcwv	fv
1	1.95	49.15	49.15	0.78	0.80	-0.31	0.70
2	1.02	25.82	74.97	0.70	0.58	-0.16	-0.57
3	0.88	22.30	97.27	0.81	0.97	0.08	0.22
4	0.11	2.73	100.00	0.11	0.03	0.98	0.03

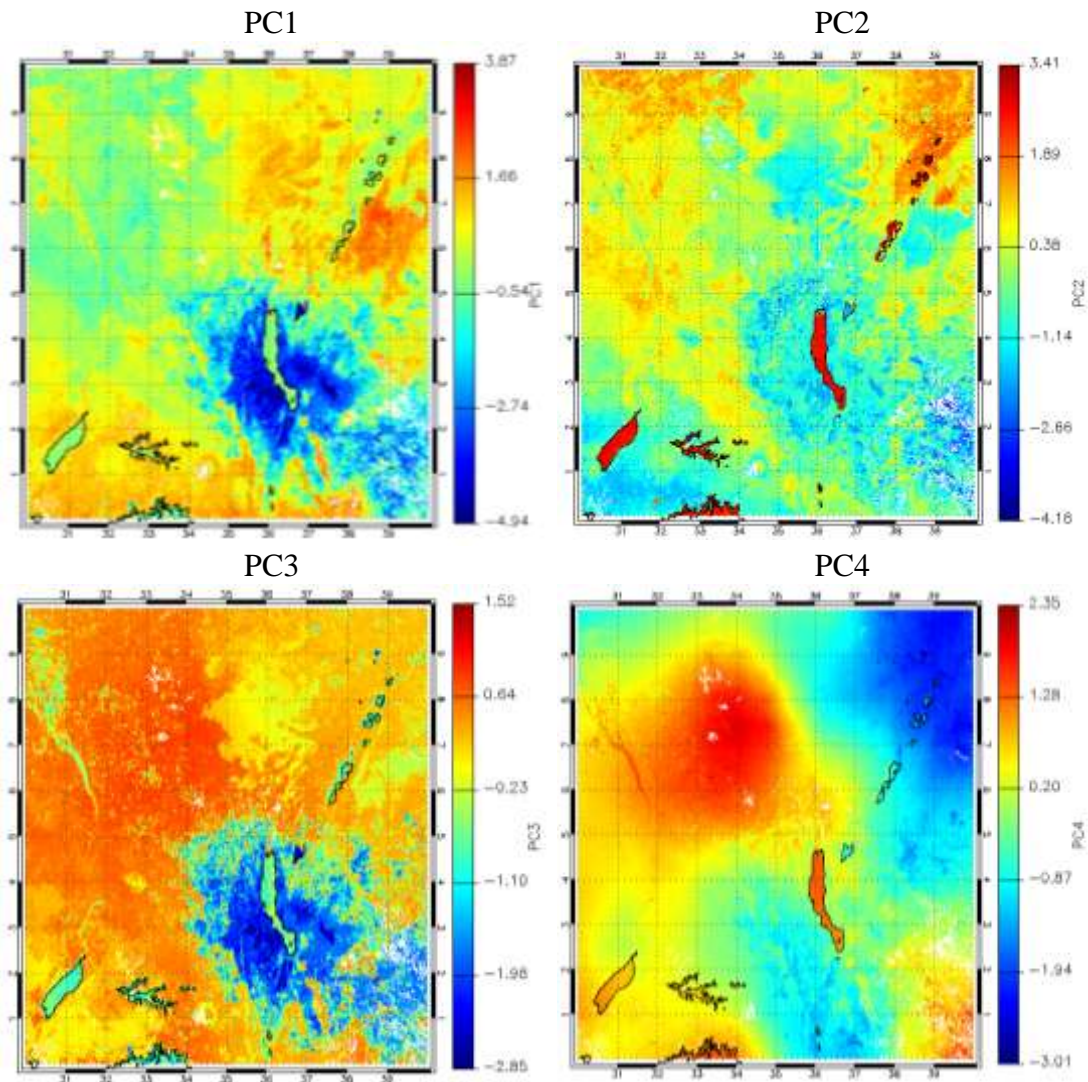


Figure 109: Principal components for the normalised PCA with respect to the MODIS LST day time December 2006 Aqua data, across the  $10^{\circ} \times 10^{\circ}$  grid of the Turkana region of  $0.01^{\circ}$  resolution. (a) PC1, (b) PC2, (c) PC3, and (d) PC4.

Additional variation in the vegetation itself has been attributed to growth cycles, with certain months more sensitive than others. This requires further spatio-temporal analysis to fully understand. Patterns in the tcwv are also observed to affect the normalised LSTs (Figure 106). The tcwv is shown to affect the central Turkana tile (PC4 in Figure 110). The identification of positive anomalies in this area would therefore be considered suspicious and likely the result of errors in the retrieval. Additional limitations within this PCA are much the same discussed for the full PCA, within Chapter 4.3.

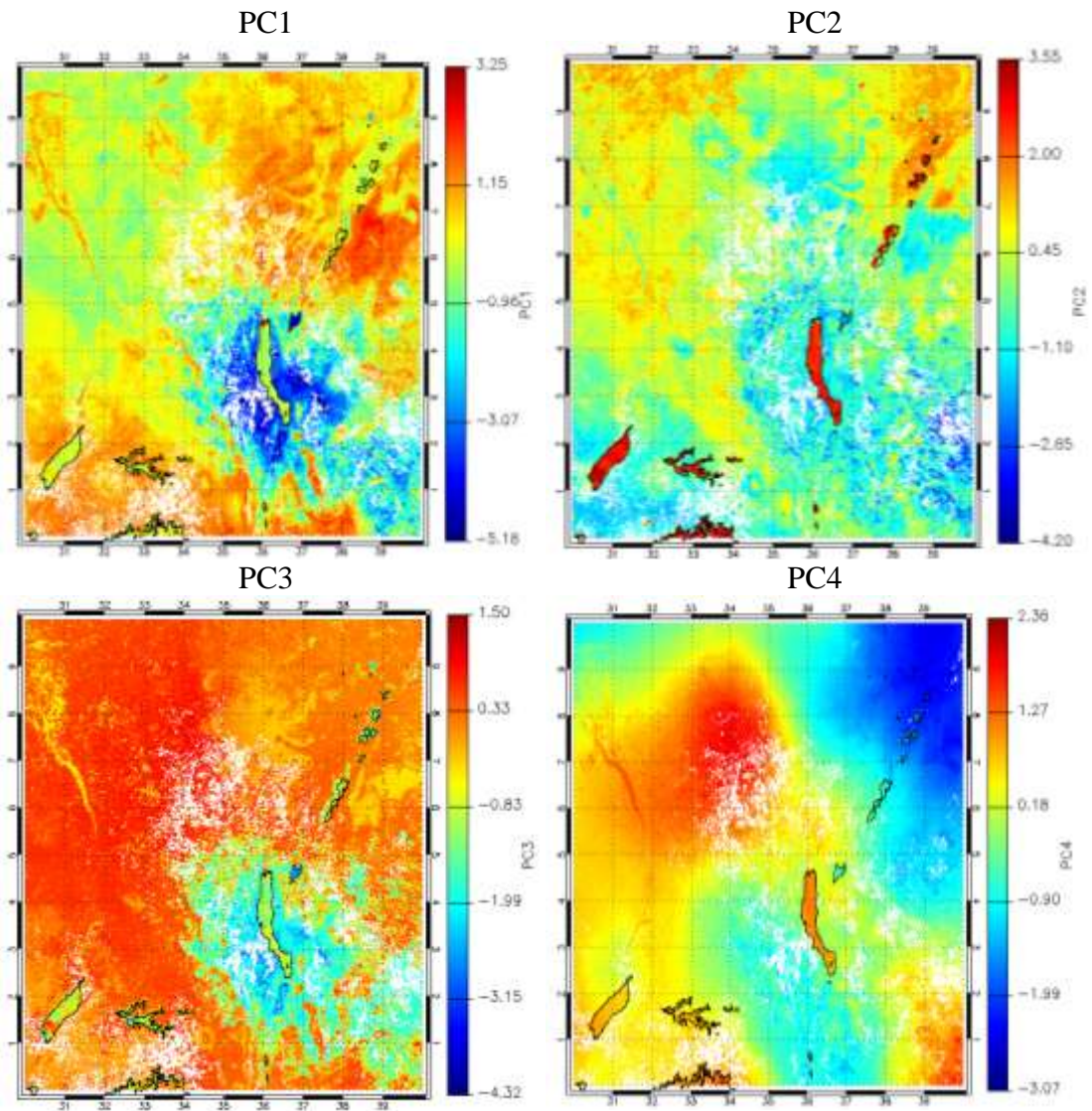


Figure 110: Principal components for the normalised PCA with respect to the MODIS LST night time December 2006 Aqua data, across the  $10^{\circ} \times 10^{\circ}$  grid of the Turkana region of  $0.01^{\circ}$  resolution. (a) PC1, (b) PC2, (c) PC3, and (d) PC4.

The restricted PCA can thus be concluded as a useful tool, still capable of delineating variation within the LST signal post normalisation. Further work is still necessary to reduce the noise generated from additional physical parameters as opposed to the geothermal anomalies. This therefore requires that the unexplained variance in the dataset is fully accounted for in terms of LST influencing parameters that can be quantified.

## **5.5 Summary of Results**

Following the identification of elevation as dominant variable, a correction has been successfully applied to produce a normalised LST dataset. The normalised dataset reveals the presence of several warmer features previously overlooked. The persistent heat flux within these areas has been confirmed by the climatology and supported by anomaly plots. The variables responsible for this increased heat flux however, remain unidentified. Additional studies including the comparison of LST with lithology have highlighted potential links but have failed to conclusively assign a dominant parameter. Consequently a restricted PCA that excludes elevation has been employed and reveals that emissivity is again significant. However, once more this cannot be conclusively confirmed as the most significant variable in terms of LST as the study fails to account for the unexplained variance that potential elevated geothermal gradients are expected to contribute to. Further work is again required to delineate the LST signal and thus is later considered within Chapter 6.1.

## **6. Conclusions and Future Work**

The main objectives of this thesis were as follows:

3. To remotely identify the locality of hydrocarbon basins within the East African Rift system.
4. To delineate the LST signal and determine the most dominant factors with respect to this; in order to delineate potential regions of geothermal activity.

These objectives are now considered within the context of the thesis findings, as summarised below. The implications of this work have also been considered, both in terms of academic research and commercial interest. Future work to progress and further support the conclusions reached within this thesis is then also discussed, with the steps expected to be most beneficial clearly highlighted.

### **6.1 Summary of Findings**

LST across the EARS is a dynamic parameter that varies both spatially and temporally. The generation of a LST time series from January 2003 to December 2013 has successfully highlighted the warmest areas across the region. These warmer regions have subsequently been shown to coincide with the previously identified rift basins across the EARS that typically lie at lower elevations; thus successfully achieving the first objective within this thesis. Moreover, the generation of this LST dataset is also a useful tool energy companies can use in terms of input parameters for basin modelling. However, it remains difficult to isolate geothermal anomalies with respect to LST variation.

It has therefore been important to understand the origin of the variation within the LST signal in order to identify the areas of unexplained variance that are more likely related to the geothermal anomalies; as stated via the second objective within this study. Delineation of the LST signal has thus been analysed via PCA, which positively highlights both spatial and temporal variation, with respect to the five variables of elevation, emissivities at two wavelengths within the infrared region, fractional

vegetation and total column water vapour. From this, it is concluded that elevation is the most dominant component with respect to the LST, as consistent with previous literature.

In light of the identification of elevation as the dominant driving factor in terms of LST, it has been corrected for using gradients derived from linear regression analysis of LST elevation to recalculate the LSTs to equivalent LSTs at 0 m. The resultant dataset shows enhanced structural features not previously identified, including several warmer features that correspond to numerous volcanics and rift flanks. The persistence of these features is positively identified by the climatology, which records the long term signature of thermal anomalies, i.e. the anomalies that are most likely to be geothermal in nature, than the year-to-year anomalies.

The work in this thesis has identified a number of features worth exploring as more likely to exhibit geothermal anomalies, partially fulfilling the goal of the second objective. This includes the six persistently warmer basins of South Kerio, Suguta, Lokichar, Turkana, Afar and Melut, which additionally correspond to the known regions of geothermal activity and hydrocarbon prospects. Moreover, the PCA anomalies of the Suguta Valley, Lokichar-Turkana basins, Chalbi Desert and Chew Bahir Basin are also worth future considerations showing similar such warmth to the six persistent basins. The discovery of several volcanoes in normalised space, including Mount Elgon and the Bale Mountains of the Ethiopian Dome, are also worth investigation given the now known higher heat fluxes. Finally, the LST gradients identified via the normalised transects should also be explored further as it is likely this will help reveal the influence of the rift, varying dependent upon crustal thickness and mantle proximity.

The remaining variance within the normalised LST is then successfully revealed via the application of a restricted PCA. From this it is concluded that surface emissivity is most dominant in the absence of elevation. The patterns of variance highlighted by the emissivity are found to positively correspond to patterns within the normalised climatology. It is therefore plausible to conclude that in order to fully delineate the signal and identify areas of true unexplained variance, thus fully achieving the second objective within this thesis; it is necessary to incorporate additional, quantifiable factors

with the aim of increasing the signal to noise ratio; where the geothermal anomaly is the signal.

## **6.2 Implications of this study**

This study has several implications, both in terms of academic research and commercial interest. In terms of the scientific implications of this study, it has been proven that the LST over the EARS is a dynamic parameter that is dependent upon a number of input parameters, most notably elevation and emissivity. The identification of such parameters as dominant will be beneficial when modelling land surface dynamics across the region. This study has in essence identified a set of known variables that must now be accounted for in order to fully reveal geothermal anomalies across this region and has subsequently ordered them in terms of their significance.

In terms of the commercial interest, this thesis has provided an extra dimension to the initial desk study implemented by oil companies. For example, the absolute mean LST datasets can now provide a means of identifying certain landforms such as basins and mountains, which are significantly affected by topography. The normalised LST dataset can in comparison, identify more geologically interesting features, such as areas of increased volcanic heat flux. Not only will the identification of such areas prove useful in terms of understanding hydrocarbon prospects that are known to coincide with elevated geothermal gradients; but it will also be beneficial for other sectors within the energy industry, including that of geothermal energy production. This will become ever more important with the search for more renewable ways to generate power.

In addition to this, the LST mean dataset generated within this study could provide input values for basin models that currently utilise set values across large swaths of the EARS. The new LST values generated by this study could therefore help constrain models and improve accuracy, with the current models not accounting for differing LSTs across the region. Variations between day time and night time datasets, as well as the corresponding maximum and minimum LST values, could also provide best and worst case scenarios in terms of hydrocarbon prospects within a given region. This will be further enhanced by the use of the normalised dataset, which provides a more

delineated signal with respect to the elevation and thus increases the likelihood of an area being identified as geothermally anomalous with respect to its surroundings, which is vital in terms of hydrocarbon exploration.

### **6.3 Future Recommendations**

Several approaches to improve and progress the results attained within this thesis are now discussed. Consideration is also given to the use of additional datasets to enhance the understanding of the origin of the LST variation. An approach to minimising the limitations caused by a lack of uncertainty analysis is also addressed.

All were considered in terms of their importance with it concluded that normalisation with respect to emissivity and uncertainty analysis were the two improvements which would most benefit the progress made within this thesis. Additional normalisation would further delineate the signal revealing higher order, unexplained structures that could potentially be related to geothermal activity. Uncertainty analysis would also be valuable to understand the certainty in LST observations. These two improvements would significantly improve the accuracy of any interpretations made from basin models for Tullow Oil plc and would additionally enhance the understanding of LST dynamics across the EARS. All improvements are now discussed, in order pertaining to the thesis structure.

#### **6.3.1 Improvement of absolute LST dataset**

Several additional steps of analysis could be considered to improve the overall accuracy of the absolute LST dataset and thus the subsequent datasets derived from this. For example, the current masking of basins by removing them from the LST dataset is often flawed by the misalignment between LST and lake shape files, as provided by Tullow Oil plc (2016). Therefore to improve the LST dataset, lakes could instead be masked using the overall tile mean. This approach would not alter the tile mean value itself and would additionally avoid skewing the results, via distorted LSTs that have likely arisen as the result of winds and currents over the lakes.

Furthermore, the way in which cloud cover is considered throughout this thesis should be rethought. This is as clear sky biases currently applied to the dataset distort the LST means reported. In addition to this, by not reporting the number of cloud free pixels within a scene or the number of cloud free pixels within a calculated mean, it is difficult to fully interpret the data as there is continuously an element of uncertainty in the sampling. To minimise the effect of this, an index reporting the number of cloud free observations to the total number of observations would be beneficial; providing an insight into the effects of sampling on the results. It would be most useful to calculate this index number throughout the thesis from the initial daily LSTs through to the monthly and yearly mean LSTs and finally, the PCA. This would additionally provide some context to the uncertainties that could be expected within each pixel and tile mean accordingly. Reporting such an index may also help explain some of the anomalously low minimum LST values observed throughout that are thought to originate from cloud cover issues.

### **6.3.2 Uncertainty Analysis**

Uncertainty analysis is also an area where this study could be improved. It is necessary to understand the uncertainties within the datasets to determine the accuracy of the results obtained. For LSTs the uncertainties can be obtained from the MODIS LST uncertainty product. This dataset was briefly considered within this thesis on a qualitative basis, i.e. areas that more typically had greater uncertainties during the daily data streams were viewed with greater caution in the final results. In order to enhance the understanding of the accuracy of the datasets presented here, the MODIS LST uncertainty product should be propagated to account for monthly and yearly averages. In turn this uncertainty should be carried through to the normalised and PCA results. Further uncertainty analysis is also required with respect to the auxiliary variables used within this thesis, with uncertainty estimates taken from the respective datasets.

### **6.3.3 Verification of Geothermal Anomalies**

In addition to the uncertainties provided as auxiliary data, validation by ground based measurements is ideally required in order to understand the accuracy of the satellite data used and to fully confirm the presence of the identified geothermal anomalies. This validation could take the form of several field measurements including seismic refraction and reflection, magnetics, gamma ray spectroscopy, gravimetric thermal and direction current approaches as described in Aretouyap et al. (2016).

### **6.3.4 Progression of PCA**

PCA analysis has proved successful in identifying the dominant drivers given the five variables provided. Therefore enhancement of this technique, on a dataset normalised with respect to elevation and emissivity, should incorporate additional parameters to further delineate the LST signal. Given that there is no plausible means by which to account for the elevated geothermal gradients and corresponding geothermal anomalies, the PCA requires the application of all known and quantifiable parameters in order to reduce the noise from these components. The geothermal signal present in the residual of the PCA might then emerge more strongly and with more confidence in the results found.

For example, the datasets of CCI soil moisture and TRMM precipitation should be incorporated as input values for PCA. This would be beneficial as the correspondence of these values to component loadings and thus their influence on LST has already been identified. Therefore by including them within the PCA, a further component of noise within the LST signal would be accounted for and explained, reducing the area of unexplained variance that is thought to correspond to geothermal anomalies.

Furthermore, the application of the PCA with respect to the topographic parameters of slope and aspect, as detailed in Chapter 2.3.8, should be considered. This would prove beneficial by further delineating the impact of elevation and better characterising the topographic relationship. This would again reduce the influence of parameter noise, i.e. factors not yet incorporated into the PCA. The slope and aspect datasets could be generated via the application of the slope and aspect tools within ESRI ArcGIS to a

DEM of the region. It likely that this would require regriding to the same spatial resolution of  $0.01^\circ$  of the MODIS LST product, as was required for the USGS ESRI lithology shape files.

In addition to physical parameters, the effects of temporal variation should also be accounted for as highlighted as significant by the time dependence of component loadings and via the climatology. This has been previously applied by Miliareisis (2009) across the Afar Depression. This study improved the identification of geothermal anomalies as a result of minimising seasonal variation to reveal transient areas of increased volcanism. A similar approach could be applied to this dataset using LST frequencies and PCA with respect to understanding the variation. A temporal correction could then be applied in order to normalise the dataset and maximise the recovery of potential geothermal anomalies.

A significant need is to also further investigate advanced PCA methods including calculation and plotting of residual data. This approach has previously been successfully applied by Miliareisis (2013) across areas that are geographically and geologically similar to the EARS, though only using absolute LSTs. Therefore the calculation of residual data with respect to the normalised dataset generated within this thesis could advance this technique further and provide a better understanding of the unexplained variance thought to correspond to geothermal anomalies.

### **6.3.5 Progression of the Normalisation of LST**

The normalisation of the LST can progressed in a number of ways, including via the correction of both physical and temporal parameters as previously mentioned. It can additionally be analysed further, considering the probability of an area being warm with respect to its surrounding throughout a given time period. These two branches of improvement are both now considered.

### **6.3.5.1 Normalisation with respect to Emissivity**

Normalisation with respect to emissivity is potentially the most important aspect of future work to be considered. Emissivity is the next logical parameter to consider, given that the two channels of emissivity were identified as equally dominant within the normalised LST dataset, i.e. in the absence of elevation. Therefore delineating this additional variable should further reveal higher order structures of unexplained variance within the LST dataset that could potentially correspond to increased geothermal activity.

In order to account for emissivity, both channels would need to be considered individually as both reveal differing structures and have varying uncertainties as a result of the different MODIS bands from which they are measured; as previously noted in Chapter 4.1.1.1. For example, the previously normalised LST dataset with respect to elevation should then be normalised with respect to Channel 31 of the MODIS emissivity dataset. This could be applied in a similar manner by calculating the relationship and corresponding gradient between LST and emissivity. The result of this could then be applied to calculate the LST at a given emissivity, for example either zero or one, where one is a perfect black body. The same technique but using channel 31 emissivity data could then be applied to the resultant LST data normalised with respect to both elevation and channel 31 emissivity.

Following the generation of a LST dataset normalised with respect to elevation and both channels of elevation, further PCA would be required to identify the next most dominant factor. This delineation of the LST can thus be seen as continuous iterative process, provided quantifiable datasets that influence LST are available. For factors such as lithology further steps would need to be taken in order to account for them within the normalisation. For example, lithological units could be assigned an index value; though the accuracy of the resultant data would need to be carefully analysed as to not remove the data from its true value.

### **6.3.5.2 Probability Mapping**

An additional approach to improve the understanding of the LST signal could be to study the most persistent features highlighted in the normalised climatology. Geothermal anomalies, as has been noted, are expected to present themselves in areas of persistent warmth. Therefore if the probability of a region being warm can be established, the search area for potential geothermal anomalies can be reduced and the definition to what is considered a geothermal anomaly enhanced.

The generation of this probability should be determined by identifying the warmest 10 % of pixels for a given month within the climatology. This can be further analysed to determine which pixels are within the top 10 % of warmer LSTs throughout the year, i.e. there is a high probability that this region will be warm regardless of diurnal shifts or seasonal patterns. This approach can then be used to determine the pixels that are found to be warmer 90 % to 99 % of the time and so forth, establishing a probability of warmth map.

### **6.3.6 Alternative LST Sensors**

Further to the MODIS data used within this study, data streams from additional satellite sensors could also be utilised to both compare and contrast results, and to also provide an extra dimension to the results obtained within this thesis; for example, increasing the temporal and spatial resolution of the data. The following now considers two additional datasets that could build upon the results obtained from the MODIS dataset. They are the higher temporal resolution SEVIRI data and the higher spatial resolution Landsat data.

#### **6.3.6.1 SEVIRI**

SEVIRI data is taken from the Meteosat series of satellites, which are in geostationary orbit 36,000 km above the equator and collect data on 15 minute cycle across Europe and northern Africa (EUMETSAT, 2016). The instrument of interest on board is SEVIRI – the Spinning Enhanced Visible and Infrared Imager. SEVIRI is one of a pair of instruments found on the Meteosat satellites that observes in 12 spectral channels of

which eight channels are in the thermal infrared at a resolution of 5 km (EUMETSAT, 2016). The data obtained from this series of satellites could be incorporated to improve the understanding of thermal inertia, which is touched upon but not extensively covered within this thesis.

The LST data retrieved from SEVIRI could be used to develop a more diurnal approach looking at shorter timescales on a daily basis applied over a more localised region of interest. This will initially be applied to a smaller area of interest, not on a regional scale. Likely candidates for such analysis could include the area surrounding Lake Turkana to better understand the cause of the LST variance. It would be hoped that one such outcome of this could show clear diurnal LST cycles from which land types could be distinguished.

Moreover, the clearer diurnal cycles observed could provide better estimates of thermal inertia. This could improve the understanding of several aspects within this study including the effect of lithological units. This could particularly help in determining whether Holocene and Quaternary sediments such as in the Suguta Valley, Chalbi Desert and Chew Bahir Basin, are the sites of greatest potential geothermal anomalies.

At 5 km, the resolution of SEVIRI is coarser than that approximate 1 km resolution of the MODIS LSTs. However, given that numerous features identified throughout this thesis are several grid points wide, it is thought that 5 km is of sufficient resolution for this purpose.

#### **6.3.6.2 Landsat 8**

In contrast to the coarser SEVIRI dataset, higher resolution LST datasets could also be employed within this study. For example, NASA's Landsat 8 dataset could be analysed as an alternative to the MODIS datasets. Landsat 8 is the latest in a series of NASA Earth observation satellites and was launched in February 2013 in a 705 km sun-synchronous orbit. It images the entire Earth every 16 days, in an 8-day offset from Landsat 7 (USGS, 2016). Aboard Landsat 8 are two instruments: the Operational Land Imager (OLI) and Thermal Infrared Sensor (TIRS). OLI collects data for nine shortwave spectral bands, all with spatial resolutions of either 15 m or 30 m. In contrast to this,

TIRS measures long wavelength thermal infrared emitted from the Earth's surface, using two thermal bands at 100 m spatial resolution (USGS, 2016).

Using finer resolution data from both OLI and TIRS would enable smaller geographical and geological features to be identified. For example, the yearly LST datasets within this study are unable to resolve features such as the Turkwel River. It is possible that by increasing the resolution available, that such features would become visible throughout, even post-averaging and thus would increase the information that can be interpreted from the plots. The increased resolution of the LST dataset would again also be beneficial for energy companies, with potential areas of interest more accurately pinpointed. This would help reduce the areal extent of potential sites of further exploration, thus increasing efficiency and lowering costs.

In addition to the aforementioned, Landsat 8 data also be utilised in conjunction with the earlier satellites that initially launched in 1972 (USGS, 2016). The Landsat series was launched to provide the most continuous temporal record of moderate resolution multispectral data of the Earth's surface across a global basis. This historic record would allow for other elements to be considered, including that of climate change within the region; providing a much more thorough temporal outlook in comparison to the smaller temporal range of MODIS.

#### **6.4 Summary of Conclusions**

Overall, this study can therefore conclude that satellite-derived LST is a useful exploration tool especially for the mapping of rift basins across the broad and inaccessible EARS. A LST dataset now exists for use within basin modelling across the area; although the study itself fails to confirm the locality of basins with an increased probability of hydrocarbon accumulations. Delineation of the variables that contribute to the LST signal finds that the effects of elevation, closely followed by that of surface emissivity are most dominant. Use of elevation-normalisation of the LST has identified some warm features which are more likely to be geothermal anomalies, but these need to be interpreted in conjunction with the remaining normalised LST variances identified through the restricted PCA. Future work to enhance and progress the study should now

include further delineation of the LST signal to identify variables whose correction would significantly increase the signal to noise ratio in residual or reconstructed LST images, where the signal is the geothermal anomaly.

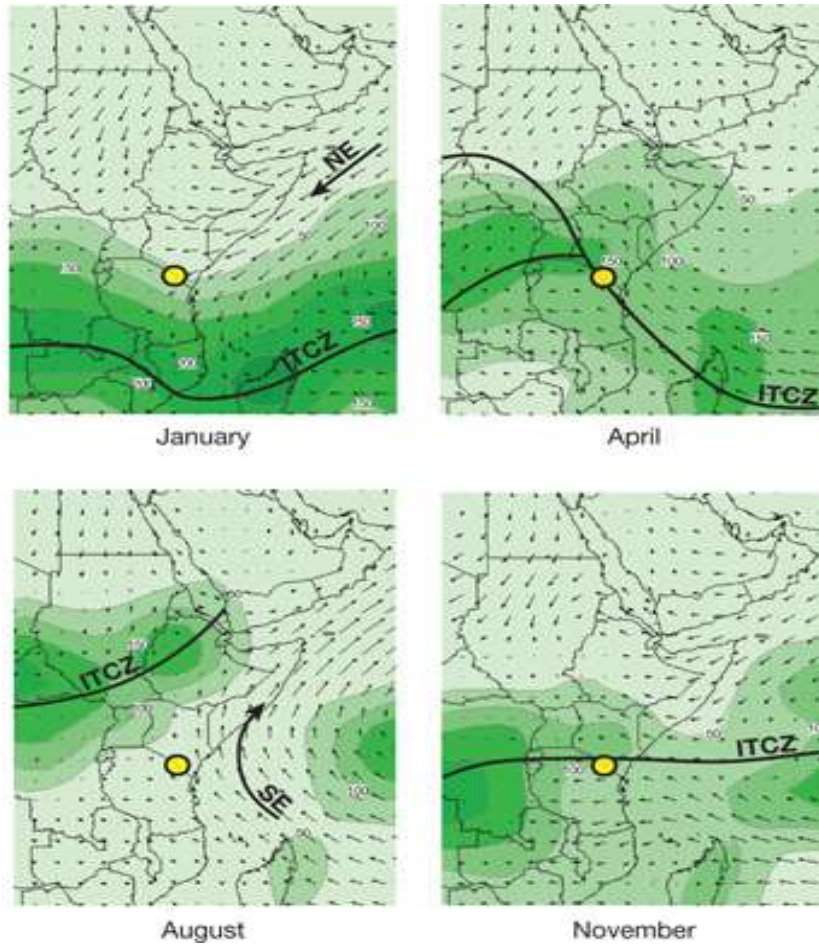
# Appendix

**Appendix 1.** Table detailing all rift basins within the EARS region, as provided by Tullow Oil plc and as shown spatially in Figure 5. The ages for geological periods can be found in the beginning of this thesis.

Basin	Basin age	Central coordinates of basin	
		Latitude (° N)	Longitude (° E)
Adama	Cenozoic to recent	8.86	39.84
Addo-do	Cenozoic to recent	10.16	40.96
Addo-do North	Cenozoic to recent	10.74	41.27
Afar Area	Cenozoic to recent	10.06	39.84
Albertine	Cenozoic to recent	1.75	30.86
Fantale-Dofan	Cenozoic to recent	9.62	40.31
Gatome	Cenozoic to recent	4.38	35.30
Lake Edward	Cenozoic to recent	-0.38	29.73
Lake Eyasi	Cenozoic to recent	-4.08	34.26
Lake Manyara	Cenozoic to recent	-3.63	35.86
Lake Kivu	Cenozoic to recent	-1.90	29.23
Lokichar	Cenozoic to recent	2.71	35.77
Lokichar west	Cenozoic to recent	2.19	35.39
Lotikipi	Cenozoic to recent	4.12	34.76
Lotikipi east	Cenozoic to recent	3.20	35.24
Magadi Trough	Cenozoic to recent	-2.02	36.16
Malawi	Cenozoic to recent	-11.92	34.47
Mikumi South	Cenozoic to recent	-8.37	36.43
Nyanza Trough	Cenozoic to recent	-0.25	34.57
Rukwa	Cenozoic to recent	-7.78	32.03
South Kerio	Cenozoic to recent	0.81	35.69
Suguta	Cenozoic to recent	0.91	36.17
Tanganyika	Cenozoic to recent	-6.06	29.85
Turkana	Cenozoic to recent	4.55	36.08
Usangu	Cenozoic to recent	-8.43	34.20
Usangu North	Cenozoic to recent	-7.10	35.66
Ziway-Shalla	Cenozoic to recent	8.11	39.05

Adigala - north	Mesozoic	10.60	42.07
Adigala - south	Mesozoic	10.08	42.03
Anza Graben	Mesozoic	2.27	38.22
Melut East	Mesozoic	9.55	33.58
Melut West	Mesozoic	7.26	32.72
Mongalla	Mesozoic	5.50	32.18
Melut	Late Jurassic Cretaceous	8.93	33.27
Pibor Post	Late Jurassic Cretaceous	6.90	33.56
Cabora Bassa	Early Karoo	-16.05	31.71
Mano Pools?	Early Karoo	-15.31	30.28
Ruhuhu	Early Karoo	-10.20	35.28
Cuvette Congolese	Karoo	-2.99	26.38
Cuvette extension?	Karoo	-8.68	25.04
Luangwa	Karoo	-12.24	32.12
Luama	Karoo	-4.96	28.55
Luhombero	Karoo	-8.60	37.05
Lukusashi	Karoo	-14.40	29.94
Mandawa	Karoo	-9.92	39.33
Mikumi	Karoo	-6.79	37.30
Mombasa	Karoo	-3.25	39.36
Remnant-Bugiri	Karoo	0.56	33.73
Remnant-Dagusi Is.	Karoo	0.15	33.57
Remnant-Entebbe	Karoo	0.06	32.45
Rovuma Trough	Karoo	-11.78	35.41
Rufiji	Karoo	-7.82	38.45
Ruhuhu	Early Karoo	-10.20	35.28
Ruhuhu extension	Karoo	-10.66	34.27
Ruvu	Karoo	-6.46	38.66
Selous	Karoo	-9.88	37.28
Zambezi	Karoo	-17.19	34.64

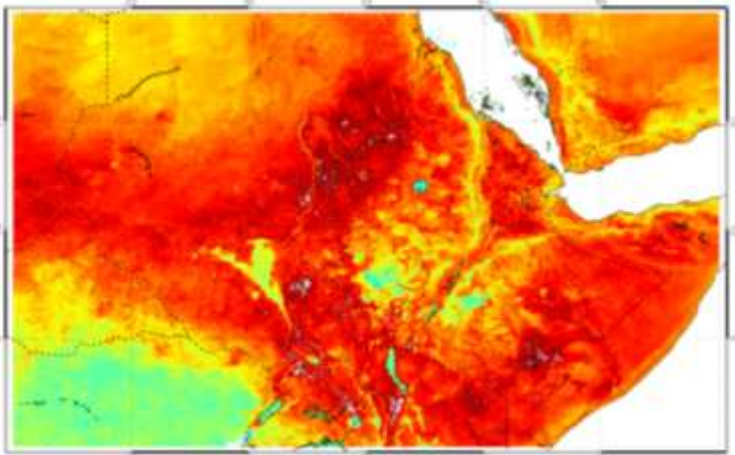
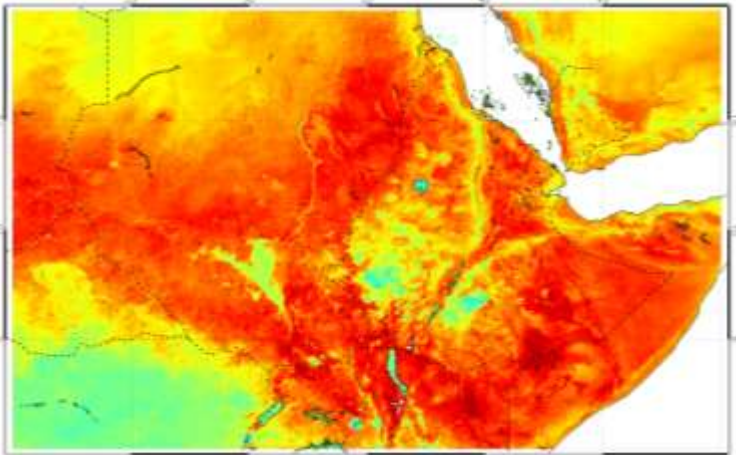
**Appendix 2.** Insets from Figure 23 showing a more detailed look at the influence of the ITCZ, as taken from Verschuren et al. (2009). Four representative months are shown to best highlight the ITCZ migration and associated precipitation (green – contours at 50 mm intervals). The associated rainfall is based upon gauge data over land and satellite data over the sea. Wind fields are also shown (arrows), with speed proportional to arrow length.



**Appendix 3A.** Monthly MODIS LSTs, for the day time, 2006 Aqua dataset, across the Afar region that is on a 30° x 20° grid of 0.01° resolution.

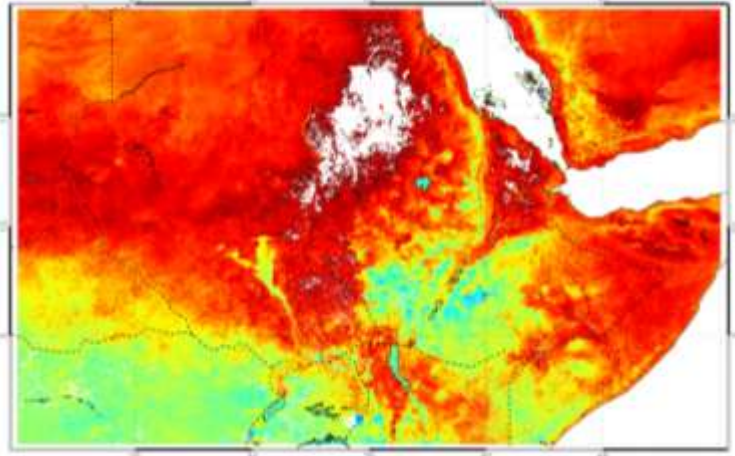
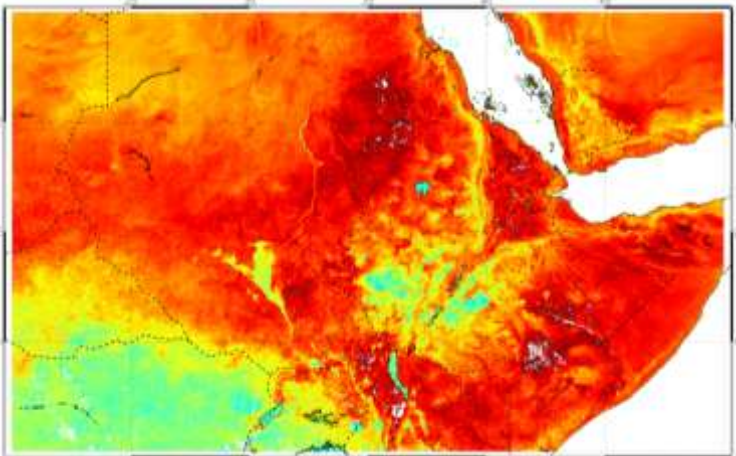
January 2006

February 2006



March 2006

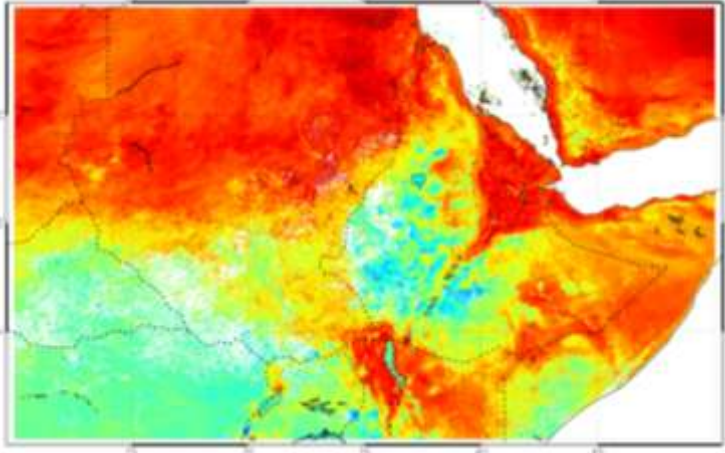
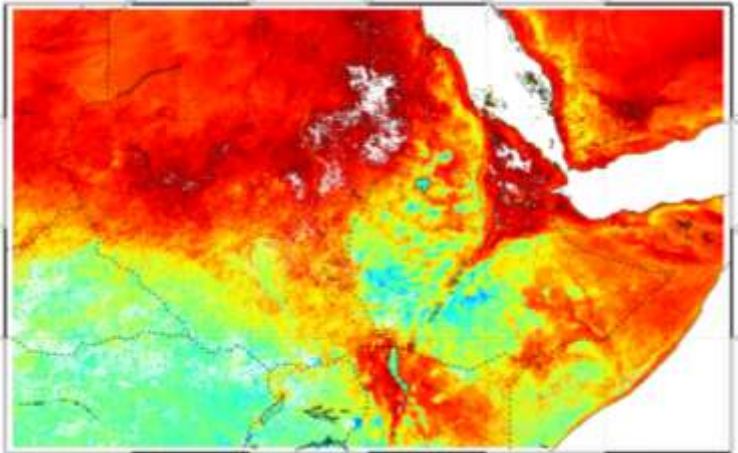
April 2006



**Appendix 3B.** Monthly MODIS LSTs, for the day time, 2006 Aqua dataset, across the Afar region that is on a 30° x 20° grid of 0.01° resolution.

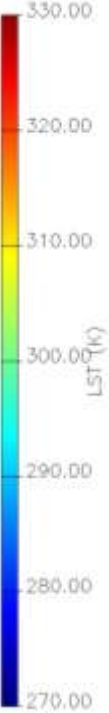
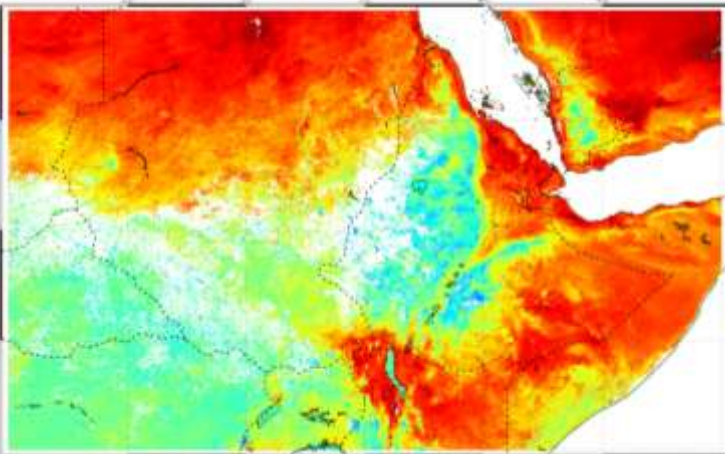
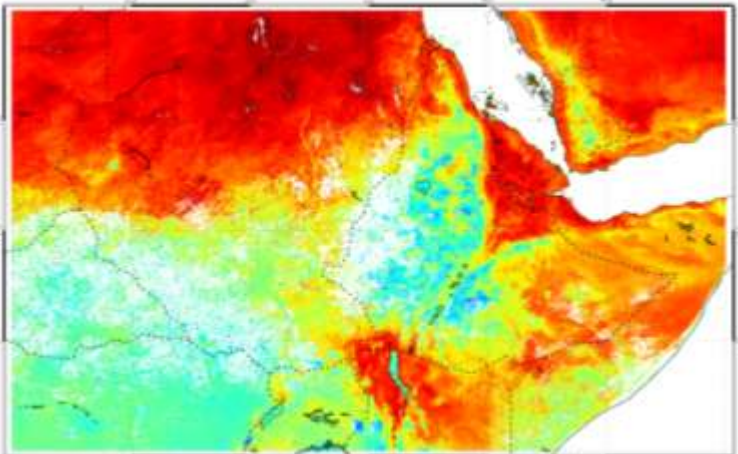
May 2006

June 2006

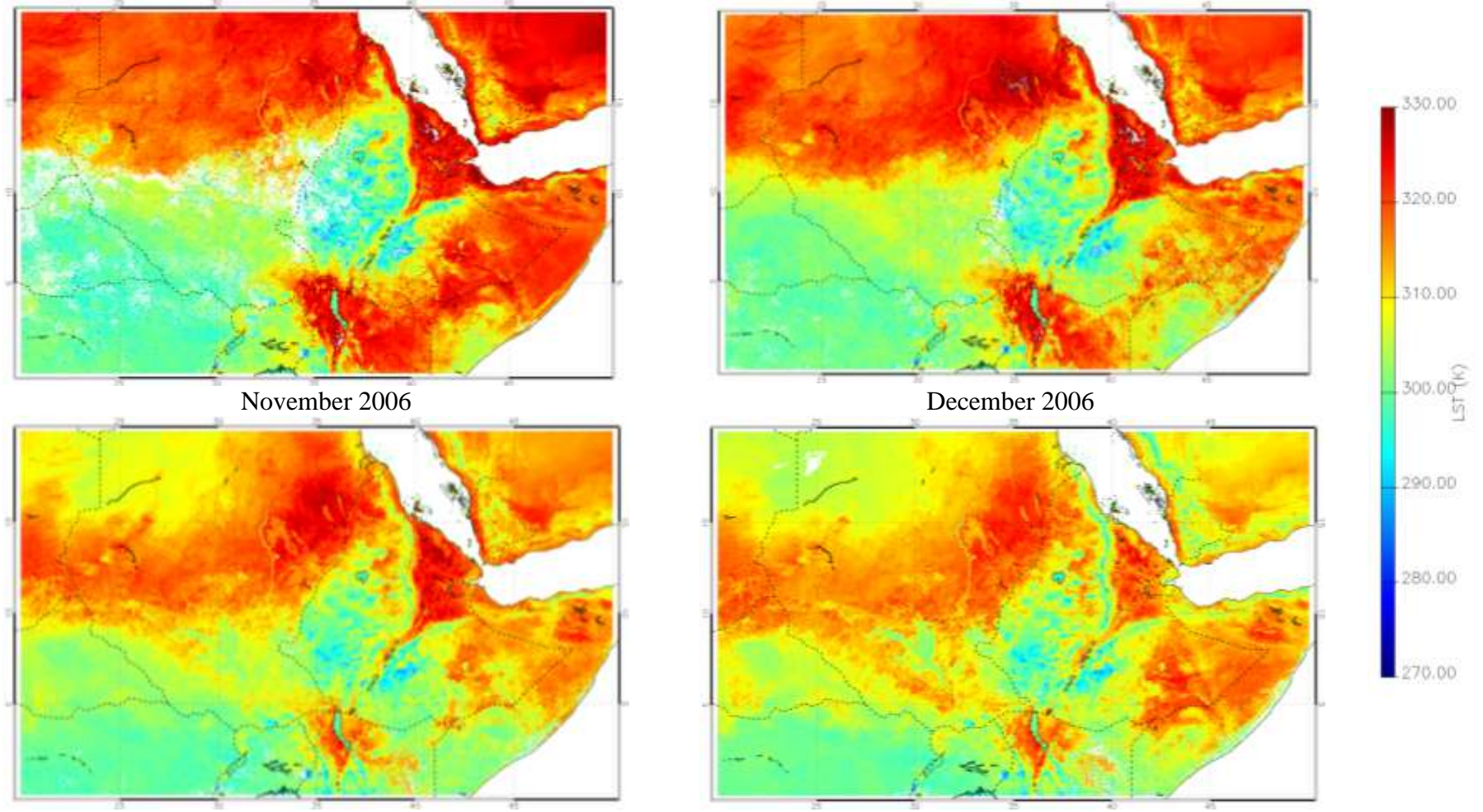


July 2006

August 2006



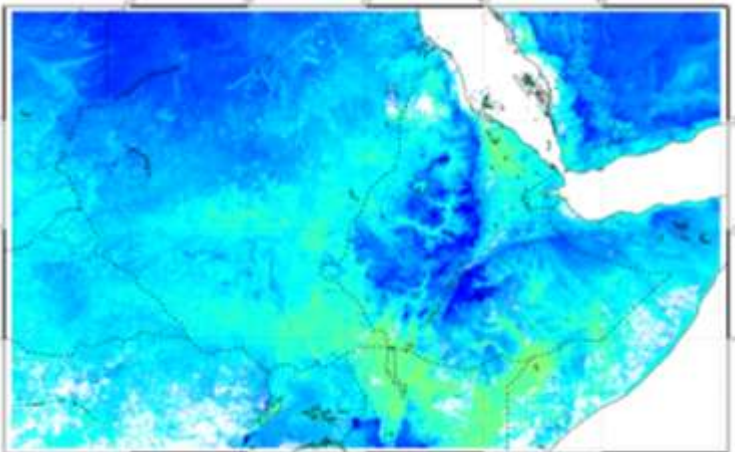
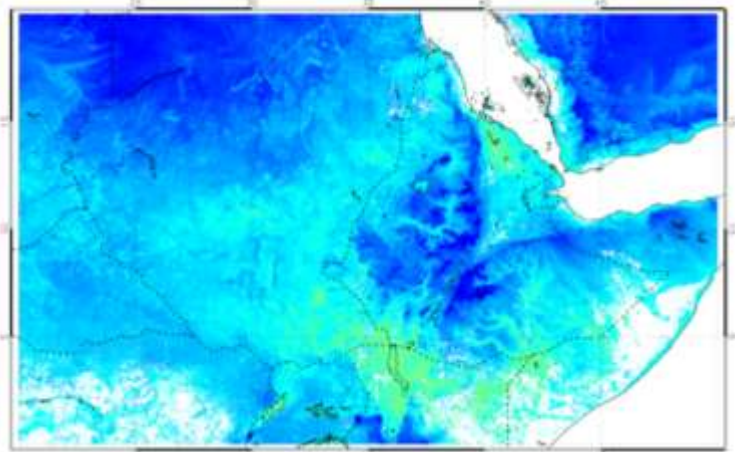
**Appendix 3C.** Monthly MODIS LSTs, for the day time, 2006 Aqua dataset, across the Afar region that is on a 30° x 20° grid of 0.01° resolution.



**Appendix 3D.** Monthly MODIS LSTs, for the night time, 2006 Aqua dataset, across the Afar region that is on a 30° x 20° grid of 0.01° resolution.

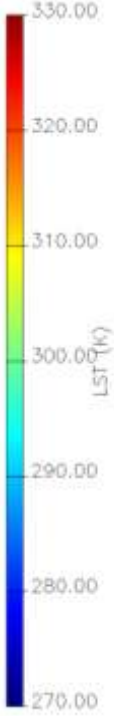
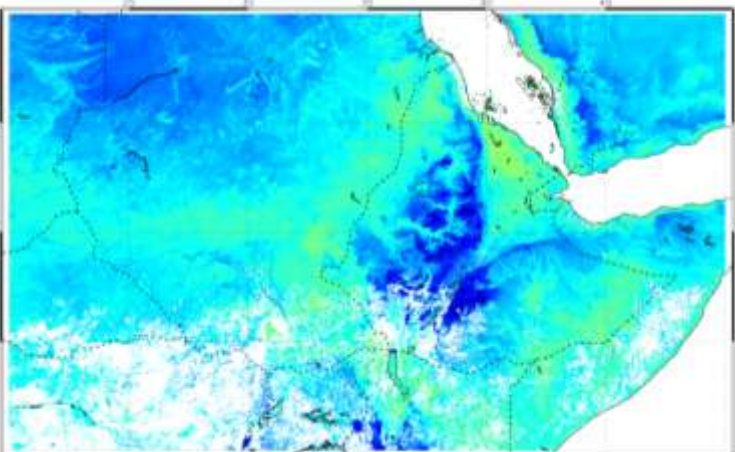
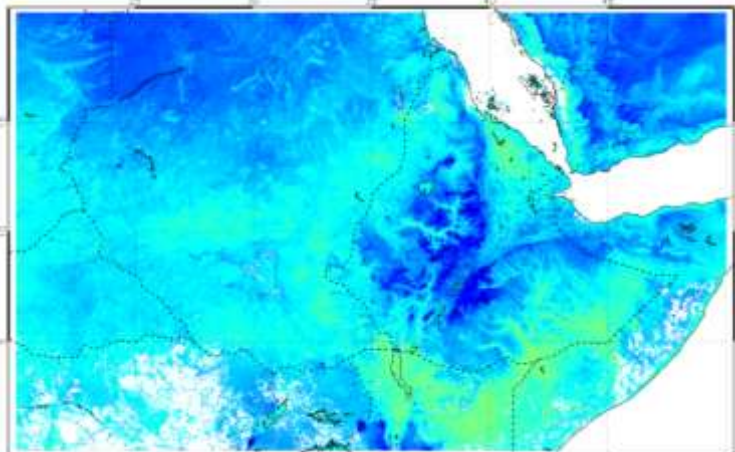
January 2006

February 2006



March 2006

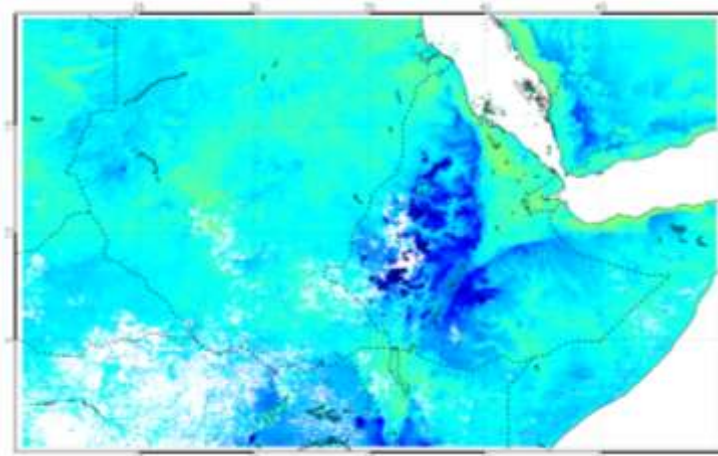
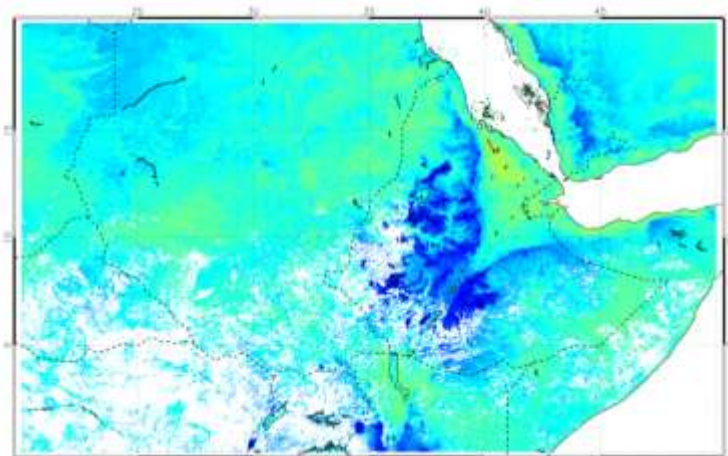
April 2006



**Appendix 3E.** Monthly MODIS LSTs, for the night time, 2006 Aqua dataset, across the Afar region that is on a 30° x 20° grid of 0.01° resolution.

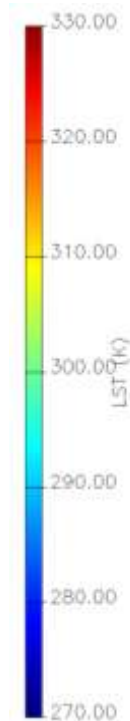
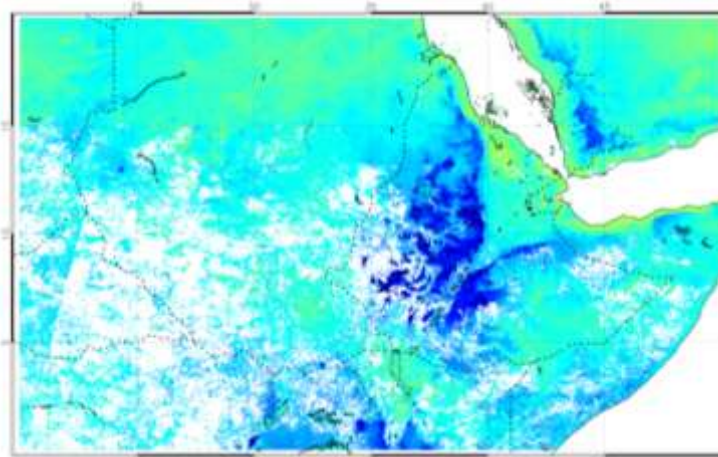
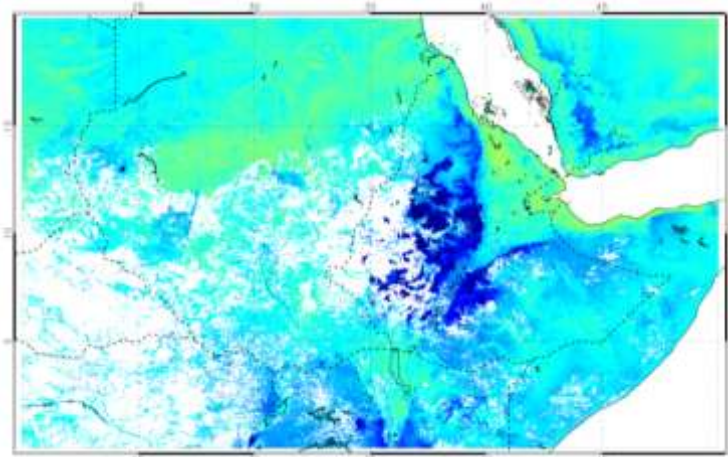
May 2006

June 2006

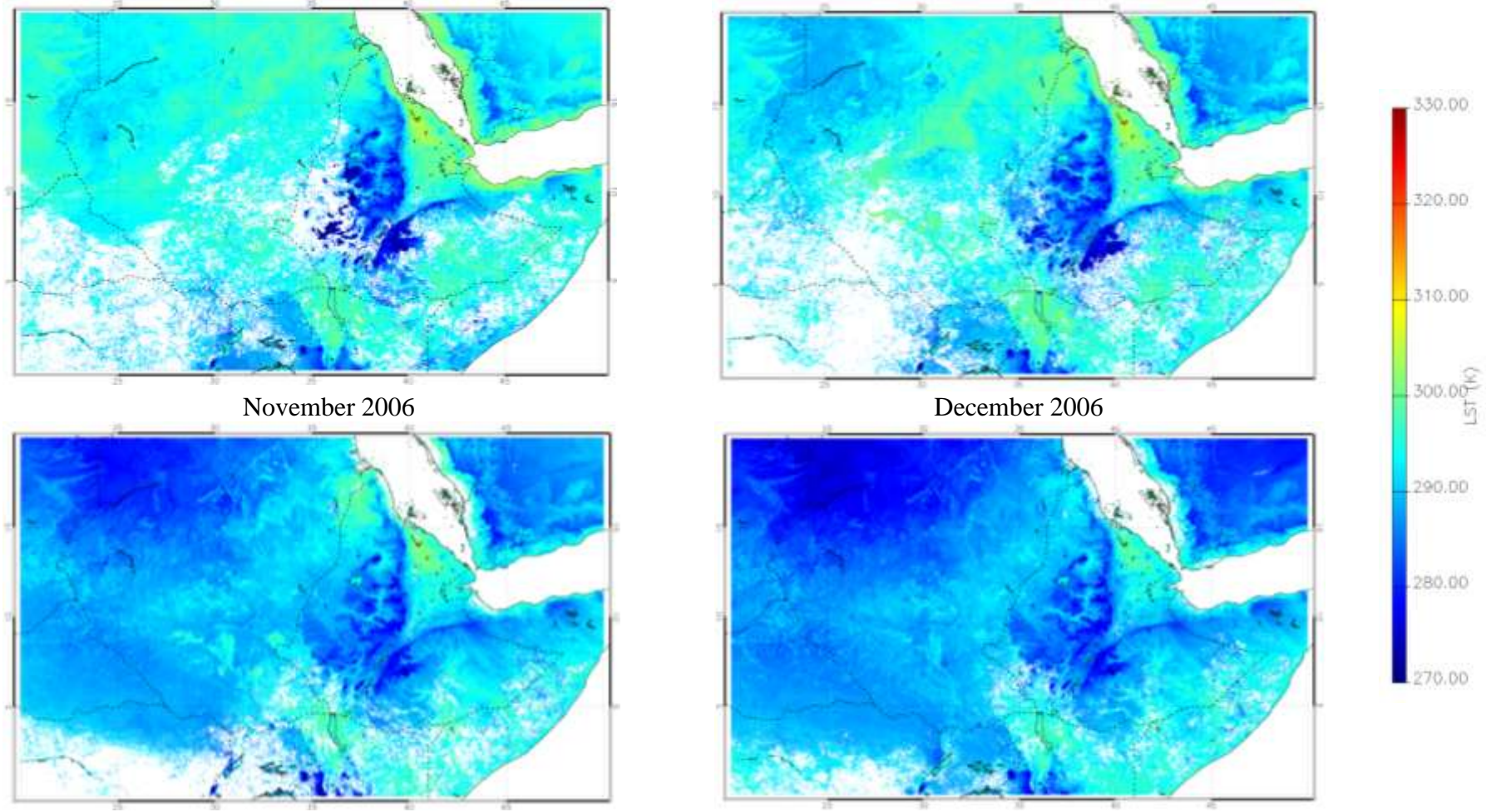


July 2006

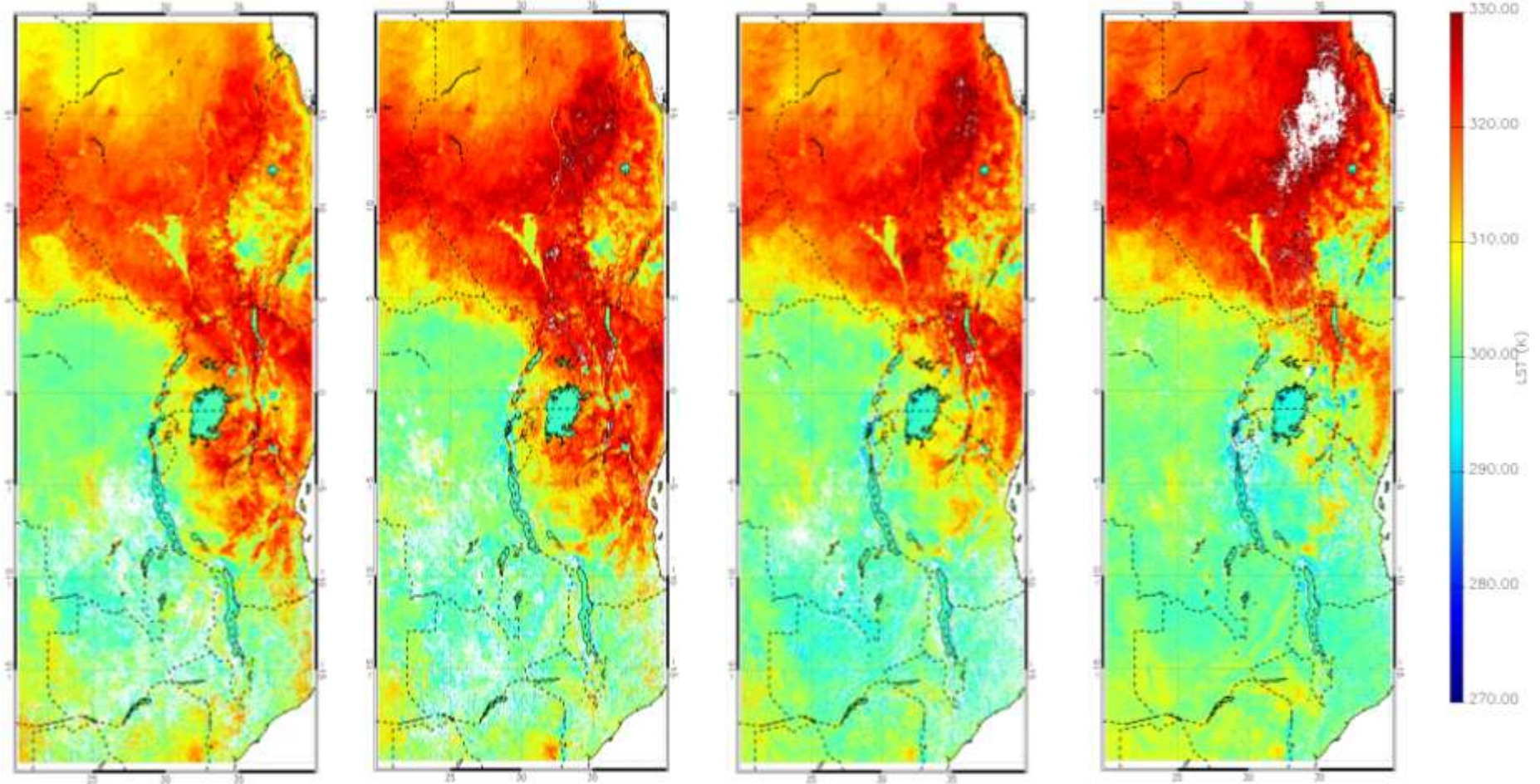
August 2006



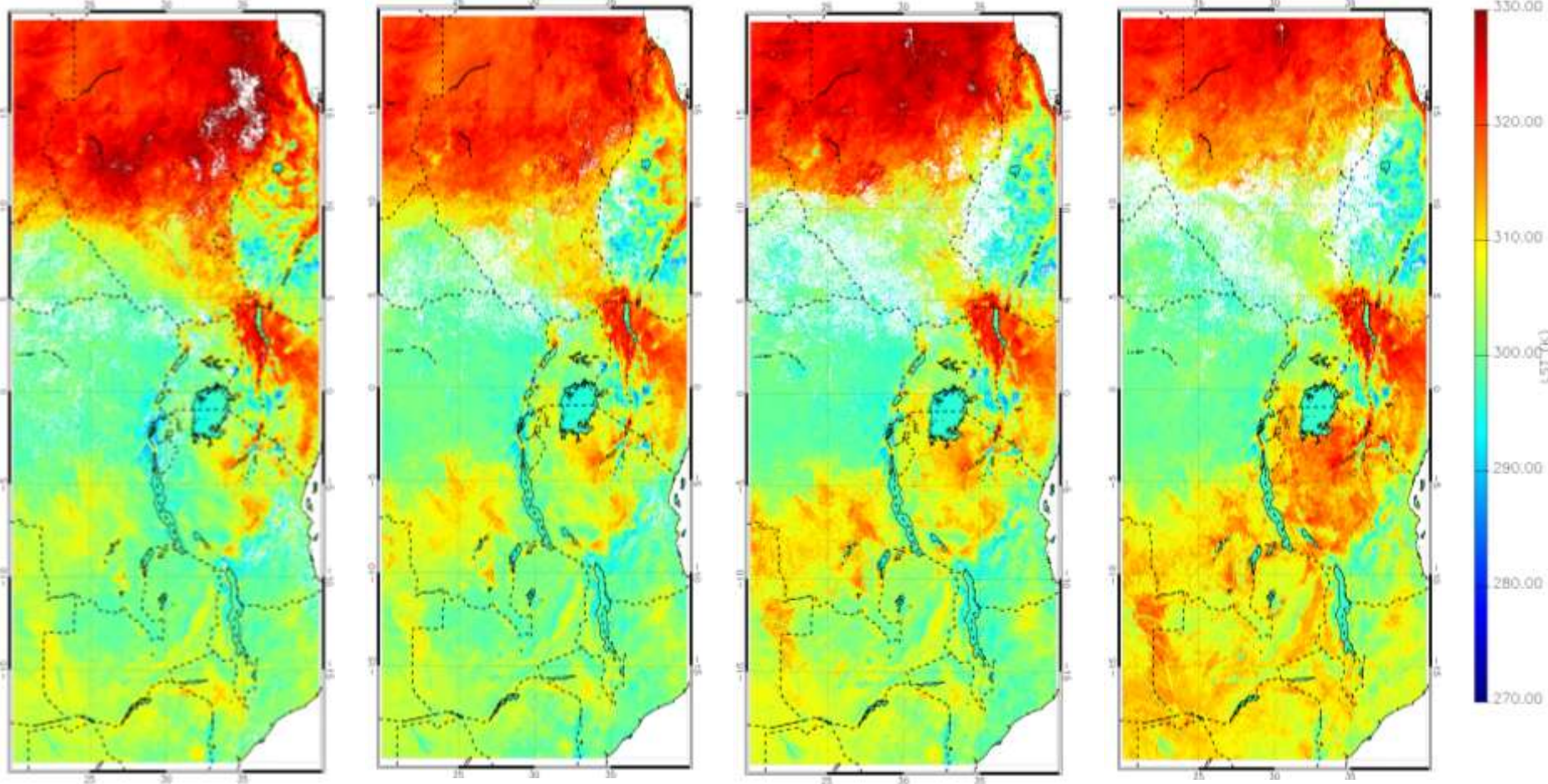
**Appendix 3F.** Monthly MODIS LSTs, for the night time, 2006 Aqua dataset, across the Afar region that is on a  $30^\circ \times 20^\circ$  grid of  $0.01^\circ$  resolution.



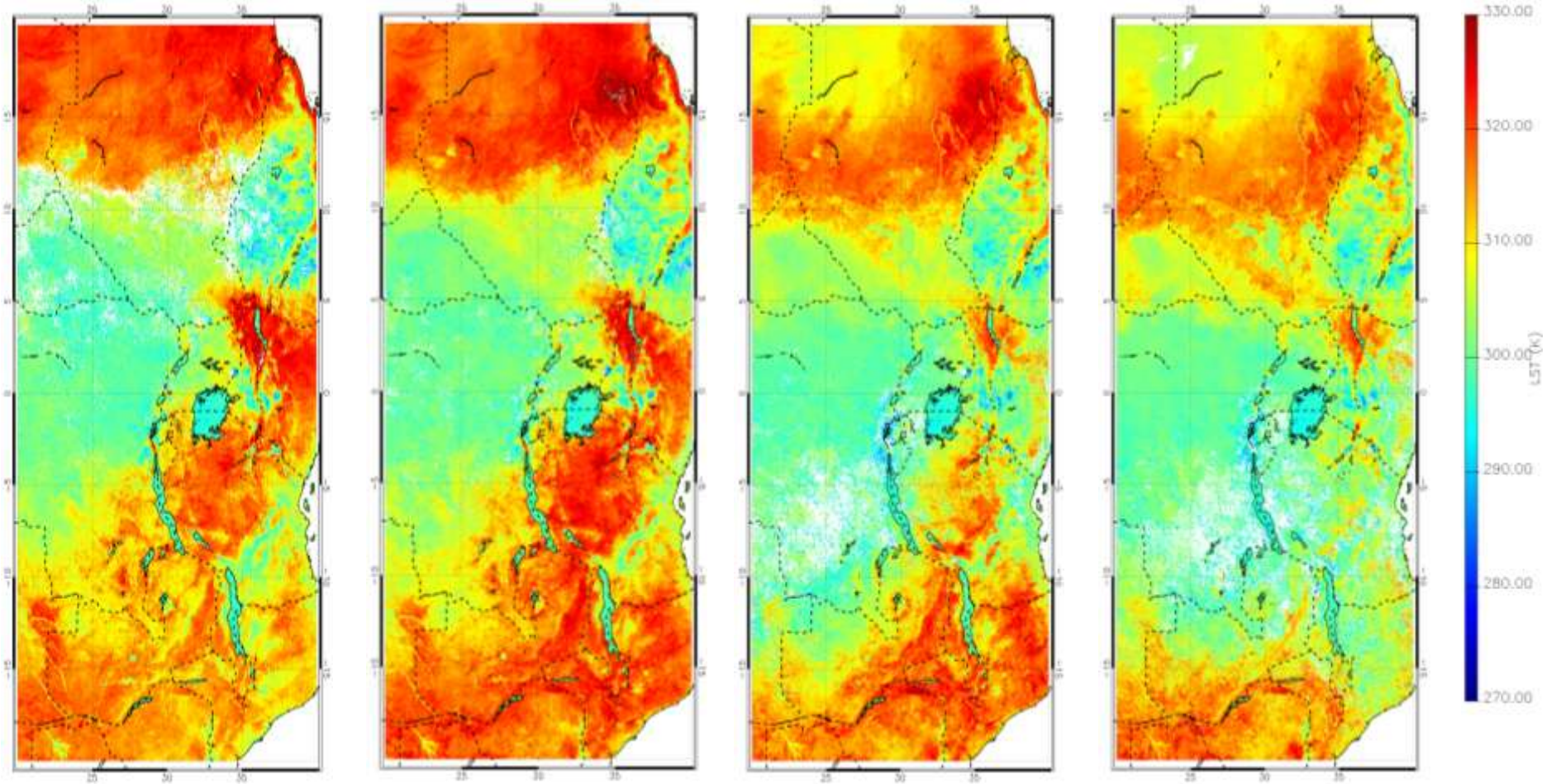
**Appendix 4A.** Monthly MODIS LSTs, for the day time, 2006 Aqua dataset, across the EARS region that is on a 20° x 40° grid of 0.01° resolution.



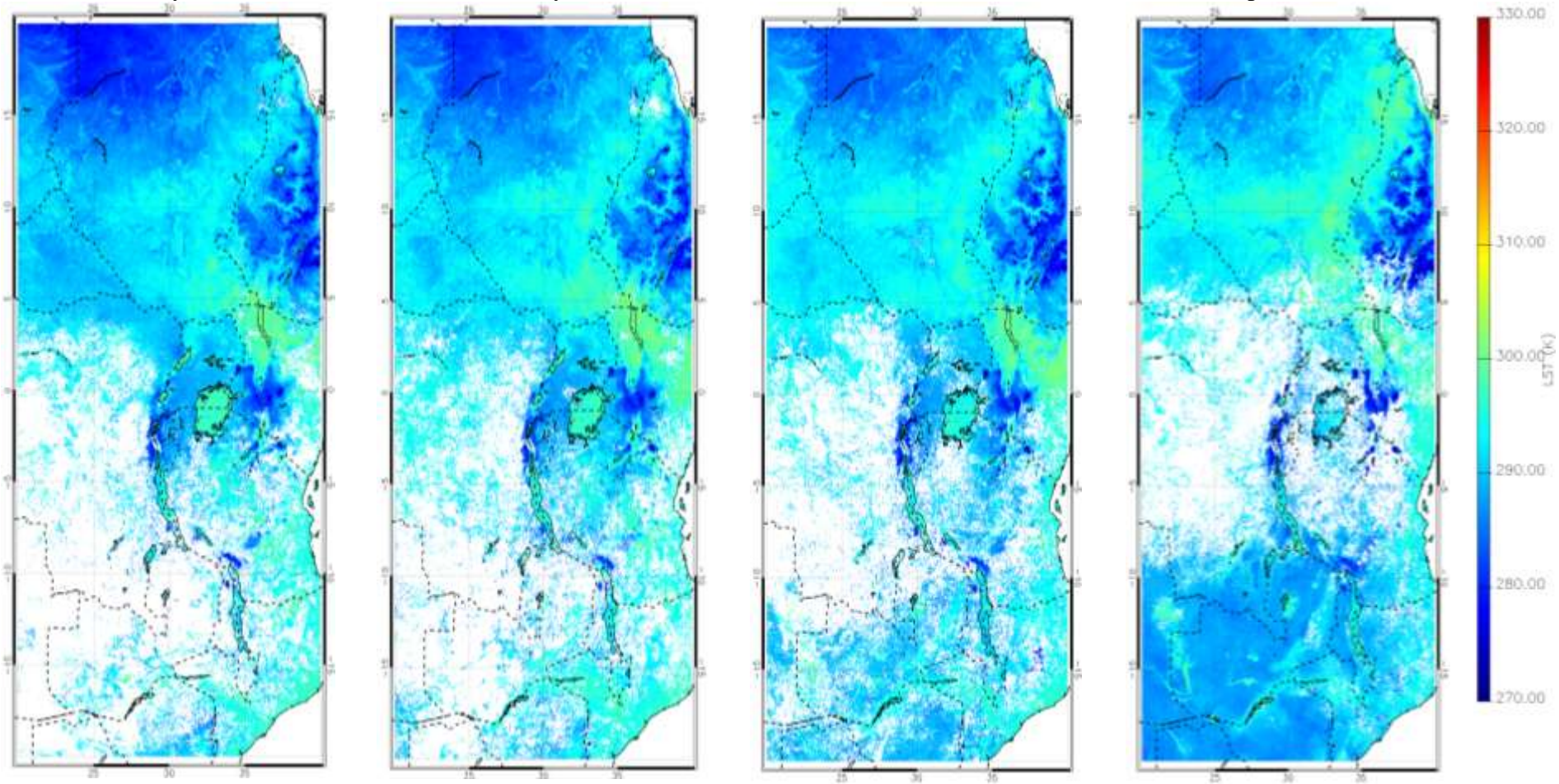
**Appendix 4B.** Monthly MODIS LSTs, for the day time, 2006 Aqua dataset, across the EARS region that is on a 20° x 40° grid of 0.01° resolution.



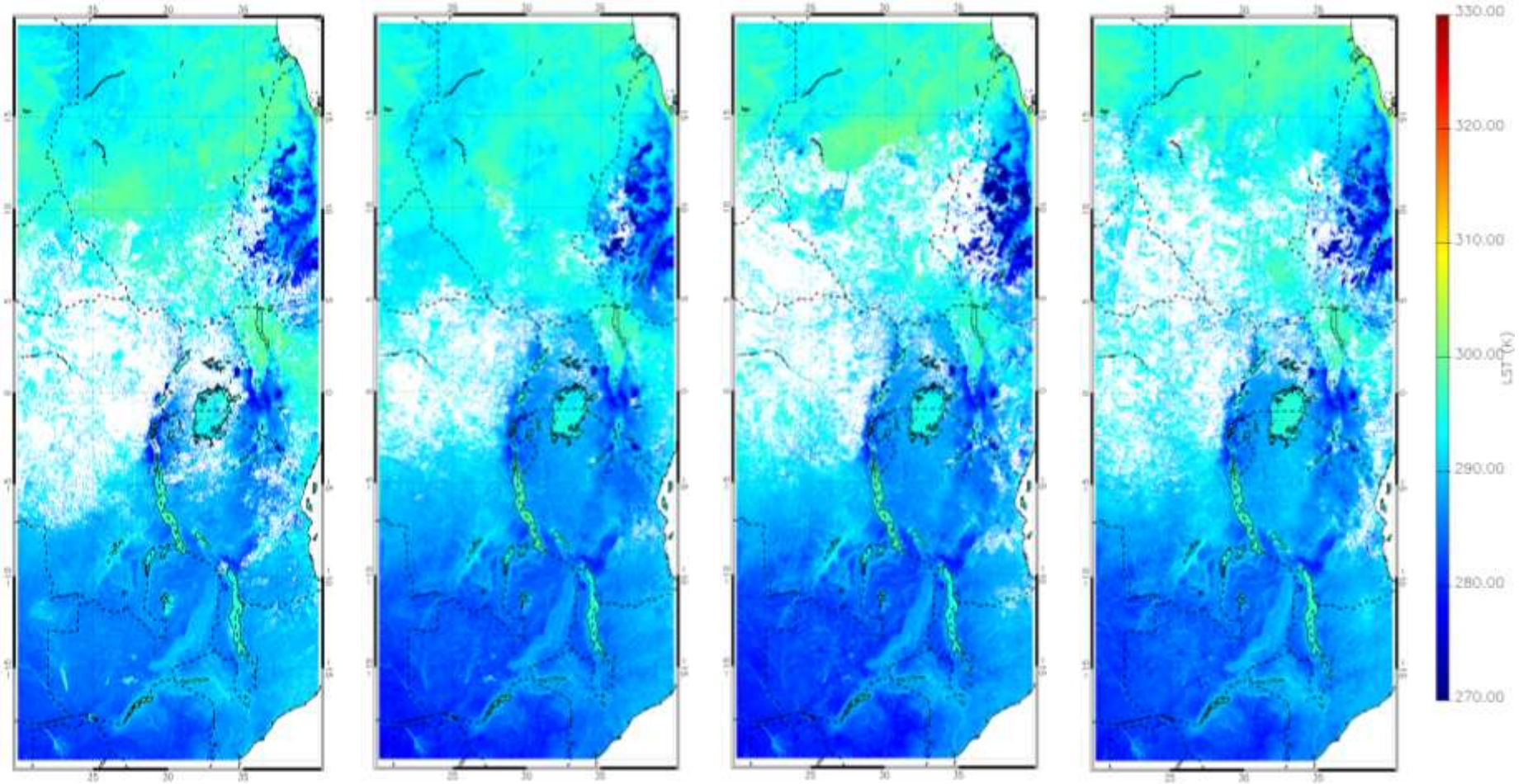
**Appendix 4C.** Monthly MODIS LSTs, for the day time, 2006 Aqua dataset, across the EARS region that is on a 20° x 40° grid of 0.01° resolution.  
September 2006                      October 2006                      November 2006                      December 2006



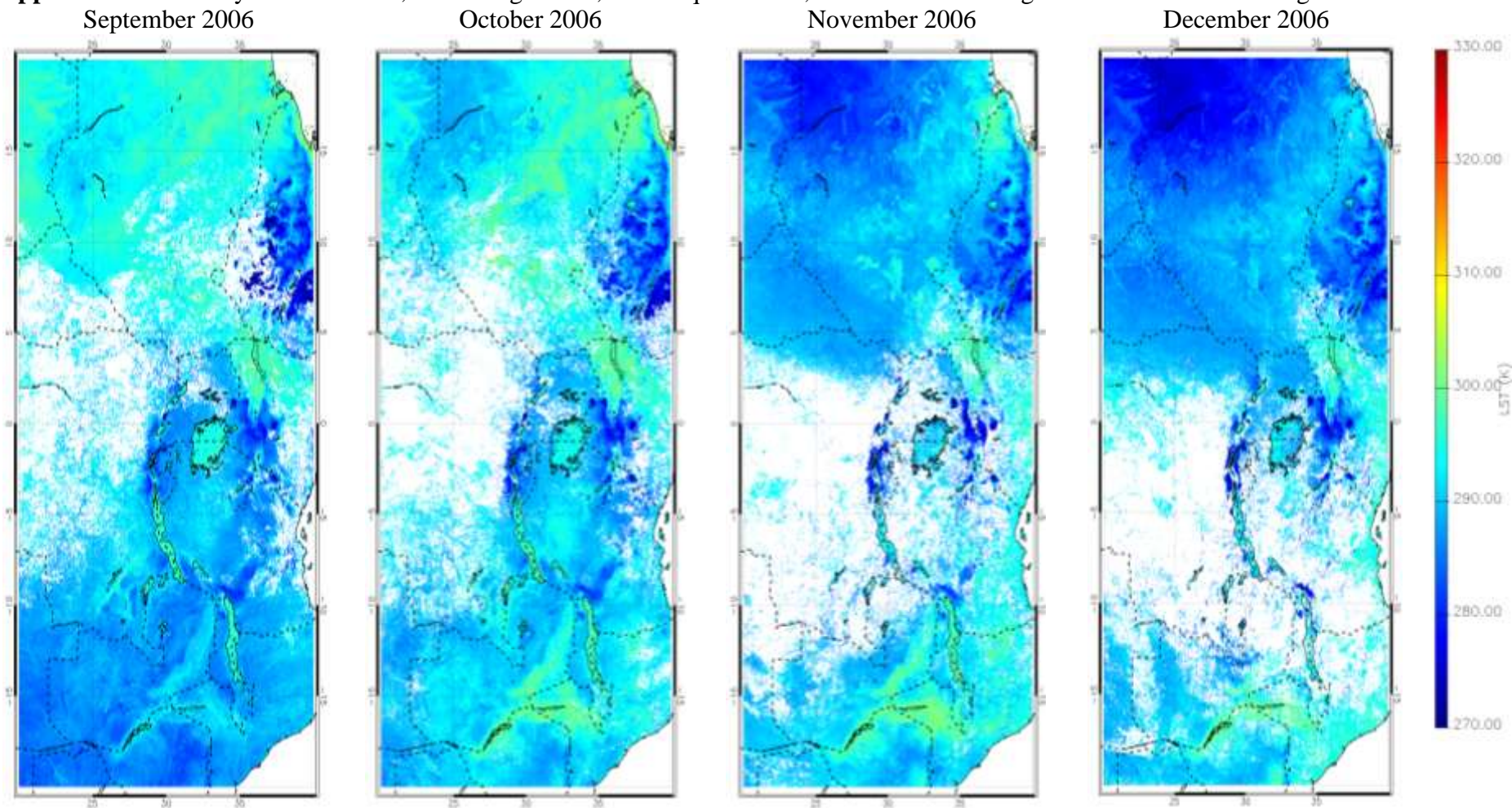
**Appendix 4D.** Monthly MODIS LSTs, for the night time, 2006 Aqua dataset, across the EARS region that is on a 20° x 40° grid of 0.01° resolution.  
January 2006                      February 2006                      March 2006                      April 2006



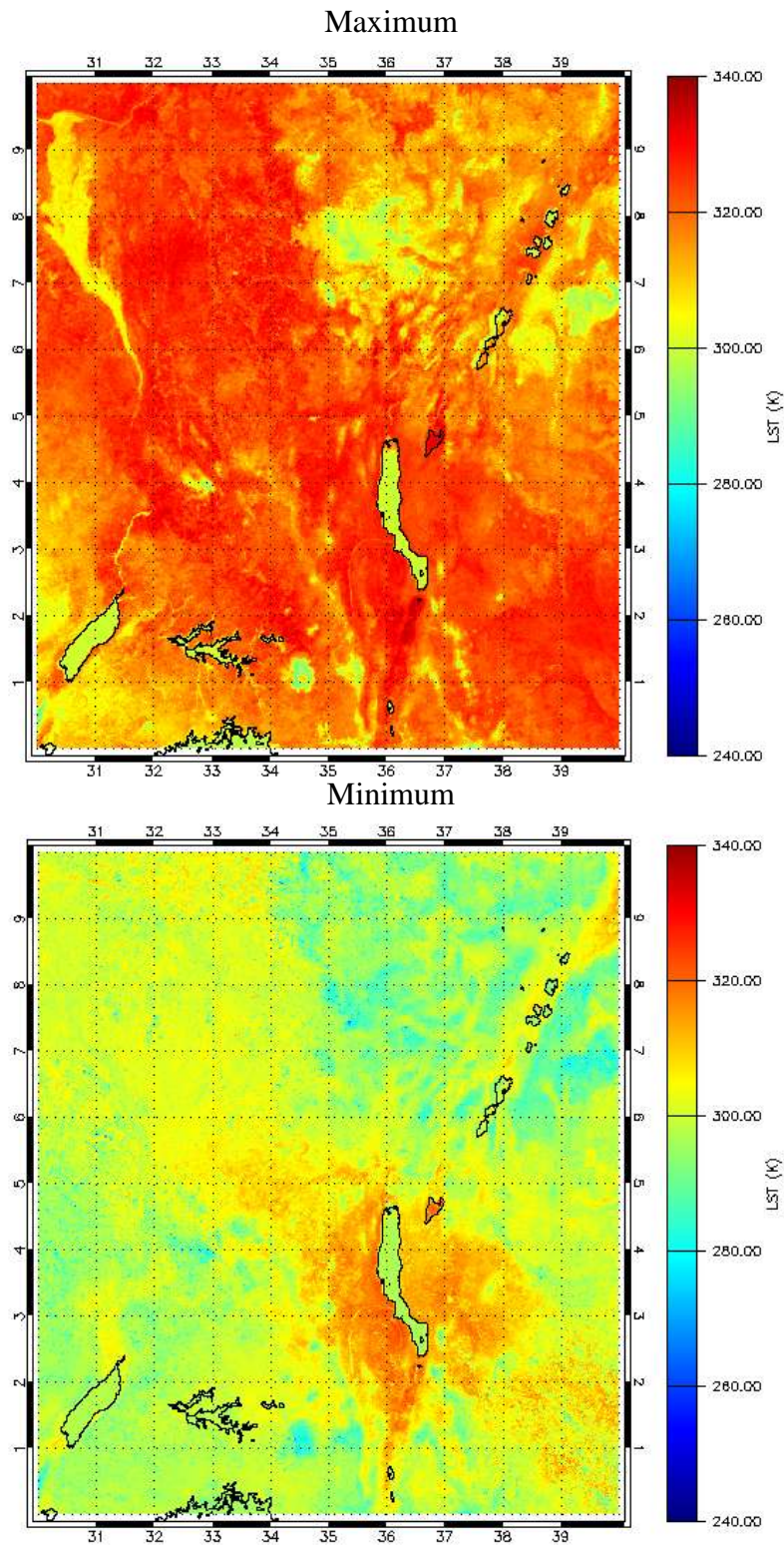
**Appendix 4E.** Monthly MODIS LSTs, for the night time, 2006 Aqua dataset, across the EARS region that is on a 20° x 40° grid of 0.01° resolution.  
May 2006                      June 2006                      July 2006                      August 2006



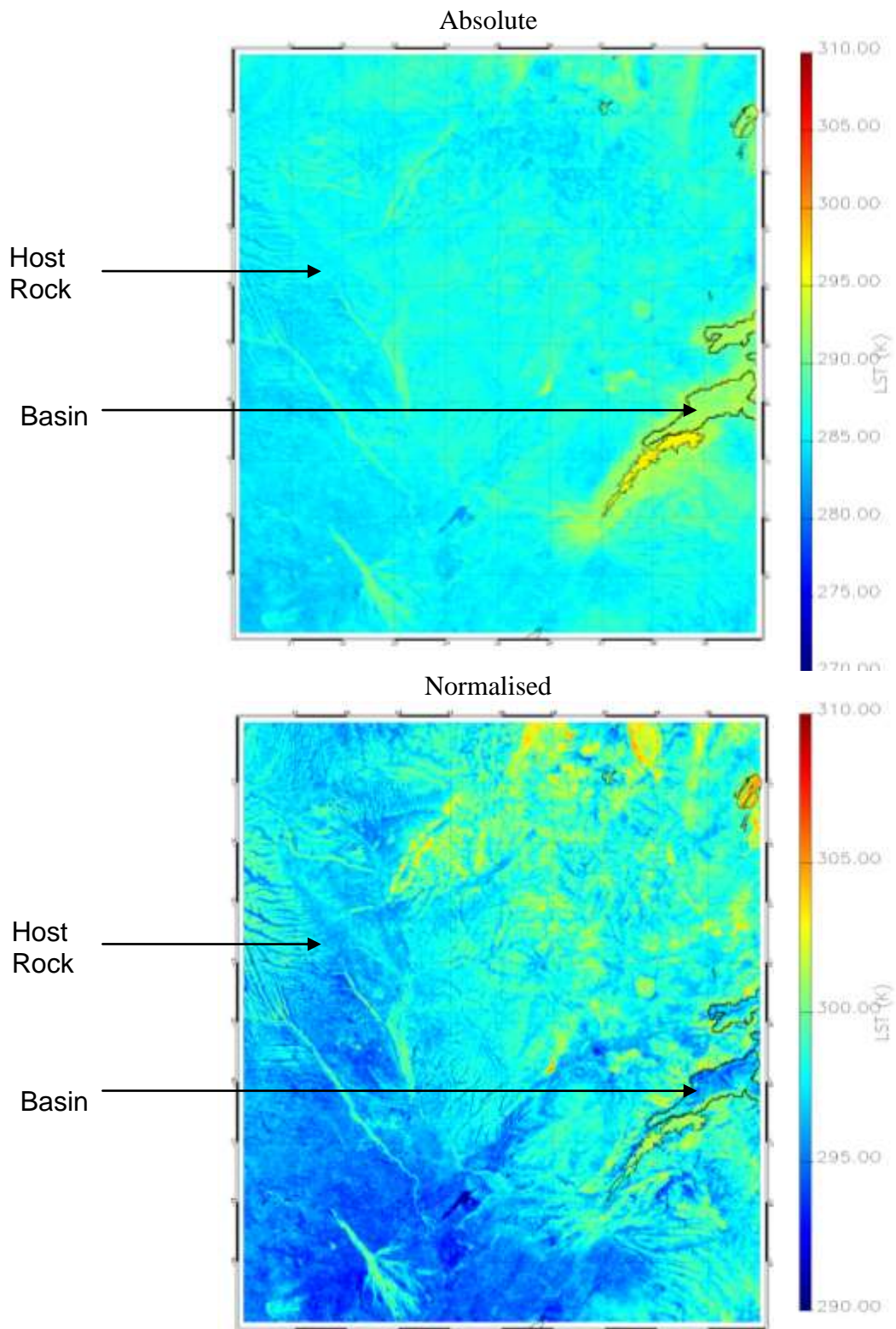
**Appendix 4F.** Monthly MODIS LSTs, for the night time, 2006 Aqua dataset, across the EARS region that is on a 20° x 40° grid of 0.01° resolution.



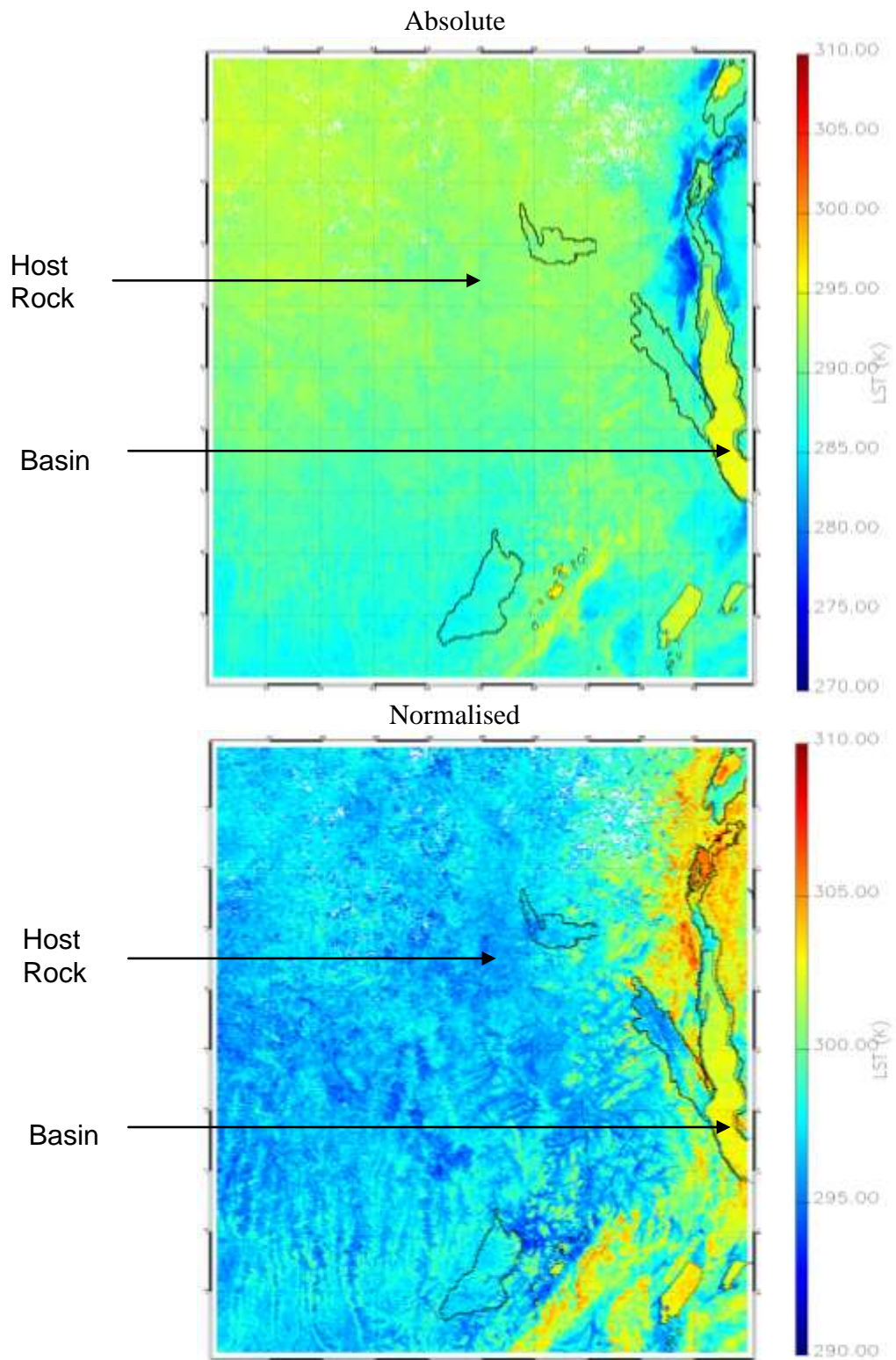
**Appendix 5.** Minimum and maximum mean MODIS LSTs per pixel, for the day time 2006 Aqua dataset, across the Turkana region that is on a  $10^\circ \times 10^\circ$  grid of  $0.01^\circ$  resolution.



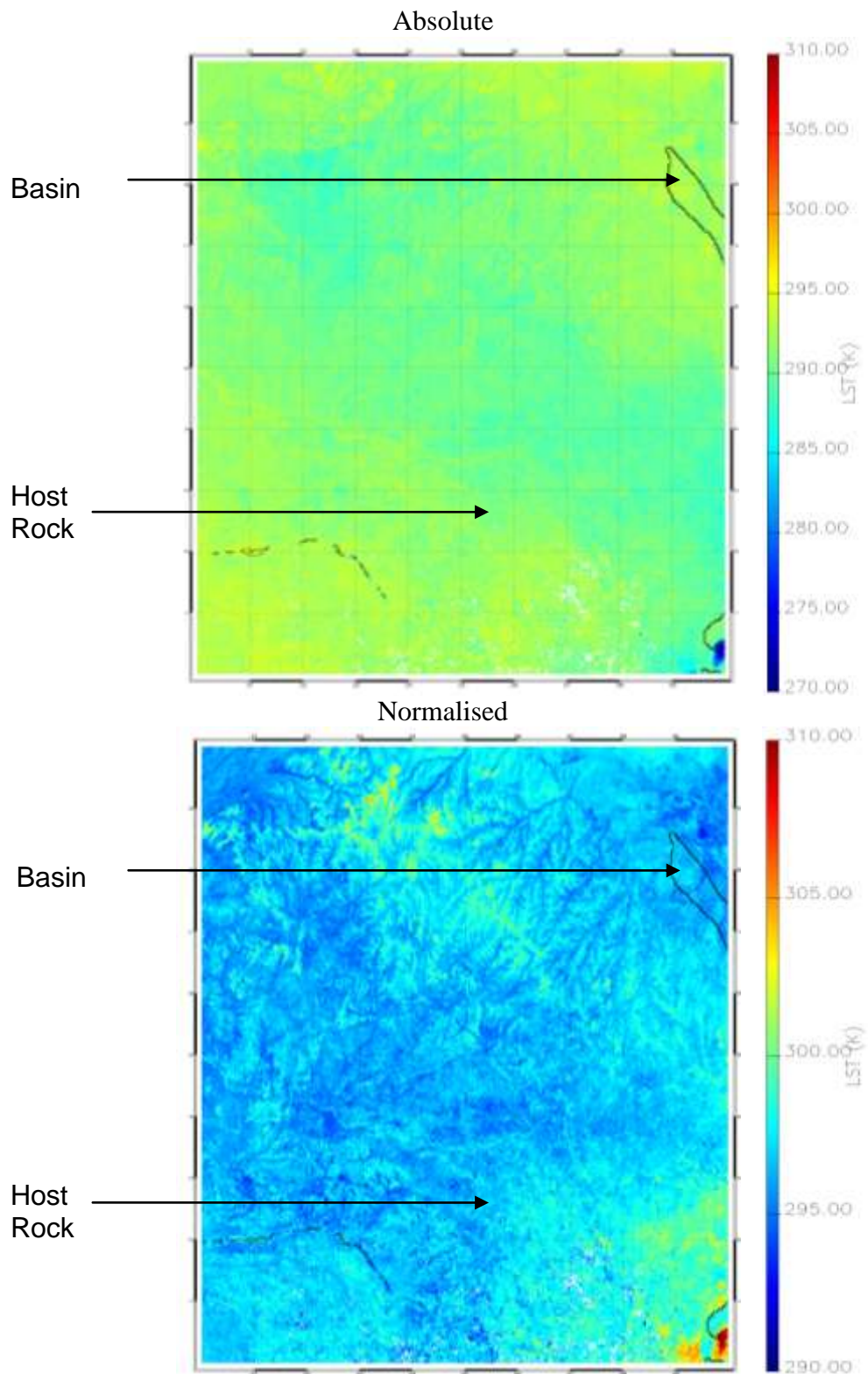
**Appendix 6A.** Absolute and normalised 2006 mean, night time MODIS LSTs, derived from the Aqua dataset, across the Lake Kariba tile that is a  $10^{\circ} \times 10^{\circ}$  grid of  $0.01^{\circ}$  resolution. Basins outlines, as supplied by Tullow Oil plc, have been overlain (black lines).



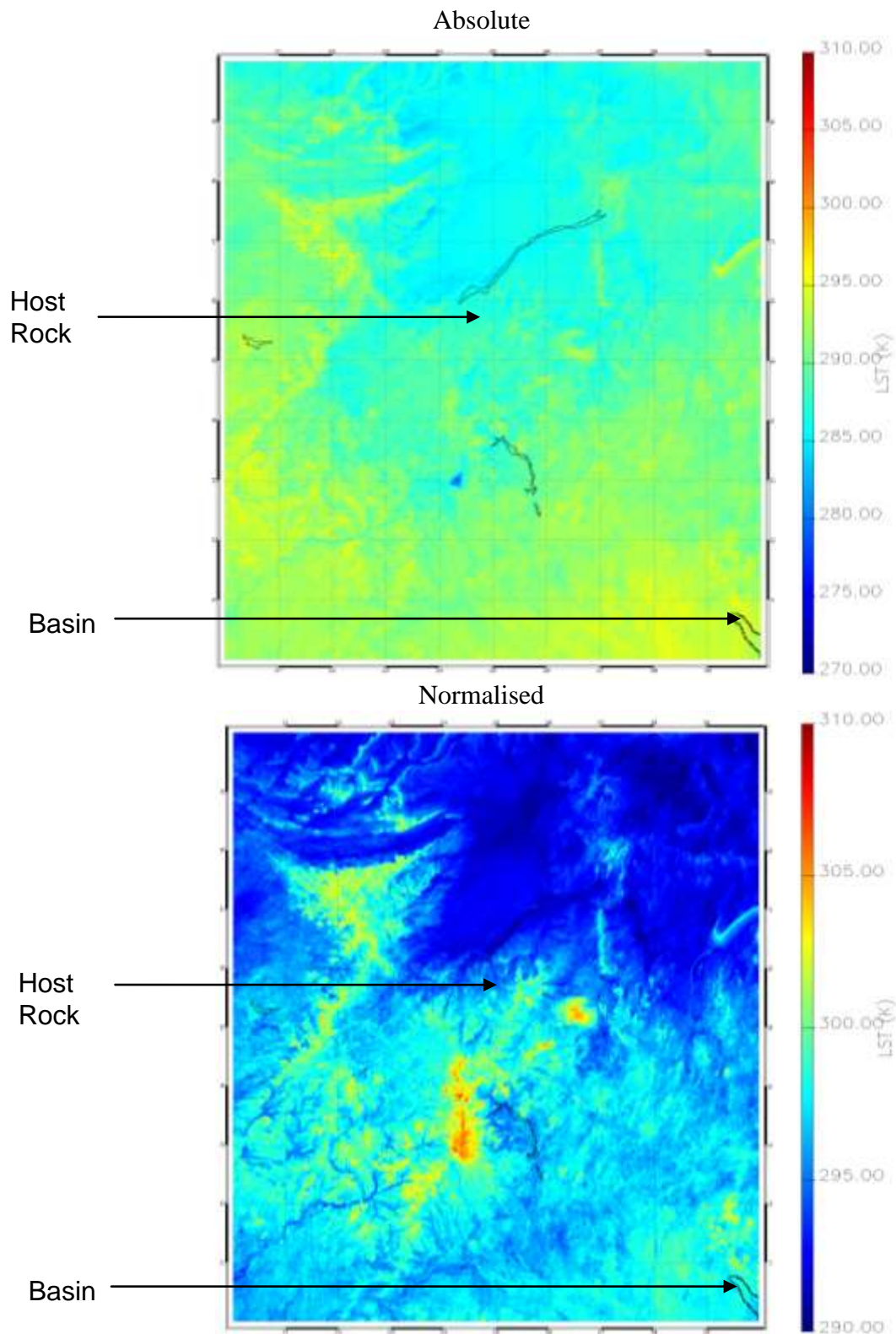
**Appendix 6B.** Absolute and normalised 2006 mean, night time MODIS LSTs, derived from the Aqua dataset, across the Lake Tanganyika tile that is a  $10^\circ \times 10^\circ$  grid of  $0.01^\circ$  resolution. Basins outlines, as supplied by Tullow Oil plc, have been overlain (black lines).



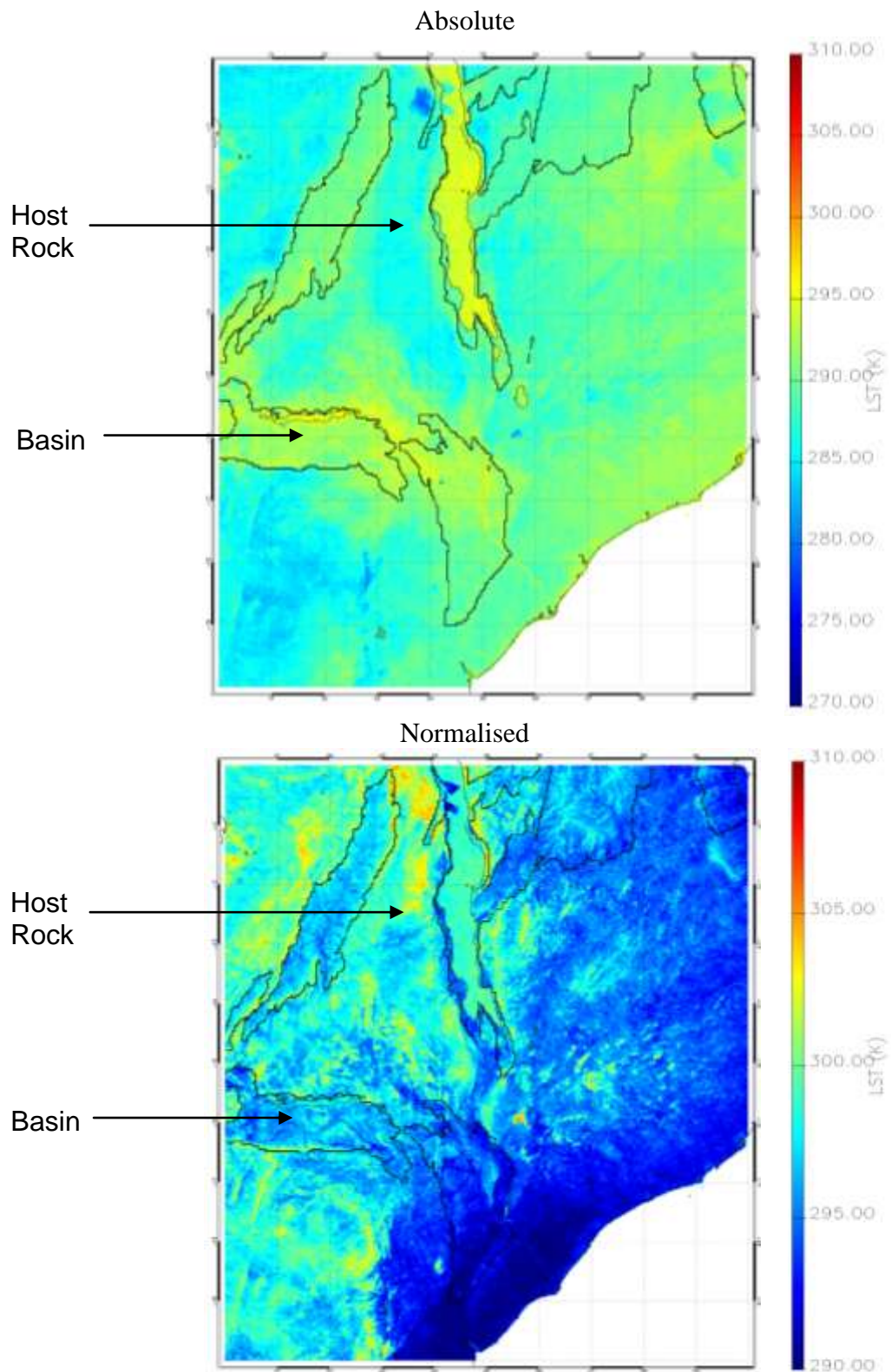
**Appendix 6C.** Absolute and normalised 2006 mean, night time MODIS LSTs, derived from the Aqua dataset, across the Lake Edward tile that is a  $10^{\circ} \times 10^{\circ}$  grid of  $0.01^{\circ}$  resolution. Basins outlines, as supplied by Tullow Oil plc, have been overlain (black lines).



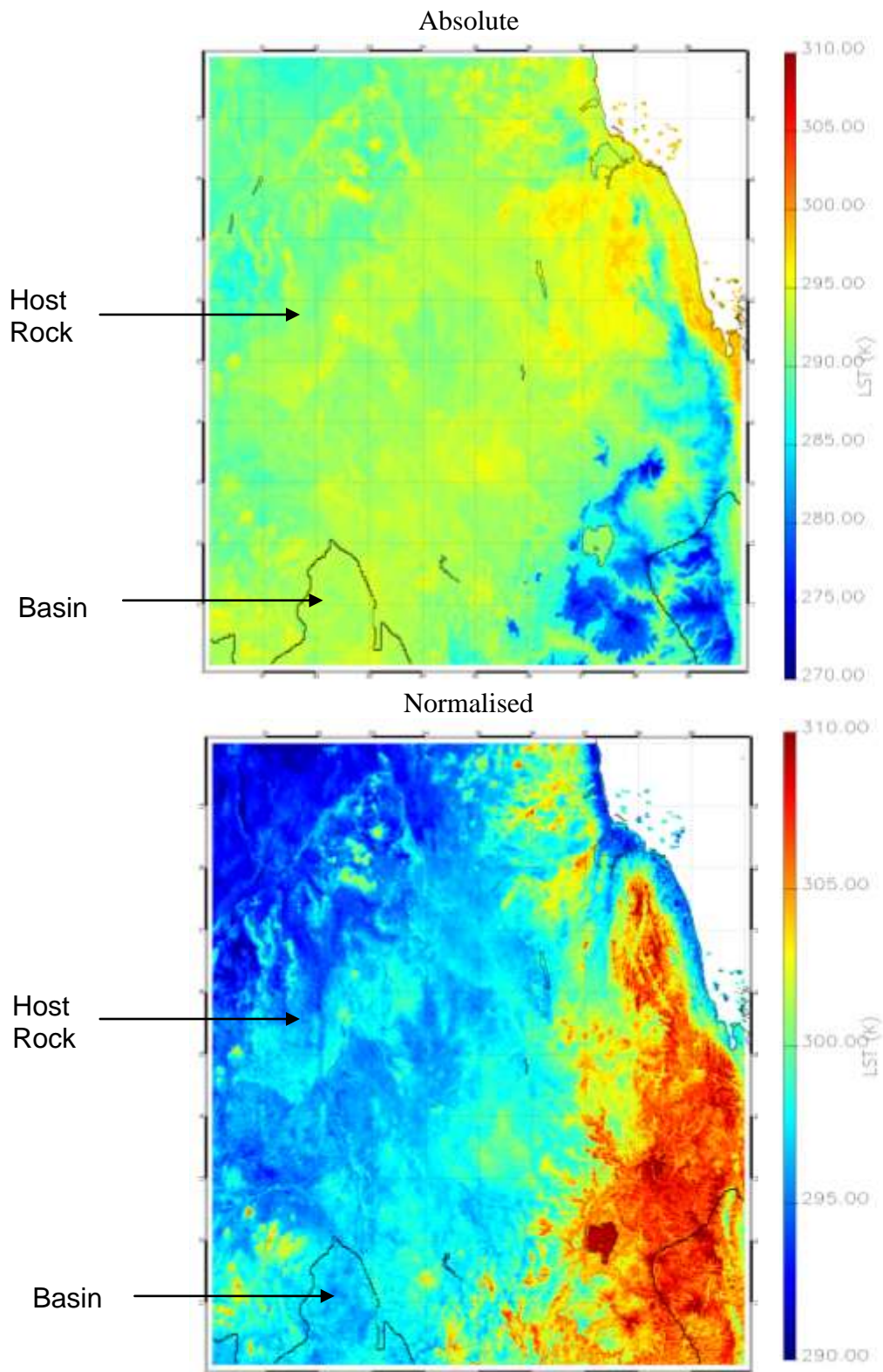
**Appendix 6D.** Absolute and normalised 2006 mean, night time MODIS LSTs, derived from the Aqua dataset, across the Libyan Desert tile that is a  $10^{\circ} \times 10^{\circ}$  grid of  $0.01^{\circ}$  resolution. Basins outlines, as supplied by Tullow Oil plc, have been overlain (black lines).



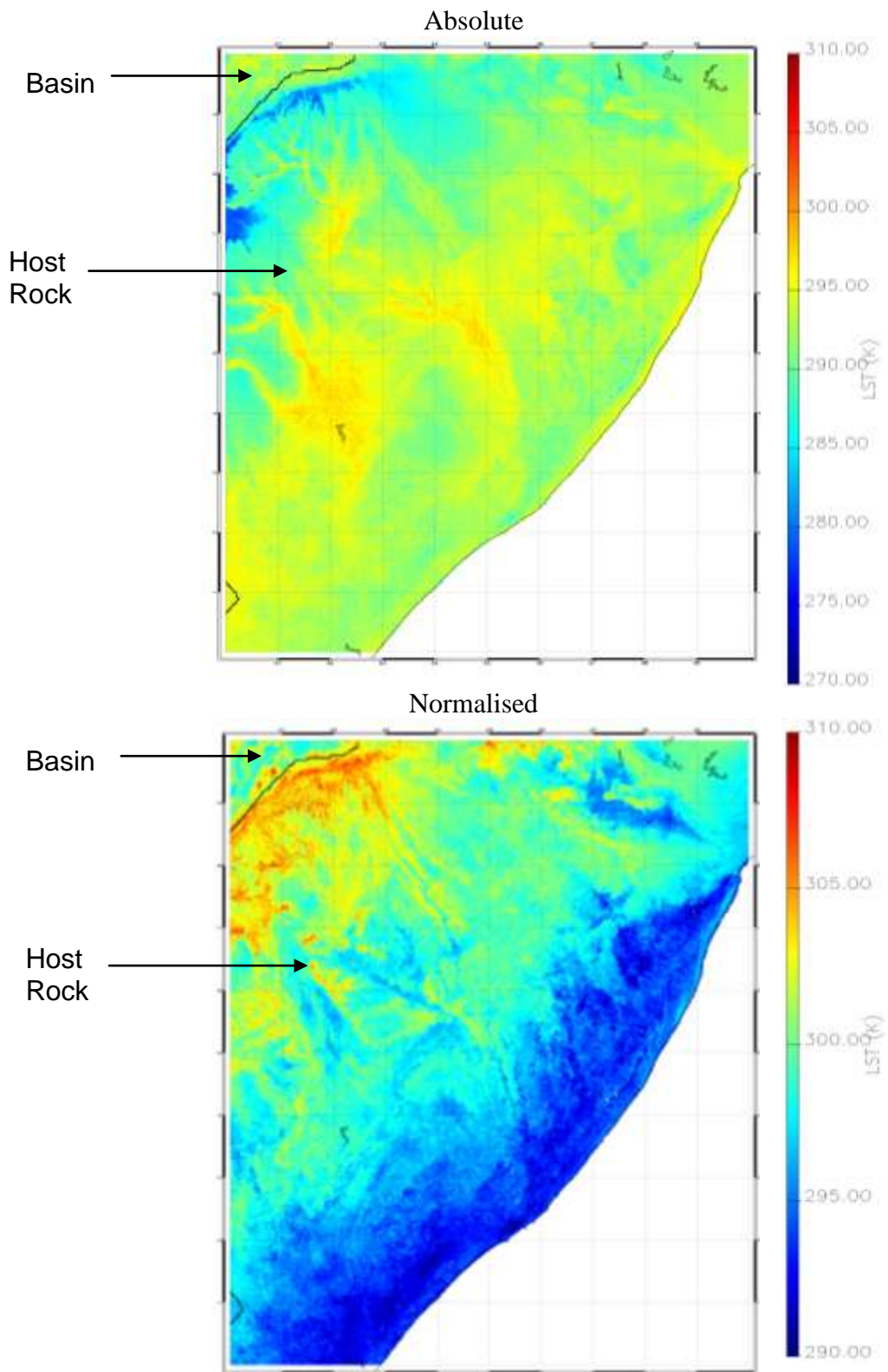
**Appendix 6E.** Absolute and normalised 2006 mean, night time MODIS LSTs, derived from the Aqua dataset, across the Lake Malawi tile that is a  $10^{\circ} \times 10^{\circ}$  grid of  $0.01^{\circ}$  resolution. Basins outlines, as supplied by Tullow Oil plc, have been overlain (black lines).



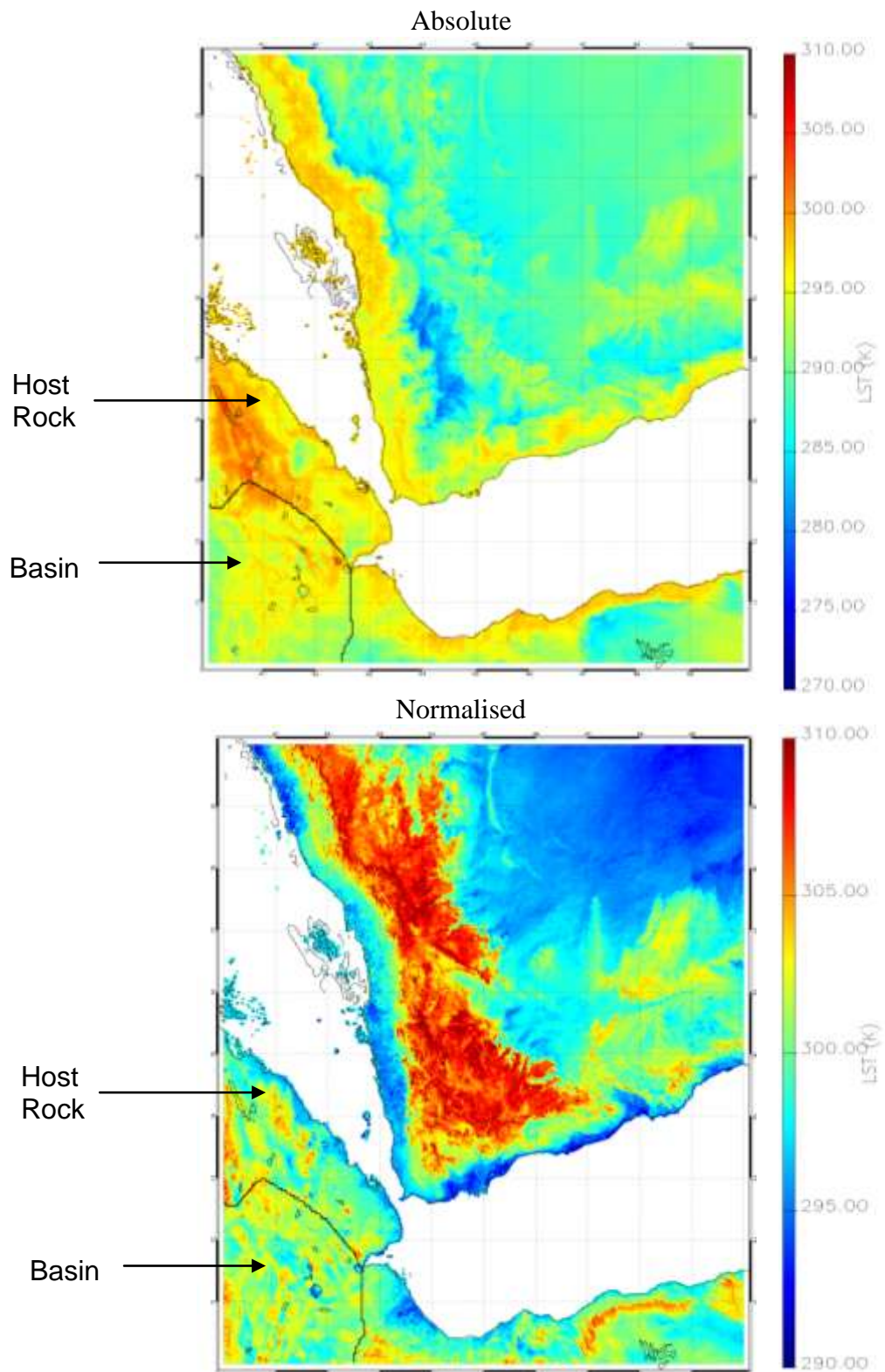
**Appendix 6F.** Absolute and normalised 2006 mean, night time MODIS LSTs, derived from the Aqua dataset, across the Eritrea tile that is a  $10^{\circ} \times 10^{\circ}$  grid of  $0.01^{\circ}$  resolution. Basins outlines, as supplied by Tullow Oil plc, have been overlain (black lines).



**Appendix 6G.** Absolute and normalised 2006 mean, night time MODIS LSTs, derived from the Aqua dataset, across the Somalia tile that is a  $10^{\circ} \times 10^{\circ}$  grid of  $0.01^{\circ}$  resolution. Basins outlines, as supplied by Tullow Oil plc, have been overlain (black lines).

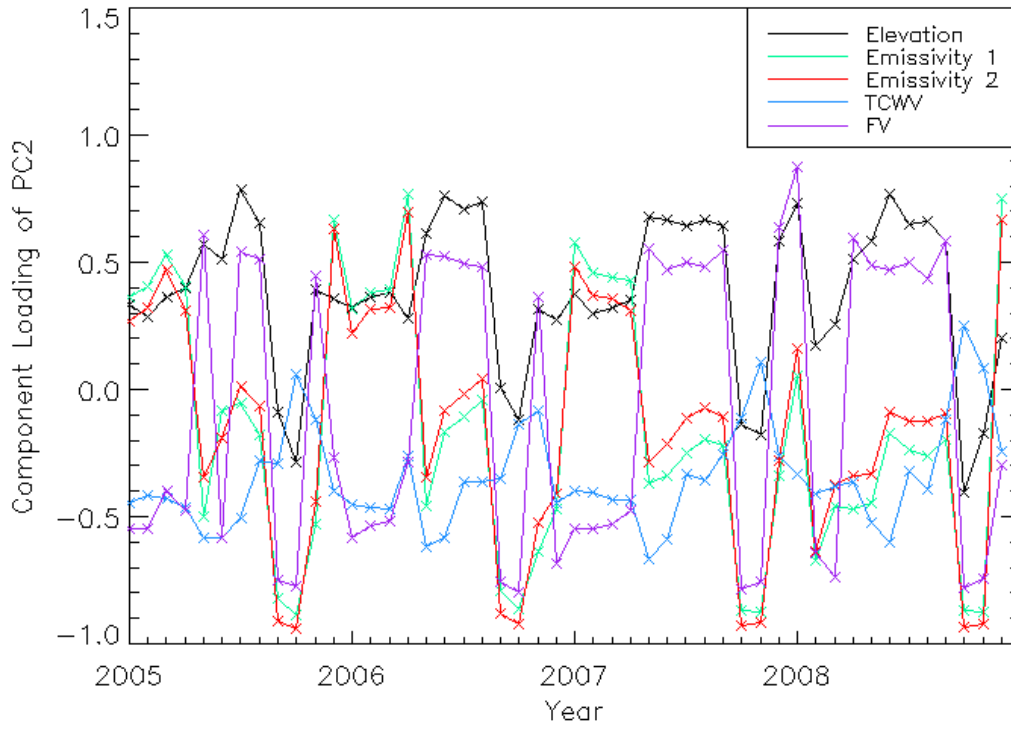


**Appendix 6H.** Absolute and normalised 2006 mean, night time MODIS LSTs, derived from the Aqua dataset, across the Afar Depression tile that is a  $10^{\circ} \times 10^{\circ}$  grid of  $0.01^{\circ}$  resolution. Basins outlines, as supplied by Tullow Oil plc, have been overlain (black lines).

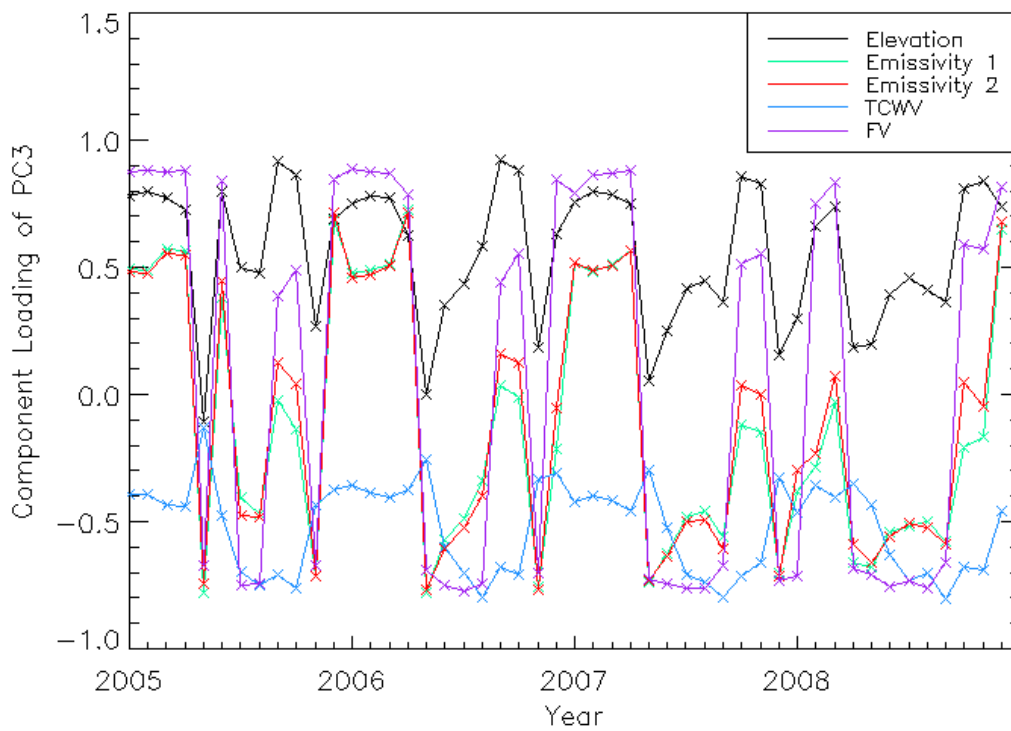


**Appendix 7A:** Absolute MODIS LST, PC2 and PC3 component loadings across the Turkana region for the period 2005 to 2008 from the Aqua dataset. The Turkana region is a  $10^{\circ} \times 10^{\circ}$  grid with the EARS of  $0.01^{\circ}$  resolution.

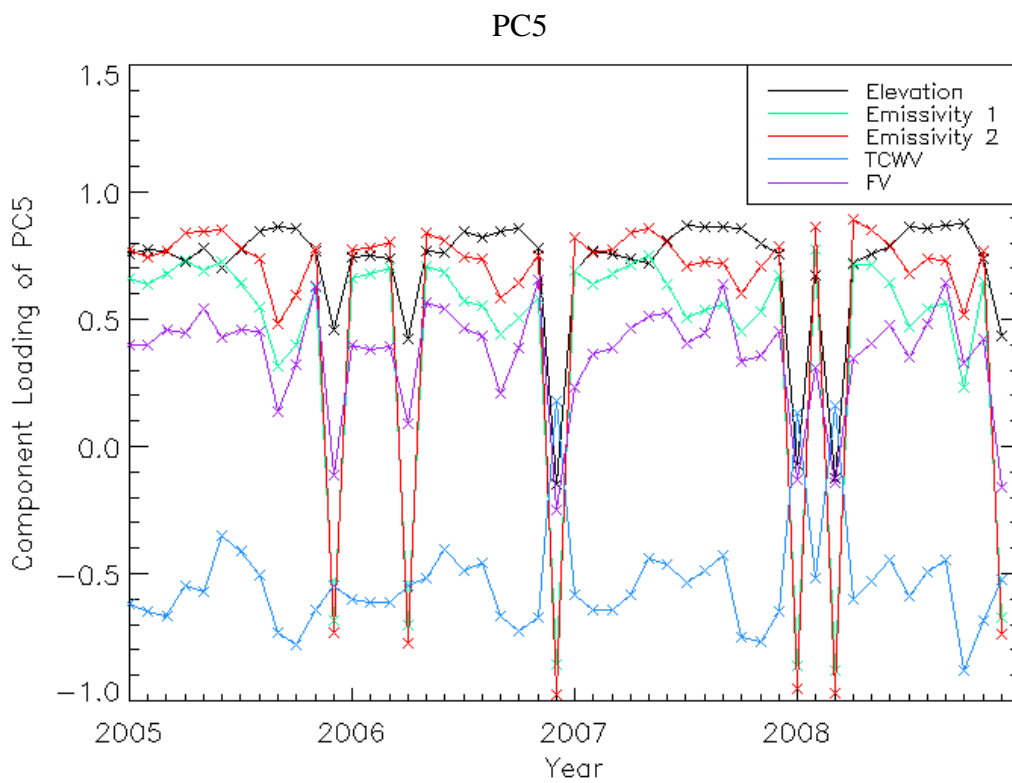
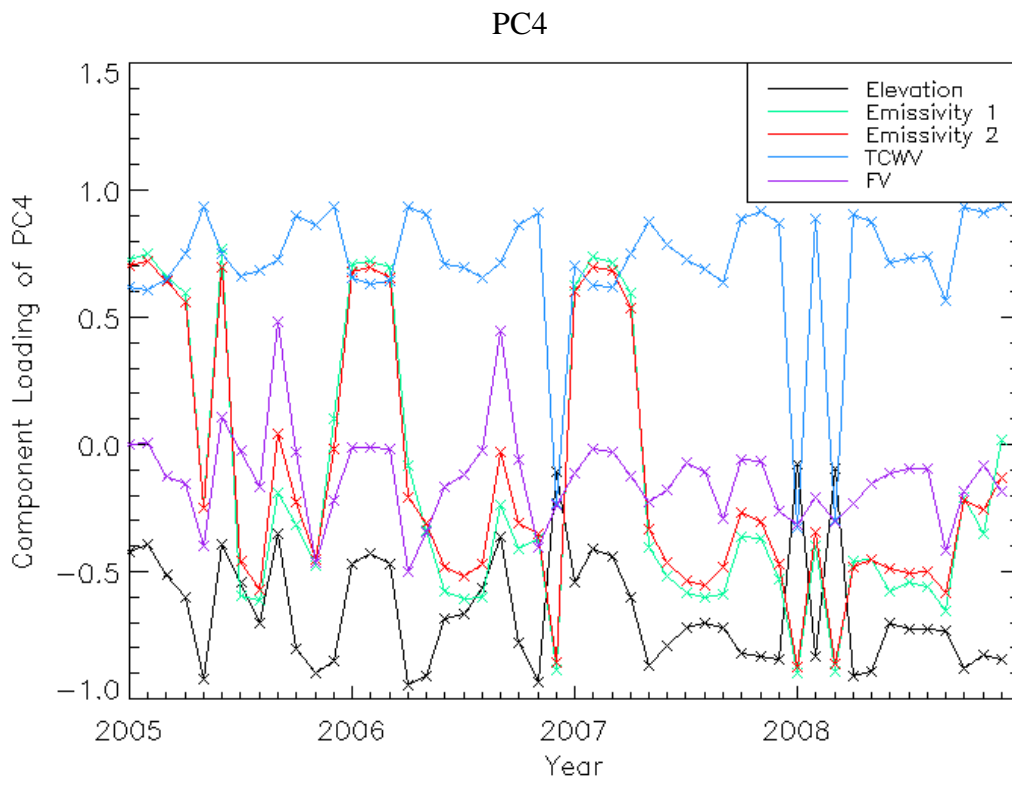
### PC2



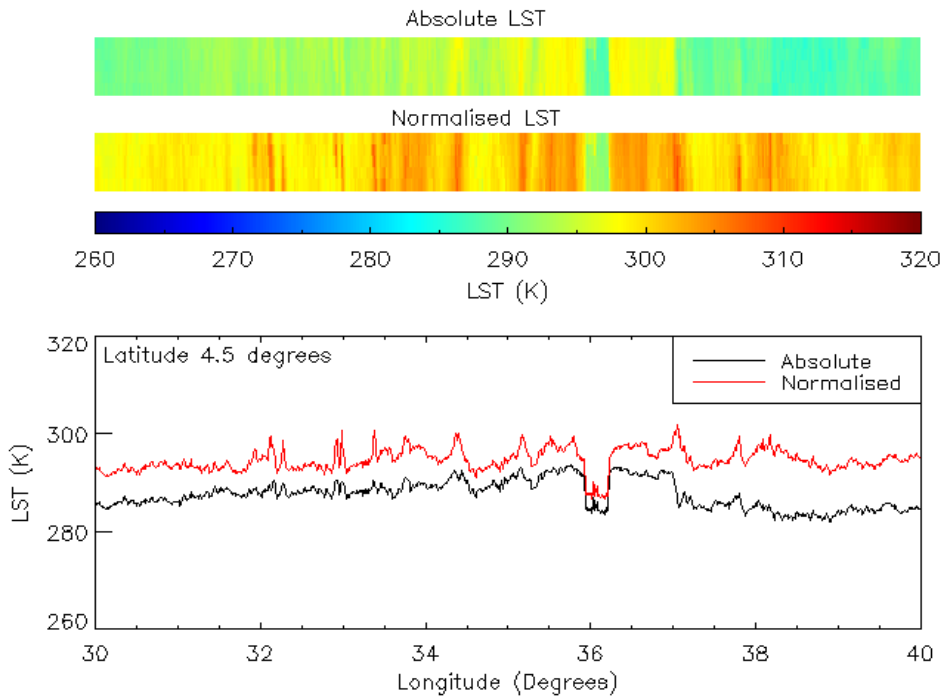
### PC3



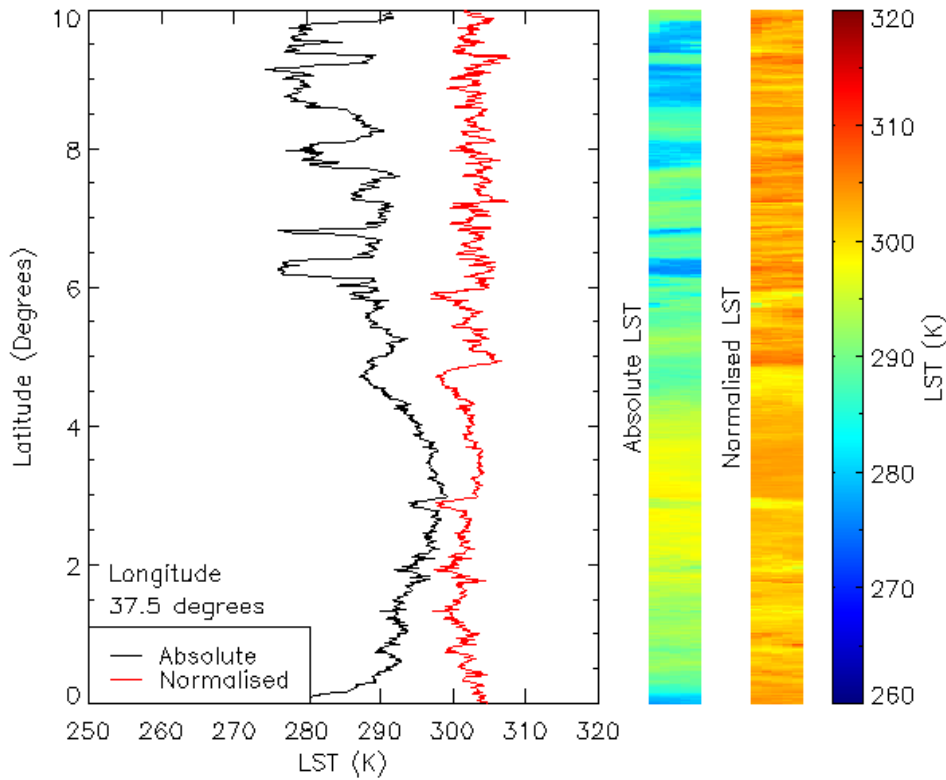
**Appendix 7B:** Absolute MODIS LST, PC4 and PC5 component loadings across the Turkana region for the period 2005 to 2008 from the Aqua dataset. The Turkana region is a  $10^{\circ} \times 10^{\circ}$  grid with the EARS of  $0.01^{\circ}$  resolution.



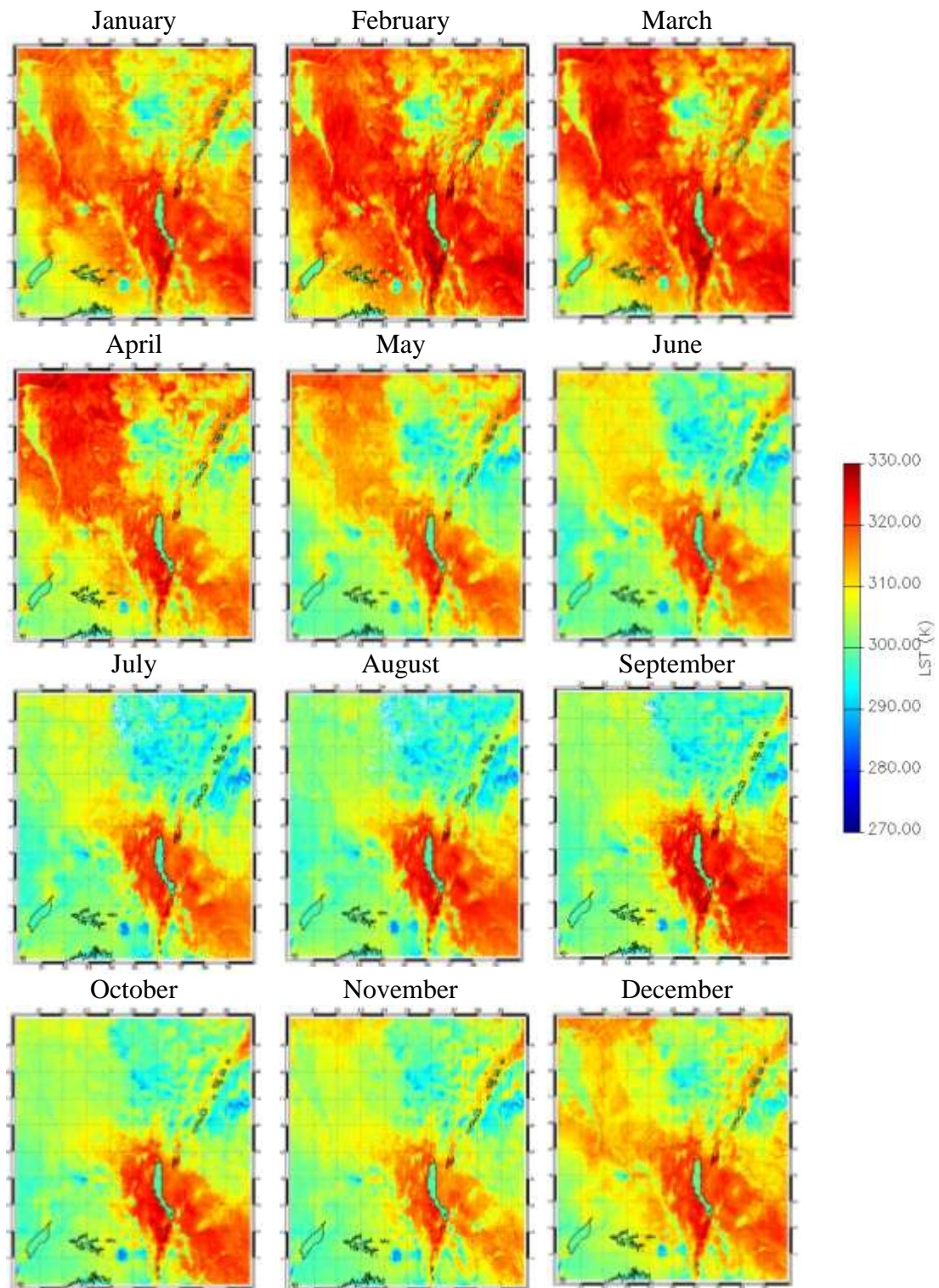
**Appendix 8A.** LST transect along 4.5° N latitude. LSTs shown are for the absolute and normalised MODIS LST means for night time 2006.



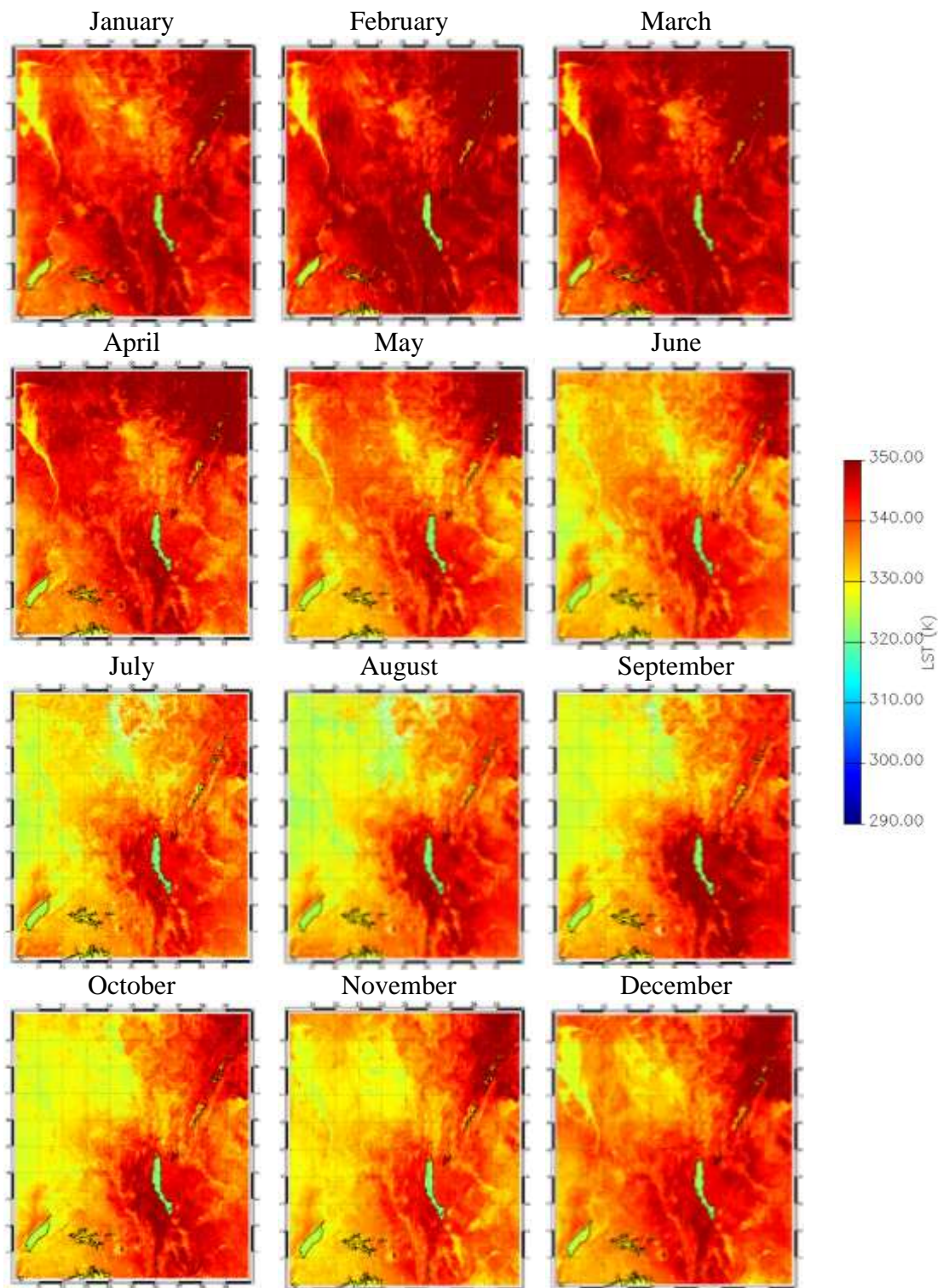
**Appendix 8B.** LST transect along 37.5° E longitude. LSTs shown are for the absolute and normalised MODIS LST means for night time 2006.



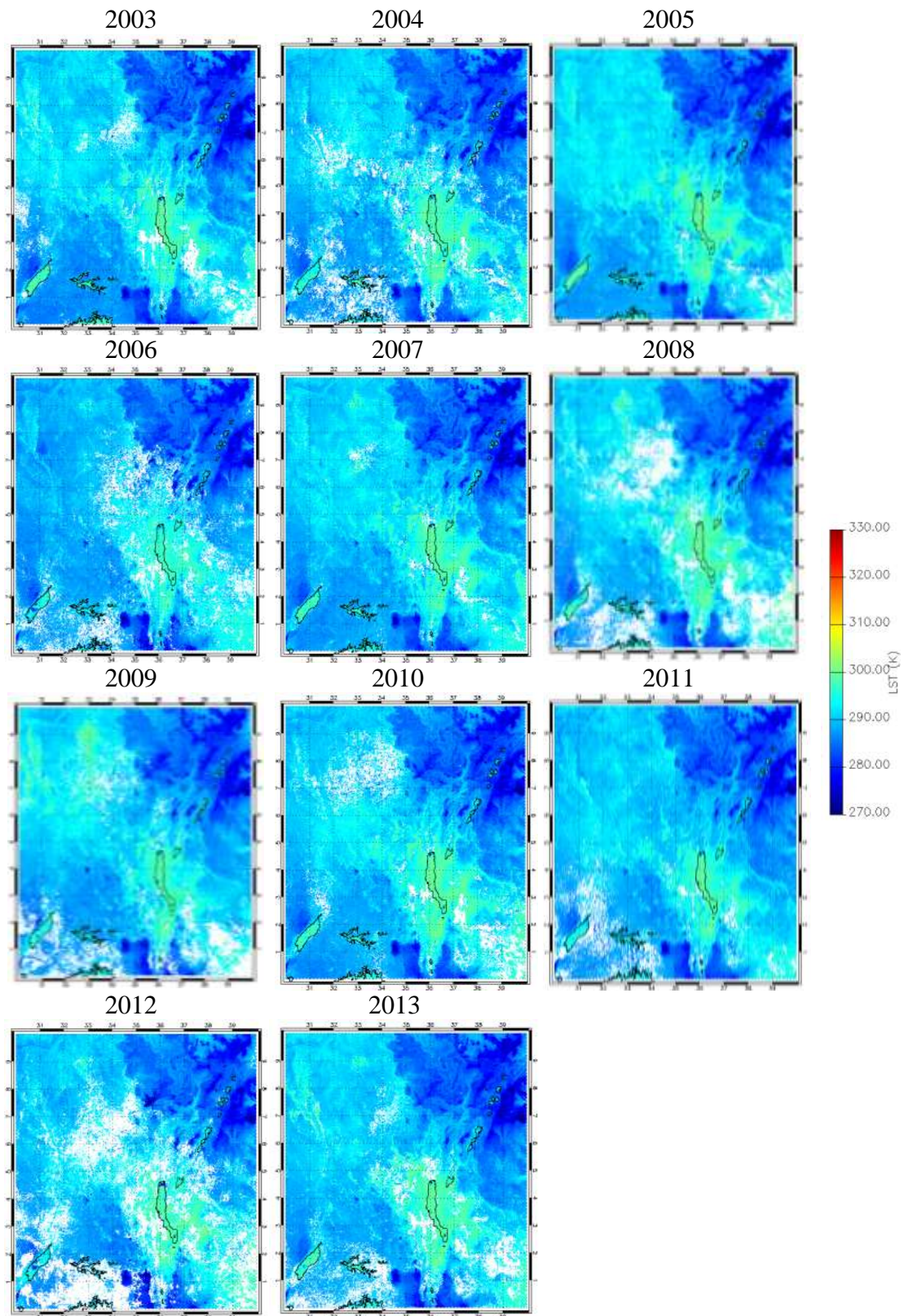
**Appendix 9A.** Absolute, day time climatology, derived from the Aqua MODIS LST dataset for 2003 through to 2013, across the 10° x 10° grid of the Turkana region at 0.01° resolution.



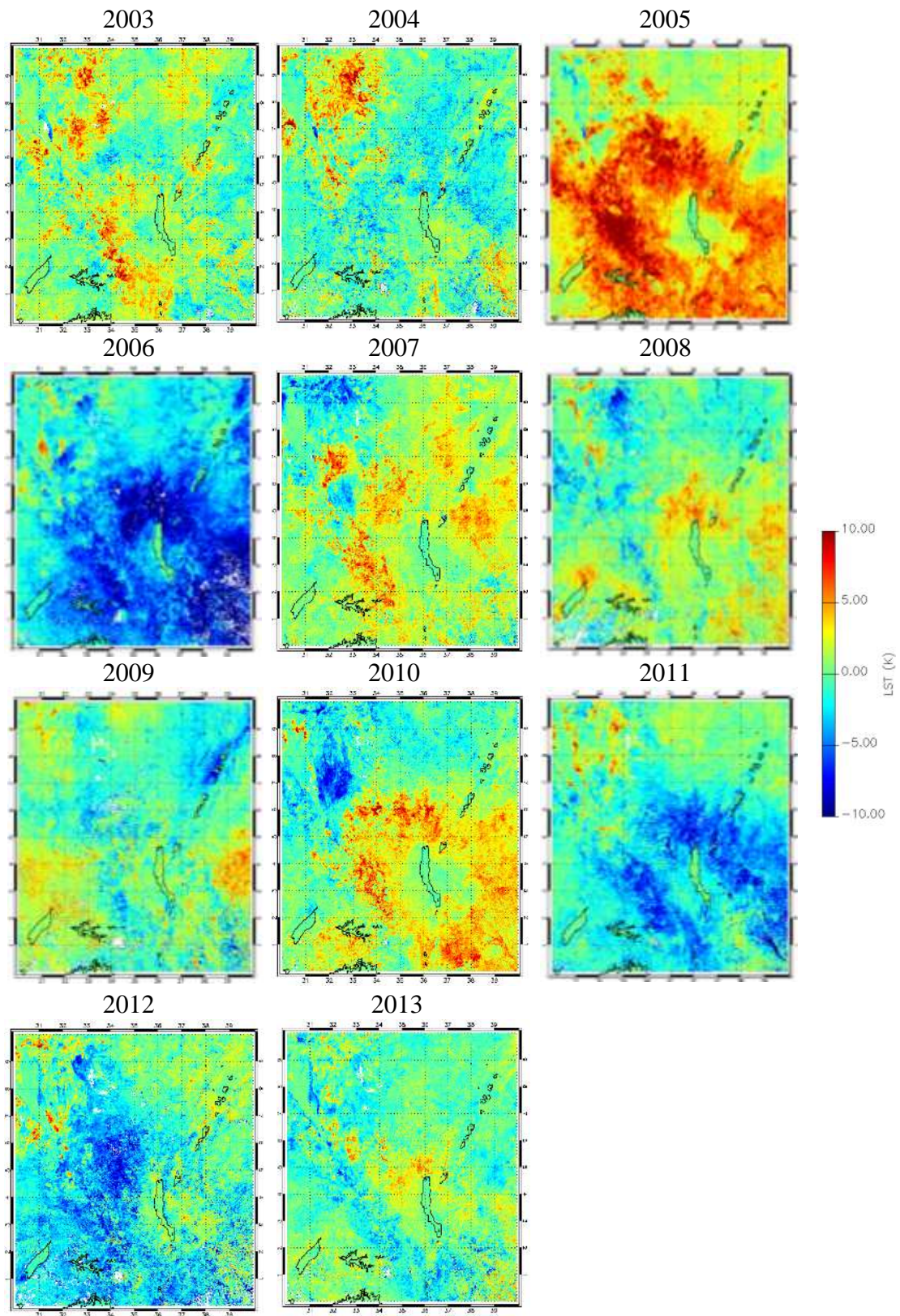
**Appendix 9B.** Normalised, day time climatology, derived from the Aqua MODIS LST dataset for 2003 through to 2013, across the  $10^{\circ} \times 10^{\circ}$  grid of the Turkana region at  $0.01^{\circ}$  resolution.



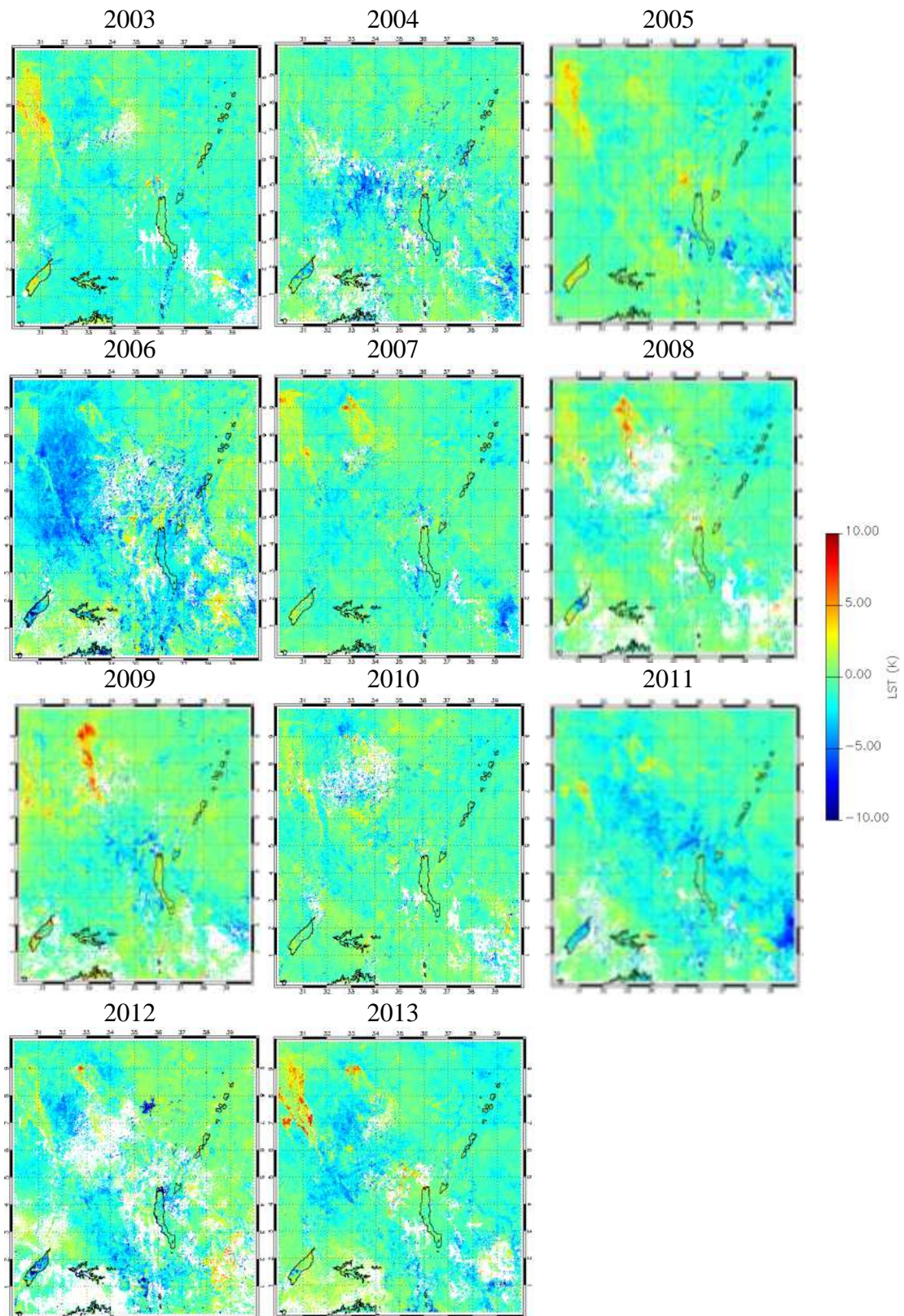
**Appendix 9C.** Absolute, night time climatology for December, derived from the Aqua MODIS LST dataset, for 2003 through to 2013, across the  $10^{\circ} \times 10^{\circ}$  grid of the Turkana region at  $0.01^{\circ}$  resolution.



**Appendix 10A.** Absolute, day time anomaly plots for December, derived from the Aqua MODIS LST dataset, for 2003 through to 2013, across the  $10^{\circ} \times 10^{\circ}$  grid of the Turkana region at  $0.01^{\circ}$  resolution.



**Appendix 10B.** Absolute, night time anomaly plots for December, derived from the Aqua MODIS LST dataset, for 2003 through to 2013, across the  $10^\circ \times 10^\circ$  grid of the Turkana region at  $0.01^\circ$  resolution.



# References

- Ackerman, S. and Knox, J.A., 2006. *Meteorology: understanding the atmosphere*. Cengage Learning.
- Africa Oil Corp, 2010. East Africa Rift Basin Oil Exploration Play. [http://www.africaoilcorp.com/i/pdf/aoi\\_may\\_2010.pdf](http://www.africaoilcorp.com/i/pdf/aoi_may_2010.pdf) [Accessed December 2015].
- Allaby, M., 2008. A Dictionary of Earth Science, third edition. *Oxford University Press*, ISBN-13: 9780199211944.
- Allen, D.J. and Darling, W.G., 1992. Geothermics and hydrogeology of the Kenya Rift Valley between Lake Baringo and Lake Turkana. *British Geological Survey Research Report SD/92/1*.
- Aretouyap, Z., Nouck, P.N. and Nouayou, R., 2016. A discussion of major geophysical methods used for geothermal exploration in Africa. *Renewable and Sustainable Energy Reviews*, 58, 775-781.
- Arino, O., Gross, D., Ranera, F., Leroy, M., Bicheron, P., Brockman, C., Defourny, P., Vancutsem, C., Achard, F., Durieux, L. and Bourg, L., 2007, July. GlobCover: ESA service for global land cover from MERIS. In *2007 IEEE International Geoscience and Remote Sensing Symposium*, 2412-2415. IEEE.
- Baret, F., Weiss, M., Lacaze, R., Camacho, F., Makhmara, H., Pacholczyk, P. and Smets, B., 2013. GEOV1: LAI and FAPAR essential climate variables and FCOVER global time series capitalizing over existing products. Part1: Principles of development and production. *Remote Sensing of Environment*, 137, 299-309.
- Becker, F. and Li, Z.L., 1995. Surface temperature and emissivity at various scales: Definition, measurement and related problems. *Remote Sensing Reviews*, 12 (3-4), 225-253.

- Bernard, V., Staffa, E., Mornstein, V. and Bourek, A., 2013. Infrared camera assessment of skin surface temperature—effect of emissivity. *Physica Medica*, 29 (6), 583-591.
- Birt, C.S., Maguire, P.K.H., Khan, M.A., Thybo, H., Keller, G.R. and Patel, J., 1997. The influence of pre-existing structures on the evolution of the southern Kenya Rift Valley - evidence from seismic and gravity studies. *Tectonophysics*, 278 (1), 211-242.
- Blackett, M., Wooster, M.J. and Malamud, B.D., 2011. Exploring land surface temperature earthquake precursors: A focus on the Gujarat (India) earthquake of 2001. *Geophysical Research Letters*, 38 (15).
- Blackwell, D.D. and Steele, J.L., 1989. Thermal conductivity of sedimentary rocks: measurement and significance. In *Thermal history of sedimentary basins* (13-36). Springer New York.
- Bonan, G., 2008. Ecological Climatology (2nd edition, 2008). *Cambridge University Press*.
- Brekke, C. and Solberg, A.H., 2005. Oil spill detection by satellite remote sensing. *Remote sensing of environment*, 95 (1), 1-13.
- British Geological Survey, 2011. Temperature and Thermal Properties Detailed. *BGS Report No: GR\_999999/1*.
- British Geological Survey, 2016, The Geological Times Scale: <http://www.bgs.ac.uk/discoveringGeology/time/timechart/home.html?src=topNav> [Accessed June 2016].
- Burns, B. and Leathwick, J.R., 1995. Geothermal vegetation dynamics. *Wellington: Department of Conservation*.
- Cai, Y., Jin, C., Wang, A., Guan, D., Wu, J., Yuan, F., Xu, L and Bu, C., 2014. Accuracy evaluation of the TRMM satellite-based precipitation data over the mid-high latitudes. *Yingyong Shengtai Xuebao*, 25(11).

- Cai, Y., Jin, C., Wang, A., Guan, D., Wu, J., Yuan, F. and Xu, L., 2015. Spatio-temporal analysis of the accuracy of tropical multisatellite precipitation analysis 3B42 precipitation data in mid-high latitudes of China. *PloS one*, 10(4), .e0120026.
- Calvin W.M., Coolbaugh M., Kratt C. & Vaughan R.G. 2005. Application of remote sensing technology to geothermal exploration. In *Rhoden, H.N., Steininger, R.C., and Vikre, P.G, Geological Society of Nevada Symposium 2005: Window to the World, Reno, Nevada, May 2005*, 1083–1089.
- Carroll, B.W. and Ostlie, D.A., 2006. *An introduction to modern astrophysics*. Benjamin Cummings.
- Cermak, V., Rybach, L., 1982. Thermal properties. In *Hellwege, K.H. (Ed.), Landolt-Beornstein Numerical Data and Functional Relationships in Science and Technology. New Series: Group V. Geophysics and Space Research, (1). Physical Properties of Rocks, subvol. A. Springer-Verlag*, 305–371.
- Chen, S., 2014. Reduction of a Symmetrical Matrix to Tridiagonal Form on GPUs. In *Ph.D thesis, University of Illinois*.
- Chorowicz, J., 2005. The east African rift system. *Journal of African Earth Sciences*, 43 (1), 379-410.
- Civiero, C., Hammond, J.O., Goes, S., Fishwick, S., Ahmed, A., Ayele, A., Doubre, C., Goitom, B., Keir, D., Kendall, J. and Leroy, S., 2015. Multiple mantle upwellings in the transition zone beneath the northern East-African Rift system from relative P-wave travel-time tomography. *Geochemistry, Geophysics, Geosystems*, 16 (9), 2949-2968.
- Clauser, C. and Huenges, E., 1995. Thermal conductivity of rocks and minerals. *Rock physics & phase relations: A handbook of physical constants*, 105-126.
- Cockerton, H.E., Street-Perrott, F.A., Barker, P.A., Leng, M.J., Sloane, H.J. and Ficken, K.J., 2015. Orbital forcing of glacial/interglacial variations in chemical weathering and silicon cycling within the upper White Nile basin, East Africa:

- Stable-isotope and biomarker evidence from Lakes Victoria and Edward. *Quaternary Science Reviews*, 130, 57-71.
- Cohen, A.S., Soreghan, M.J. and Scholz, C.A., 1993. Estimating the age of formation of lakes: an example from Lake Tanganyika, East African Rift system. *Geology*, 21 (6), 511-514.
- Coolbaugh, M.F., Taranik, J.V. and Kruse, F.A., 2000, Mapping of surface geothermal anomalies at Steamboat Springs, NV using NASA Thermal Infrared Multispectral Scanner (TIMS) and Advanced Visible and Infrared Imaging Spectrometer (AVIRIS) data. In *Proceedings of 14th Thematic Conference, Applied Geologic Remote Sensing*, 623-630.
- Coolbaugh, M.F., Kratt, C., Fallacaro, A., Calvin, W.M. and Taranik, J.V., 2007. Detection of geothermal anomalies using advanced spaceborne thermal emission and reflection radiometer (ASTER) thermal infrared images at Bradys Hot Springs, Nevada, USA. *Remote Sensing of Environment*, 106 (3), 350-359.
- Corti, G., 2012. Evolution and characteristics of continental rifting: Analog modelling-inspired view and comparison with examples from the East African Rift System. *Tectonophysics*, 522, 1-33.
- Danley, P.D., Husemann, M., Ding, B., DiPietro, L.M., Beverly, E.J. and Peppe, D.J., 2012. The impact of the geologic history and paleoclimate on the diversification of East African cichlids. *International journal of evolutionary biology*.
- De Almeida, T.I.R., Penatti, N.C., Ferreira, L.G., Arantes, A.E. and do Amaral, C.H., 2015. Principal component analysis applied to a time series of MODIS images: the spatio-temporal variability of the Pantanal wetland, Brazil. *Wetlands Ecology and Management*, 23 (4), 737-748.
- Dee, D.P., Uppala, S.M., Simmons, A.J., Berrisford, P., Poli, P., Kobayashi, S., Andrae, U., Balmaseda, M.A., Balsamo, G., Bauer, P. and Bechtold, P., 2011. The ERA-Interim reanalysis: Configuration and performance of the data assimilation system. *Quarterly Journal of the royal meteorological society*, 137 (656), 553-597.

- Dorigo, W., Jeu, R., Chung, D., Parinussa, R., Liu, Y., Wagner, W. and Fernández-Prieto, D., 2012. Evaluating global trends (1988–2010) in harmonized multi-satellite surface soil moisture. *Geophysical Research Letters*, 39 (18).
- Dou, L., Xiao, K., Cheng, D., Shi, B. and Li, Z., 2007. Petroleum geology of the Melut Basin and the Great palogue Field, Sudan. *Marine and petroleum geology*, 24 (3), 129-144.
- Duchscherer, Jr., W., 1982, Geochemical exploration for hydrocarbons, no new tricks - but an old dog. *Oil and Gas Journal*, 163-176.
- Dunkelman, T.J., Karson, J.A. and Rosendahl, B.R., 1988. Structural style of the Turkana rift, Kenya. *Geology*, 16 (3), 258-261.
- Dunkelman, T.J., Rosendahl, B.R. and Karson, J.A., 1989. Structure and stratigraphy of the Turkana rift from seismic reflection data. *Journal of African Earth Sciences (and the Middle East)*, 8 (2), 489-510.
- Dunkley, P.N., Smith, M., Allen, D.J. and Darling, W.G., 1993. The geothermal activity and geology of the northern sector of the Kenya Rift Valley. *British Geology Survey Research Report: SC/93/1*.
- Ebinger, C.J., 1989. Tectonic development of the western branch of the East African rift system. *Geological Society of America Bulletin*, 101 (7), 885-903.
- Ebinger, C., 2005. Continental break-up: the East African perspective. *Astronomy & Geophysics*, 46 (2), 2-16.
- Einarsson, G.M. and Kristinsson, S.G., 2010. Thermal Imaging of Geothermal Features. In *Proceedings World Geothermal Congress*, 25-29.
- Environmental Systems Research Institute, Inc., 2007. ArcGIS 9.2 Desktop Help: <http://webhelp.esri.com/arcgisdesktop/9.2/> [Accessed July 2016].
- EUMETSAT, 2016. METEOSAT DESIGN - Meteosat Second Generation spacecraft: <http://www.eumetsat.int/website/home/Satellites/CurrentSatellites/Meteosat/MeteosatDesign/index.html> [Accessed March 2016].

- European Space Agency (ESA), 2012. Soil Moisture CCI: Overview: <http://www.esa-soilmoisture-cci.org/node/93> [Accessed June 2016].
- Fairhead, J.D., 1976. The structure of the lithosphere beneath the Eastern Rift, East Africa, deduced from gravity studies. *Tectonophysics*, 30 (3), 269-298.
- Farr, T.G., Rosen, P.A., Caro, E., Crippen, R., Duren, R., Hensley, S., Kobrick, M., Paller, M., Rodriguez, E., Roth, L. and Seal, D., 2007. The shuttle radar topography mission. *Reviews of geophysics*, 45 (2).
- Fang, L., Yu, Y., Xu, H. and Sun, D., 2014. New Retrieval Algorithm for Deriving Land Surface Temperature from Geostationary Orbiting Satellite Observations. *IEEE Transactions on Geoscience and Remote Sensing*, 52 (2), 819-828.
- Fjaer, E., Holt, R.M., Horsrud, P., Raaen, A.M. and Rines, R., 2008. *Petroleum Related Rock Mechanics, second ed. Elsevier Science Publ., Amsterdam.*
- Foster, D.A. and Gleadow, A.J., 1996. Structural framework and denudation history of the flanks of the Kenya and Anza Rifts, East Africa. *Tectonics*, 15 (2), 258-271.
- Foster, D.A. and Gleadow, A.J., 1992. The morphotectonic evolution of rift-margin mountains in central Kenya: constraints from apatite fission-track thermochronology. *Earth and Planetary Science Letters*, 113 (1), 157-171.
- Fu P. and Rich P.M., 2002. A geometric solar radiation model and its applications in agriculture and forestry. *Computers and Electronics in Agriculture*, 37 (1-3): 25-35.
- Gallo, K., Hale, R., Tarpley, D. and Yu, Y., 2011. Evaluation of the relationship between air and land surface temperature under clear-and cloudy-sky conditions. *Journal of Applied Meteorology and Climatology*, 50 (3), 767-775.
- Ghent D., 2012. Land Surface Temperature Validation and Algorithm Verification. *Report to European Space Agency.*

- Gong, G., 2005. Physical properties of alpine rocks: a laboratory investigation. In *Ph.D. thesis. University of Geneva.*
- Gradstein, F.M., Ogg, J.G., Schmitz, M. and Ogg, G., 2012. *The geologic time scale 2012 2-volume set.* Elsevier.
- Griffiths, C.M., Brereton, N.R., Beausillon, R., Castillo, D., 1992. Thermal conductivity prediction from petrophysical data: a case study. In: Hurst, A., Griffiths, C.M., Worthington, P.F. (Eds.), *Geological Applications of Wireline Logs II. Geological Society, London, 299–315. Special Publication No. 65, London.*
- Harvey, T. J., 1976. The paleolimnology of Lake Mobutu Sese Seko, Uganda-Zaire: The last 28,000 years. In *Ph.D. thesis. Duke University.*
- Holmes, C.S. and Swift, S.C., 1970. Calculation of circulating mud temperatures. *Journal of Petroleum Technology*, 22 (06), 670-674.
- Huffman, G.J. and Bolvin, D.T., 2014. TRMM and Other Data Precipitation Data Set Documentation. NASA: Goddard Earth Sciences Data and Information Services Center (GES DISC): [ftp://precip.gsfc.nasa.gov/pub/trmmdocs/3B42\\_3B43\\_doc.pdf](ftp://precip.gsfc.nasa.gov/pub/trmmdocs/3B42_3B43_doc.pdf) [Accessed May 2016].
- Iyengar, G.R., Ramesh, K.J., Paliwal, R.K. and Madan, O.P., 2001. Structural characteristics of the Inter Tropical Convergence Zone over the equatorial Indian Ocean during INDOEX-1999 field phase experiment. *CURRENT SCIENCE (SUPPLEMENT)*, 80, 18.
- Janza, F.J., 1975. Interaction mechanisms. *Manual of remote sensing*, 1, 75-179.
- Jessop, A.M., 1990. Thermal Geophysics. *Elsevier.*
- Jha, M.N., Levy, J. and Gao, Y., 2008. Advances in remote sensing for oil spill disaster management: state-of-the-art sensors technology for oil spill surveillance. *Sensors*, 8 (1), 236-255.

- Joiner, J. and Poli, P., 2005. Note on the effect of horizontal gradients for nadir-viewing microwave and infrared sounders. *Quarterly Journal of the Royal Meteorological Society*, 131(608), 1783-1792.
- Justice, C.O., Townshend, J.R.G., Vermote, E.F., Masuoka, E., Wolfe, R.E., Saleous, N., Roy, D.P. and Morisette, J.T., 2002. An overview of MODIS Land data processing and product status. *Remote sensing of Environment*, 83 (1), 3-15.
- Kearey, P., Klepeis, K.A. and Vine, F.J., 2013. Global tectonics. *Blackwell Publishing*.
- Kiage, L.M. and Liu, K.B., 2009. Palynological evidence of climate change and land degradation in the Lake Baringo area, Kenya, East Africa, since AD 1650. *Palaeogeography, Palaeoclimatology, Palaeoecology*, 279 (1), 60-72.
- Kuper, G., 2016. The Relevance of Surface Temperature in Predicting Source Rock Maturity and Hydrocarbon Generation. *Tullow Oil Plc. NV Technical Team – Petroleum Systems Team*.
- Lagat, J., 2010. Direct utilization of geothermal resources in Kenya. In *Proceedings of the World Geothermal Congress 2010, Bali, Indonesia*.
- Lehigh University, 2010. Environmental Literacy and Inquiry – Heat flow, Geothermal Gradient: <http://www.ei.lehigh.edu/eli/tectonics/support/heatflow/heatflow2.html> [Accessed February 2016].
- Leilei, L., Jianrong, F. and Yang, C., 2014. The relationship analysis of vegetation cover, rainfall and land surface temperature based on remote sensing in Tibet, China. In *IOP Conference Series: Earth and Environmental Science*, 17 (1).
- Li, H., Sun, D., Yu, Y., Wang, H., Liu, Y., Liu, Q., Du, Y., Wang, H. and Cao, B., 2014. Evaluation of the VIIRS and MODIS LST products in an arid area of Northwest China. *Remote Sensing of Environment*, 142, 111-121.
- Liang, S., Li, X. and Wang, J. eds., 2012. *Advanced remote sensing: terrestrial information extraction and applications*. Academic Press.

- Liu, Y.Y., Dorigo, W.A., Parinussa, R.M., de Jeu, R.A.M., Wagner, W., McCabe, M.F., Evans, J.P., van Dijk, A.I.J.M., 2012. Trend-preserving blending of passive and active microwave soil moisture retrievals, *Remote Sensing of Environment*, 123, 280-297.
- Liu, S. and Lei, X., 2013. December. Geothermal regime of Tarim basin, NW China: insights from borehole temperature logging. In *AGU Fall Meeting Abstracts*, 1, 2464.
- Liu, Y.Y., Parinussa, R.M., Dorigo, W.A., De Jeu, R.A.M., Wagner, W., van Dijk, A.I.J.M., McCabe, M.F., & Evans, J.P., 2011. Developing an improved soil moisture dataset by blending passive and active microwave satellite based retrievals. *Hydrology and Earth System Sciences*, 15, 425-436.
- Liu, Y., Yamaguchi, Y. and Ke, C., 2007. Reducing the discrepancy between ASTER and MODIS land surface temperature products. *Sensors*, 7 (12), 3043-3057.
- McCarthy, K., Rojas, K., Niemann, M., Palmowski, D., Peters, K. and Stankiewicz, A., 2011. Basic petroleum geochemistry for source rock evaluation. *Oilfield Review*, 23 (2), 32-43.
- Mariita, N.O. and Keller, G.R., 2007. An integrated geophysical study of the northern Kenya rift. *Journal of African Earth Sciences*, 48 (2), 80-94.
- Mather P, 2004. Computer processing of remotely-sensed images. *Wiley, New York*.
- Midttømme, K. and Roaldset, E., 1998. The effect of grain size on thermal conductivity of quartz sands and silts. *Petroleum Geoscience*, 4 (2), 165-172.
- Miliaresis, G.C., 2009. Regional thermal and terrain modelling of the Afar Depression from MODIS multi-temporal monthly night LST data. *International Journal of Remote Sensing*, 30 (9), 2429-2436.
- Miliaresis, G., 2012. Selective variance reduction of multi-temporal lst imagery in the east Africa rift system. *Earth Science Informatics*, 5 (1), 1-12.

- Miliaresis, G.C., 2013. Terrain analysis for active tectonic zone characterization: a new application for MODIS night LST (MYD11C3) data set. *International Journal of Geographical Information Science*, 27 (7), 1417-1432.
- Miller, J.B., 1975. LANDSAT image studies as applied to petroleum exploration in Kenya. NASA. *Lyndon B. Johnson Space Center NASA Earth Resources Survey. Symposium*, 1-B, 605-624.
- Mira, M., Valor, E., Boluda, R., Caselles, V. and Coll, C., 2007. Influence of soil water content on the thermal infrared emissivity of bare soils: Implication for land surface temperature determination. *Journal of Geophysical Research: Earth Surface*, 112 (F4).
- Modest, M.F., 2013. Radiative heat transfer. *Academic press*.
- Mohr, P.A., 1963. The Geology of Ethiopia. *Haile Selassie University Press, Addis Ababa*.
- Mwangi, M., 2005. Country update report for Kenya 2000-2005. In *Proceedings World Geothermal Congress Turkey*, 24-29 April 2005, 24-29.
- NASA, 2015. Precipitation Measurement Missions: TRMM Mission comes to an end after 17 years: <http://pmm.nasa.gov/trmm/mission-end> [Accessed: May 2016].
- NASA, 2016. MODIS: <http://modis.gsfc.nasa.gov/> [Accessed March 2016].
- NASA Earth Observatory, Images, 2016. Finding the Hottest Spots on Earth by Satellite: Image of the Day: <http://earthobservatory.nasa.gov/IOTD/view.php?id=77779> [Accessed February 2016].
- NASA: Goddard Earth Sciences Data and Information Services Center (GES DISC), 2014, Readme for TRMM Product 3B43 (V7): [http://disc.sci.gsfc.nasa.gov/precipitation/documentation/TRMM\\_README/TRMM\\_3B43\\_readme.shtml](http://disc.sci.gsfc.nasa.gov/precipitation/documentation/TRMM_README/TRMM_3B43_readme.shtml) [Accessed: May 2016].

- National Physics Laboratory, 2014. What is emissivity and why is it important? (FAQ - Thermal): [http://www.npl.co.uk/reference/faqs/what-is-emissivity-and-why-is-it-important-\(faq-thermal\)](http://www.npl.co.uk/reference/faqs/what-is-emissivity-and-why-is-it-important-(faq-thermal)) [Accessed June 2016].
- Nicholson, S.E., 1999. Historical and modern fluctuations of lakes Tanganyika and Rukwa and their relationship to rainfall variability. *Climatic Change*, 41 (1), 53-71.
- NOAA, 2015. GOES Land Surface Temperature: <http://www.ospo.noaa.gov/Products/land/glst/> [Accessed March 2026].
- Nunez, M.N., Ciapessoni, H.H., Rolla, A., Kalnay, E. and Cai, M., 2008. Impact of land use and precipitation changes on surface temperature trends in Argentina. *Journal of Geophysical Research: Atmospheres*, 113 (D6).
- Odada, E.O., Onyando, J. and Obudho, P. A., 2006. Lake Baringo Experience and Lessons learned brief. *University of Nairobi, Nairobi, Kenya*.
- Olago, D.O. and Odada, E.O., 2000. An inter-basinal comparison of the sedimentology of Late Holocene to recent sediments in the Rift Valley, Lake Turkana, Kenya. *Journal of African Earth Sciences*, 31 (2), 237-252.
- Omenda, P.A., 1998. The geology and structural controls of the Olkaria geothermal system, Kenya. *Geothermics*, 27 (1), 55-74.
- Omenda, P.A., 2008: Geothermal activity of the East African Rift. In *Short Course III on Exploration for Geothermal Resources, organized by UNU-GTP and KenGen, Naivasha*.
- Oxford Index: A search and discovery gateway, 2016. Geothermal Gradient. *Oxford University Press*: <http://oxfordindex.oup.com/view/10.1093/oi/authority.20110803095849139> [Accessed February 2016].
- Palmer, J.M., 1995. The measurement of transmission, absorption, emission, and reflection. *Handbook of optics*.

- Pouteau R., Rambal S., Ratte J.P., Gogé F., Joffre R. and Winkel T., 2011. Downscaling MODIS-derived maps using GIS and boosted regression trees; the case of frost occurrence over the Andean highlands of Bolivia. *Remote Sensing of Environment*, 115: 117-129.
- Presley, M.A., 2002, March. What can thermal inertia do for you? In *Lunar and Planetary Science Conference*, 33, 1144.
- Press, W.H., Flannery, B.P., Teukolsky, S.A., Vetterling, W.T. and Kramer, P.B., 1987. Numerical recipes: the art of scientific computing.
- Qiuji, C. and Chuting, L., 2015. Land Surface Temperature Retrieval Based on Landsat ETM+/TM--Taking Xi'an City as an Example. *Open Cybernetics & Systemics Journal*, 9, 228-235.
- Rees, W.G., 2013. Physical principles of remote sensing. *Cambridge University Press*.
- Ring, U., 2014. The East African Rift System. *Austrian Journal of Earth Science*, 107 (1), 132-146.
- Rop, B.K., 2013. Petroleum potential of the Chalbi basin, NW Kenya. *Journal of the Geological Society of India*, 81 (3), 405-414.
- Russell, J.M., Johnson, T.C., Kelts, K.R., Lærdal, T. and Talbot, M.R., 2003. An 11 000-year lithostratigraphic and paleohydrologic record from equatorial Africa: Lake Edward, Uganda–Congo. *Palaeogeography, Palaeoclimatology, Palaeoecology*, 193 (1), 25-49.
- Rybach, L. and Muffler, L.J.P., 1981. Geothermal Systems: Principles and Case Histories. *John Wiley & Sons*.
- Sabins, F.F., 1996. Remote Sensing Principles and Interpretation. *W. H. Freeman*.
- Saemundsson, K., 2008. East African rift system: An overview. In *Short Course III, UNU-GTP, Lake Naivasha, Kenya*.

- Saraf, A.K., Mishra, B.P., Choudhury, S. and Ghosh, P., 2005. Digital elevation model (DEM) generation from NOAA–AVHRR night-time data and its comparison with USGS-DEM. *International journal of remote sensing*, 26 (18), 3879-3887.
- Savage, R.J. and Williamson, P.G., 1978. The early history of the Turkana Depression. *Geological Society, London, Special Publications*, 6 (1), 375-394.
- Schlumberger, 2016, Oilfield Glossary, <http://www.glossary.oilfield.slb.com/> [Accessed June 2016].
- Schmugge, T., Ogawa, K. and DE ROSNAY, P., 2007. Satellite observations of the land surface emissivity in the 8-12  $\mu\text{m}$  window: effect of soil moisture. *IAHS-AISH publication*, 16-21.
- Schön, J.H., 2015. Physical properties of rocks: fundamentals and principles of petrophysics. *Elsevier*.
- Schull, T.J., 1988. Oil Exploration in Nonmarine Rift Basins of Interior Sudan. *Houston Geological Society Bulletin*, 30 (5), 13.
- Sepulchre, P., Ramstein, G., Fluteau, F., Schuster, M., Tiercelin, J.J. and Brunet, M., 2006. Tectonic uplift and Eastern Africa aridification. *Science*, 313 (5792), 1419-1423
- Shako, L. and Mutua, J., 2011. Geo-scientific data integration to evaluate geothermal potential using GIS. In *Proceedings, Kenya Geothermal Conference, November, Nairobi*.
- Smith, L.I., 2002. A tutorial on principal components analysis. *Cornell University, USA*, 51 (52), 65.
- Smith, R. N. B., Blyth, E. M., Finch, J. W., Goodchild, S., Hall, R. L. and Madry, S., 2006. Soil state and surface hydrology diagnosis based on MOSES in the Met Office Nimrod now casting system. *Meteorological Applications*, 13 (02), 89–109.

- Smith, B. and Sandwell, D., 2003. Accuracy and resolution of shuttle radar topography mission data. *Geophysical Research Letters*, 30 (9).
- Stroppiana, D., Antoninetti, M. and Brivio, P.A., 2014. Seasonality of MODIS LST over Southern Italy and correlation with land cover, topography and solar radiation. *European Journal of Remote Sensing*, 47, 133-152.
- Susskind, J., Rosenfield, J. and Reuter, D., 1983. An accurate radiative transfer model for use in the direct physical inversion of HIRS2 and MSU temperature sounding data. *Journal of Geophysical Research: Oceans*, 88 (C13), 8550-8568.
- Talbot, M.R., Morley, C.K., Tiercelin, J.J., Le Hérisse, A., Potdevin, J.L. and Le Gall, B., 2004. Hydrocarbon potential of the Meso-Cenozoic Turkana Depression, northern Kenya. II. Source rocks: quality, maturation, depositional environments and structural control. *Marine and Petroleum Geology*, 21 (1), 63-78.
- Tianyu, L., Guonian, L., & Tongning W, 2012. Application of land surface temperature inversion based on emissivity mixture analysis at sub-pixel scale in geothermal exploration. In *Proceedings of Second International Workshop on Earth Observation and Remote Sensing Applications*.
- Tiercelin, J.J., Pflumio, C., Castrec, M., Boulégué, J., Gente, P., Rolet, J., Coussement, C., Stetter, K.O., Huber, R., Buku, S. and Mifundu, W., 1993. Hydrothermal vents in Lake Tanganyika, East African Rift system. *Geology*, 21 (6), 499-502.
- Tissot, B.P. and Welte, D.H., 1984. Petroleum Formation and Occurrence, Second Revised and Enlarged Edition. *Springer-Verlag*.
- Trenberth, K.E. and Shea, D.J., 2005. Relationships between precipitation and surface temperature. *Geophysical Research Letters*, 32 (14).
- Trenberth, K.E., Fasullo, J.T. and Kiehl, J., 2009. Earth's global energy budget. *Bulletin of the American Meteorological Society*, 90 (3), 311-323.
- Tullow Oil plc, 2013. Tullow's East Africa Rift Basin campaign in Uganda and Kenya. In *East Africa Forum Finding Petroleum – London*.

- Tullow Oil plc, 2014. Tullow in Kenya, <http://www.tulloil.com/Media/docs/default-source/operations/tullow-kenya-profile.pdf?sfvrsn=2> [Accessed July 2016].
- UCLouvain and ESA, 2011, GLOBCOVER 2009 Product description and validation report:  
[http://due.esrin.esa.int/files/GLOBCOVER2009\\_Validation\\_Report\\_2.2.pdf](http://due.esrin.esa.int/files/GLOBCOVER2009_Validation_Report_2.2.pdf)  
[Accessed June 2016].
- U.S Geological Survey, 2016, Landsat 8 (L8) Data Users Handbook Version 2.0:  
<https://landsat.usgs.gov/sites/default/files/documents/Landsat8DataUsersHandbook.pdf>
- Valenti, G.L., Phelps, J.C. and Eisenberg, L.L., 1996. Geological remote sensing for hydrocarbon exploration in Papua New Guinea. In *Thematic conference on geologic remote sensing, Las Vegas, NV (United States), 27-29 Feb 1996*.
- Van Damme, D. and Pickford, M., 2003. The late Cenozoic Thiaridae (Mollusca, Gastropoda, Cerithioidea) of the Albertine Rift Valley (Uganda-Congo) and their bearing on the origin and evolution of the Tanganyikan thalassoid malacofauna. *Hydrobiologia*, 498 (1-3), 1-83.
- Van De Kerchove, R., Lhermitte, S., Veraverbeke, S. and Goossens, R., 2013. Spatio-temporal variability in remotely sensed land surface temperature, and its relationship with physiographic variables in the Russian Altay Mountains. *International Journal of Applied Earth Observation and Geoinformation*, 20, 4-19.
- Verschuren, D., Damsté, J.S.S., Moernaut, J., Kristen, I., Blaauw, M., Fagot, M., Haug, G.H., van Geel, B., De Batist, M., Barker, P. and Vuille, M., 2009. Half-precessional dynamics of monsoon rainfall near the East African Equator. *Nature*, 462 (7273), 637-641.

- Vétel, W., Le Gall, B. and Walsh, J.J., 2005. Geometry and growth of an inner rift fault pattern: the Kino Sogo Fault Belt, Turkana Rift (North Kenya). *Journal of Structural Geology*, 27 (12), 2204-2222.
- Vidot, J., 2014. Overview of the status of radiative transfer models for satellite data assimilation. In *ECMWF Seminar on the Use of Satellite Observations in NWP, 8–12 September 2014*.
- Vosteen, H.D. and Schellschmidt, R., 2003. Influence of temperature on thermal conductivity, thermal capacity and thermal diffusivity for different types of rock. *Physics and Chemistry of the Earth, Parts A/B/C*, 28 (9), 499-509.
- Wagner, W., W. Dorigo, R. de Jeu, D. Fernandez, J. Benveniste, E. Haas, M. Ertl, 2012. Fusion of active and passive microwave observations to create an Essential Climate Variable data record on soil moisture. *ISPRS Annals of the Photogrammetry, Remote Sensing and Spatial Information Sciences, Volume I-7, 2012. XXII ISPRS Congress, 25 August – 01 September 2012, Melbourne, Australia*.
- Wan, Z., 1999. MODIS Land-Surface Temperature Algorithm Theoretical Basis Document (LST ATBD) Version 3.3. *Institute for Computational Earth System Science, University of California, Santa Barbara*.
- Wan, Z., 2006. Collection-5 MODIS land surface temperature products users' guide. *ICESSE, University of California, Santa Barbara*.
- Wan, Z. and Dozier, J., 1996. A generalized split-window algorithm for retrieving land-surface temperature from space. *Geoscience and Remote Sensing, IEEE Transactions on*, 34 (4), 892-905.
- Wan, Z. and Li, Z.L., 1997. A physics-based algorithm for retrieving land-surface emissivity and temperature from EOS/MODIS data. *Geoscience and Remote Sensing, IEEE Transactions on*, 35 (4), 980-996.

- Wender, L.E. and Sabins, F.F., 1991. Geologic interpretation of satellite images, Saudi Arabia. In. *Society of Petroleum Engineers Middle East Oil Show, 16-19 November 1991*.
- Wichura, H., Bousquet, R., Oberhänsli, R., Strecker, M.R. and Trauth, M.H., 2010. Evidence for middle Miocene uplift of the East African Plateau. *Geology*, 38 (6), 543-546.
- Wu, R., Chen, J. and Wen, Z., 2013. Precipitation-surface temperature relationship in the IPCC CMIP5 models. *Advances in Atmospheric Sciences*, 30, 766-778.
- Yang, H., Meer, F.V.D., Zhang, J. and Kroonenberg, S.B., 2000. Direct detection of onshore hydrocarbon microseepages by remote sensing techniques. *Remote sensing reviews*, 18 (1), 1-18.
- Yao, X., Fu, B., Lü, Y., Sun, F., Wang, S. and Liu, M., 2013. Comparison of four spatial interpolation methods for estimating soil moisture in a complex terrain catchment. *PloS one*, 8 (1), 54660.
- Yineger, H., Kelbessa, E., Bekele, T. and Lulekal, E., 2007. Ethnoveterinary medicinal plants at bale mountains national park, Ethiopia. *Journal of Ethnopharmacology*, 112 (1), 55-70.
- Zeng, C., Shen, H., Zhong, M., Zhang, L. and Wu, P., 2015. Reconstructing MODIS LST based on multitemporal classification and robust regression. *Geoscience and Remote Sensing Letters, IEEE*, 12 (3), 512-516.
- Zoran, M., 2012. MODIS and NOAA-AVHRR 1 and surface temperature data detect a thermal anomaly preceding the 11 March 2011 Tohoku earthquake. *International journal of remote sensing*, 33 (21), 6805-6817.
- Zouzias, D., Miliareisis, G.C. and Seymour, K.S., 2011. Probable regional geothermal field reconnaissance in the Aegean region from modern multi-temporal night LST imagery. *Environmental Earth Sciences*, 62 (4), 717-723.

*Data for this research was taken from NASA Land Processes Distributed Active Archive Center (LP DAAC). USGS/Earth Resources Observation and Science (EROS) Center, Sioux Falls, South Dakota (2001).*

*This research used the ALICE High Performance Computing Facility at the University of Leicester.*